

1996

Boundary layer development in multi-stage low pressure turbines

David Elmer Halstead
Iowa State University

Follow this and additional works at: <https://lib.dr.iastate.edu/rtd>

 Part of the [Aerospace Engineering Commons](#), and the [Mechanical Engineering Commons](#)

Recommended Citation

Halstead, David Elmer, "Boundary layer development in multi-stage low pressure turbines " (1996). *Retrospective Theses and Dissertations*. 11528.
<https://lib.dr.iastate.edu/rtd/11528>

This Dissertation is brought to you for free and open access by the Iowa State University Capstones, Theses and Dissertations at Iowa State University Digital Repository. It has been accepted for inclusion in Retrospective Theses and Dissertations by an authorized administrator of Iowa State University Digital Repository. For more information, please contact digirep@iastate.edu.

INFORMATION TO USERS

This manuscript has been reproduced from the microfilm master. UMI films the text directly from the original or copy submitted. Thus, some thesis and dissertation copies are in typewriter face, while others may be from any type of computer printer.

The quality of this reproduction is dependent upon the quality of the copy submitted. Broken or indistinct print, colored or poor quality illustrations and photographs, print bleedthrough, substandard margins, and improper alignment can adversely affect reproduction.

In the unlikely event that the author did not send UMI a complete manuscript and there are missing pages, these will be noted. Also, if unauthorized copyright material had to be removed, a note will indicate the deletion.

Oversize materials (e.g., maps, drawings, charts) are reproduced by sectioning the original, beginning at the upper left-hand corner and continuing from left to right in equal sections with small overlaps. Each original is also photographed in one exposure and is included in reduced form at the back of the book.

Photographs included in the original manuscript have been reproduced xerographically in this copy. Higher quality 6" x 9" black and white photographic prints are available for any photographs or illustrations appearing in this copy for an additional charge. Contact UMI directly to order.

UMI

A Bell & Howell Information Company
300 North Zeeb Road, Ann Arbor MI 48106-1346 USA
313/761-4700 800/521-0600

Boundary layer development in multi-stage low pressure turbines

by

David Elmer Halstead

A dissertation submitted to the graduate faculty
in partial fulfillment of the requirement for the degree of
DOCTOR OF PHILOSOPHY

Major: Mechanical Engineering

Major Professors: Theodore H. Okiishi and David C. Wisler

Iowa State University

Ames, Iowa

1996

Copyright © David Elmer Halstead, 1996. All rights reserved.

UMI Number: 9712556

**Copyright 1996 by
Halstead, David Elmer**

All rights reserved.

**UMI Microform 9712556
Copyright 1997, by UMI Company. All rights reserved.**

**This microform edition is protected against unauthorized
copying under Title 17, United States Code.**

UMI
300 North Zeeb Road
Ann Arbor, MI 48103

Graduate College
Iowa State University

This is to certify that the doctoral dissertation of
David Elmer Halstead
has met the dissertation requirements of Iowa State University

Signature was redacted for privacy.

Co-Major Professor

Signature was redacted for privacy.

Co-Major Professor

Signature was redacted for privacy.

For the Major Program

Signature was redacted for privacy.

For the Graduate College

TABLE OF CONTENTS

LIST OF FIGURES	vii
LIST OF TABLES	xiii
NOMENCLATURE	xiv
ACKNOWLEDGEMENTS	xix
ABSTRACT	xxi
CHAPTER 1. INTRODUCTION AND OBJECTIVES	1
1.1 Nature of Problem	1
1.2 Objectives	2
1.3 Overview of Approach	3
CHAPTER 2. REVIEW OF PAST RESEARCH	4
2.1 Flat Plate Studies in Wind Tunnels	4
2.2 Turbine Cascade Tests	6
2.3 Tests of Single and Multi-Stage Turbines	8
CHAPTER 3. SURFACE HOT-FILM ANEMOMETRY	11
3.1 Principles of Technique	11
3.2 Applications to the Study of Boundary Layer Development	16
3.3 Interpretation of Surface Hot-Film Measurements	20
3.3.1 Boundary Layer Development with Separated-Flow Transition	20
3.3.2 Boundary Layer Development with Attached-Flow Transition	23
CHAPTER 4. TEST FACILITY	30
4.1 Test Vehicle	30
4.2 Turbine Operating Domain	34
4.3 Overall Turbine Performance	37
CHAPTER 5. EXPERIMENTAL INSTRUMENTATION AND MEASUREMENTS	40
5.1 Thermal Anemometry System	40
5.2 Surface Hot-Film Measurements	42
5.2.1 Description of Sensors	42
5.2.2 Instrumentation of Airfoil	44
5.2.3 Operation of Sensors and Acquisition of Measurements	46
5.3 X Hot-Film Probe Measurements	50
5.3.1 Calibration Procedures	50
5.3.2 Additional Considerations	57
5.3.3 Acquisition of Measurements	58
5.4 Pressure Measurements	59

CHAPTER 6. DATA ANALYSIS	61
6.1 Analysis of Surface Hot-Film Measurements	61
6.1.1 Time-Domain Analysis	61
6.1.2 Frequency-Domain Analysis	65
6.1.3 Description of Data Presentation	67
6.1.3.1 Space-Time Diagrams	67
6.1.3.2 Space-Frequency Diagrams	70
6.2 Analysis of X Probe Measurements	70
6.2.1 Inter-Bladerow Velocity Field	72
6.2.2 Turbulence Characteristics	74
6.2.2.1 Turbulence Intensity and Turbulence Kinetic Energy	74
6.2.2.2 Integral Length Scale	77
6.3 Aerodynamics Measurements	80
6.3.1 Profile Loss Coefficient	80
6.3.2 Velocity Distributions and Airfoil Loading	80
6.4 Uncertainty Analysis	81
CHAPTER 7. MEASUREMENTS OF BOUNDARY LAYER DEVELOPMENT	83
7.1 Test Matrix	83
7.2 Summary of Major Findings	87
7.2.1 Baseline Test Condition	87
7.2.2 Effects of Reynolds Number	91
7.2.3 Effects of Loading	92
7.2.4 Effects of Nozzle Clocking	92
7.2.5 Pressure Surface	93
7.3 Boundary Layer Development for Baseline Test Point	93
7.3.1 Nozzle Suction Surface	93
7.3.1.1 Wake-Induced Path	97
7.3.1.2 Path Between Wakes	99
7.3.1.3 Calming Regions	100
7.3.1.4 Instantaneous Time Traces	102
7.3.1.5 Mean Quasi Wall Shear and Periodic Unsteadiness	107
7.3.1.6 Boundary Layer Development and the Jet-Wake Effect	111
7.3.1.7 Frequency-Averaged Spectra	117
7.3.2 Rotor Suction Surface	119
7.3.2.1 Wake and Non-Wake Paths	127
7.3.2.2 Additional Observations	128
7.3.2.3 Instantaneous Time Traces	129
7.3.2.4 Mean Quasi Wall Shear and Periodic Unsteadiness	130
7.3.2.5 Frequency-Averaged Spectra	131
7.3.3 Nozzle Pressure Surface	131
7.3.3.1 Separation and Transition near the Leading Edge	138
7.3.3.2 Development of the Reattached Boundary Layer	139
7.3.4 Rotor Pressure Surface	140
7.4 Effects of Reynolds Number	148
7.4.1 High (Takeoff) Reynolds Number	149
7.4.2 Intermediate Reynolds Number	163
7.4.3 Low (Cruise) Reynolds Number	167
7.5 Effects of Loading	168
7.5.1 Nozzle Suction Surface	169

7.5.2 Rotor Suction Surface	175
7.5.3 Nozzle Pressure Surface	179
7.6 Effects of Nozzle Clocking	183
7.6.1 Nozzle Suction Surface	184
7.6.2 Nozzle Pressure Surface	188
CHAPTER 8. FLOWFIELD UNSTEADINESS AND WAKE INTERACTION	192
8.1 Average Turbulence Characteristics	192
8.1.1 Plane 1.0	194
8.1.2 Plane 1.5	194
8.1.3 Plane 2.0	198
8.1.4 Stage 2	201
8.1.5 Additional Observations	205
8.2 Wake Interaction in LP Turbines	206
8.3 Time-Varying Flowfield	209
8.3.1 Plane 2.0	209
8.3.2 Plane 2.5	214
8.3.3 Plane 3.0	214
CHAPTER 9. ANALYSES AND DISCUSSION	218
9.1 Comparisons of Experimental and Computational Results	218
9.1.1 Description of Boundary Layer Codes	218
9.1.2 Influence of Turbulence Intensity and Pressure Gradient	219
9.1.3 Predictions of Transition Location	223
9.1.4 Aerodynamic Loss	226
9.2 LP Turbine Performance – the Bigger Picture	231
9.3 Accounting for Transition	235
9.3.1 Location of Transition Onset	235
9.3.2 Length of Transition	235
9.3.3 Unsteady Boundary Layer Analysis	236
9.3.4 Advanced Computational Fluid Dynamics (CFD)	236
9.4 Simulating the LP Turbine Disturbance Environment	237
CHAPTER 10. CONCLUSIONS	241
CHAPTER 11. RECOMMENDATIONS FOR FURTHER RESEARCH	244
APPENDIX A. GENERAL DISCUSSION OF TRANSITION	245
APPENDIX B. FREQUENCY RESPONSE OF HOT-FILM ANEMOMETRY SYSTEM	248
APPENDIX C. GENERAL ANALYSIS OF TIME UNSTEADY MEASUREMENTS	252
APPENDIX D. FOURIER TRANSFORM METHODS	257
APPENDIX E. A PROCEDURE TO CALCULATE TURBULENCE LENGTH SCALE FOR PERIODICALLY UNSTEADY FLOWFIELDS	279

APPENDIX F. TEMPERATURE ADJUSTMENT OF ZERO-FLOW VOLTAGES	297
APPENDIX G. TRAJECTORY OF FLUID ELEMENTS/EVENTS IN s^*-t^* SPACE	299
BIBLIOGRAPHY	302

LIST OF FIGURES

Figure 3.1.	Surface hot–film anemometry for measurement of wall shear stress (after Hanratty and Campbell, 1983)	12
Figure 3.2.	Calibration of a surface hot–film sensor (from Suder, O’Brien, and Reshotko, 1988)	15
Figure 3.3.	Surface hot–film measurements from a turbine cascade for $Re_{ssl}=6.1 \times 10^5$ and $Tu_{in}=0.8\%$ (from Halstead, 1989)	21
Figure 3.4.	Comparison of surface hot–film measurements with boundary layer predictions	24
Figure 3.5.	Surface hot–film measurements from a turbine cascade for $Re_{ssl}=1.27 \times 10^6$ and $Tu_{in}=6.4\%$	25
Figure 4.1.	Schematic of LSRT facility	31
Figure 4.2.	Configuration of two–stage low pressure turbine	33
Figure 4.3.	Turbine blading terminology (after Glassman, 1972)	36
Figure 4.4.	Operating domain of LSRT	37
Figure 4.5.	Overall performance of two–stage turbine	38
Figure 5.1.	Data acquisition system for time unsteady measurements	41
Figure 5.2.	Array of surface hot–film sensors	43
Figure 5.3.	Stage 2 nozzle and rotor instrumented with hot–film array along suction surface	45
Figure 5.4.	RMS variation of mean value and second–order moment as a function of time trace number	48
Figure 5.5.	X hot–film probe	51
Figure 5.6.	Calibration domain of X probe	53
Figure 5.7.	Mesh of calibration domain for lookup table	57
Figure 5.8.	Graphical representation of calibration lookup table	58
Figure 6.1.	Determination of average “event” convection velocity from cross correlation analysis	66

Figure 6.2.	Example s - t diagram for an individual turbulent spot (from Halstead et al. 1995)	68
Figure 6.3.	Locus of voltage pairs for a single time trace superimposed onto the X probe calibration domain (Nozzle 2 exit, time trace #100)	71
Figure 6.4.	Decomposition of the two-dimensional velocity field	72
Figure 6.5.	Definitions of streamwise and transverse components of fluctuation velocity	76
Figure 7.1.	Test matrix for boundary layer measurements	84
Figure 7.2.	Normalized surface velocity at midspan for various loading levels (numbers correspond to those in Figures 7.1 and Table 7.1)	86
Figure 7.3.	S - t diagram schematics of boundary layer development for LSRT	88
Figure 7.4.	Ensemble-averaged shear stress characteristics along suction surface of Nozzle 2, test point 6B	94
Figure 7.5.	Time-averaged shear stress characteristics along suction surface of Nozzle 2, test point 6B	96
Figure 7.6.	Instantaneous time traces of quasi wall shear stress along suction surface of Nozzle 2, test point 6B	103
Figure 7.7.	Shear stress characteristics along suction surface of Nozzle 2, test point 6B	108
Figure 7.8.	The jet-wake effect along the suction surface of a turbine airfoil	112
Figure 7.9.	Variation of turbulence intensity and velocity at edge of boundary layer along nozzle suction surface, $0.5s^*$	116
Figure 7.10.	Frequency-averaged spectra of hot-film sensor output along suction surface of Nozzle 2, test point 6B, ($Q_0=-95$, $Q_{15}=-50$)	118
Figure 7.11.	Ensemble-averaged shear stress characteristics along suction surface of Rotor 2, test point 6B	120
Figure 7.12.	Time-averaged shear stress characteristics along suction surface of Rotor 2, test point 6B	121
Figure 7.13.	Instantaneous time traces of quasi wall shear stress along suction surface of Rotor 2, test point 6B	122
Figure 7.14.	Shear stress characteristics along suction surface of Rotor 2, test point 6B	123

Figure 7.15. Frequency-averaged spectra of hot-film sensor output along suction surface of Rotor 2, test point 6B, ($Q_0=-95$, $Q_{15}=-50$)	125
Figure 7.16. Ensemble-averaged shear stress characteristics along pressure surface of Nozzle 2, test point 6B	132
Figure 7.17. Time-averaged shear stress characteristics along pressure surface of Nozzle 2, test point 6B	133
Figure 7.18. Instantaneous time traces of quasi wall shear stress along pressure surface of Nozzle 2, test point 6B	134
Figure 7.19. Shear stress characteristics along pressure surface of Nozzle 2, test point 6B	135
Figure 7.20. Frequency-averaged spectra of hot-film sensor output along pressure surface of Nozzle 2, test point 6B, ($Q_0=-95$, $Q_{15}=-50$)	137
Figure 7.21. Ensemble-averaged shear stress characteristics along pressure surface of Rotor 2, test point 6B	141
Figure 7.22. Time-averaged shear stress characteristics along pressure surface of Rotor 2, test point 6B	142
Figure 7.23. Instantaneous time traces of quasi wall shear stress along pressure surface of Rotor 2, test point 6B	143
Figure 7.24. Shear stress characteristics along pressure surface of Rotor 2, test point 6B	144
Figure 7.25. Frequency-averaged spectra of hot-film sensor output along pressure surface of Rotor 2, test point 6B, ($Q_0=-95$, $Q_{15}=-50$)	146
Figure 7.26. Space-time diagrams of random unsteadiness along suction surface of Nozzle 2	150
Figure 7.27. Space-time diagrams of skew along suction surface of Nozzle 2	152
Figure 7.28. Time-averaged distributions of random and periodic unsteadiness along suction surface of Nozzle 2	154
Figure 7.29. Time-averaged distributions of skew along suction surface of Nozzle 2	156
Figure 7.30. Space-time diagrams of periodic unsteadiness along suction surface of Nozzle 2	158
Figure 7.31. Distributions of normalized quasi wall shear stress along suction surface of Nozzle 2	160
Figure 7.32. Instantaneous time traces along suction surface of Nozzle 2	161

Figure 7.33. Space–frequency diagrams of normalized RMS spectra along suction surface of Nozzle 2	164
Figure 7.34. Space–time diagrams of random unsteadiness along suction surface of Nozzle 2	170
Figure 7.35. Space–time diagrams of skew along suction surface of Nozzle 2	171
Figure 7.36. Time–averaged distributions of random and periodic unsteadiness along suction surface of Nozzle 2	172
Figure 7.37. Time–averaged distributions of skew along suction surface of Nozzle 2	173
Figure 7.38. Instantaneous time traces along suction surface of Nozzle 2	174
Figure 7.39. Shear stress characteristics along suction surface of Rotor 2 at baseline loading, test point 6B	177
Figure 7.40. Shear stress characteristics along suction surface of Rotor 2 at increased loading, test point 5B	178
Figure 7.41. Space–time diagrams of random unsteadiness along pressure surface of Nozzle 2	180
Figure 7.42. Instantaneous time traces along pressure surface of Nozzle 2	181
Figure 7.43. Space–frequency diagrams of normalized RMS spectra along pressure surface of Nozzle 2	182
Figure 7.44. The effect of Nozzle 1 clocking on turbulence intensity at inlet to Nozzle 2	184
Figure 7.45. Space–time diagrams of random unsteadiness along suction surface of Nozzle 2, test point 6B ($Q_0=0.56$, $Q_{10}=9.66$)	185
Figure 7.46. Space–time diagrams of periodic unsteadiness along suction surface of Nozzle 2, test point 6B ($Q_0=-9.0$, $Q_{10}=6.0$)	186
Figure 7.47. Space–frequency diagrams of normalized RMS spectra along suction surface of Nozzle 2, test point 6B ($Q_0=-95$, $Q_{15}=-50$)	187
Figure 7.48. Space–time diagrams of random unsteadiness along pressure surface of Nozzle 2, test point 5D ($Q_0=1.29$, $Q_{10}=19.09$)	190
Figure 7.49. Space–time diagrams of periodic unsteadiness along pressure surface of Nozzle 2, test point 5D ($Q_0=-12.0$, $Q_{10}=18.0$)	191
Figure 8.1. Circumferential–averaged turbulence characteristics of the LSRT at midspan	193

Figure 8.2.	Circumferential variation of flowfield at exit of Nozzle 1	197
Figure 8.3.	Time varying flowfield at exit of Nozzle 1, 5 percent pitch	199
Figure 8.4.	Circumferential variation of flowfield at exit of Rotor 1	200
Figure 8.5.	Circumferential variation of flowfield at exit of Nozzle 2	203
Figure 8.6.	Circumferential variation of flowfield at exit of Rotor 2	204
Figure 8.7.	Normalized integral length scale of the LSRT at midspan	206
Figure 8.8.	Wake interaction in a multi-stage LP turbine	207
Figure 8.9.	Measurements of unsteady flowfield at inlet to Nozzle 2 (Plane 2.0)	210
Figure 8.10.	X probe measurement locations at Plane 2.0 relative to Nozzle 1	211
Figure 8.11.	Variation in turbulence kinetic energy across Nozzle 2 bladerow	215
Figure 8.12.	Measurements of unsteady flowfield at exit of Rotor 2 (Plane 3.0)	216
Figure 9.1.	Aerodynamic characteristics along Nozzle 2, test point 5A	220
Figure 9.2.	Aerodynamic characteristics along Nozzle 2, test point 5E	221
Figure 9.3.	Boundary layer characteristics diagrams for suction surface of Nozzle 2	225
Figure 9.4.	Comparison of measured and predicted values of profile loss coefficient for Nozzle 2	227
Figure 9.5.	Breakdown of predicted loss coefficient for Nozzle 2, test point 5A, boundary layer calculation from KEP	230
Figure 9.6.	Effects of Reynolds number on LP turbine performance (after Hourmouziadis, 1989)	232
Figure 9.7.	Different loading distributions for turbine airfoils (after Halstead et al., 1995)	234
Figure B.1.	Optimal response waveform for hot-films using the square-wave test	249
Figure B.2.	Typical response waveform for surface hot-film anemometry system	249
Figure B.3.	Temporal response from an idealized disturbance convecting past a sensor fixed in space	250
Figure C.1.	Example of time unsteady measurements obtained from a surface hot-film sensor	253

Figure D.1.	Graphical representation of the mean square spectral density of $X(f)$ (one-sided: $G(f)$, two-sided: $S(f)$)	261
Figure D.2.	Discretization of a continuous waveform	265
Figure D.3.	Graphical illustration of aliasing	266
Figure D.4.	Schematic of discretized Fourier transform	272
Figure D.5.	General storage arrangement of arrays associated with FFT computer routine (after Press et al., 1992)	278
Figure E.1.	Calculation procedure to determine integral length scale and turbulence energy spectra	280
Figure E.2.	Example set of velocity time traces measured using an X hot-film probe, data acquired at exit to Nozzle 2 (Plane 2.5)	281
Figure E.3.	Mean square spectral density for streamwise and transverse coordinate directions, data acquired at exit to Nozzle 2 (Plane 2.5)	286
Figure E.4.	Autocorrelation functions for streamwise and transverse coordinate directions, data acquired at exit to Nozzle 2 (Plane 2.5)	290
Figure E.5.	Cumulative summations of correlation integrals to determine integral time scales, data acquired at exit to Nozzle 2 (Plane 2.5)	291
Figure E.6.	Turbulence energy spectra for streamwise coordinate direction, data acquired at exit to Nozzle 2 (Plane 2.5)	292
Figure E.7.	Individual trace MSSDs for streamwise coordinate direction, data acquired at exit to Nozzle 2 (Plane 2.5)	294
Figure G.1.	Illustration of event trajectories in s^*-t^* space ($k=1.0$, $V_{\infty,n}^*=1.0$)	301

LIST OF TABLES

Table 4.1. Pitchline blading parameters of LSRT	35
Table 6.1. Estimated uncertainty intervals based on 20 to 1 odds	82
Table 7.1. Test conditions for boundary layer measurements	84

NOMENCLATURE

A_{sensor}	surface area of sensor element
A, A', A''	calibration constants of surface hot–film sensors
B, B'	calibration constants of surface hot–film sensors
c	numerical constant
c_z	axial chord
c_p	specific heat at constant pressure
e	AC–coupled anemometer output voltage
E	anemometer output voltage
$E_{\text{cal},i}$	X probe calibration voltage for i^{th} flow condition
$E_{\text{corr},i}$	X probe calibration voltage for i^{th} flow condition, corrected for temperature
E_1, E_2	anemometer output voltages from X hot–film probe
E_0	zero–flow voltage from surface hot–film
$E_{0,\text{adj}}$	zero–flow voltage adjusted for temperature
f, f^*	frequency, normalized frequency
Δf	interval between discrete frequency elements
f_c	nyquist frequency
f_{cutoff}	cutoff frequency of hot–film anemometry at –3 db attenuation
f_{lp}	cutoff frequency of low–pass filter
f_0	fundamental frequency associated with discrete time record
f_s	sampling frequency
\mathcal{F}_k	dimensionless wave number
G	mean square spectral density defined for non–negative frequencies (one–sided)
\mathcal{G}_k	dimensionless energy spectrum
ΔH_t	change in total enthalpy
k	thermal conductivity of fluid, turbulence kinetic energy, reduced frequency
K	acceleration factor
L	length of sensor element in streamwise direction
LE	leading edge
L_{max}	largest sensor dimension
L_{eff}^+	dimensionless effect length of heated sensor

\dot{m}	mass flowrate
N, NPT	number of data samples per time trace
N_{stages}	number of stages
N_{blade}	number of blades
NTR	number of time traces per ensemble
OHR	overheat ratio
P	pressure
PDF	probability density function
Pr	molecular Prandtl number
q_w	heat transfer from sensor to fluid
q_s	heat transfer from sensor to substrate
q_{tot}	total heat transfer dissipated by sensor
q_0	heat transfer from sensor to substrate to zero flow
Q_0, Q_{10}, Q_{15}	minimum and maximum values of color contours
\vec{Q}, Q	mass flux vector, mass flux magnitude
RMS	root-mean-square
RPM	turbine rotational speed
r	spatial distance
R	autocorrelation function, sensor resistance
Re	Reynolds number based on bladerow exit conditions
\overline{Re}	stage-averaged Reynolds number
Re_{NS}	non-steady Reynolds number
Re_{θ}	momentum thickness Reynolds number
R_{xy}	cross-correlation function
$R_{\text{sen,hot}}$	electrical resistance of heated sensor
$R_{\text{sen,cold}}$	electrical resistance of sensor at ambient temperature
R_{lead}	electrical resistance of leads
\mathcal{R}	correlation coefficient
S	mean square spectral density for all frequencies (two-sided)
S_{xy}	cross spectral density function for all frequencies (two-sided)
s	surface distance from leading edge, streamwise coordinate
s^*	normalized surface distance

s_{tot}	streamwise distance from leading to trailing edge
t	time
Δt	time period between data samples
t^*	time normalized by blade passing period
T	duration of time record
TE	trailing edge
$T_{t,\text{cal}}$	total temperature of calibration flow
T_u	turbulence intensity
T_{op}	operating temperature of hot-film sensor
T_t	local total temperature
T_0	ambient temperature during acquisition of zero-flow voltages
ΔT	temperature difference between sensor and fluid
\mathcal{T}	torque produced by turbine
\mathcal{T}	integral time scale
U_m	midspan blade speed
u, v	velocity components in streamwise and transverse directions
u', v', w'	fluctuation velocities in streamwise, transverse, and radial directions
u^*	friction velocity, $\sqrt{\tau_w/\rho}$
\vec{V}, V	velocity vector, velocity magnitude in absolute frame of reference
V_∞	local freestream velocity
V^*	normalized velocity
w, w_{app}	width of wake, apparent width of wake
W	width of sensor in cross-flow direction, velocity magnitude in relative flow direction
x	arbitrary time record, streamwise coordinate direction
X, Y, Z	Fourier coefficients of $x, y,$ and z time records
y	arbitrary time record, transverse coordinate direction
z	arbitrary time record, axial direction
Z_{inc}	incompressible Zweifel loading coefficient
α	temperature coefficient of resistance of sensor, absolute flow angle
α_0	offset angle of X hot-film probe
β	relative flow angle

δ, δ_t	thicknesses of momentum and thermal boundary layers
ε	normalized eddy length scale
η	turbine efficiency
θ	tangential direction, momentum thickness
Θ	angle between absolute and relative flow directions
λ	wavelength of disturbance
Λ	integral length scale
μ	absolute viscosity
ν	kinematic viscosity
ρ	static density
σ, σ_z	solidity based on chord, solidity based on axial chord
τ	time constant, time period, time shift
$\tau_w, q\tau_w$	wall shear stress, quasi wall shear stress
ϕ	specific flow
ψ	specific work
ω	FFT operator, turbine rotational speed
ω_p	profile loss coefficient

Subscripts

bp	blade passing
do	throat width
ex	bladerow exit
fs	freestream
i	i^{th} data sample of time trace, i^{th} element of frequency spectra
in	bladerow inlet
j	index for discrete correlation functions
k	index for discrete frequency elements
m	index for discrete frequency elements of Z
N	number of discrete elements describing surface velocity distribution
n	n^{th} time trace of ensemble, index for discrete time records x, y, and z; index for discrete surface velocity distribution
P	periodic
ps	pressure surface

rms	root-mean-square
R	random
s	static
ss, ssl	suction surface, suction surface length
t	total
u	streamwise direction
w	wake
z	axial direction
θ	tangential direction
0	starting point of integration

Superscripts

—	time average
~	ensemble average
*	complex conjugate
''	per unit area

ACKNOWLEDGEMENTS

I foremost wish to thank my family and friends for their support during this work. This dissertation is dedicated to my parents — to my mother, Helen, and in loving memory of my father, George. This work is a reflection of their ideals and commitment to fostering opportunity and aspirations. I especially wish to thank my wife, Cathy. Her patience and support has been unwavering over the long course of this work. She has inspired me through the difficult times and helped celebrate the successful. And lastly, to Carolyn, whose mere smile is a constant reminder of the important things in life.

This research was guided capably by my co-major professors, Prof. Ted Okiishi and Dr. David Wisler. More than by any other person, my development as a researcher and engineer has been advanced by Prof. Okiishi. Over the years of our association, he has served as major professor, teacher, advisor, critic, and most of all, a good friend. I have benefitted greatly from his example of uncompromising character, loyalty, and integrity. While at GE Aircraft Engines, Dr. Wisler provided invaluable mentoring of this research program as well as to the broader aspects of the aerospace profession. He deserves special mention for championing the mutually beneficial interaction between GEAE and Iowa State University at a time when such programs are routinely terminated.

In addition, I wish to thank sincerely the members of my program-of-study committee: Profs. Richard Hindman, George Serovy, William Cook, and Kenneth McConnell. Special thanks are owed to Profs. Cook and McConnell. I learned much from their skillful and meticulous approach to research and experimentation. Additionally, I benefitted greatly from collaboration with Professors Gregory Walker of the University of Tasmania and Howard Hodson of the University of Cambridge over the course of this work.

I also extend thanks to my colleagues at the Aerodynamics Research Laboratory at GEAE. In particular, Dr. Hyoun Woo Shin generously shared his expertise in experimental fluid mechanics during the course of this work. The seasoned experience and craftsmanship of

Messrs. William Groll and Donald Menner were a tremendous asset to the experimental program. They made my job in the laboratory much easier.

Lastly, I am grateful to GE Aircraft Engines for sponsoring this work and for permission to publish this dissertation.

ABSTRACT

Comprehensive experiments were conducted to study the development of boundary layers along airfoil surfaces of multi-stage low pressure turbines. The test vehicle consisted of a large scale, low speed turbine containing two stages of blading. Tests were carried out over a wide range of Reynolds numbers and loadings relevant to low pressure turbines of modern commercial engines.

Unsteady measurements of the boundary layer were acquired using arrays of densely-packed, surface hot-film sensors mounted to the airfoil suction and pressure surfaces. Airfoils from the second stage nozzle and rotor bladerows were instrumented. Measurements of the time unsteady velocity and turbulence were obtained at the inlet and exit of each turbine bladerow. For the first time, quantitative measurements of turbulence length scale are reported for a multi-stage low pressure turbine.

For all test conditions, the boundary layers along the blade suction surfaces of the embedded second stage were predominantly laminar and transitional. In general, the boundary layers developed along two distinct but coupled paths. The first developed approximately beneath the wake that convects through the bladerow. The second occurred between the wakes. Along both paths, regions of laminar, transitional, and turbulent flow were identified. The two paths were coupled by regions of calmed flow that developed behind turbulent spots. The calmed regions, characterized by elevated levels of non-turbulent shear stress, effectively suppressed boundary layer separation in areas of adverse pressure gradient.

Along the suction surfaces at high Reynolds numbers, equivalent to aircraft takeoff conditions, some transitional flow persisted to the trailing edge. At low, cruise Reynolds numbers, the boundary layer was laminar along more than seventy percent surface distance.

Both the airfoil boundary layers and bladerow aerodynamic loss were influenced significantly by clocking of upstream bladerows.

Along the pressure surface, boundary layer development for all test conditions was influenced strongly by the adverse pressure gradient at the leading edge. At decreased loading, transition occurred abruptly due to the presence of a laminar separation bubble. At increased loading where the incidence angle was lower, attached-flow transition was observed. In all cases, little periodic unsteadiness persisted downstream of transition.

CHAPTER 1. INTRODUCTION AND OBJECTIVES

1.1 Nature of Problem

Low pressure (LP) turbines are used in aircraft engines to provide power requirements of fan and compressor components. Designers of LP turbines continually strive to improve efficiency and decrease cost, weight, and part count. Much of the design optimization process is related to issues of aerodynamics.

Overall efficiency and performance of an LP turbine depends greatly on viscous flow effects. A significant portion of the viscous loss is associated with the development of boundary layers along blade surfaces. Consequently, LP turbine designers must account for boundary layer development in order to, first, accurately predict and, second, optimize aerodynamic performance.

In the turbine community, there is a level of disagreement concerning the nature of these boundary layers and the level of sophistication required to model them. Some people feel that because of the high degree of flowfield unsteadiness and turbulence present downstream of the combustor and high pressure turbine, the LP turbine boundary layers will be predominantly turbulent. For a number of reasons, others feel that the airfoil boundary layer in LP turbines contain significant regions of laminar and transitional flow. First, the combined effect of high temperatures and low pressures in the LPT produce the lowest Reynolds numbers of any aircraft engine component. At aircraft cruise (altitude) conditions, Reynolds numbers based on surface distance can be as low as 120,000 — five to ten times less than those in a compressor. Secondly, because of its location downstream of the high pressure turbine, LP blading predominantly does not require cooling. Hence disturbances to the boundary layers associated with film cooling injection are not present. Lastly, because turbines rely on aerodynamic expansion to extract work from the fluid, significant flow acceleration occurs (in a global sense) across the bladerows.

The level of technical sophistication required to account for boundary layer development during the LPT design process varies greatly depending on which view is correct. For the first

viewpoint, turbulence models are available that reasonably simulate wall boundary layers. The latter, however, requires additional knowledge of the location and extent of boundary layer transition and/or laminar separation and how they are influenced by periodic unsteadiness.

This work seeks to resolve these issues. The comprehensive data set reported in this dissertation will be valuable to designers requiring an understanding of the boundary layer development process and to code developers in need of benchmark data for computational fluid dynamics (CFD) validation. Methods relating to the experimental setup and data analysis are presented in a degree of detail so as to be useful to researchers employed in similar studies.

1.2 Objectives

Three primary objectives are addressed in this dissertation. With each objective are specific questions for which answers were sought from this research program.

1. Ascertain the development of unsteady boundary layers in multi-stage turbine environments. Does a significant amount of laminar and transitional flow occur along the blading of an *embedded* stage in an LP turbine? Where and by what means does transition occur? What is the effect of wakes on the boundary layer development? How do Reynolds number, loading, and unsteadiness influence the boundary layer?
2. Evaluate the extent to which the detailed development features need to be modeled for design and analysis purposes. What practical simplifications to the flowfield can be made? How important is periodic unsteadiness to the problem? Are steady or quasi-steady approaches valid? How does the treatment of transition influence loss prediction?
3. Document the unsteady flowfield and disturbance environment in a multi-stage LP turbine. What is the intensity and scale of the turbulence? How does the unsteady flowfield develop through the turbine?

1.3 Overview of Approach.

This dissertation documents a comprehensive study of boundary layer development along airfoil surfaces of a multi-stage low pressure turbine. Boundary layer measurements were obtained using densely-packed arrays of surface hot-films. Both pressure and suction surfaces of the airfoils were instrumented. The instrumentation setup allowed up to 24 sensors to be operated simultaneously from leading to trailing edge. The procedure for installation of the hot-film arrays to the airfoils and for operation of the sensors is given. Also provided is a description of methods used to process and interpret surface hot-film data.

Boundary layer measurements are reported for a wide range of Reynolds numbers and loading levels relevant to an LP turbine of a modern commercial engine. Supporting aerodynamic data are included in the form of surface velocity distributions and bladerow loss coefficient for the various test conditions.

The unsteady flowfield and disturbance environment influencing the boundary layers are also documented and correlated with the observed boundary layer development. Measurements were obtained at the inlet and exit of all bladerows of the turbine. Results are compared to wake interaction models. Measurements of turbulence length scales from a multi-stage LP turbine are reported for the first time. To this end, a method to compute turbulence length scales in a periodically varying flowfield is documented thoroughly in an appendix.

CHAPTER 2. REVIEW OF PAST RESEARCH

Our present knowledge of boundary layers and boundary layer transition as applied to turbines is drawn from both fundamental and applied research efforts. A number of important contributions relevant to this work are considered in this chapter. To facilitate the discussion given below as well as throughout this dissertation, the general processes of boundary layer transition, the characteristics of turbulent spots, and the terminology associated with transition are described in Appendix A. This material was taken directly from Section 4.0 of the paper by Halstead et al. (1995).

2.1 Flat Plate Studies in Wind Tunnels

Excellent fundamental studies have been carried out in wind tunnel facilities for both steady and unsteady mean flows. In the arena of steady-flow experiments, boundary layer development and transition have been investigated at elevated levels of turbulence intensity pertinent to turbine environments. For zero pressure gradient flow, Suder, O'Brien, and Reshotko (1988) found that transition occurred via the bypass mode for turbulence intensities greater than about 0.65%. Their results also suggested that, in addition to intensity, turbulence length scale and energy spectrum influence the location of transition onset and hence should be documented in all boundary layer studies. Transitioning boundary layers under the influence of favorable and adverse pressure gradients have been studied by Blair (1982) and Gostelow, Blunden, and Walker (1994). For the latter, a significant reduction in transition length was observed for increasing adverse pressure gradient.

Because of the varied flow conditions in which boundary layer transition occurs, researchers have attempted to formulate correlations for the onset and length of transition. An impressive and comprehensive set of such measurements were reported by Abu-Ghannam and Shaw (1980) for a wide range of turbulence intensity and streamwise pressure gradient. Their correlation of transition onset (and modifications thereof) is frequently employed in the turbo-

machinery industry. Measurements of transition location obtained as part of this work are compared to their correlation.

Much of our understanding of the detailed processes associated with transition from laminar to turbulent boundary layer flow is due to studies carried out more than 40 years ago. Schubauer and Skramstad (1948) were the first to document experimentally the occurrence of linear instability (Tollmien–Schlichting) waves as a precursor to transition. Emmons (1951) and Schubauer and Klebanoff (1956) first observed turbulent spots and recognized their relation to boundary layer transition. Regions of calmed flow that followed behind turbulent spots were discovered by the latter authors. The time–unsteady measurements obtained in this study using surface hot–film sensors reveal these same features along an embedded turbine airfoil.

Since these early studies, investigations of turbulent spots have been extended to include the effects of streamwise pressure gradient. A compilation of these findings are provided in Gostelow, Melwani, and Walker (1995). Also, comprehensive investigations have focused on the calmed region (Seifert, 1995, and Gostelow et al., 1996).

Studies of transition along a flat plate have been carried out with a time–varying mean flow. Loehrke, Morkovin, and Fejer (1975) reviewed a number of investigations in which the mean velocity was varied sinusoidally. From these works, it was found that the manner in which transition occurred depended on a non–steady Reynolds number. When this Reynolds number exceeded a certain value, regions of transitional flow were observed at the frequency of the free–stream oscillation and at a streamwise location significantly upstream of the corresponding steady–flow case. These findings are relevant to turbomachines as wakes from upstream blades produce periodic variations of the mean flow.

Other investigators have simulated wake interaction of multiple bladerow turbomachines by translating rods upstream of a flat plate. The wake from a rod produces both the velocity perturbation and increased turbulence intensity characteristic of airfoil wakes. In studies of Pfeil and Herbst (1979) and Pfeil, Herbst, and Schroder (1982), the boundary layer along the

plate occurring beneath the wake became turbulent near the leading edge while between wakes, the boundary layer remained laminar. They further observed that, as the wake-induced turbulent strips convected downstream, they grew in streamwise extent in a manner similar to turbulent spots. At a given instant in time then, the boundary layer along the plate varied from laminar to turbulent with the laminar portion diminishing in extent as one moved downstream. Incidentally, the location along the plate at which wake-induced transition first occurred was far upstream of that predicted by linear stability theory, suggesting a bypass transition mode.

Orth (1992) has extended the studies of Pfeil and co-workers to include the effects of pressure gradient. He found that, between wake-induced strips, the non-turbulent calmed region occurring behind the strips persisted far downstream of where they were last observed for the equivalent steady-flow case. It was also concluded that wake turbulence, and not the periodic perturbation of the mean flow, was the primary influence on the location of transition onset.

In a recent two-part publication, Funazaki (1996) reported measurements of an unsteady, transitional boundary layer along a flat plate disturbed by very strong wakes. A model of wake-induced transition was proposed that successfully matched his data set.

2.2 Turbine Cascade Tests

Investigations of turbine boundary layers have been carried out in cascade facilities both with and without the presence of wake-generating rods.

In a number of steady-flow experiments, surface hot-film sensors and other instrumentation have been used successfully to obtain an understanding of laminar, transitional, turbulent, and separational boundary layers along turbine airfoils. Hodson (1985c) studied boundary layer development near the leading edge of a turbine airfoil. Using surface hot-films, he was able to identify a small separation bubble near the leading edge and track its subsequent influence on the downstream boundary layer. In a study by Hoheisel et al. (1987), the influence of turbulence intensity and airfoil pressure distribution on loss behavior of a turbine cascade was published. Detailed measurements of the suction surface boundary layer were included.

Using a transonic cascade facility, Ashworth and LaGraff (1989) obtained measurements of the growth and convective characteristics of turbulent spots at high Mach number. Their results were consistent with those from low speed tests. Halstead (1989) conducted tests over a wide range of inlet turbulence intensities and Reynolds numbers. Features of boundary layer development with attached-flow and separated-flow transition were documented along the suction surface using surface hot-film anemometry. Ladwig and Fottner (1993) completed an interesting experiment which sought to quantify the effects of nozzle/nozzle (or rotor/rotor) interaction in turbine performance. The interaction was simulated by placing a stationary, wake-generating rod at various transverse locations in front of a turbine cascade. A significant variation in cascade loss with rod position was observed. For the lowest measured loss, they surmised that the wake turbulence suppressed a laminar separation bubble along the aft portion of the suction surface.

Some of the more significant investigations documenting the effects of rod-generated wakes on the performance of LP turbine airfoils have been carried out at Whittle Laboratory by Hodson and co-workers. In a paper by Schulte and Hodson (1994), detailed boundary layer measurements and cascade loss coefficients were compared for tests run with and without wakes. They found that with wakes present, profile loss at low, cruise Reynolds numbers was reduced in comparison to the no-wakes case. The opposite was observed at higher, takeoff Reynolds numbers. Also, the authors noted that the periodic velocity perturbation brought about by the wake had a dominating influence on the boundary layer which contained a laminar separation bubble aft of mid chord. In a similar investigation (Schulte and Hodson, 1996), measurements of loss coefficient implied the possible existence of an optimal reduced frequency associated with wake passing such that a minimum loss is achieved. Lastly, Curtis et al. (1996) examined loss characteristics of a number of different pressure distributions along the suction surface. These tests were conducted in the same facility used by Schulte and Hodson. As before, rods were used to simulate the wakes of an upstream bladerow. Curtis et al. report a potential to in-

crease airfoil loading without incurring a loss penalty. Because wake unsteadiness played an important role in boundary layer development for these tests, they concluded that CFD, in its present stage of evolution, can not predict accurately the magnitude of loss observed.

Before proceeding, a note is in order concerning the use of rods to generate wakes. As shown by Halstead et al. (1995) and documented by others, wakes produced by rods will possess a much higher level of turbulence intensity than for an airfoil with the same loss coefficient. Measurements of wake turbulence intensity obtained as part of this work range from about 5 to 6%. In contrast, intensities of the rod-generated wakes from Funazaki (1996), Schulte and Hodson (1996) and Curtis et al. (1996) were equal to 10% or more. The ramifications of these differences are considered later in this dissertation.

2.3 Tests of Single and Multi-Stage Turbines

In the last 15 years, an increasing number of investigators studying boundary layers in turbines have turned to rotating facilities. One of the first studies was that of Dring et al. (1982) in which a single-stage turbine was employed. They obtained a comprehensive data set that enabled them to access the interaction between the nozzle and downstream rotor. Using surface hot-film measurements, they observed that the boundary layer along the suction surface of the rotor varied from laminar to turbulent in concert with the passing wakes. Hodson (1984) carried out a very instructive experiment in which measurements at midspan of a rotor from his single-stage turbine were compared directly with measurements from a cascade airfoil with the identical midspan geometry. At equivalent Reynolds numbers, the profile loss at midspan of the turbine rotor was about 50 percent higher than that of the cascade airfoil operating with steady inlet conditions. The increase in loss was attributed to differences of the suction surface boundary layers. Along the turbine rotor, boundary layer transition varied in time with wake passing and occurred earlier. No flow separation was observed. In contrast, the boundary layer along the cascade airfoil remained laminar until near the trailing edge where a laminar separation bubble occurred.

Hodson and Addison (1989) reported additional measurements from the same turbine but now operated over a range of Reynolds numbers and incidence angles. For all Reynolds numbers considered, turbulent spots in the presence of the passing wakes were observed consistently in an otherwise laminar boundary layer. Incidence angle was varied to the extent that leading-edge separation was attained along either the suction or pressure surfaces. In all cases, characteristics of the boundary layers could be discerned from the surface hot-film data. It should be noted that the turbulence levels at the inlet to these turbines (i.e., Dring et al. and Hodson et al.) were much lower than those of an actual production LP turbine.

Test results from three multi-stage LP turbines have been published by Hourmouziadis, Buckl, and Bergmann (1987), Schroder (1991), and Hodson, Huntsman, and Steele (1994). The turbine blading for each was derived from actual hardware of the PW-2037, V2500, and Trent 700 engines, respectively. The suction surfaces of nozzle airfoils from the second stage for the Hourmouziadis et al. work and from the third stage for the Schroder and Hodson et al. work were instrumented with surface hot-film sensors. Airfoil velocity distributions and some flow visualization were used in conjunction with the hot-film data to discern boundary layer characteristics. Test conditions from which data were reported pertained to low and intermediate Reynolds numbers. In all cases, significant regions of laminar and transitional flow were observed along the suction surfaces of the embedded nozzles. Hourmouziadis et al. and Schroder provided convincing evidence that laminar separation bubbles were present along the back portion of the suction surface where the flow is diffusing. No pressure surface data were obtained and only limited aerodynamic data were given. Measurements of disturbance environment for the Hodson et al. work also were not reported. Hourmouziadis et al. did obtain turbulent measurements but only at a location far downstream of the last turbine bladerow. Measurements obtained between bladerows of the V2500 turbine were documented by Schroder and Arndt (1993) but, as explained by Arndt, the absolute levels of turbulence intensity were not accurate due to calibration uncertainty. However, Arndt was able to show, in relative terms, rather spectacular evidence of flow-

field variations related to blade count differences between bladerows in the same frame of reference. This general phenomenon is termed rotor/rotor and nozzle/nozzle interaction.

Summary. In conjunction with experimental investigations such as those just described, a number of researchers have concentrated on modeling and prediction of the observed unsteady, transitional boundary layers. Two comprehensive reviews that assess the experimental and analytical progress accomplished to date have been offered by Mayle (1991) and by Walker (1993).

In total, the work cited above represents a significant advancement of the understanding of boundary layers in LP turbines. With the exception of the multi-stage tests, where limited data are available, attempts were made in many of these investigations to simulate at least a portion of the flow environment of an actual LP turbine. However, because of questions regarding the relevance of these simulations, the direct application of the test results to turbine design has been hampered.

The primary contribution of this research program is that a comprehensive study of boundary layer development is carried out in an accurate model of a true multi-stage LP turbine. Because of its large scale in comparison to engine hardware, measurements can be made with a high degree of resolution both along blade surfaces and between bladerows. The flexibility of the LSRT facility permits investigation over a wide range of relevant turbine operating conditions. At any given test point, measurements of blade surface boundary layer using surface hot-film anemometry, the airfoil pressure distributions, the unsteady velocity field and disturbance environment, the overall turbine performance, and detailed aerodynamic bladerow performance can be acquired.

CHAPTER 3. SURFACE HOT-FILM ANEMOMETRY

The experimental method of surface hot-film anemometry (HFA) involves the determination of local wall shear stress using small, heated elements positioned on a surface of a body. Compared to other approaches, the primary advantage of this method is that it can be applied in a nearly non-obtrusive manner and that unsteady fluctuations in shear stress can be resolved. Since the earliest use of surface HFA, dating back to the early 1930's, significant improvements in sensor manufacturing, instrumentation, and experimental procedure have led to a well-understood means in which static and dynamic variations in wall shear stress could be measured.

In the first of section of this chapter, the principles of surface hot-film anemometry will be presented. To this end, the relationship between sensor output and wall shear stress will be developed. Next, more recent applications of surface HFA to determine characteristics of boundary layer development are described. These methods do not require rigorous calibration of the sensors but instead employ experimental procedures and data analyses that provide semi-quantitative measurements. In the last section, the interpretation of surface hot-film measurements to infer boundary behavior is considered. To facilitate this discussion, clear examples are provided from measurements reported by Halstead (1989). The various techniques of analyzing data, described in the second section, are applied.

3.1 Principles of Technique

The principles of surface hot-film anemometry are rooted in a derivable relationship between the heat transferred from the heated sensor element to the colder fluid and the local wall shear stress. This is illustrated schematically in Figure 3.1. The two-dimensional sensor is oriented with its long side perpendicular to the flow direction. The sensor element is operated, using conventional anemometry, at a temperature, T_s , significantly greater than that of the fluid. The rate of heat transfer from the sensor is determined by the electrical power consumed.

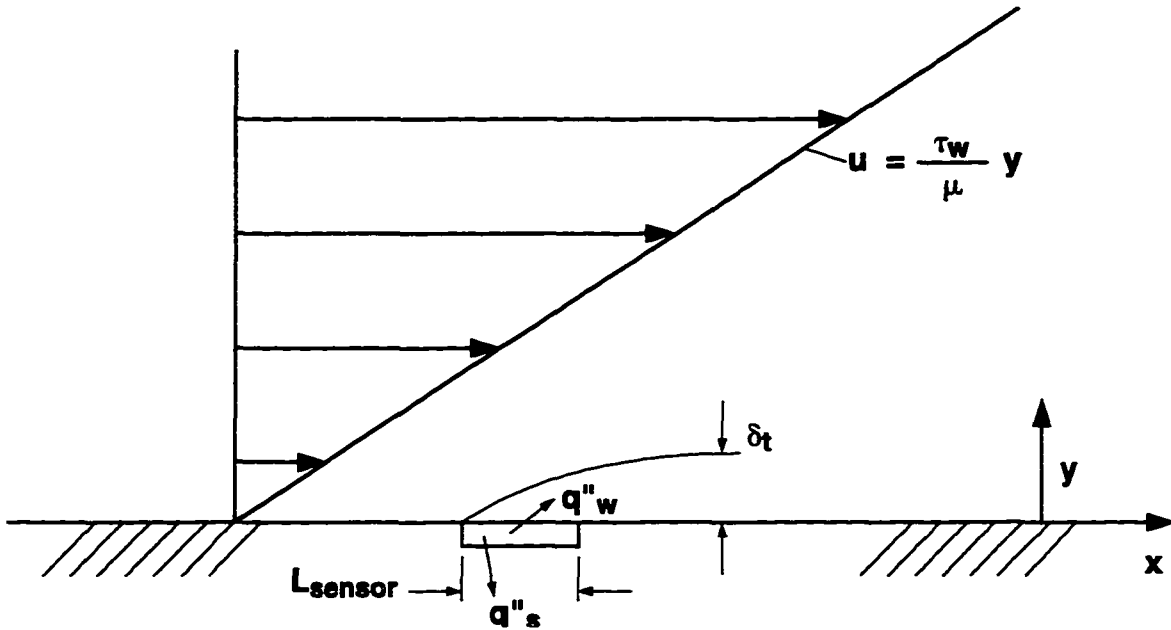


Figure 3.1. Surface hot-film anemometry for measurement of wall shear stress (after Hanratty and Campbell, 1983)

As described by Hanratty and Campbell(1983), a simple analytical expression for the relationship between local wall shear stress and the heat transfer from the sensor can be derived, provided the following criteria are satisfied.

1. The existing velocity boundary layer is not disturbed by the presence of the sensor.
2. The thermal boundary layer is sufficiently thin such that it lies within the region of linear variation of the velocity boundary layer. From Figure 3.1, this implies that the velocity gradient must be equal to τ_w/μ across the thermal boundary, δ_t .
3. The planar dimensions of the sensor element are sized such that conventional thermal boundary layer analysis is valid. This requires:
 - a. the length of the sensor, L , to be large relative to δ_t so that streamwise diffusion and y -direction transport can be neglected, and
 - b. the width of the sensor, W , to be large relative to δ_t so that transverse diffusion can be neglected.

Regarding criterion 2, the most restrictive condition occurs in turbulent flow where δ_t must be thinner than the laminar sublayer. This imposes an upper limit to the streamwise length, L , of the sensor (Hanratty and Campbell, 1983) given by

$$L_{\text{eff}}^+ < 64 \text{Pr}$$

where Pr = molecular Prandtl number

$$\begin{aligned} L_{\text{eff}}^+ &= \text{dimensionless effective length of heated sensor} \\ &= \frac{u^*}{\nu} L_{\text{eff}} \end{aligned}$$

Note that because of thermal conduction in the substrate, the “effective” length of the sensor can be significantly greater than its physical length. Consequently, this criterion is often difficult to satisfy.

To satisfy criterion 3a, the sensor must be of adequate length to satisfy the constraint (ibid.)

$$L_{\text{eff}}^+ \text{Pr} > 200$$

In contrast to that from the previous paragraph, this constraint dictates the minimum allowable length of the sensor. Because the sensor aspect ratio, W/L , is typically much greater than one, criterion 3b is satisfied readily by the above inequality.

Provided the above criteria are met, the relationship between heat transfer from the sensor and local wall shear stress can be determined from the solution of the thermal energy equation. The result, whose derivation is described in Bellhouse and Schultz (1966), is given by Equation 3.1.

$$\frac{q_w''}{\Delta T} = a \left(\frac{k^2 c_p \rho}{\mu L} \right)^{1/3} \tau_w^{1/3} \quad (3.1)$$

The value of the numerical constant “a” is dependent on the particular integral method employed in the derivation. The term ΔT is the temperature difference between the sensor and fluid. For conditions where the fluid temperature does not vary appreciably and the flow is non-compressible, the quantity with the brackets is treated as a constant.

The relationship given by Equation 3.1 was derived with no consideration to conductive heat transfer from the sensor to the substrate. From experiments, Bellhouse and Schultz (1966) showed that the actual heat transfer from the sensor can be expressed by

$$\frac{q_w''}{\Delta T} = A' \left(\frac{E^2}{\Delta T} \right) + B' \quad (3.2)$$

The first term on the right hand side of Equation 3.2 is related to the total heat transfer, q_{tot}'' , dissipated by the sensor. In terms of electrical power, q_{tot}'' is equal to

$$q_{tot}'' = \frac{E^2}{R} \frac{1}{A_{sensor}}$$

where E is the output voltage from the anemometer. For a sensor operating at constant temperature (i.e., constant resistance), the resistance and sensor area are absorbed into the constant A' . The variable, B' , is associated with the heat loss to the substrate. For hot-film sensors, this substrate heat loss is generally greater than convective heat transfer to the fluid and hence must be taken into account.

The conventional working form of the relationship of wall shear stress to the measured output from the sensor combines Equations 3.1 and 3.2 as indicated below.

$$\tau_w^{1/3} = A \left(\frac{E^2}{\Delta T} \right) + B \quad (3.3)$$

The constant, A , is a function of both fluid and sensor properties while, as before, B is associated with heat loss to the substrate. Equation 3.3 then constitutes the calibration relationship for surface hot-films. An example of a calibration curve, obtained by Suder, O'Brien, and Reshotko (1988), is shown in Figure 3.2. Consistent with Equation 3.3, the cube root of wall shear varies linearly with the square of the sensor output voltage.

Before moving ahead, it is important to note some limitations associated with surface hot-film anemometry as just described. First, one disadvantage of this measurement technique

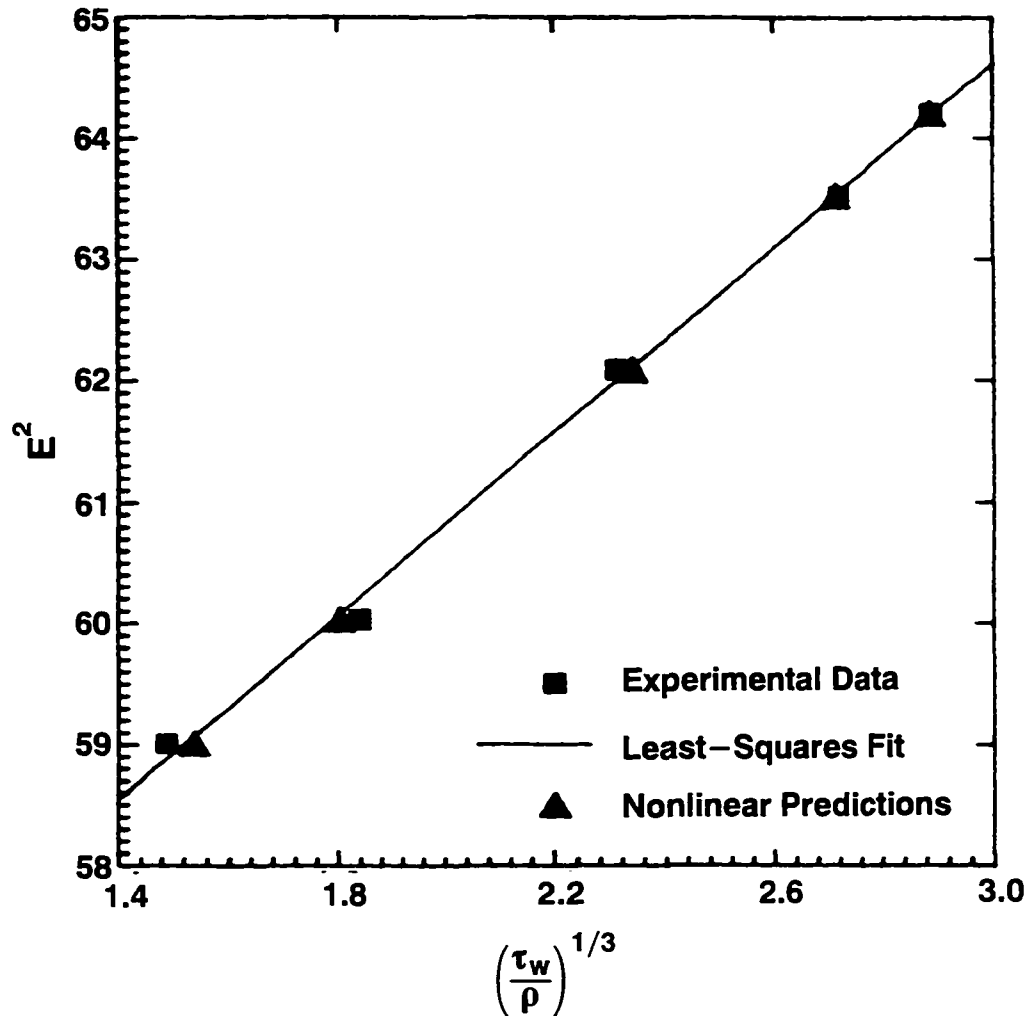


Figure 3.2. Calibration of a surface hot-film sensor (from Suder, O'Brien, and Reshotko, 1988)

is that the measured voltage varies with only the sixth root of wall shear stress. Consequently, small changes in voltage correspond to very large changes in wall shear stress.

Secondly, when rigorous calibration of the sensors is undertaken, special care is required. The calibration constants, A and B, have been found to differ depending on whether the boundary layer is laminar or turbulent. These differences can lead to errors of up to 15 percent (Bellhouse and Schultz, 1966). Suder, O'Brien, and Reshotko (1988) found that, for sensors calibrated in turbulent flow, the magnitude of the change in shear stress occurring in transitional flow (as the boundary layer varies from laminar to turbulent states) was not measured accurately. Fur-

thermore, large deviations in calibration have been documented for apparently small changes in sensor position relative to the wall and for nearly imperceptible accumulation of debris on the sensors (Hanratty and Campbell, 1983). These effects can be minimized by carrying out timely and in situ calibrations.

Lastly, because the “thermal footprint” of the sensor can be much larger than the sensor itself (due to substrate conduction), the dynamic frequency response is substantially less than that of a hot-wire probe (Freymuth and Fingerson, 1977). However, researchers have been able to achieve a frequency response greater than 20 khz which is adequate to investigate fluctuations in wall shear stress (e.g., Hodson, Huntsman, and Steele, 1994, Solomon and Walker, 1995).

3.2 Applications to the Study of Boundary Layer Development

In recent years, numerous studies of boundary layer development along airfoils have been carried out successfully using surface hot-film anemometry. The instrumentation employed in these studies include arrays of hot-films consisting of as many as 50 sensors spaced as closely as 0.1 inch apart. To accommodate curved surfaces, the sensors are typically manufactured onto a thin, flexible substrate that can be wrapped around the airfoil. The sensors have been operated individually or simultaneously in groups. The latter capability provides a means to track individual “events” (whose signature is a variation in wall shear stress) as they convect along the airfoil surface.

Such investigations have been carried out for isolated airfoils (e.g., Pucher and Gohl, 1987, Stack, Mangalam, and Berry, 1987), aircraft wings (e.g., Mangalam, Wusk, and Kuppaa, 1991), cascades of airfoils (e.g., Hodson, 1985c, Halstead, 1989), and multi-bladerow turbomachines (e.g., Hodson, Huntsman, and Steele, 1994, Halstead et al., 1995, and Solomon and Walker, 1995).

For these studies, the primary objective motivating the use of surface hot-film anemometry was to determine the characteristics of the boundary layer – whether laminar, turbulent, transitional, or separated – along an airfoil. Unlike more fundamental studies (e.g., Bellhouse

and Schultz, 1966), an exact quantitative measure of wall shear stress was not required. Because of this differing objective and because rigorous calibration of the large numbers of sensors is not practical or necessary, a somewhat different approach has evolved for the analysis of hot-film measurements as compared to that described by Equation 3.3 in the previous section. This approach is considered below.

The relationship between heat transfer from the sensor to the fluid and wall shear stress given initially by Equation 3.1 can be rewritten as

$$A'' \tau_w^{1/3} = q_{\text{tot}} - q_s \quad (3.4)$$

The right hand side represents the convective heat transfer to the fluid and is determined from the difference of the total heat dissipated by the sensor, q_{tot} , and the heat loss to the substrate, q_s . The former is calculated directly as described in the previous section. The heat loss to the substrate, however, is difficult to determine accurately. In the case where a rigorous calibration is undertaken, as illustrated in Figure 3.2, the value of q_s can be deduced by extrapolating to zero wall shear. For investigations where direct calibration is not carried out, Hodson (1985c) found that substrate heat loss could be approximated by that which occurs at “zero-flow” condition. Applying this simplification, Equation 3.4 can be written as the following proportionality

$$\tau_w^{1/3} \propto q_{\text{tot}} - q_0 \quad (3.5)$$

and, in terms of anemometer output voltages, as

$$\tau_w^{1/3} \propto E^2 - E_0^2 \quad (3.6)$$

In reality, the heat transfer from the sensor at zero flow, q_0 , is greater than q_s due primarily to natural convection (Blackwelder and Eckelmann, 1977), hence the proportionality sign. Consequently, this simplification is *not* appropriate if absolute values of wall shear are desired. However, the proportionality given by Equation 3.6 accurately reflects the *relative* variation of wall shear with heat transfer.

The above proportionality between anemometer output voltage and wall shear stress is entirely valid as it pertains to a single hot-film sensor. That is to say, the relative variation in wall shear along an airfoil can be determined by way of Equation 3.6 using, for example, a single, moveable sensor. Such an approach was adopted by Hodson(1984) and Halstead(1989). For multi-sensor applications, however, this relationship is not adequate in its present form. This is because small manufacturing variations between sensors and slight differences in the achieved ΔT will result in differing values of $E^2 - E_0^2$ from sensors subjected to the same level of wall shear stress. In other words, from sensor to sensor, there can exist slight variations in convective heat transfer to the fluid for the identical value of wall shear. To remove this variability, Hodson and Addison (1989) suggest the following normalization

$$\tau_w^{1/3} \propto \frac{E^2 - E_0^2}{E_0^2} \quad (3.7)$$

Some subtle but important issues regarding this normalization are worth noting. As apparent from our discussion above, E_0^2 , is associated with *conductive* heat transfer from the sensor to the substrate. Consequently, we are actually normalizing the term associated with convective heat transfer, $E^2 - E_0^2$, with that associated with conduction. As Hodson (1985b) correctly points out, such an approach is valid *only* if the “rates of heat transfer to the air and substrate are similar functions of the same variables.” Simply put, any variations from one sensor to another are assumed to influence conductive and convective heat transfer in equal proportions. Given the manufacturing repeatability of hot-film sensors now attained and the experimental procedures used to operate them, this approach for normalization has been shown to account successfully for such sensor-to-sensor variability (ibid., Pucher and Gohl, 1987, and Schroder, 1991).

To conclude this development, actual measurements from surface hot-films are then analyzed by way of Equation 3.8

$$q\tau_w = \left(\frac{E^2 - E_0^2}{E_0^2} \right)^3 \quad (3.8)$$

The term, $q\tau_w$, is referred to as quasi wall shear stress after Solomon and Walker (1995). To reiterate, it is a measure of the “relative” variation of wall shear stress. Implicit to the formulation of Equation 3.8 is that, as boundary layer separation is approached, $E^2 - E_0^2$ and hence the quasi wall shear stress approach zero.

Because the quantities E^2 and E_0^2 are similar in magnitude, the accuracy of $q\tau_w$ is very dependent on the accurate determination of the zero flow voltage. This not an easy task however. The level of sophistication required varies with test facility. For those facilities where the total temperature of the air does not vary significantly from that during facility operation, a standard approach is to operate each sensor individually and monitor its output voltage. The associated heat transfer is primarily that of transient conduction into a semi-infinite, non-homogeneous solid (i.e., sensor substrate, adhesive, airfoil). The value of the zero flow voltage is taken at the point where its variation with time is small. Obviously, there is some arbitrariness associated with this procedure. The key is to maintain consistency from one sensor to the next. As will be described in Chapter 5, small differences on total temperature from zero flow to running conditions can be taken into account when using this method.

A more sophisticated approach is required in flow environments where the air temperature during testing is significantly different from that at zero flow. Such has been the case, for example, in the high-speed facilities employed by Schroder (1991) and Hodson, Huntsman, and Steele (1994). The test vehicles for both were actually engine LP turbine components. Consequently, there was a significant decrease in temperature from stage to stage through the turbine because of work extraction. Hence for a given sensor setup, ΔT (and consequently E_0) will change during facility operation from its zero flow condition. To compensate, Schroder (ibid.) adjusted the overheat temperature, ΔT , of each sensor during rig operation so that it was equal to that when E_0 was obtained at zero flow.

As a historical note, it should be pointed out that for many of the early investigations (Pucher and Gohl, 1987, Vijayaraghavan and Kavanagh, 1987, Halstead, 1989, and Hodson and

Addison, 1989), workers presented hot–film results in the form of mean voltage ratio, that being

$$\frac{E - E_0}{E_0} \quad (3.9)$$

rather than in the form of quasi wall shear stress (Equation 3.8). From the above discussion, it is readily evident that the former is also proportional to wall shear stress – albeit in a less direct sense. Due primarily to the contributions of Hodson and his co–workers, the methodology evolved from that of mean voltage ratio to quasi wall shear stress. The result is a relationship tied more closely to the actual physics of hot–film anemometry. A direct comparison of these two approaches is made by way of experimental measurements presented in the section that follows.

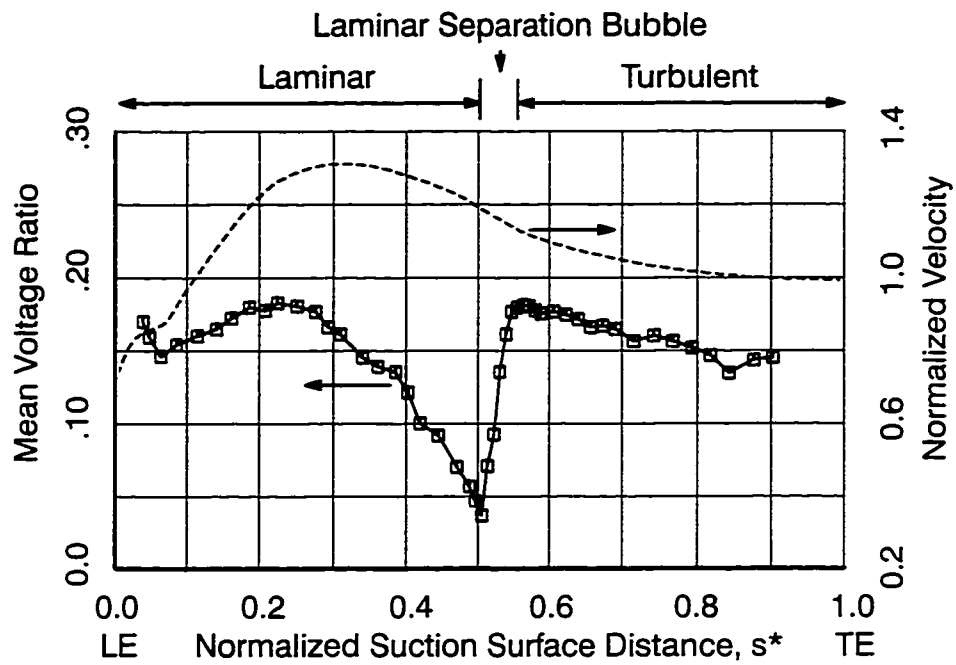
3.3 Interpretation of Surface Hot–Film Measurements

Characteristics of boundary layer development determined using surface hot–film sensors will now be illustrated by way of measurements acquired by Halstead(1989). In that work, hot–film data were obtained along the suction surface of a turbine airfoil in cascade. The mean flowfield was steady. The development of the boundary layer along the airfoil was altered by varying turbulence intensity and Reynolds number. Hot–film measurements were obtained using a single sensor that could be positioned at closely–spaced intervals from the leading to trailing edges of the airfoil.

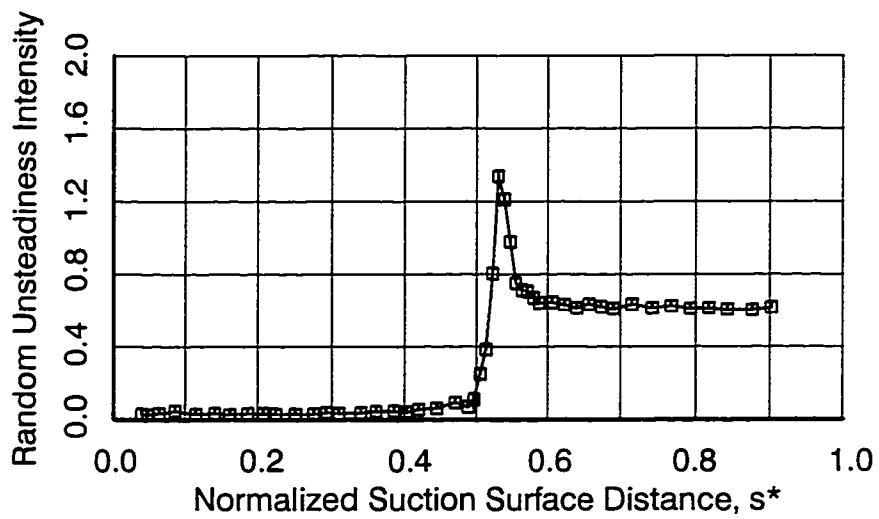
The two data sets that will be considered pertain to cases where separated and attached–flow transition were documented. Important and useful extensions of the data analysis relative to that of Halstead(1989) will be noted.

3.3.1 Boundary Layer Development with Separated–Flow Transition

Hot–film measurements obtained at low Reynolds number ($Re_{ssl}=6.1 \times 10^5$) and low inlet turbulence ($Tu_{in}=0.8\%$) are presented in Figure 3.3. As indicated by the ordinate of Figure 3.3a, the variation in wall shear stress was expressed as the mean voltage ratio given by Equation 3.9. The fluctuations in wall shear are presented in part b in the form e_{rms}/E_0 . The abscissa of each



a) mean voltage ratio and normalized velocity distribution



b) random (RMS) unsteadiness intensity

Figure 3.3. Surface hot-film measurements from a turbine cascade for $Re_{ssl}=6.1 \times 10^5$ and $Tu_{in}=0.8\%$ (from Halstead, 1989)

is normalized surface distance along the suction surface. Superimposed in Figure 3.3a is the suction surface velocity distribution, normalized by its exit value.

Regions of laminar, separational, and turbulent flow as identified by Halstead(1989) are indicated in Figure 3.3a. The boundary layer along the initial fifty percent surface length downstream of the leading edge was laminar. After a strong acceleration around the leading edge, the mean voltage ratio decreased monotonically to $0.49s^*$ indicating decreasing wall shear. The associated random unsteadiness was at a low relative level. Fluctuations in the raw time traces (ibid.) were nearly imperceptible.

The level of mean shear stress and unsteadiness increased sharply downstream of $0.5s^*$. Flow visualization revealed a separation bubble at this location (ibid.). Complete reattachment occurred by about $0.56s^*$ and coincided with the local maximum in mean voltage ratio. The peak in wall shear fluctuation, occurring at $0.53s^*$, was associated with the rapid transition to turbulence in the separated shear layer.

Downstream of reattachment, the mean voltage ratio decreased in response to the decreasing level of diffusion back to the trailing edge. The raw traces from along this portion of the airfoil contained evidence of turbulent fluctuations (ibid.). As suggested in Figure 3.3b, the amplitude of these fluctuations was less than that of the transitional flow but, as expected, was significantly greater than that of the laminar flow.

The “signature” of laminar separation, transition, and reattachment as shown in Figure 3.3 has been documented by other researchers (Pucher and Gohl, 1987, and Stack, Mangalam, and Berry, 1987). In all cases, the observed length of transition was short relative to the airfoil surface length.

Since the measurements of Figure 3.3 were first reported, the analysis approach for hot-film measurements has evolved from that of mean voltage ratio (Equation 3.9) to that of quasi wall shear stress (Equation 3.8). To compare these approaches, the measurements of Figure 3.3a have been reprocessed into the form of the latter. The resulting distribution of quasi wall shear

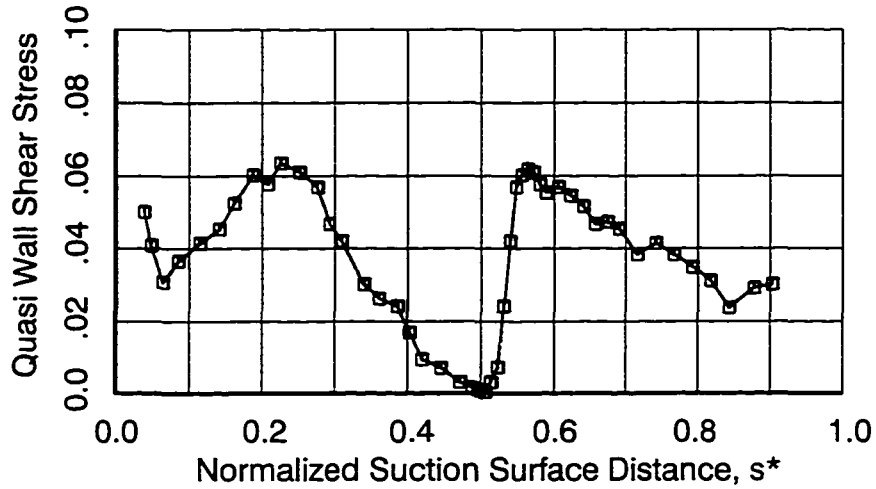
stress is presented in Figure 3.4a. In comparison to Figure 3.3a, it is evident that all trends were preserved. However, because quasi wall shear is proportional to the *sixth* power of the mean voltage ratio, the variation in magnitude of the former is greatly stretched relative to the latter. Most prominent in the distribution of quasi wall shear in Figure 3.4a is the near zero value at the location of laminar separation.

To further assess this approach for the analysis of surface hot-film data, the experimental results are compared to a numerical prediction in Figure 3.4b. The calculation was carried out using a modified version of the STAN5 boundary layer code as described by Halstead, Okiishi, and Wisler (1990). The ordinate is local wall shear stress normalized by the exit (not local) dynamic head and hence is comparable directly to quasi wall shear stress. The agreement between the measurements and calculation is self-evident. The only significant difference relates to the predicted location of separation. As noted by the above authors, this is attributed to the inability of the parabolic boundary layer equations to account for elliptic effects that occur near separation.

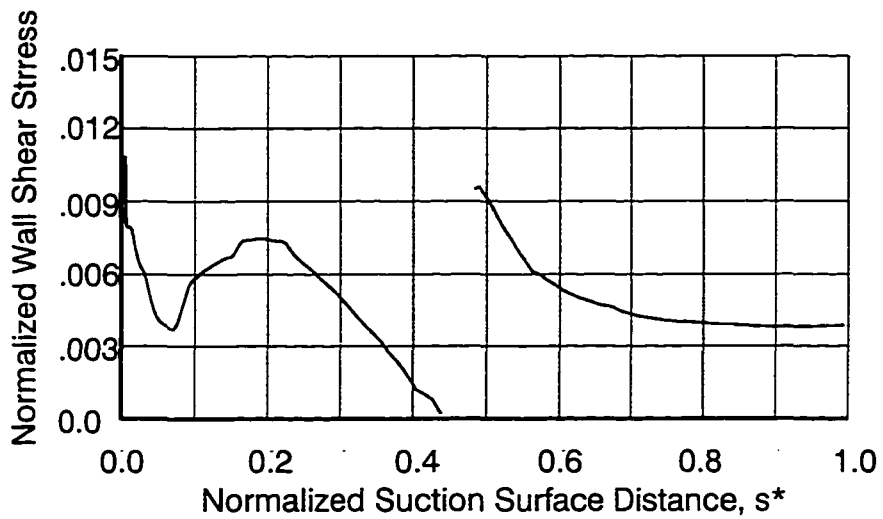
3.3.2 Boundary Layer Development with Attached-Flow Transition

Characteristics of attached boundary layer flow are exhibited in Figure 3.5. These measurements were obtained at a higher Reynolds number ($Re_{ssl}=1.27 \times 10^6$) and higher inlet turbulence intensity (6.4%). The normalized velocity distribution is identical to that for the lower Reynolds number case just described. Flow visualization from along the suction surface indicated that no boundary layer separation was present.

As was done above, the mean voltage ratio presented in Halstead(1989) has been recast into quasi wall shear stress. The resulting distribution is shown in Figure 3.5a. Regions of laminar, transitional, and turbulent flow are identified. Corresponding distributions of intermittency, random unsteadiness, and skew provided in Figures 3.5b–d reveal transitional characteristics of the boundary layer. These latter quantities were computed from instantaneous time traces ob-

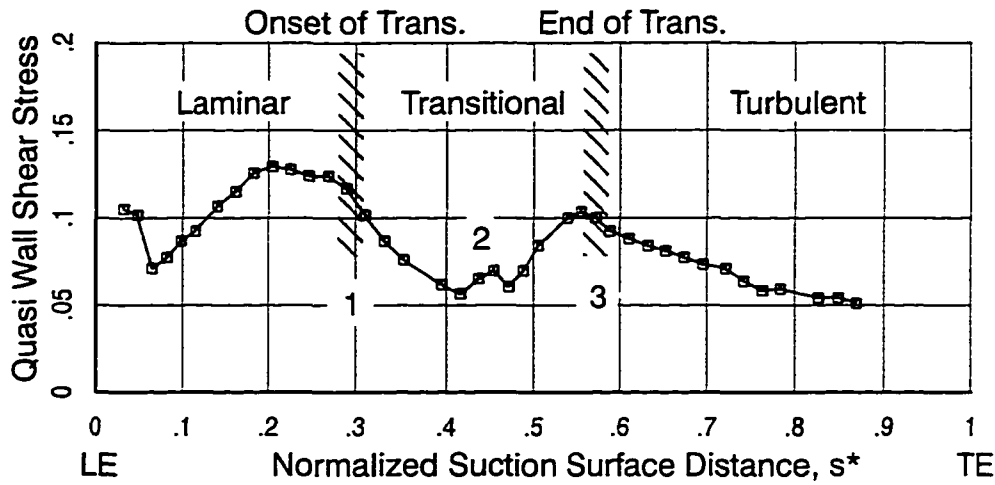


a) quasi wall shear stress determined from surface hot-film measurements

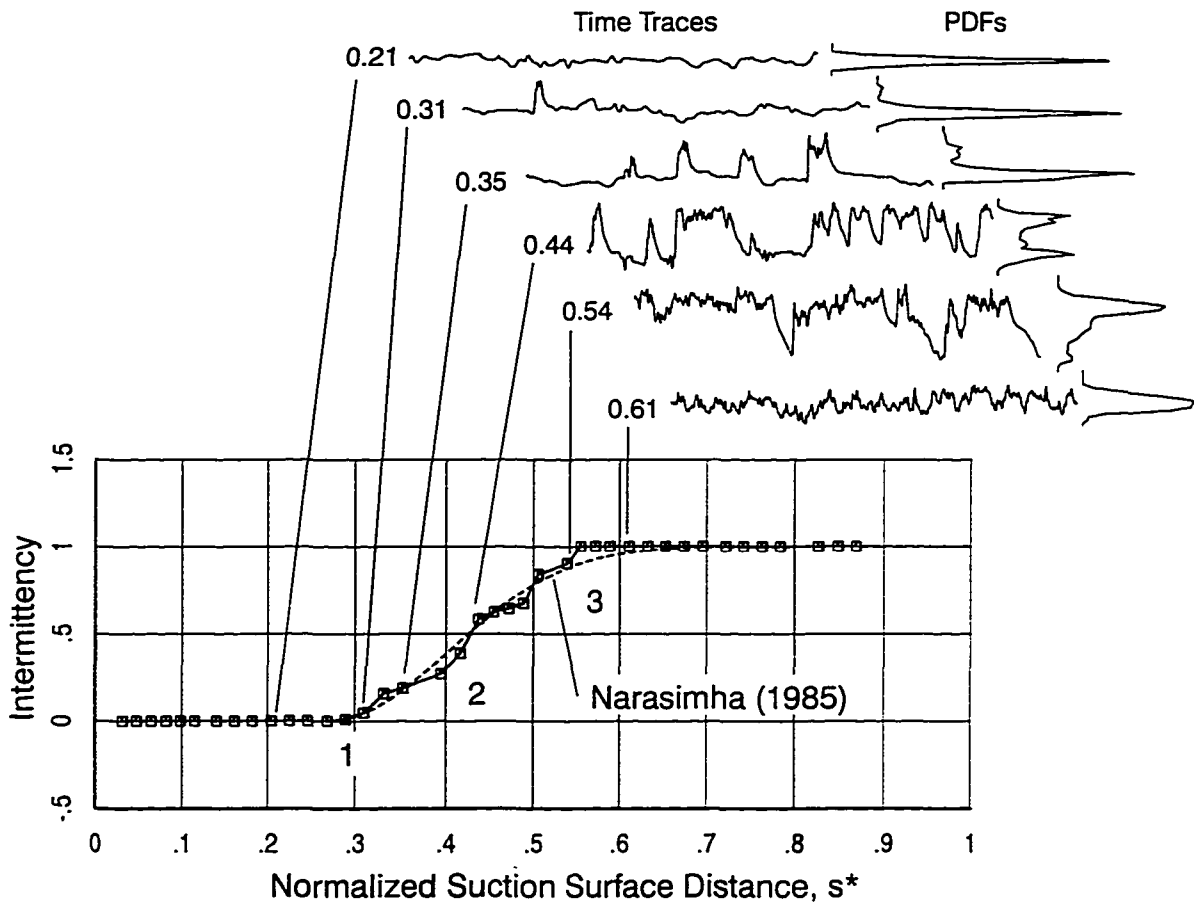


b) normalized wall shear stress calculated using 2D boundary layer analysis

Figure 3.4. Comparison of surface hot-film measurements with boundary layer predictions

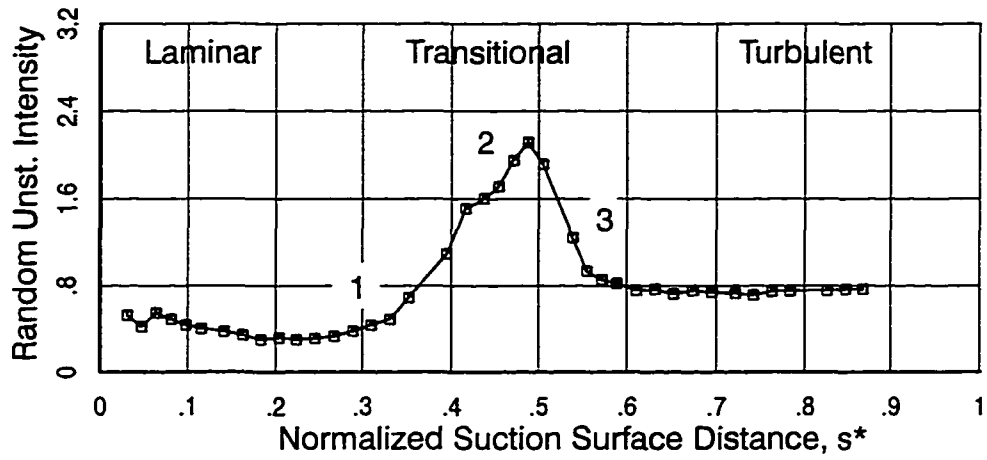


a) quasi wall shear stress

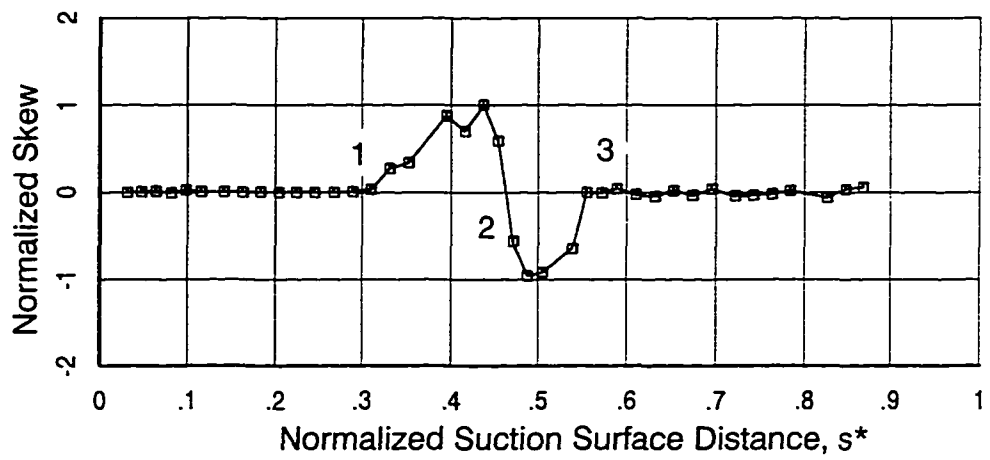


b) intermittency and selected time traces

Figure 3.5. Surface hot-film measurements from a turbine cascade for $Re_{ss1}=1.27 \times 10^6$ and $Tu_{in}=6.4\%$



c) random (RMS) unsteadiness intensity



b) normalized skew

Figure 3.5. continued

tained at each measurement location. Six selected traces are included in Figure 3.5b. To the right of each is their respective probability density function (PDF).

The transitional nature of the boundary layer along the suction surface is very apparent from the time traces in Figure 3.5b. The traces upstream of $0.3s^*$ contain, in a relative sense, fluctuations of low amplitude and frequency. This is characteristic of a laminar boundary layer perturbed by high freestream turbulence. The first indication of transition occurs in the trace at $0.31s^*$ where a single spike of wall shear stress is observed. Additional such events are evident at $0.35s^*$. The variation in shear stress of these events indicate that they are signatures of individual turbulent spots (Appendix A). At $0.44s^*$, transition is near the half-way point as the fluctuating shear stress resides an equal amount of time at laminar and turbulent levels. Aft of $0.61s^*$, the traces contain only turbulent fluctuations.

The onset and extent of boundary layer transition can be quantified in terms of intermittency, random unsteadiness, and skew. Intermittency is defined generally as the fraction of time the boundary layer is turbulent. Narasimha (1985) further qualifies this definition by adding that, more specifically, it is the fraction of time the shear stress at the wall is at a turbulent level. Intermittency is equal to 0.0 for laminar flow, varies from 0.0 to 1.0 for transitional flow, and is equal to 1.0 for turbulent flow. From the time traces of hot-film data, values of intermittency were calculated using simple thresholding as described by Ashworth, LaGraff, and Schultz (1989). The results shown in Figure 3.5b are in general agreement with the universal intermittency distribution of Narasimha (1985). Had the time traces been acquired for a longer duration, it is likely a smoother distribution from the measurements would have resulted.

Random unsteadiness and skew from surface hot-film measurements are also useful in deciphering boundary layer behavior. Random unsteadiness, shown in Figure 3.5c, is a measure of the amplitude of the fluctuations about the mean. It is computed as the root-mean-square of the fluctuations normalized by the local time-averaged.

Skew is a less familiar quantity and has been used only recently to interrogate surface hot–film measurements, albeit with varying degrees of success (Schroder, 1991, Hodson, Huntsman, and Steele, 1994). Skew is computed as the third order center moment. For this work, it is normalized using the local time mean. In addition, the computed values presented in Figure 3.5d are scaled by the absolute value of the largest computed value to facilitate presentation.

At the onset of transition, identified by point 1 in Figure 3.5, intermittency rises above zero (Figure 3.5b) and random unsteadiness increases above its laminar level (Figure 3.5c). Additionally, values of skew become positive (Figure 3.5d) in accord with the skewing of the PDFs, examples of which are shown for 0.31 and 0.35s*. That skew is virtually zero prior to transition indicates that the fluctuations in laminar shear stress are, in a relative sense, symmetric about the mean.

Near the midpoint of transition, labeled point 2, intermittency is equal to about 0.5. Random unsteadiness is now near its peak value due to the continual switching from laminar to turbulent levels of shear stress. Skew, after reaching a positive maximum, decreases to zero at the transition midpoint. This zero crossing indicates that the fluctuations are symmetric about the mean. However, as evident from the time trace at 0.44s* in Figure 3.5b, the associated PDF is bimodal.

For the latter stages of transition (point 3), random unsteadiness decreases as fewer laminar events persist in an otherwise turbulent flow. Skew is negative in value as the PDFs now exhibit asymmetry towards the laminar levels of shear stress. Upon completion of transition, skew is back to a near–zero level which indicates symmetry in the turbulent fluctuations. The corresponding values of random unsteadiness are greater in magnitude than for the laminar flow but less than for the transitional flow.

To conclude then, we see that surface hot–film measurements provide a reliable means by which to discern boundary layer characteristics. Calibration of sensors to absolute values of wall shear stress was not necessary for this interrogation. Hot–film data reduced in the form of

quasi wall shear stress provide an adequate measure of the relative variation in shear stress while the transitional characteristics of the boundary layer can be determined from the instantaneous time traces, random unsteadiness, and skew.

CHAPTER 4. TEST FACILITY

The research described in this dissertation was carried out at the Aerodynamics Research Laboratory of General Electric Aircraft Engines (GEAE) utilizing their Low Speed Research Turbine. Descriptions of the test vehicle and turbine configuration are contained in the first section of this chapter. A summary of the turbine operating domain and overall aerodynamic performance constitute the second and third sections, respectively. A description of the detailed measurements used to achieve the program objectives are outlined in Chapter 5.

4.1. Test Vehicle

The Low Speed Research Turbine (LSRT) is a facility used to test large-scale models of high-speed, multi-stage turbines in an environment where detailed measurements of the flowfield can be obtained. A schematic of the facility is shown in Figure 4.1. The turbine has a vertical axis of revolution with a constant casing diameter of 60.0 in. Ambient air is drawn through the turbine from the inlet at the top of the machine to the plenum located beneath using a large centrifugal blower. A calibrated bellmouth/inlet system filters the air and provides a measure of its mass flowrate. Flowing conditioning screens (24 mesh by 0.012 in. wire) located upstream of the test turbine establish a uniform flowfield at the inlet. After the air passes through two stages of turbine blading, outlet guide vanes direct the flow to a zero-swirl condition at the entrance to the plenum diffuser. Inlet guide vanes to the blower and bleed ports located on the outer cylinder of the plenum control the mass flowrate through the turbine. A variable-speed AC motor drives the centrifugal blower with additional power provided by the test turbine using a right-angle gear box. Air exhausted from the blower is directed into an air handling/mixing system located outside the laboratory. Here, the exhausted air is mixed with outside air in varying proportions and directed back into the laboratory. This system is adjusted during facility operation to maintain nominally constant temperature and pressure conditions within the laboratory.

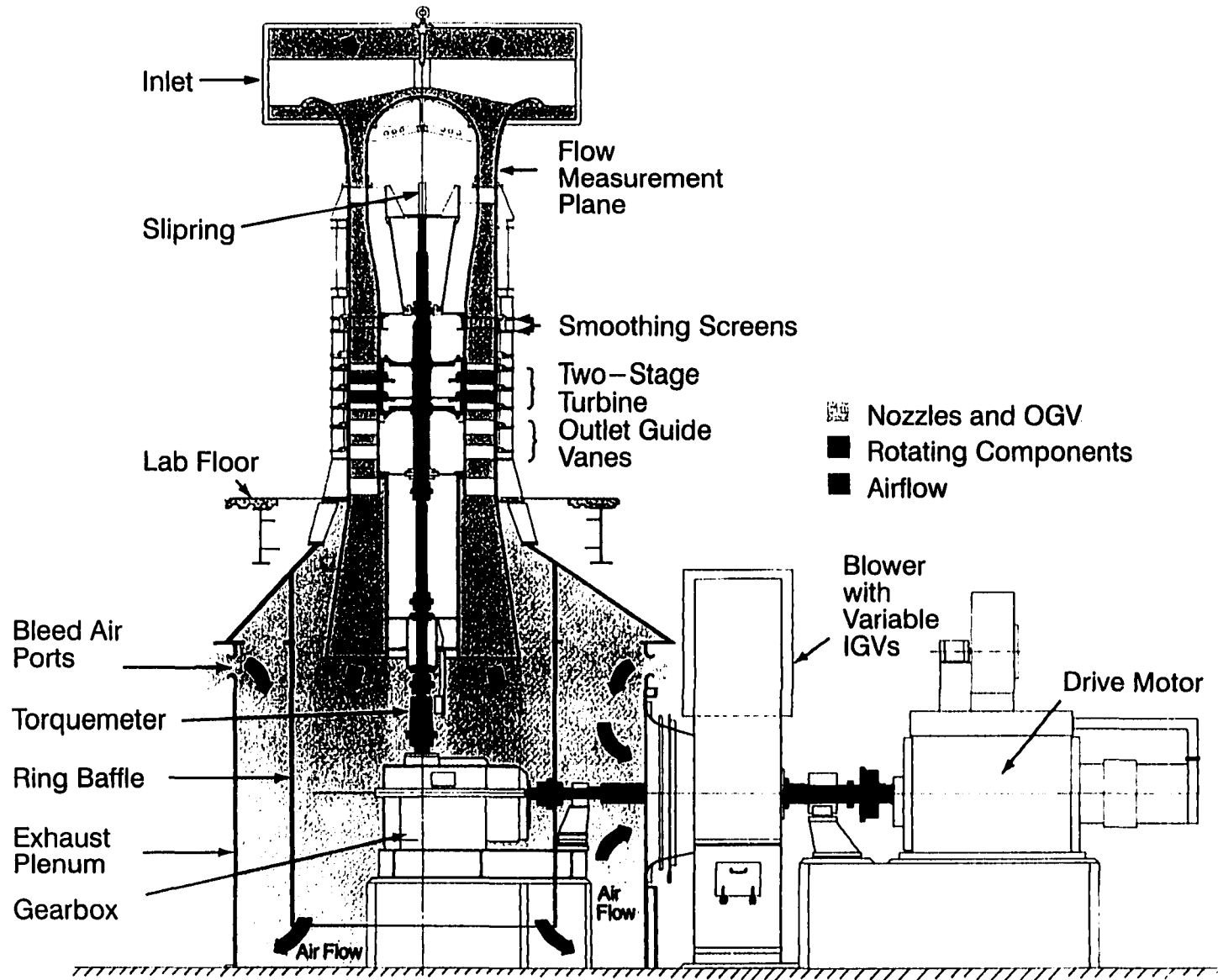


Figure 4.1. Schematic of LSRT facility

A computer-controlled data acquisition system is used to operate the facility and to obtain numerous time-averaged measurements required to deduce turbine performance. Shaft rotational speed of the turbine is acquired using a 60 tooth gear with a magnetic pickup. Speed is held constant to within $\pm 0.01\%$ of the maximum speed of 615 rpm. Work output from the turbine is measured using a strain-gage torque meter accurate to within $\pm 0.4\%$ at design-point operation. All differential pressures are acquired using transducers maintained in temperature-controlled environments. Accuracy of these transducers is $\pm 0.015\%$ of full scale. Pressure measurements from the relative frame of reference are acquired using a slipring in conjunction with a rotating multiplexer, pressure transducer, and voltage amplifier. Turbine inlet temperature is measured to an accuracy of $\pm 1.0^\circ$ F using nine RTDs positioned at various locations within the bellmouth inlet. Environmental conditions are determined from dry bulb and dew point temperatures, obtained using a hygrometer, and from atmospheric pressure, measured with an absolute pressure gage. These measurements are accurate to within $\pm 1.0^\circ$ F and ± 0.0025 psi, respectively, and provide a means to account for moisture content of the air.

A meridional view of the test turbine is provided in Figure 4.2 and, to its immediate right, blading cross-sections are shown as oriented when viewed from the casing towards the hub. The turbine consists of a two-stage configuration with the second being the test stage from which detailed aerodynamic measurements are obtained. Air enters the turbine in an axial direction at the Nozzle 1 inlet as denoted. An annulus height of 12 inches and hub-to-tip radius ratio of 0.6 are maintained through the turbine. The casings are constructed of transparent, Plexiglass windows mounted into steel casing frames. The clear windows provide visual access to facilitate flow visualization and placement of instrumentation. Individual nozzle airfoils are mounted into rings that allow each bladerow to be moved circumferentially past fixed instrumentation for surveying across nozzle blade passages. Both nozzle bladerows are shrouded at the hub. The turbine airfoils are constructed primarily of a molded fiberglass/epoxy material affixed to aluminum trunnions. Airfoils instrumented with arrays of surface static pressure taps are

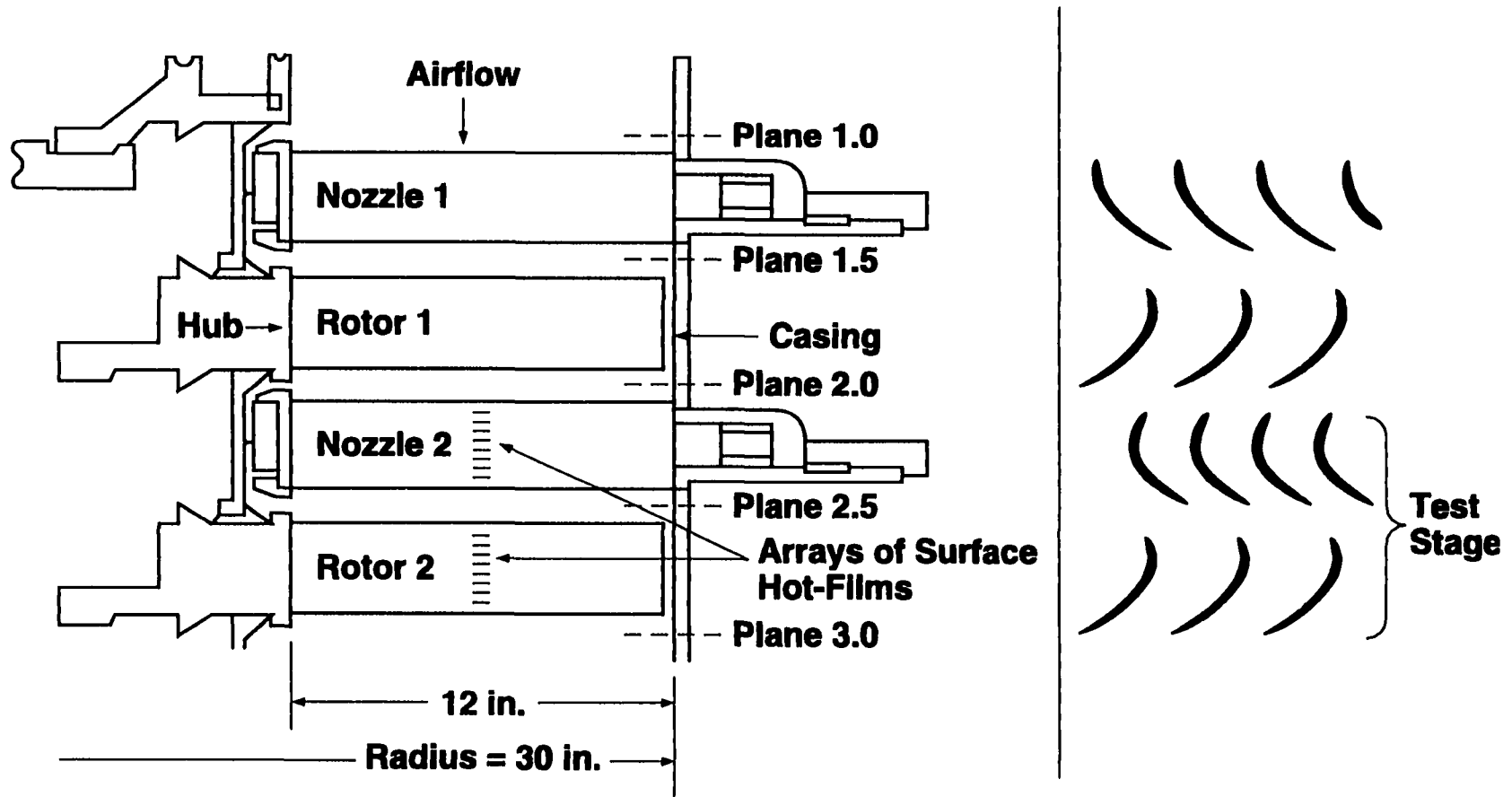


Figure 4.2. Configuration of two-stage low pressure turbine

manufactured entirely of aluminum to facilitate the required machining processes. Stringent surface quality and blade shape tolerances are maintained during airfoil manufacture. The resulting airfoil surfaces are hydraulically smooth for the Reynolds numbers encountered in the facility. As shown in the figure, selected nozzle and rotor blades from the test stage are instrumented with arrays of hot-film sensors mounted to their surfaces and positioned at midspan. Measurements obtained using this instrumentation comprise a major portion of this research. A detailed description of the installation and operation of these sensors is included in the following chapter.

The LSRT blading consists of a low-speed, aerodynamic model derived from a low pressure turbine (LPT) family representative of typical commercial GE aircraft engines. Pitchline (midspan) design parameters are provided in Table 4.1 with blading terminology described in Figure 4.3 (after Glassman, 1972). Design of the low-speed blading is accomplished by applying principles of geometric and aerodynamic similarity in relation to their high-speed counterparts as discussed in Wisler (1985). Similarity parameters including Reynolds number, flow coefficient, pressure coefficient, reaction, radius ratio, solidity, aspect ratio, clearance-to-height and axial spacing-to-chord ratios, as well as airfoil pressure distribution, are judiciously matched during the design process. The complex disturbance environment of multi-stage machines is achieved using the two-stage configuration. Such a research facility, characterized by its large size and low speed, has been shown to provide detailed, accurate, and low-cost measurements of flowfields that closely simulate those of actual engine components (ibid.).

4.2. Turbine Operating Domain

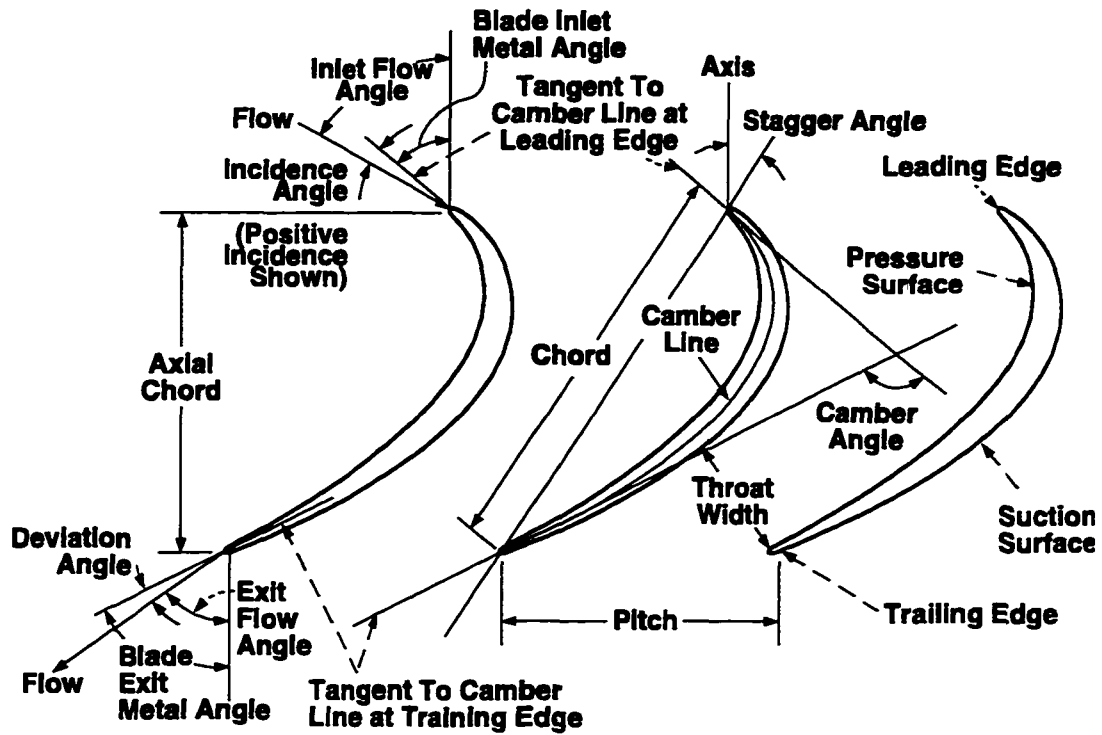
The operating domain of the LSRT is provided in Figure 4.4 and is defined in terms of specific flow, ϕ , and Reynolds number, \overline{Re} . A selected coordinate pair (ϕ, \overline{Re}) chosen from within this operating space uniquely determines the test condition of the turbine. Flow coefficient is given as the abscissa and represents a measure of the airflow through the turbine. It is defined as the average axial velocity through the machine, \overline{V}_z , normalized by the blade rotational speed

Table 4.1. Pitchline blading parameters of LSRT

	Nozzle 1	Rotor 1 / Rotor 2	Nozzle 2
Solidity	1.64	1.48	1.68
Aspect Ratio (based on chord)	3.97	3.87	5.10
Aspect Ratio (based on throat)	13.10	12.67	17.37
Chord [in.]	3.03	3.14	2.35
Axial Chord [in.]	2.33	2.61	2.17
Suction Surface Length, [in.]	3.36	3.98	3.13
Pressure Surface Length, [in.]	3.15	3.61	2.79
Throat Width [in.]	0.916	0.947	0.691
Stagger Angle [deg]	39.8	34.9	22.9
Camber [deg]	60.0	96.8	102.4
Number of Airfoils	82	72	108
Axial Gap [in.]	1.00	1.00	

at midspan, U_m . The average axial velocity is determined from the mass flowrate observed at the flow measurement plane, the average static density across the turbine, and the turbine annulus area. The flow coefficient of this turbine configuration can be varied continuously from values less than 0.8 to a maximum of about 1.25.

Turbine Reynolds numbers based on suction surface length (ssl) and throat width(d_0) constitute the left and right ordinates, respectively, of the operating domain. Using standard turbine convention, the Reynolds number is defined in terms of bladerow exit velocity, kinematic viscosity, and the desired characteristic length (ssl or d_0), all averaged across the test stage at midspan. As indicated in Figure 4.4, the Reynolds number range of this research turbine extends from values less than those associated with cruise(altitude) conditions to values greater than at takeoff, as compared to its high-speed, LP turbine counterpart. All subsequent references to



$$\text{Aspect Ratio (Based on Throat)} = \frac{\text{Blade Height}}{\text{Throat Width}}$$

$$\text{(Based on Chord)} = \frac{\text{Blade Height}}{\text{Chord}}$$

$$\text{Solidity } \sigma = \frac{\text{Chord}}{\text{Pitch}}$$

$$\sigma_z = \frac{\text{Axial Chord}}{\text{Pitch}}$$

Figure 4.3. Turbine blading terminology (after Glassman, 1972)

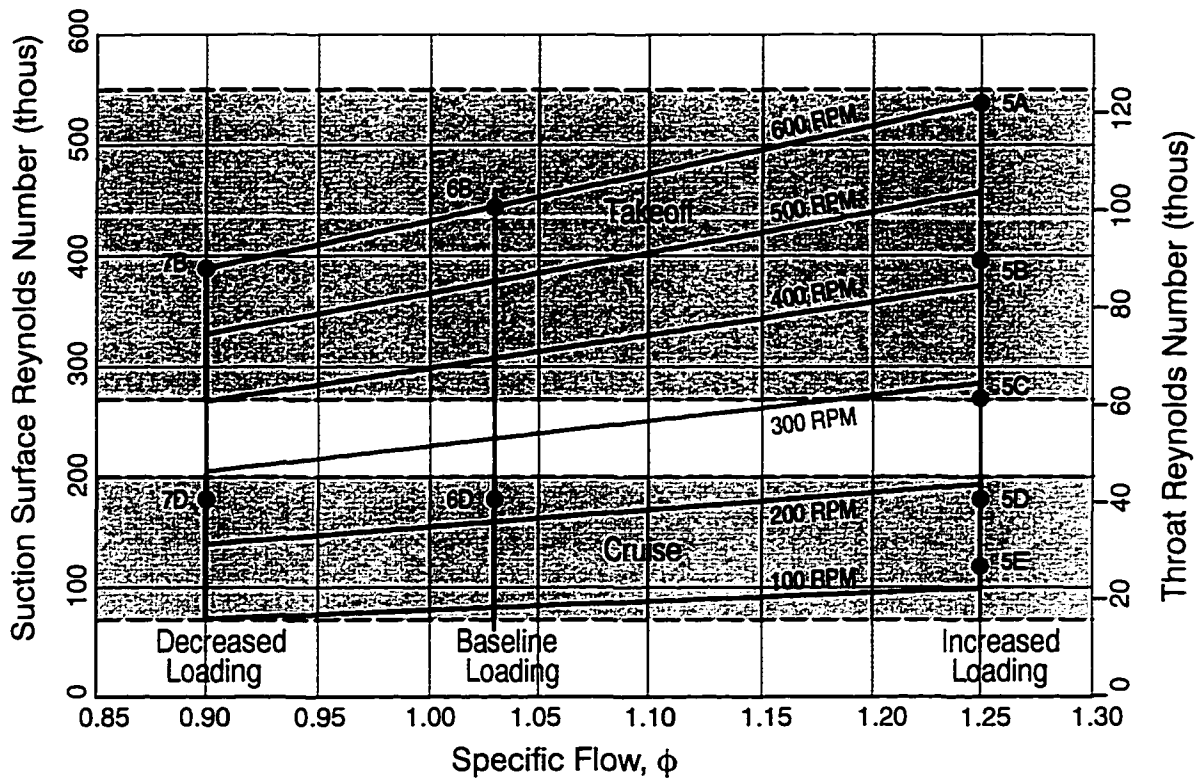


Figure 4.4. Operating domain of LSRT

Reynolds number associated with this work will be in terms of its value relating to suction surface length unless otherwise noted.

Superimposed onto the operating domain are lines of constant turbine rotational speed. In general, rotational speed for a given test condition (ϕ , \overline{Re}) is also a weak function of environmental conditions, hence its exact value is determined on a day-to-day basis during facility operation.

Test conditions at which detailed aerodynamic and boundary layer measurements were obtained are given as the filled symbols in Figure 4.4. They extend over the entire operating domain of the turbine.

4.3. Overall Turbine Performance

Overall aerodynamic performance of the two-stage turbine is reported in Figure 4.5 in the form of the Smith diagram (Smith, 1965). The abscissa is specific flow as described pre-

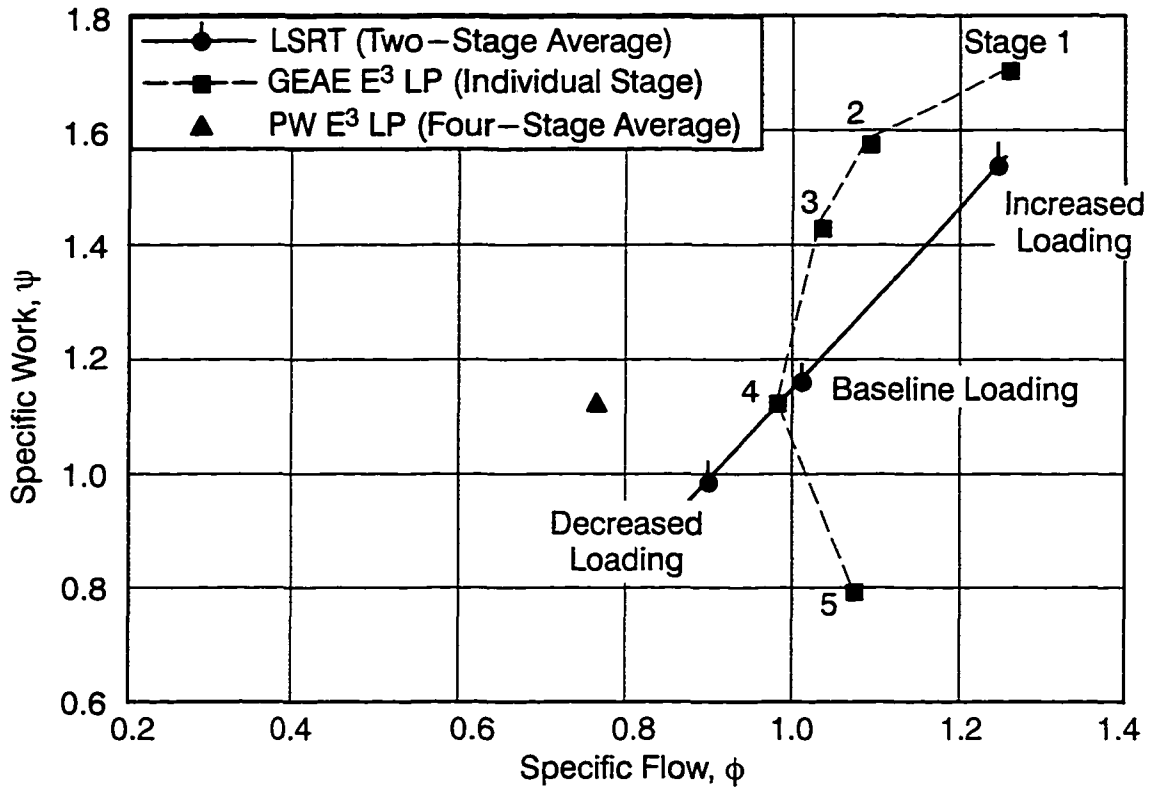


Figure 4.5. Overall performance of two-stage turbine

viously. The ordinate is specific work determined on a stage-averaged basis. It is defined by Equation 4.1 as the normalized change in total enthalpy across the turbine.

$$\psi = \frac{\Delta H_t}{2U_m^2 N_{\text{stages}}} \quad (4.1)$$

The numerator is calculated using the measured torque and mass flow as indicated by Equation 4.2.

$$\Delta H_t = \frac{T\omega}{\dot{m}} \quad (4.2)$$

The three loading levels at which detailed aerodynamic and boundary layer measurements were obtained are denoted in the figure. Further details of the specific test conditions are provided in Chapter 7 in conjunction with the boundary layer measurements.

For comparison to the LSRT, loading levels of two LP turbines designed for NASA's Energy Efficient Engine (E³) program are included on Figure 4.5. Stage loading for GEAE's five stage turbine (Brideman, Cherry, and Pedersen, 1983) is given on an individual-stage basis. That for the Pratt and Whitney (PW) turbine (Dubiel, Gray, and Howe, 1989) was provided as a four-stage average only.

CHAPTER 5. EXPERIMENTAL INSTRUMENTATION AND MEASUREMENTS

This chapter contains a description of the experimental instrumentation and measurement techniques employed during the course of this research. The first section provides a discussion of the thermal anemometry system used to obtain all time unsteady measurements. The surface hot-film measurements, obtained to document the detailed features of boundary layer development along the blade surfaces, are described extensively in Section 5.2. This includes discussion of the hot-film sensors, instrumentation of turbine airfoils with the sensors, and data acquisition. Measurements of the unsteady flowfield obtained between each bladerow are presented in the third section. Lastly, pressure measurements used to determine detailed aerodynamic performance of the test-stage blading are described in Section 5.4.

5.1. Thermal Anemometry System

A schematic of the data acquisition system for the time unsteady measurements is shown in Figure 5.1. The heart of this system consists of 24 channels of constant-temperature anemometry (TSI IFA-100) used to operate the surface hot-film sensors and hot-film probes. All channels can be operated simultaneously. Signal conditioning of the bridge output voltage from each anemometer channel is provided internally and consists of gain, offset, high-pass, and low-pass filter adjustments. A visual display of the anemometer output for system diagnostics was provided by a digital oscilloscope (Tektronix 468).

Analog-to-digital (A/D) conversion of all time unsteady measurements was accomplished using a computer-controlled system manufactured by Kinetic Systems. This unit consists of 12 modules with each containing one digitizer with 12-bit resolution. Each module is capable of handling up to eight channels of input. Sampling frequencies of up to 250 khz and storage of up to 4 million samples can be divided among the active channels of each module. The input range for each channel is ± 5 volts. The A/D system was controlled using a Micro-VAX computer.

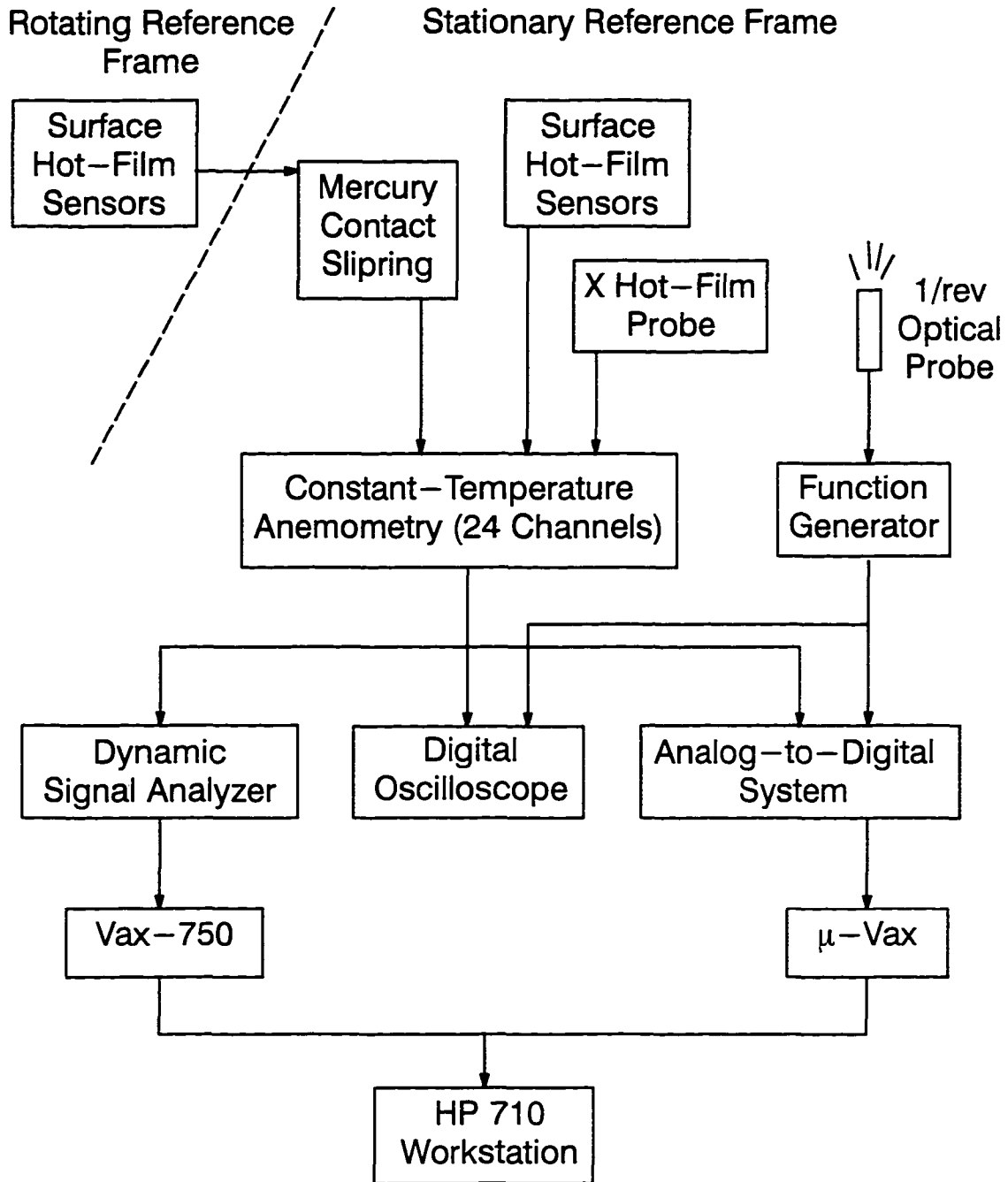


Figure 5.1. Data acquisition system for time unsteady measurements

Acquisition of instantaneous time traces by the A/D system and digital oscilloscope was initiated using an external trigger source. The trigger was initiated on a once-per-revolution basis as a single rotor blade with reflective tape on its tip rotated past an optical sensor mounted to the LSRT casing. Using this external trigger system, acquisition of each time trace is “phase-locked” with the rotor. Hence all acquired traces are associated with the identical rotor passages. This has been shown to be a very useful means by which to acquire measurements from periodically unsteady flowfields such as those found in turbomachinery (Gostelow, 1977).

Frequency spectra of the anemometer output were obtained using an HP 6452A Dynamic Signal Analyzer. The discretized frequency spectrum consisted of 801 equally-spaced elements. The bandwidth of the analyzer could be adjusted to a width of up to 100 khz. On-board analysis capabilities enabled frequency-averaging of individual spectra. All computed spectra were transferred via IEEE-488 interface to a VAX 11-750 computer for storage.

Measurements acquired from the rotating frame of reference were taken through a mercury-contact slipring (Meridian Laboratory) mounted atop the turbine shaft as illustrated in Figure 4.1. Electronic noise from the slipring was less than $1\ \mu\text{V}$. This enabled the low-level signals from the sensor arm of the bridge circuit to be passed directly from the rotating to stationary reference frame without pre-amplification.

All data were transferred to an HP 710 workstation for subsequent analysis after acquisition was completed.

5.2 Surface Hot-Film Measurements

Detailed measurements of boundary layer characteristics were obtained using arrays of densely-packed, surface hot-film sensors. Descriptions of the instrumentation and measurement technique are contained in this section.

5.2.1 Description of Sensors

A schematic of an array of surface hot-film sensors is shown in Figure 5.2. The inset shows an individual sensor in more detail. The arrays were custom-designed specifically for

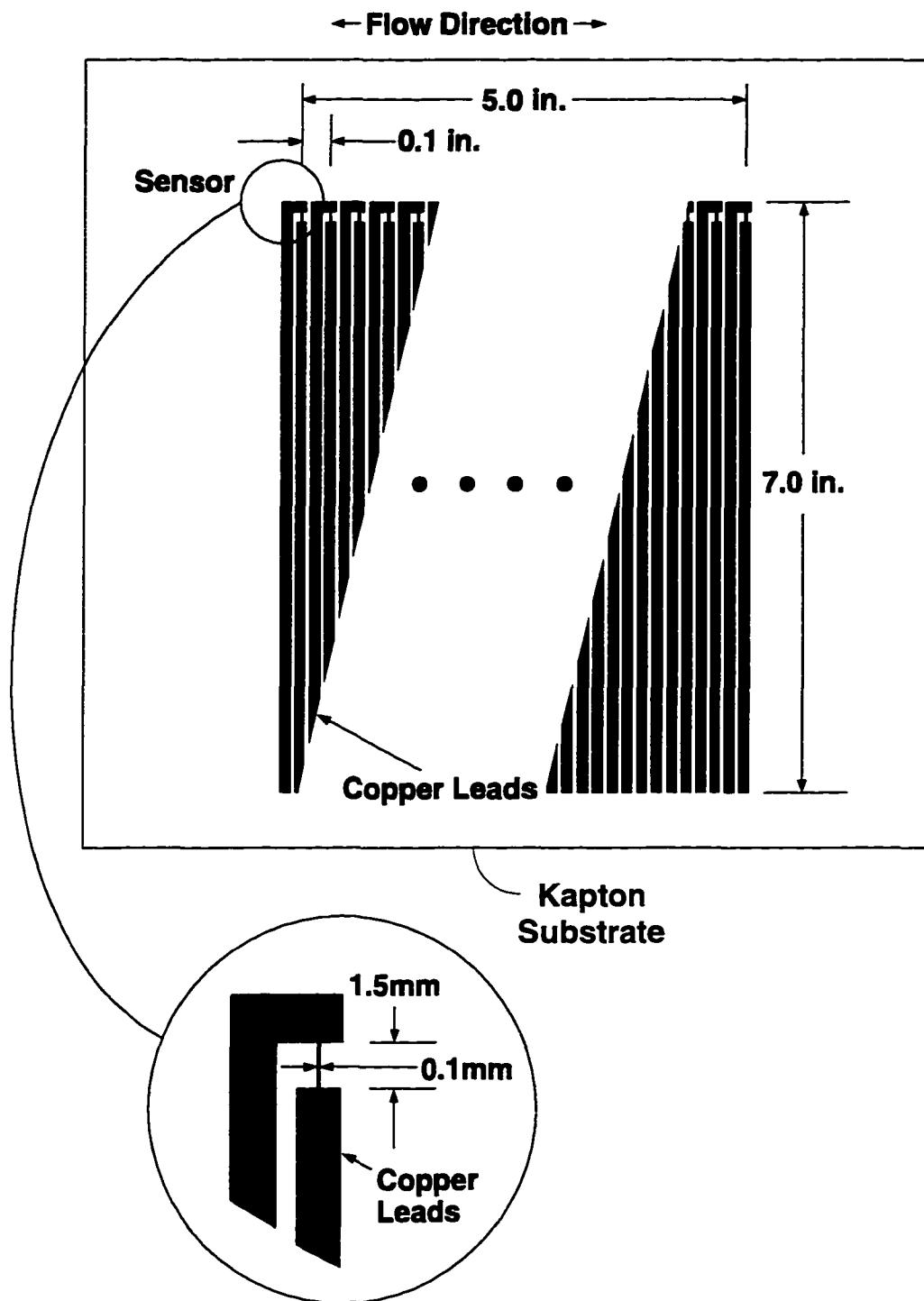


Figure 5.2. Array of surface hot-film sensors

instrumentation of the LSRT blading. They were manufactured by Analytical Services & Materials, Inc. Each array consists of 50 individual sensors placed linearly 0.1 in. apart onto a 14 in. by 14 in. sheet of kapton substrate measuring 0.002 in. in thickness. The flexibility of this substrate allows one to affix readily an array of sensors to test articles with curved surfaces. Each individual sensor element consists of a 2500 angstrom nickel film measuring 0.0039 in. (0.10 mm) in length (parallel to the flow direction) and 0.059 in. (1.5 mm) in width (perpendicular to the flow direction). Copper leads measuring 0.0005 in. in thickness and 7 in. in length were routed from each sensor in a direction perpendicular to the array as shown. The nominal electrical resistances of the sensor and leads were 6 ohms and 0.7 ohms, respectively.

5.2.2 Instrumentation of Airfoil

Turbine airfoils were instrumented by permanently affixing arrays of hot-films to rotors and nozzles of the test stage(Stage 2). A total of four airfoils were instrumented — two rotors and two nozzles. For each, the hot-film arrays were positioned such that all active sensors were located on one surface only, either the suction or pressure surface. Pictured in Figure 5.3 are the nozzle and rotor airfoils instrumented with hot-film arrays along their suction surfaces.

The instrumentation procedure consisted of a number of steps. First, the kapton substrate containing a sensor array was trimmed such that the sensors could be positioned in a streamwise orientation at midspan of the airfoil. In doing so, the copper leads were oriented in a direction along the span from the sensors to the trunnion end of the airfoil. Approximately one inch of blank kapton substrate was maintained along one streamwise side of the sensor array. This portion of the substrate was wrapped around the leading edge during installation to avoid surface discontinuities. Along the opposite side of the array, the substrate was trimmed so that the sensor array extended to the trailing edge.

The next step was to ensure that the sized array conformed exactly to the airfoil shape when wrapped around it. Slight compound and leading-edge curvatures along the nozzle and rotor surfaces necessitated additional alterations. This was accomplished by strategically locat-

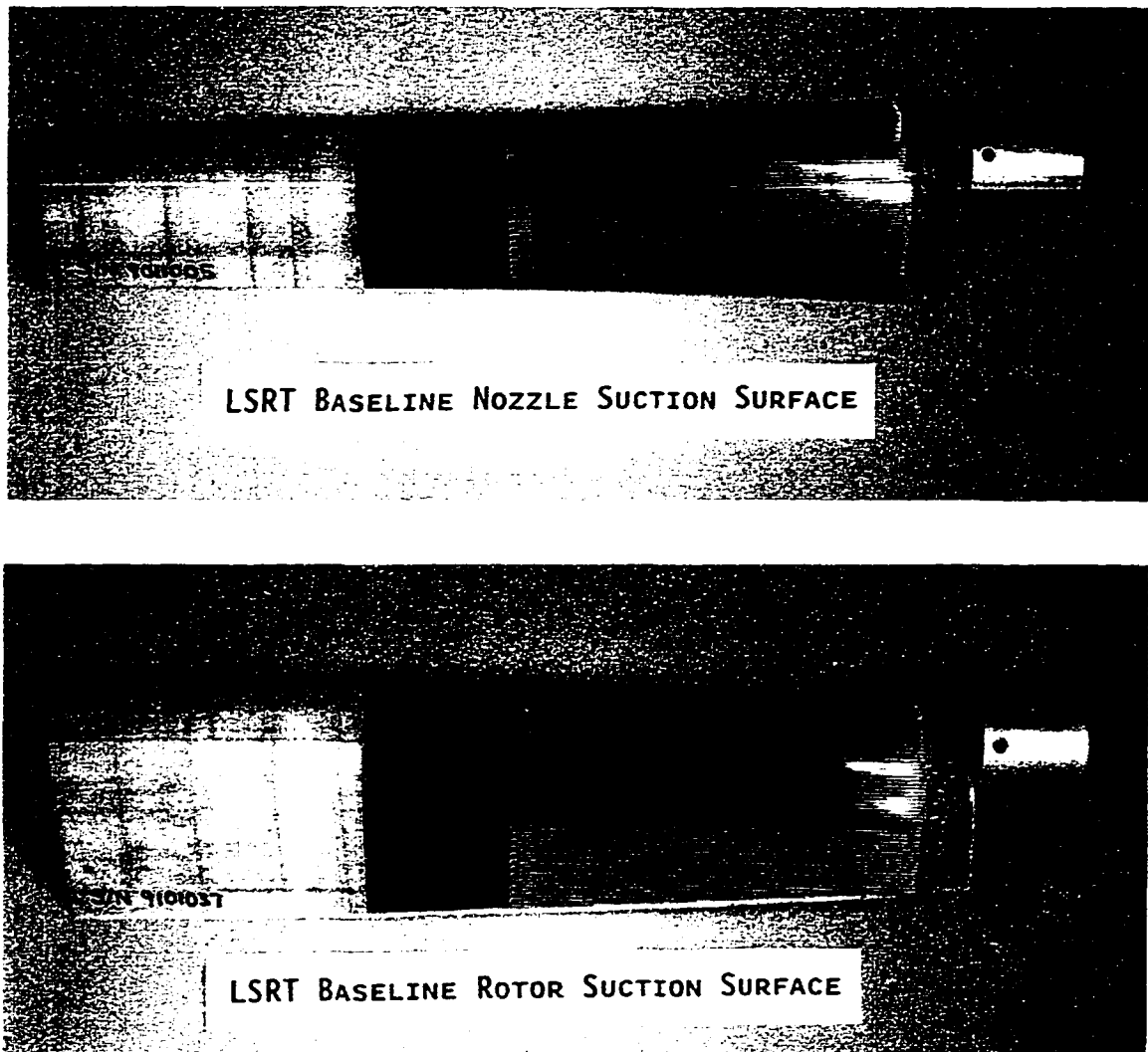


Figure 5.3. Stage 2 nozzle and rotor instrumented with hot-film array along suction surface using partial cuts in the substrate or by removing long, narrow slivers from the substrate as dictated by the curvature. As a result, the kapton sheet could “contract” or “stretch” as needed to conform exactly with the airfoil surface.

Next, the airfoil was prepared by sanding and cleaning its surface using 400 grit paper and isopropyl alcohol. To remove dust particles from all bonding surfaces, a final cleaning was done using an anti-static brush and small air jet. A two-part adhesive (3M 2216) was then mixed and applied to the bonding surfaces of the airfoil and sensor array. After carefully positioning

the sensor array onto the airfoil, the article was placed in a custom-made silicon rubber mold. Uniform compressive pressure was applied to the mold. Small cavities strategically located in the mold provided reservoirs for the excess adhesive forced from between the sensor array and airfoil. Two sheets of 0.001 in. thick Teflon were placed between the test article and the rubber mold during compression to prevent shearing stresses from being transmitted from the mold to the sensor array. While under compression, the adhesive was left to cure at room temperature for 12 hours. After extracting the instrumented airfoil from the mold, all excess adhesive was removed by wet-sanding to establish a smooth interface along the edges of the sensor array and the airfoil. A glue-line thickness of 0.001 in. or less was maintained consistently during mounting of all sensors.

The final step of the instrumentation involved installation of leadwires and connectors. Multi-stranded 32-gauge hookup wire, brought through a hole drilled in the trunnion, was soldered to the ends of each copper lead. Up to 70 hookup wires were required for each sensor array. Each group of leadwires from an airfoil was terminated using a low-resistance, multi-pin connector which could be interfaced with the anemometry system on an individual basis.

5.2.3 Operation of Sensors and Acquisition of Measurements

The surface hot-film sensors were operated using the constant-temperature anemometry system described in Section 5.1. As mentioned above, there were four airfoils instrumented with hot-film arrays. Because of the number of sensors involved, only one array was interfaced with the anemometry system at a time. By knowing the cold resistance of each sensor (measured at zero flow), the heated sensor resistance was calculated for the desired overheat ratio and dialed into the respective channel of the anemometer. For these tests, sensors were operated at an overheat ratio, defined as the ratio of heated to cold resistance, of 1.3.

In theory, the target heated resistance of each sensor need only be determined once provided that, from hookup to hookup, the cable/lead resistances are properly nulled. However, for this test program which extended over the course of more than 170 hours of rig operation, it was

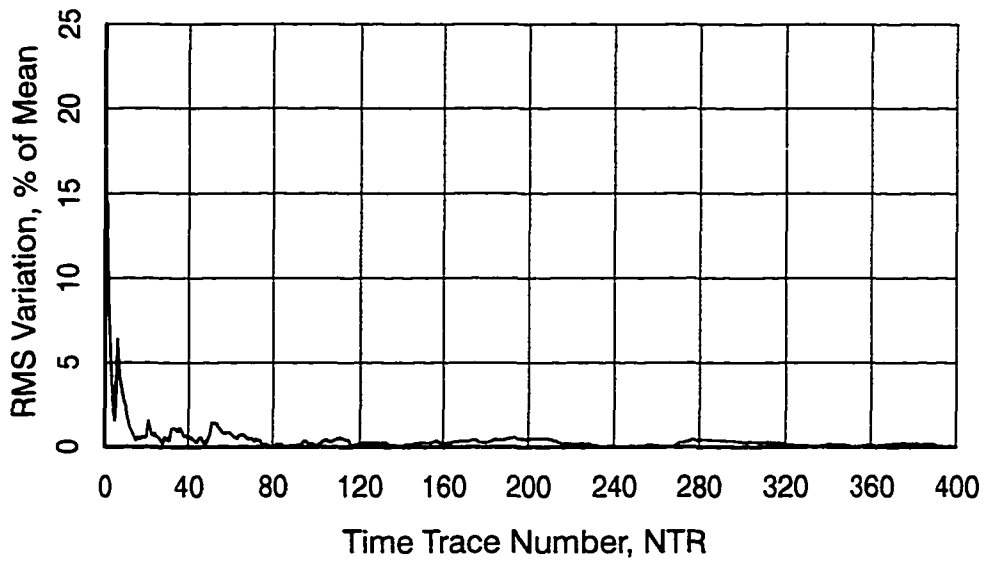
found that the cold sensor resistance increased slightly but consistently. Consequently, the heated sensor resistances were determined prior to each test run in order to maintain consistency of overheat ratio. The change in cold sensor resistance resulted from a decrease in sensor cross-sectional area caused in turn by erosion from dust particles. This occurred in spite of the air filtration at the bellmouth inlet. All told, observable changes in resistance occurred only over the course of weeks, hence individual test runs (generally lasting 2–4 hours) were not impacted.

Zero flow voltages and the corresponding air temperature were measured before and after each test run to provide up-to-date, semi-quantitative calibrations. To this end, each sensor was operated individually for thirty seconds after which the output voltage was recorded. At the end of this time period, its value was nearly constant.

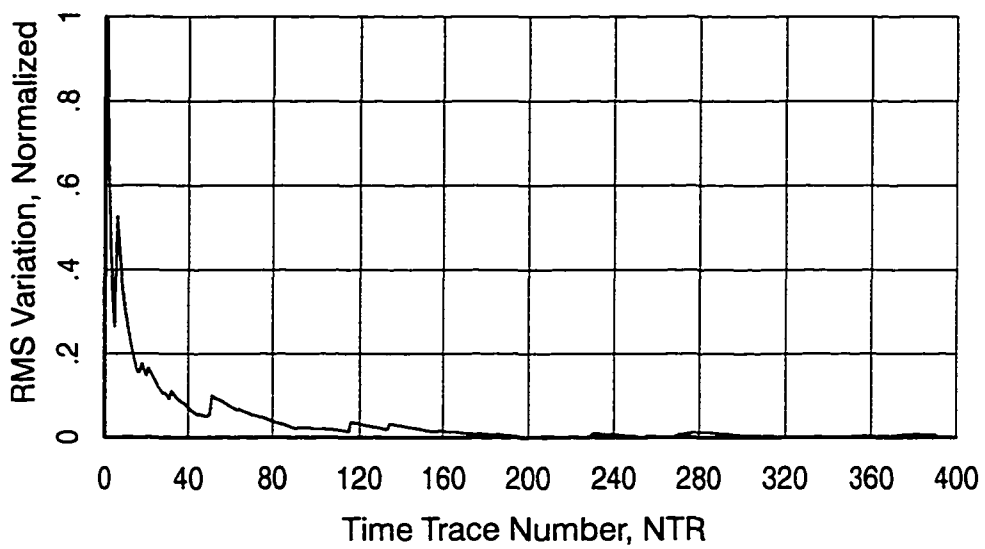
The electronic frequency response of the surface anemometry system was determined using the square-wave test as described in Appendix B. It was found to be nominally 50 khz. For each test run, all anemometer channels were tuned to their optimal frequency response with the turbine set to the desired test condition.

During a given test run, hot-film sensors were operated individually or simultaneously in groups of up to 24. For individual-sensor operation, data were acquired one sensor at a time from leading to trailing edge. These data provide a measure of quasi wall shear stress that is not influenced in absolute level by heat conduction and convection that occurs when neighboring sensors are operating. Multi-sensor data, obtained from operating a group of selected sensors simultaneously, provide a means by which to track individual events as they convect along the blade surface.

Time-domain measurements from the surface hot-film sensors were acquired in ensembles of phase-locked time traces. For each ensemble, an adequate number of traces was obtained to ensure that statistical quantities could be computed accurately. This was determined by way of the RMS variation of the mean and second order moment of the measurements as a function of time trace number. An example from this investigation is illustrated in Figure 5.4.



a) mean value (DC component)



b) normalized second order moment

Figure 5.4. RMS variation of mean value and second-order moment as a function of time trace number

The RMS variations were determined from an arbitrarily-selected ensemble of time traces. Calculations are carried out for a selected instant in time which, in the context of digitized time traces, corresponds to the same i^{th} data point of each successive trace. For this interrogation, 400 time traces were obtained, as evident from the abscissa of the figure. The RMS variation of the mean component (Figure 5.4a) was computed and normalized with respect to the mean value determined from all 400 phase-locked components. As the number of time traces increases above about 70, deviations in the mean are less than about 0.5 percent. Results from the second order moment, given in Figure 5.4b, indicate very little variation as time trace number exceeds about 160. Based on these findings, the minimum number of time traces acquired per ensemble for the calculation of ensemble-averaged quantities was equal to 200.

Numerous criteria relating to digitization of the time unsteady hot-film data were imposed to insure the digital representations were obtained accurately. The sample period of each time trace was set equal to an integer number of blade/wake passing events ranging from five to nine. The low-pass filter of the anemometer signal conditioner was selected to be the maximum of either 20^+ times the blade/wake passing frequency or 10 khz. On-line frequency analysis from the dynamic signal analyzer was used on a case-by-case basis to insure that the low-pass filter setting (i.e., the upper limit of the frequency bandwidth) had been adequately selected. Sampling frequency of the A/D system was set typically to about 5 times that of the low-pass filter to prevent aliasing during digitization. From these criteria, it follows that at least 100 data points were obtained per blade-passing period.

Anemometer output voltages from the surface hot-films were acquired using both DC and AC coupling to enhance the resolution of the digitized signals. Using DC-coupled time traces, the single value of time-average voltage was calculated on-line and stored. Maximum amplification of the DC signals was limited to a factor of 5 to 10 in order to not over-range the digitizer. AC-coupled time traces were obtained using a 0.1 hz high-pass filter and amplifier gains of up to 100. All AC-coupled time traces from each ensemble were stored in their entirety

(nominally 200,000 data samples per ensemble). During data reduction, the complete voltage signal was reconstructed by combining the DC component with the associated AC-coupled time traces.

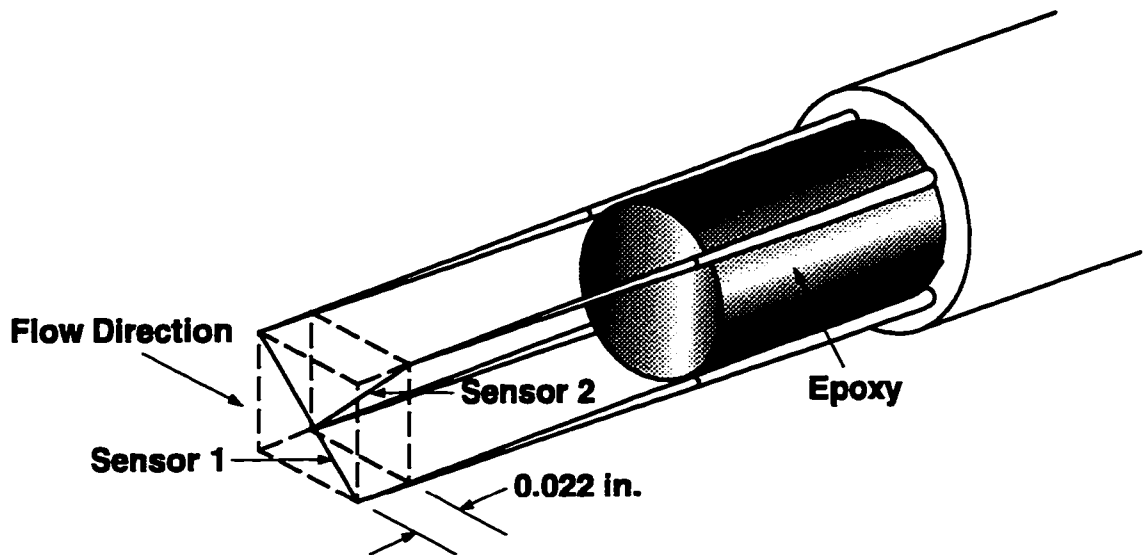
Mean-square frequency spectra of the hot-film sensor output were computed on-line using the dynamic signal analyzer. Each spectrum was constructed from a frequency average of 100 individual spectra. The input signal to the analyzer was AC coupled. The upper limit of the frequency bandwidth was selected so that the duration of each time record used for spectral analysis was at least 20 times the blade-passing period. Triggering of the signal analyzer was done internally to eliminate biasing associated with the input time records. This mode was chosen because the duration of each time record read in by the analyzer could not be set to an integer number of blade-passing periods. The Hanning window was used in conjunction with the spectral analysis to reduce “filter leakage” of the periodic frequency components.

5.3. X Hot-Film Probe Measurements

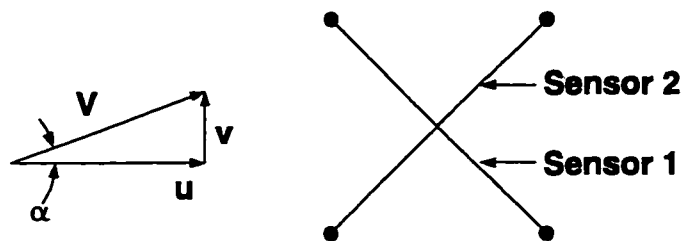
Measurements of the time unsteady flowfield at the inlet and exit of the bladerows were acquired using a model 1240-20 X hot-film probe manufactured by TSI. This probe consists of two sensing elements oriented perpendicular to each other and at 45° angles to the mean flow direction as shown in Figure 5.5a. Measurements resolve the two-dimensional velocity vector in the plane of the sensors which, for this probe configuration, is perpendicular to the probe stem (i.e., a cross-flow orientation). Each sensing element consists of a high-purity platinum film 0.04 in. in length bonded to a 0.002 in. diameter cylindrical quartz substrate measuring 0.065 in. in length. The planes of the two films are separated by 0.022 in. yielding a sensor probe volume of 1.76×10^{-5} in.³. The sensors were operated using the anemometry system described in Section 5.1 at overheat ratios recommended by the manufacturer.

5.3.1. Calibration Procedure

Calibration of the X probe was carried out using the method of Lueptow, Breuer, and Haritonidis (1988) and Gresko (1988) as implemented by Shin (1993). This technique takes ad-



a) probe geometry



b) decomposition of velocity vector

Figure 5.5. X hot-film probe

vantage of the mathematically unique and well-behaved functional relationship between the output voltages of the sensors $\{E_1, E_2\}$ and the two-dimensional velocity vector, \vec{V} , in the plane of the sensors. This is to say the following functions exist and can be determined:

$$V = V(E_1, E_2) \quad \text{and} \quad \alpha = \alpha(E_1, E_2) \quad (5.1)$$

Here, V is the magnitude of the velocity vector, given as $V = |\vec{V}|$, and α is the angle of the flow

with respect to the sensor array as denoted in Figure 5.5b. Using this convention, the vector is shown decomposed into its streamwise (u) and transverse (v) components.

Probe calibration for this work was carried out in terms of the mass flux vector, \vec{Q} , instead of the velocity vector where $\vec{Q} = \rho\vec{V}$. This additional step was warranted as static density varied by as much as 10 percent from the inlet to exit plane of the turbine and, in general, this value of density can be significantly different from the static density of the calibration flow. Consequently, Equation 5.1 is rewritten as

$$Q = Q(E_1, E_2) \quad \text{and} \quad \alpha = \alpha(E_1, E_2) \quad (5.2)$$

where $Q = |\vec{Q}|$. The objective of the calibration then is to determine the functional relationships given by Equation 5.2 for the desired range of mass flux/velocity and flow angle as dictated by the flowfield to be measured.

To this end, calibration data are obtained by exposing the X probe to a range of mass fluxes while orienting the probe at varying yaw angles with respect to the calibration flow. At all discrete flow conditions and probe orientations, the output voltage from each sensor is recorded. The result is a set of unique voltage pairs $\{E_1, E_2\}$ corresponding to the calibration space dictated by the range of mass flux and angle. An example of such a calibration data set is shown in Figure 5.6. The abscissa and ordinate are the sensor output voltages, E_1 and E_2 , respectively. For this work, calibration data were acquired at six mass fluxes (corresponding to velocities extending from about 50 to 300 ft/s) while the flow angle was varied from -30° to $+30^\circ$ in 5° increments. Lines radiating from the lower left to upper right result from variations in mass flux with the flow angle remaining constant. Conversely, each arc results from voltage pairs obtained by varying probe yaw angle while mass flux was held constant. Adjacent calibration points shown in Figure 5.6 are adjoined by straight line segments and indicate the well-behaved nature of the X probe output voltages with respect to the mass flux vector throughout the calibration space.

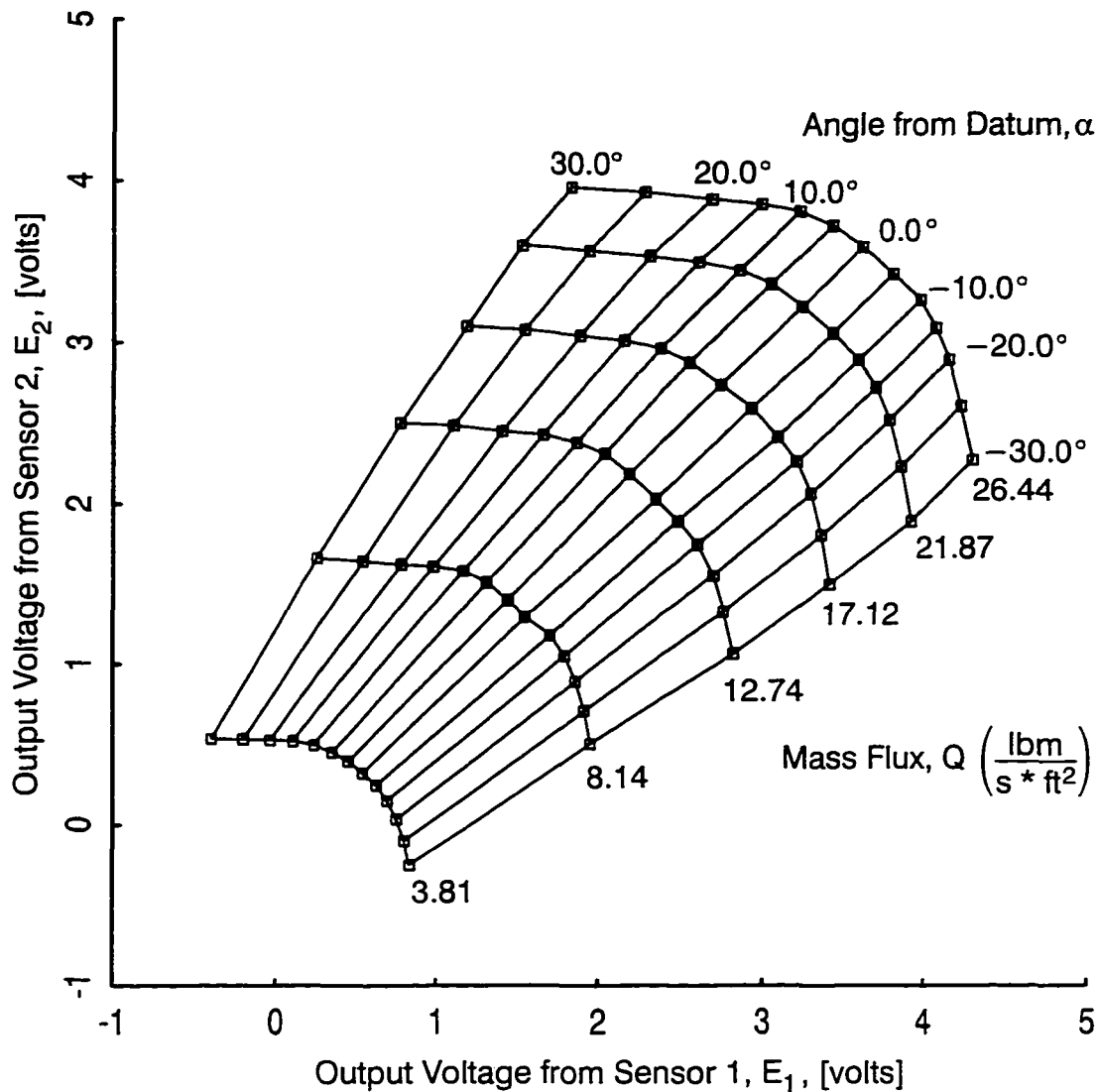


Figure 5.6. Calibration domain of X probe

The functional relationships given by $\alpha(E_1, E_2)$ and $Q(E_1, E_2)$ are now determined by constructing "lookup tables" for each of the mass flux components in terms of E_1 and E_2 . This is accomplished by creating a high-resolution mesh over the calibration space. Gresko (1988) has shown that the optimal mesh is one in which the $\{E_1, E_2\}$ voltage pairs are first transformed from Cartesian into polar coordinates. This transformation takes advantage of the fan-like nature of the calibration data thus ensuring optimal spatial resolution over the entire domain. The

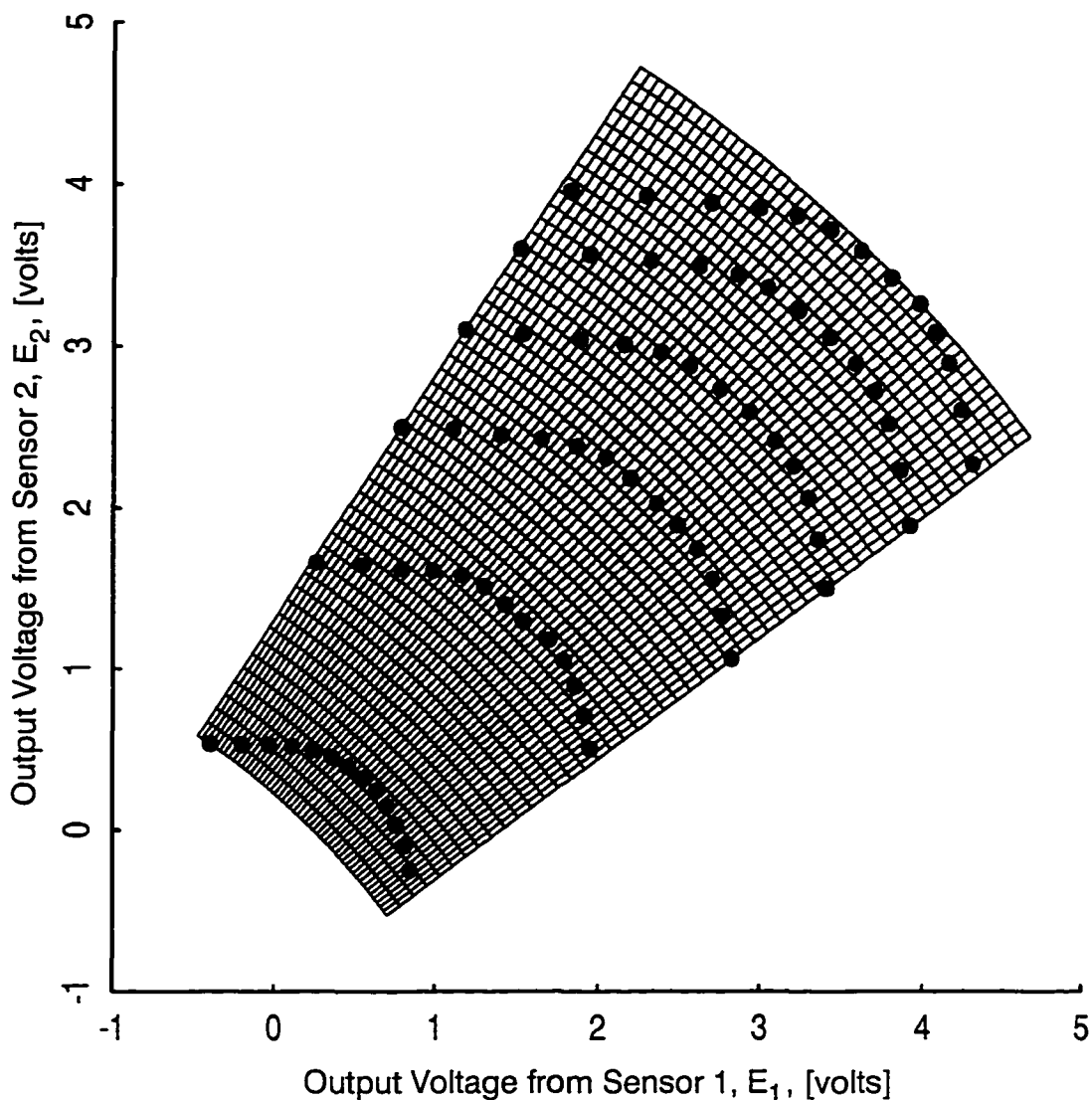
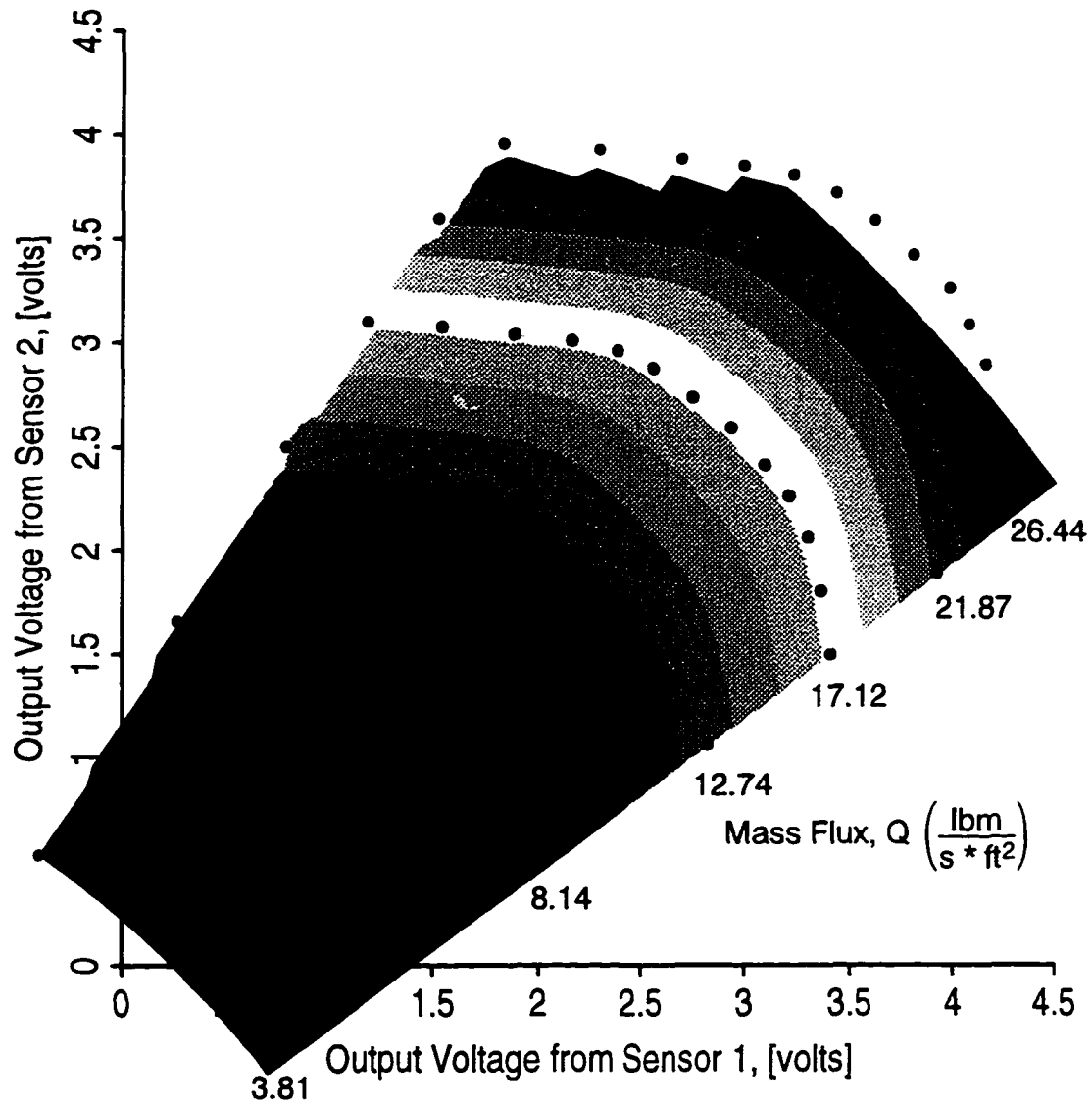


Figure 5.7. Mesh of calibration domain for lookup table

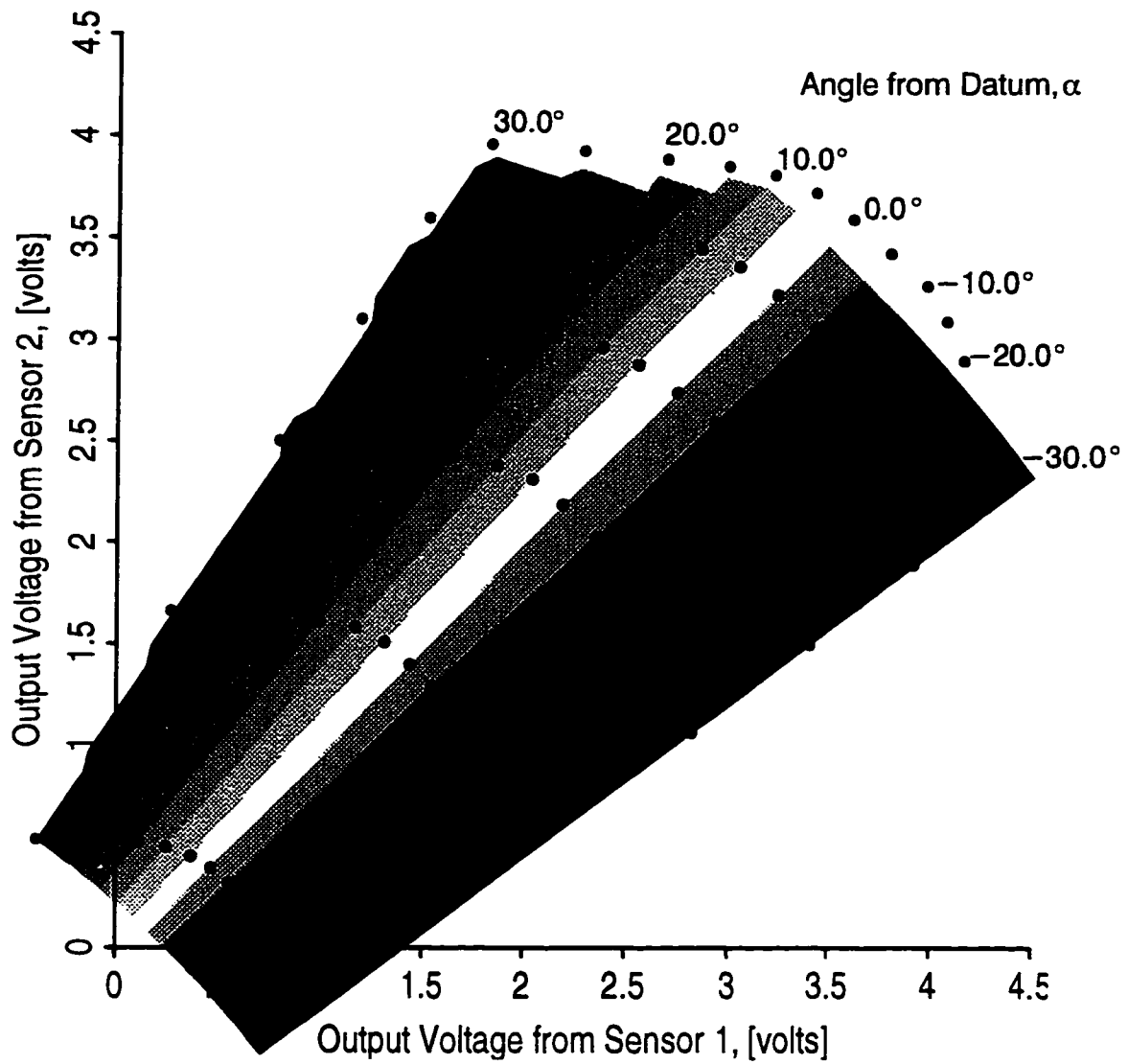
resulting mesh for the calibration domain, given in Figure 5.7, consists of 50 radial and 50 angular elements.

Lookup tables for each of the flux vector components are constructed using cubic spline curve fits of the calibration data evaluated at each of the 2500 nodes (intersection points) of the mesh. In actuality then, these lookup tables are discrete representations of the functions $Q(E_1, E_2)$ and $\alpha(E_1, E_2)$. Each function is shown graphically as a color contour in Figure 5.8 for the calibration data set presented in Figure 5.6.



a) mass flux ($Q_0=2.4$, $Q_{15}=26.4$)

Figure 5.8. Graphical representation of calibration lookup table



b) flow angle from datum ($Q_0 = -35.0$, $Q_{13} = +30.0$)

Figure 5.8. continued

After lookup tables have been constructed, the mass flux vector is determined on a point-by-point basis from the voltage pair $\{E_1, E_2\}$ using bilinear interpolation between adjacent points of the calibration mesh. The maximum error in the vector components computed from the lookup table to those from the calibration data were 0.2 percent and 0.3 percent for Q and α , respectively. This accuracy is a direct result of the high resolution of the mesh and smooth character of the component functions. Gresko (1988) found these error levels to be more than an order of magnitude less than those found from applying traditional “King’s Law”-based calibration methods. The clear advantage of the present approach is that it requires no assumptions about the physical laws governing the cooling of the sensors and is completely independent of the specific geometry of the X probe sensor array.

5.3.2 Additional Considerations

Temperature Correction. Prior to constructing the lookup tables, the voltage pairs from the calibration data set were corrected to account for slight variations in total temperature of the flow incurred during calibration. This was accomplished using the following relation as suggested by TSI (1970)

$$E_{\text{corr},i} = \sqrt{\frac{T_{\text{op}} - T_{\text{t,cal}}}{T_{\text{op}} - T_{\text{t,cal},i}}} E_{\text{cal},i} \quad (5.3)$$

where T_{op} = sensor temperature during operation

$T_{\text{t,cal}}$ = average total temperature of calibration flow

$T_{\text{t,cal},i}$ = total temperature of calibration flow, i^{th} flow condition

Using this formulation, all calibration voltages $E_{\text{cal},i}$ are corrected to the same temperature, $T_{\text{t,cal}}$. Personal experience has shown this relation to be valid for airstream temperature excursions of more than 10°F.

Prong Vibration. During initial calibration of the X probe, evidence of significant prong vibration was found from frequency-averaged spectra of the sensor output. Distinct “spikes” in the energy spectra occurred at frequencies of 7.5 and 8.0 khz for sensors 1 and 2.

respectively. As intuition would suggest, the vibration frequency associated with sensor 1 is somewhat less than that for sensor 2 because of the longer prong length of the former. To stiffen the prongs, a two-part epoxy(3M 1838) was used to fill in the region between the four prongs near their base as indicated in Figure 5.5a. For this modified probe, the prong natural frequencies increased by a factor of about three and the amplitude of the energy spikes in the spectra decreased by a factor of 50. No additional probe modifications were undertaken as the increased natural frequencies were sufficiently outside the frequency bandwidth of interest. Also, the change in probe configuration was within acceptable limits so as not to influence adversely the flowfield at the sensor array.

5.3.3 Acquisition of Measurements

X hot-film probe measurements were obtained at midspan only to coincide with the locations of the surface hot-film arrays. Data were acquired at the five measurement planes from Nozzle 1 inlet to Rotor 2 exit denoted in Figure 4.2. At each measurement plane, the sensor array was aligned with the time-average flow angle as determined visually using a tuft probe/protractor device. The angle that the sensor array was offset from axial, α_0 , was recorded for later data analysis. For planes 1.5 – 3.0, the nozzle bladerows were indexed circumferentially past the stationary probe over one blade pitch. During acquisition of the X probe data, test conditions of the turbine were frequently recorded so that values of total temperature and static density at each measurement plane through the machine could be determined.

For each test point, data from the X probe were acquired in ensembles of phase-locked time traces. The time duration of each trace was equal to 15 wake-passing periods to provide sufficient information for later computation of frequency spectra. The low-pass filter of the anemometer signal conditioner was set to a maximum value of either 10khz or 20 times blade passing frequency. Camp and Shin (1994) have shown that the latter criterion is sufficient in order to determine accurately turbulence intensity and length scale in turbomachinery flowfields. In addition, on-line analysis of the frequency spectra was carried out using the dynamic

signal analyzer to insure that the energy content of the flowfield turbulence was not significant for frequencies greater than the selected setting of the low-pass filter. To prevent aliasing, the sampling frequency of the A/D system was set to 5 times that of the low-pass filter. As a result of the above criteria, at least 100 data points were obtained per blade-passing period.

In a manner identical to that employed for the surface hot-film data, it was determined that each ensemble was adequately represented by 300 individual time traces. All anemometer output voltages from the X probe were acquired using DC and AC coupling as described for the surface hot-film measurements.

5.4 Pressure Measurements

Detailed aerodynamic performance of the test stage blading was established using inter-bladerow traverses and airfoil surface pressure measurements. Data were obtained at test conditions coincident with those of the surface hot-film and X probe measurements.

Inter-bladerow measurements of total and static pressure were acquired using individual, single element probes positioned radially at midspan. Circumferential traverses were obtained at Planes 2.0, 2.5, and 3.0 (identified in Figure 4.2) by indexing the nozzle bladerows past the stationary probes. Total pressures were measured using a standard Kiel probe having a head diameter of 1/16 in. (United Sensor KAC-36). Measurements were obtained at 23 positions across the nozzle bladerow pitch. Increments between successive measurement locations were varied to adequately resolve the wake profile at the nozzle exit (Plane 2.5). Static pressures were acquired using a probe designed and manufactured in-house. It consisted of a 1/32 in. diameter tube with four side-wall holes located 4 diameters downstream of its sealed, hemispheric nose. A yarn tuft mounted near the end of the probe was used to align the tube in the direction parallel to the airflow. Values of static pressure were acquired at the identical circumferential locations as were the totals. Static and total pressures from the three measurement planes were obtained sequentially during rig operation using a single transducer and multiplexer. The transducer had a range of 2 psig and was accurate to within $\pm 0.015\%$ of full scale. Measurements were ob-

tained in order of decreasing pressure with adequate settling time provided between acquisition of each.

Distributions of static pressure along the rotor and nozzle surfaces were obtained using rows of static taps extending from near the leading to trailing edge. Each tap was 0.020 in. in diameter and oriented perpendicular to the airfoil surface. They numbered 13 and 15 along the pressure and suction surface of the nozzle and, analogously, numbered 14 and 16 for the rotor. Measurements from the nozzle were acquired using the pressure system just described while those for the rotor were obtained using the rotating pressure measurement system described in Section 4.1.

CHAPTER 6. DATA ANALYSIS

Described in this chapter are various procedures used to analyze the measurements obtained over the course of this research. Analysis and presentation format of the surface hot-film data are considered in the first section. Section 6.2 contains a similar description for the X hot-film probe measurements. For both, the time-domain analysis is based on the concept of ensemble averaging. A general overview of this approach is given in Appendix C. For frequency-domain analyses, Fourier transform methods were employed as applied to discretely-sampled data. The pertinent mathematics are described in Appendix D. Additionally, over the course of the analysis of the X probe data, a unique approach to the calculation of turbulence length scales for periodically unsteady flowfields was developed. While not a primary objective of this project, the procedure provided a viable means to document the turbulence characteristics in turbomachine flowfields. Consequently, the calculation procedure is presented in Appendix E.

Analysis of the aerodynamics measurements is described in the third section. Uncertainty analyses pertaining to all measurements is contained in the last section.

6.1 Analysis of Surface Hot-Film Measurements

Analysis of the surface hot-film data as they pertain to the time and frequency domains are described first in this section. This is followed by a discussion of data presentation including the use of space-time and space-frequency diagrams.

6.1.1 Time-Domain Analysis

The ensemble of surface hot-film data from each sensor is first converted, on a point-by-point basis, from measured voltage to values of quasi wall shear stress. This is accomplished by way of Equation 6.1 which is based on the principles of surface hot-film anemometry described in Chapter 3.

$$q\tau_{w_{ni}} = \left[\frac{E_{ni}^2 - E_{0adj}^2}{E_{0adj}^2} \right]^3 \quad (6.1)$$

Here, the subscript “ni” denotes the i^{th} data sample of the n^{th} time trace of the ensemble. The total number of data samples per time trace is equal to NPT while the total number of time records per ensemble is NTR. The instantaneous output voltage, E_{ni} , is constructed from the separately-acquired DC and AC components as described in Chapter 5.

The value of zero-flow voltage appearing in Equation 6.1 has been adjusted relative to the measured value, E_0 , as indicated by Equation 6.2. This is to account for differences in air temperature between the zero-flow condition and that occurring during turbine operation.

$$E_{0adj} = \sqrt{1 + \frac{\alpha (T_0 - T_t)}{\text{OHR} - 1}} E_0 \quad (6.2)$$

The temperatures T_0 and T_t correspond to the ambient air temperature during acquisition of E_0 and to the local total temperature of the airflow during rig operation, respectively. The variable, α , is the temperature coefficient of resistance of the sensor element as provided by the manufacturer. The complete derivation of Equation 6.2 is given in Appendix F.

For each ensemble represented by Equation 6.1, the magnitude of quasi wall shear stress is quantified both in terms of its ensemble-averaged distribution and its time-averaged value. These formulations are written here as Equations 6.3 and 6.4, respectively.

$$q\tilde{\tau}_{w_i} = \frac{1}{\text{NTR}} \sum_{n=1}^{\text{NTR}} q\tau_{w_{ni}} \quad i = 1, \text{NPT} \quad (6.3)$$

$$\overline{q\tau_w} = \frac{1}{\text{NPT}} \sum_{i=1}^{\text{NPT}} q\tilde{\tau}_{w_i} \quad (6.4)$$

As noted in Appendix C, ensemble-averaged distributions are time dependent. For clarity however, this time dependence is not shown explicitly. Ensemble-averaged distributions of quasi wall shear stress will be presented in Chapter 7 in both DC (Equation 6.3) and AC-coupled for-

mat. The latter form is calculated using Equation 6.5. It was found to be especially useful for revealing the periodic nature of the developing boundary layer. Normalization of Equation 6.5 with $\overline{q\tau_w}$ enables direct comparison of the magnitude of periodic fluctuation to that of the time mean.

$$\frac{q\tilde{\tau}_{w,i} - \overline{q\tau_w}}{\overline{q\tau_w}} \quad (6.5)$$

The amplitude of the fluctuations in shear stress is quantified by the mean square of the random unsteadiness. The ensemble-averaged distribution and time-averaged value are determined using Equations 6.6 and 6.7, respectively

$$\overline{q\tilde{\tau}_{w,i}^2} = \frac{1}{NTR} \sum_{n=1}^{NTR} (q\tau_{w_n} - q\tilde{\tau}_{w,i})^2 \quad i = 1, NPT \quad (6.6)$$

$$\overline{q\tau_w^2} = \frac{1}{NPT} \sum_{i=1}^{NPT} \overline{q\tilde{\tau}_{w,i}^2} \quad (6.7)$$

Note that in order to distinguish random from periodic unsteadiness, the second-order moment in Equation 6.6 is centered about the ensemble mean, $q\tilde{\tau}_{w,i}$, and not the time mean. For this work, the above relationships are recast into intensities of root-mean-square (RMS) unsteadiness as follows:

$$\text{ensemble-averaged distribution:} \quad \frac{\sqrt{\overline{q\tilde{\tau}_{w,i}^2}}}{q\tilde{\tau}_{w,i}} \quad i = 1, NPT \quad (6.8)$$

$$\text{time-averaged value:} \quad \frac{\sqrt{\overline{q\tau_w^2}}}{\overline{q\tau_w}} \quad (6.9)$$

The resulting quantities are referred to here simply as random unsteadiness.

Time-averaged periodic unsteadiness is computed using Equation 6.10. The results are then normalized into intensity as shown by Equation 6.11. The derivation of the former is described in Appendix C.

$$\overline{q\tau_{wp}^2} = \frac{1}{NPT} \sum_{n=1}^{NPT} (q\tilde{\tau}_{w_i} - \overline{q\tau_w})^2 \quad i = 1, NPT \quad (6.10)$$

$$\text{intensity:} \quad \frac{\sqrt{\overline{q\tau_{wp}^2}}}{\overline{q\tau_w}} \quad (6.11)$$

The asymmetry of the random fluctuations about the ensemble mean is calculated from the third-order moments given by Equations 6.12 and 6.13.

$$\tilde{q\tau_{w_i}^3} = \frac{1}{NTR} \sum_{n=1}^{NTR} (q\tau_{w_{ni}} - q\tilde{\tau}_{w_i})^3 \quad i = 1, NPT \quad (6.12)$$

$$\overline{q\tau_w^3} = \frac{1}{NPT} \sum_{i=1}^{NPT} \tilde{q\tau_{w_i}^3} \quad (6.13)$$

Normalization of the ensemble-averaged distribution and time-averaged value is accomplished by way of Equations 6.14 and 6.15, respectively. For this work, these quantities are referred to as skew.

$$\frac{\tilde{q\tau_{w_i}^3}}{q\tau_{w_i}^3} \quad i = 1, NPT \quad (6.14)$$

$$\frac{\overline{q\tau_w^3}}{q\tau_w^3} \quad (6.15)$$

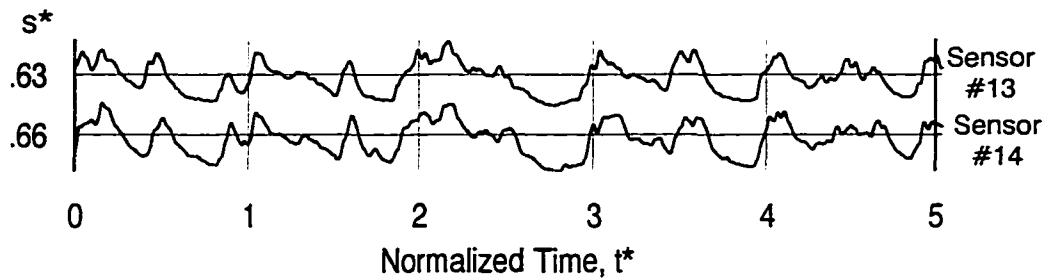
Selected instantaneous time traces are presented in Chapter 7 to provide a means to investigate individual events as they convect along the airfoil surfaces. Such traces are associated with multi-sensor operation in which groups of time traces were obtained simultaneously. These measurements are presented in an AC-coupled fashion and normalized by the local time mean shear stress as shown by Equation 6.16.

$$\frac{q\tau_{w_{ni}} - \overline{q\tau_w}}{q\tau_w} \quad (6.16)$$

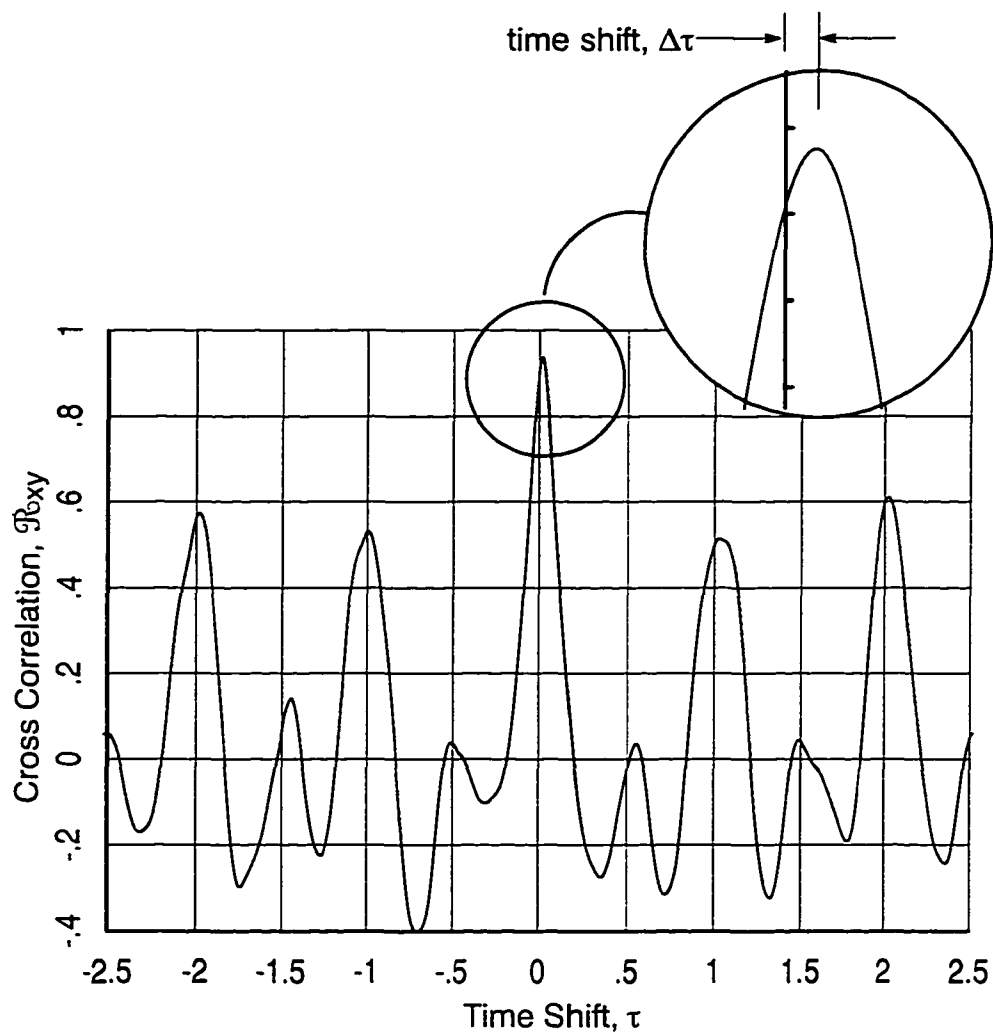
The instantaneous time records are further interrogated to determine the average convective velocity of events moving along the airfoil surfaces. This is accomplished by comparing instantaneous time traces obtained simultaneously from neighboring sensors, an example of which is shown in Figure 6.1a. The two traces shown in part a of the figure were obtained from along the suction surface of Nozzle 2 for test point 5A. The numbers to the left indicate the fraction of surface length from the leading edge where the sensors were located. Each trace extends in time for five blade-passing periods. The average time required for disturbances to convect from one sensor to the next is determined from the cross-correlation function of the two time traces. As shown in Figure 6.1b, this convection time is taken to be the time shift, $\Delta\tau$, of the peak in the cross correlation from τ equal to zero. For this work, the cross correlation for each pair of time records was determined from the inverse Fourier transform of their cross spectral density. The required computations are described in Appendix D. For a given pair of ensembles obtained from neighboring sensors, the associated time shift is taken as the average of the shifts computed for each individual pair of time traces. It is worth noting from Figure 6.1b that the cross correlation shows clearly the distinct periodic nature of the flow occurring at time shifts corresponding to that of blade passing.

6.1.2 Frequency–Domain Analysis

The spectral distribution of energy associated with the unsteady fluctuations is quantified in terms of the normalized, RMS spectrum of the anemometer output voltage. For each sensor, the mean square spectrum is obtained directly on a frequency–averaged basis as described in Chapter 5. After down loading from the analyzer, the square root of each discrete spectral element is normalized by the time–averaged voltage from the associated sensor. The result, designated the normalized RMS spectrum, provides a means to compare the spectral characteristics of the fluctuations in shear stress from sensor to sensor along the airfoil. Calculations of the spec-



a) instantaneous time traces (from along suction surface of Nozzle 2, test point 5A, $Re_{SSI}=5.27 \times 10^5$)



b) cross correlation coefficient

Figure 6.1. Determination of average “event” convection velocity from cross correlation analysis

tra are presented in decibel units of measure as indicated by Equation 6.17.

$$20 \log_{10} \frac{\sqrt{e_i'^2(f_i)}}{\bar{E}} \quad i = 1, 801 \quad (6.17)$$

6.1.3 Description of Data Presentation

As described in Chapter 5, surface hot-film measurements are obtained from sensors extending from leading to trailing edge along given airfoil surfaces. Measurements obtained from each individual sensor are then used to compute the time-, ensemble- and frequency-averaged quantities as described above. Distributions of these quantities along the airfoil surface are presented with respect to normalized surface distance, s^* , where

$$s^* = \frac{\text{distance from leading edge}}{\text{total surface distance}} = \frac{s}{s_{\text{tot}}} \quad (6.18)$$

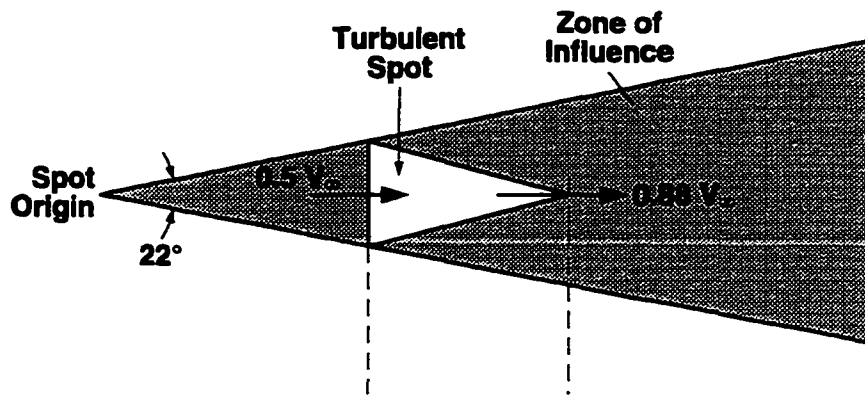
6.1.3.1 Space-Time Diagrams

The ensemble-averaged quantities, computed as described above, constitute functions of two independent variables; namely that of time and distance. For this work then, these functions are presented in the form of contour plots where the abscissa and ordinate consist of normalized surface distance and time, respectively. The time coordinate is normalized using blade passing period defined by Equation 6.19.

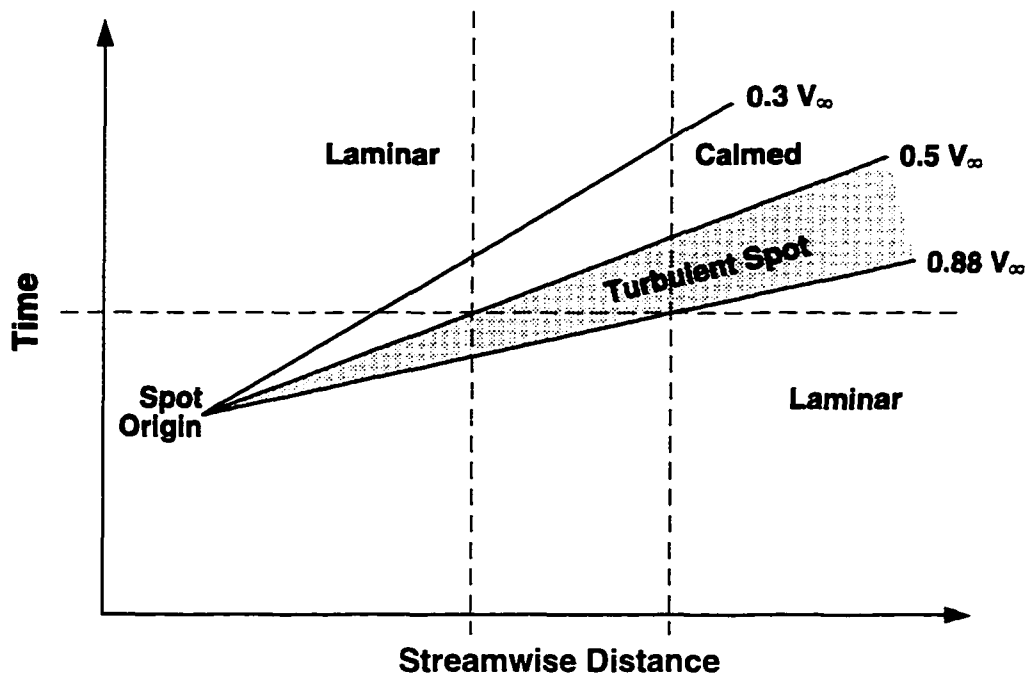
$$t^* = \frac{t}{\tau_{\text{bp}}} \quad (6.19)$$

$$\text{where} \quad \tau_{\text{bp}} = \frac{60}{(\text{RPM}) (N_{\text{blades}})}$$

Values of the ensemble-averaged quantities, presented herein as color contours, simply represent mathematically a surface whose domain is defined in s^* - t^* space. The resulting contour plot is known as a space-time or s - t diagram. For this diagram, the convective velocity of an event following a trajectory in s - t space is equal to the reciprocal of the slope of that trajectory.



a) growth and convection of a turbulent spot (plan view)



b) s-t diagram

Figure 6.2. Example s-t diagram for an individual turbulent spot (from Halstead et al., 1995)

An instructive and relevant example of the use of an s-t diagram involves the description of a turbulent spot as shown in Figure 6.2. Part a of this figure illustrates the convective and growth characteristics of an individual spot as determined by Schubauer and Klebanoff (1956) and idealized by McCormick (1968). In plan view, turbulent spots are approximately triangular in shape. For zero pressure gradient, the convection velocities of the leading and trailing bound-

aries are 0.88 and $0.5 V_\infty$, respectively. As the spot moves downstream of its origin, it maintains a self-similar shape and sweeps out the hatched region, its zone of influence. The s - t diagram of the turbulent spot is given in part b of the same figure. Trajectories are drawn at 0.88 and $0.5 V_\infty$ to define the leading and trailing boundaries of the spot and at $0.3V_\infty$ to define the trailing boundary of the calmed region. As noted above, the convective velocity associated with each is equal to the inverse slope of the corresponding trajectory. The shaded region in part b describes the streamwise and temporal growth of the spot as it moves downstream. For an s - t diagram, lines drawn at constant time (parallel to the “ s ” axis) provide an instantaneous snapshot of the flow along the surface. Meanwhile, vertical lines provide the time-varying nature of the flow at a given location along the surface.

Because velocity in general changes along an airfoil surface, the trajectories such as those in Figure 6.2 will not be straight lines. By taking into account the airfoil velocity distributions, trajectories are computed for the bladerows of the LSRT using Equation 6.20.

$$t_N^* - t_0^* = k \sum_{n=1}^N \frac{\Delta s_n^*}{c V_{\infty,n}^*} \quad (6.20)$$

where
$$k = \frac{f_{bp} s_{tot}}{V_{ex}}$$

The variable, k , is a reduced frequency that represents the ratio of convective to periodic time scales associated with the flowfield. It can be thought of as an approximate measure of how many wake segments occur within a blade passage at a given time. The numerator within the summation of Equation 6.20 is equal to the incremental value in normalized surface distance, $(s_n^* - s_{n-1}^*)$, while $V_{\infty,n}^*$ is that of local freestream velocity along the airfoil, normalized by the exit velocity. The constant “ c ” is equal to the fraction of freestream velocity at which an event is convecting. A complete derivation of Equation 6.20 is provided in Appendix G.

6.1.3.2 Space–Frequency Diagrams

Frequency–averaged spectra obtained from each sensor along the airfoil also are presented in the form of contour plots where the independent variables are normalized surface distance and frequency. The latter, now constituting the ordinate, is normalized with blade passing frequency as indicated by Equation 6.21. The resulting contour plot is designated a space–frequency or s–f diagram. The color contours represent the amplitude of the normalized RMS spectra (Equation 6.17) in $s^*–f^*$ space.

$$f^* = \frac{f}{f_{bp}} \quad \text{where} \quad f_{bp} = \frac{1}{\tau_{bp}} \quad (6.21)$$

6.2 Analysis of X Probe Measurements

As described in Chapter 5, X hot–film probe data were obtained at the inlet and exit of each turbine blade row. For a given test condition and measurement location, an ensemble of phase–locked time records of anemometer output voltage were acquired simultaneously from each sensor of the X probe. The pair of ensembles is represented symbolically as $\{E_1, E_2\}_{ni}$.

Analysis of the X probe data begins by converting, on a point–by–point basis, all voltage pairs into the two–dimensional velocity vector using the following three–step procedure. First the measured bridge voltages are corrected for differences in total temperature between the calibration and turbine airflows using Equation 6.22. Here, $T_{t,cal}$ and T_t correspond to the total temperatures of the calibration jet and turbine flows, respectively, while T_{op} is the operating temperature of the sensor. This correction is identical in form to that described in Section 5.3.2.

$$E_{corr} = \sqrt{\frac{T_{op} - T_{t,cal}}{T_{op} - T_t}} E_{meas} \quad (6.22)$$

Secondly, corrected voltages of the ensemble pair are converted to components of the mass flux vector, $\{Q, \alpha\}_{ni}$, using the calibration lookup table described in Section 5.3.1. As an example, a locus of corrected voltages taken from a single time record are shown in Figure 6.3

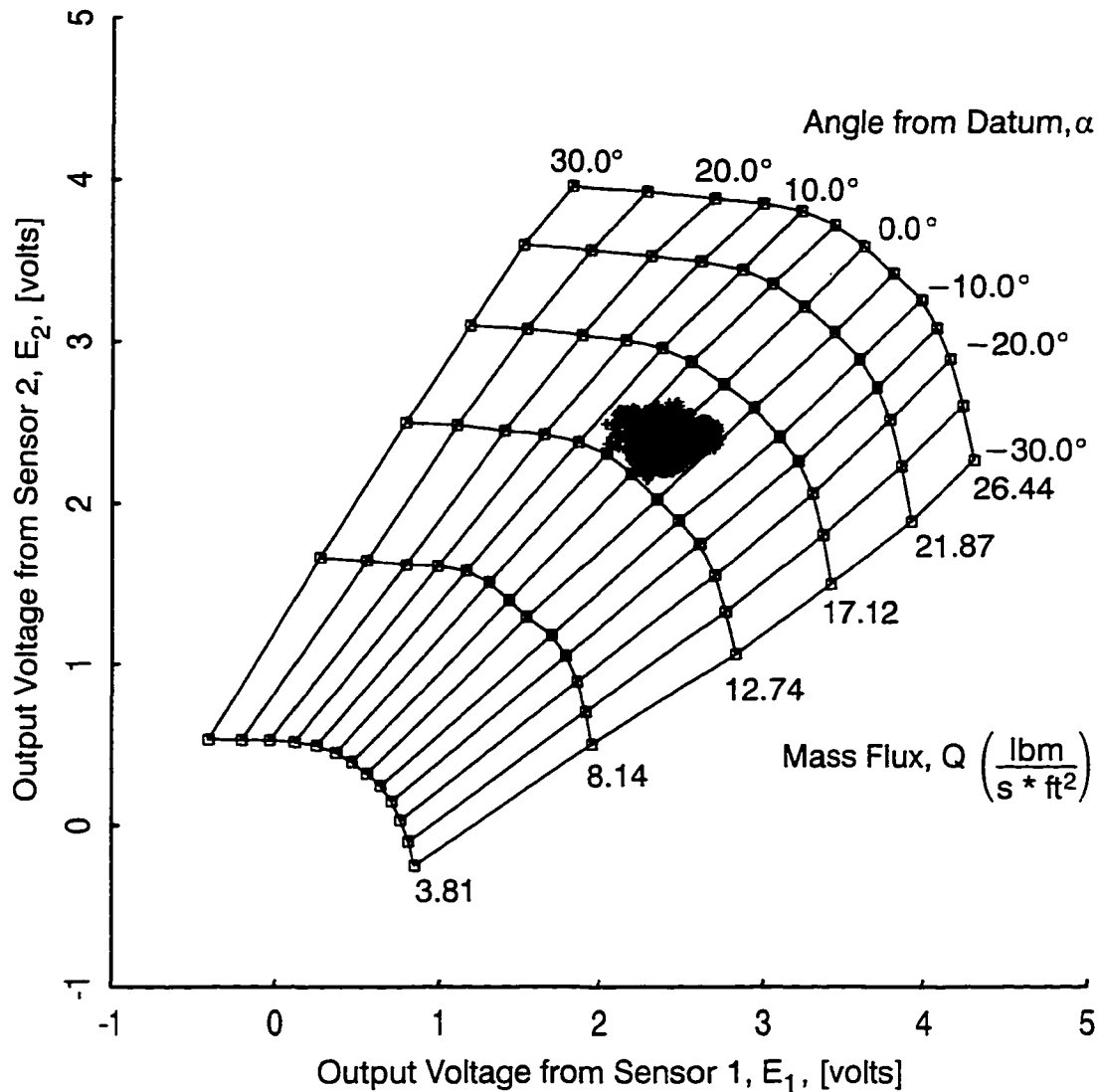


Figure 6.3. Locus of voltage pairs for a single time trace superimposed onto the X probe calibration domain (Nozzle 2 exit, time trace #100)

superimposed onto the calibration domain. The group of voltage pairs centers around a flow angle of 0° as a consequence of aligning the X sensor array with the mean flow direction. The observed clustering of the voltage pairs for this time trace is representative of all acquired time records.

As a final step to the data conversion process, the velocity magnitude, V_{ni} , is determined by dividing each component of mass flux by the local static density. The result is the ensemble pair $\{V, \alpha\}_{ni}$ which represents a time-resolved measurement of the two-dimensional velocity

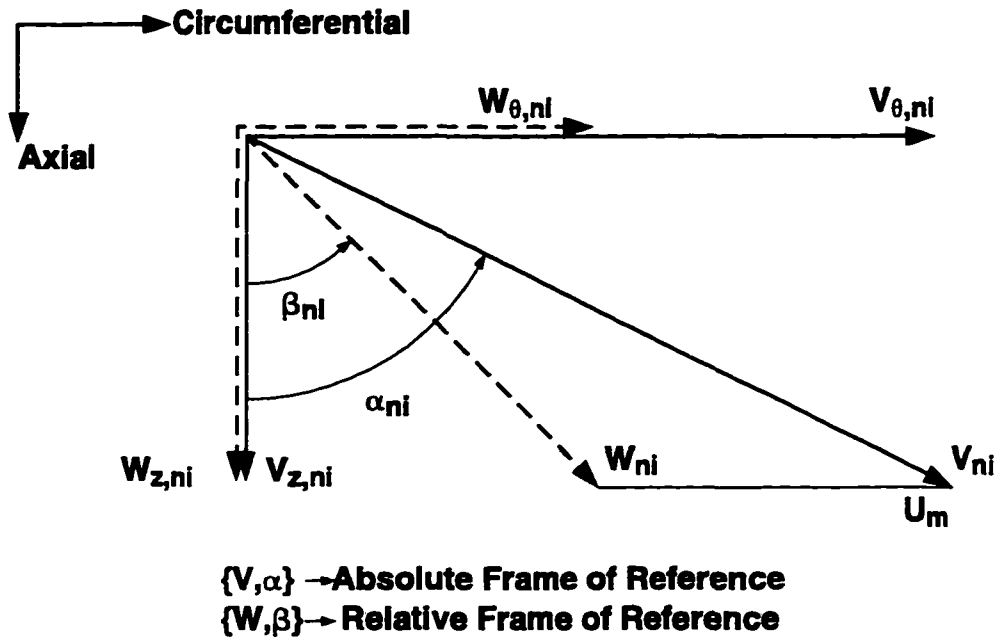


Figure 6.4. Decomposition of the two-dimensional velocity field

vector. The actual vector analyses described in the following section are carried out not with respect to $\{V, \alpha\}_{ni}$ but instead to the components, $\{V_z, V_\theta\}$, determined by way of Equation 6.23. As illustrated in Figure 6.4, the “z” component of velocity coincides with the turbine axial direction and the “ θ ” component with the circumferential direction.

$$V_{z,ni} = V_{ni} \cos \alpha_{ni} \quad i=1, \text{NPT} \quad n=1, \text{NTR} \quad (6.23a)$$

$$V_{\theta,ni} = V_{ni} \sin \alpha_{ni} \quad i=1, \text{NPT} \quad n=1, \text{NTR} \quad (6.23b)$$

6.2.1 Inter-Bladerow Velocity Field

The nature of the two-dimensional velocity field occurring between bladerows is quantified in terms of the velocity magnitude and flow angle. Both ensemble-averaged distributions and time-averaged values are determined. Analyses are carried out with respect to the absolute (stationary) and relative (rotating) frames of reference. The framework of the analysis relating to the absolute reference frame will be described in detail. Any significant differences associated with the relative frame of reference will be duly noted.

The ensemble-averaged distributions of velocity magnitude and flow angle in the absolute frame of reference are computed from Equation 6.24.

$$\tilde{V}_i = \sqrt{\tilde{V}_{z,i}^2 + \tilde{V}_{\theta,i}^2} \quad i=1, \text{ NPT} \quad (6.24a)$$

$$\tilde{\alpha}_i = \tan^{-1}(\tilde{V}_{z,i}/\tilde{V}_{\theta,i}) \quad i=1, \text{ NPT} \quad (6.24b)$$

As before, the time dependence of the ensemble-averaged quantities is not shown explicitly. Note that they appropriately are *not* computed directly from the pair $\{V, \alpha\}_{ni}$ but rather, from the vector components in the z and θ directions. The ensemble averages of these latter components, which appear in Equation 6.24, are computed as follows:

$$\tilde{V}_{z,i} = \frac{1}{\text{NTR}} \sum_{n=1}^{\text{NTR}} V_{z,ni} \quad i=1, \text{ NPT} \quad (6.25a)$$

$$\tilde{V}_{\theta,i} = \frac{1}{\text{NTR}} \sum_{n=1}^{\text{NTR}} V_{\theta,ni} \quad i=1, \text{ NPT} \quad (6.25b)$$

The relationship between velocity vectors in the absolute and relative frames of reference is illustrated in Figure 6.4. In the rotor frame of reference, the axial and circumferential components of the relative velocity vector are determined using Equation 6.26 where U_m is the midspan blade speed. The magnitude and angle of the relative velocity vector are then determined in a manner analogous to that described above for the absolute frame.

$$W_{z,ni} = V_{ni} \cos \alpha_{ni} \quad i=1, \text{ NPT} \quad n=1, \text{ NTR} \quad (6.26a)$$

$$W_{\theta,ni} = V_{ni} \sin \alpha_{ni} - U_m \quad i=1, \text{ NPT} \quad n=1, \text{ NTR} \quad (6.26b)$$

Time-averaged values of velocity magnitude and flow angle associated with the absolute frame of reference are computed as indicated by Equation 6.27.

$$\bar{V} = \sqrt{\bar{V}_z^2 + \bar{V}_\theta^2} \quad (6.27a)$$

$$\bar{\alpha} = \tan^{-1}(\bar{V}_z/\bar{V}_\theta) \quad (6.27b)$$

Time averages of the axial and circumferential components of velocity required in the above relationships are determined from temporal integration of Equation 6.25 (i.e., summation and averaging with respect to subscript “i”). Again, relative frame values are determined in an analogous manner.

6.2.2 Turbulence Characteristics

The character of the random unsteadiness associated with the velocity field is quantified by way of turbulence intensity and kinetic energy, and integral length scale. A description of each is provided below.

6.2.2.1 Turbulence Intensity and Turbulence Kinetic Energy

The amplitude of the random fluctuations are quantified in terms of turbulence intensity and turbulence kinetic energy. Turbulence intensity is defined in general by Equation 6.28 as the root-mean-square of the velocity fluctuations, averaged with respect to the three coordinate directions and normalized by the mean velocity (Schlichting, 1979). Isotropic turbulence is statistically independent of direction, which is to say $\overline{u'^2} = \overline{v'^2} = \overline{w'^2}$. For homogeneous turbulence, the fluctuation components are statistically independent of position in space but can vary in direction.

$$\overline{Tu} = \frac{\sqrt{\frac{1}{3}(\overline{u'^2} + \overline{v'^2} + \overline{w'^2})}}{\bar{V}} \quad (6.28)$$

Turbulence kinetic energy is a dimensional measure of the fluctuation amplitude and is defined, per unit mass, as

$$\bar{k} = \frac{1}{2}(\overline{u'^2} + \overline{v'^2} + \overline{w'^2}) \quad (6.29)$$

It is determined by subtracting the mean kinetic energy from the instantaneous kinetic energy

of the velocity field and then taking the time mean of the result (Cebeci and Smith, 1974). Numerous higher order turbulence models successfully employ transport equations governing the behavior of \bar{k} . As evident from Equations 6.28 and 6.29, turbulence intensity and kinetic energy are related as follows

$$\bar{k} = \frac{3}{2} \overline{u^2} V^2 \quad (6.30)$$

For this work, the fluctuation velocities appearing in Equations 6.28 and 6.29 are found from the difference between the instantaneous velocity vector, $\{V, \alpha\}_{ni}$, and the corresponding ensemble-averaged vector, $\{\tilde{V}, \tilde{\alpha}\}_i$. In Figure 6.5, the fluctuation velocity of the i^{th} element of the n^{th} time record is denoted V'_{ni} . For this work, this fluctuation velocity is decomposed vectorially into “streamwise” and “transverse” components. Denoted u'_{ni} and v'_{ni} respectively in Figure 6.5, they are computed for the entire ensemble using Equation 6.31.

$$u'_{ni} = V_{ni} \cos(\Delta\alpha_{ni}) - \tilde{V}_i \quad i=1, \text{NPT} \quad n=1, \text{NTR} \quad (6.31a)$$

$$v'_{ni} = V_{ni} \sin(\Delta\alpha_{ni}) \quad i=1, \text{NPT} \quad n=1, \text{NTR} \quad (6.31b)$$

$$\text{where} \quad \Delta\alpha_{ni} = \alpha_{ni} - \tilde{\alpha}_i$$

The ensemble-averaged distribution and time-averaged value of the mean-square fluctuation velocity in the streamwise direction are determined using Equations 6.32 and 6.33, respectively. Analogous expressions apply for the transverse component.

$$\tilde{u}_i'^2 = \frac{1}{\text{NTR}} \sum_{n=1}^{\text{NTR}} u_{ni}'^2 \quad i=1, \text{NPT} \quad (6.32)$$

$$\overline{u}_i'^2 = \frac{1}{\text{NPT}} \sum_{i=1}^{\text{NPT}} \tilde{u}_i'^2 \quad (6.33)$$

Given that no measurement of the radial component of fluctuation velocity, $\overline{w'}$, is available, its mean square is assumed to be equal to the arithmetic average of the streamwise and trans-

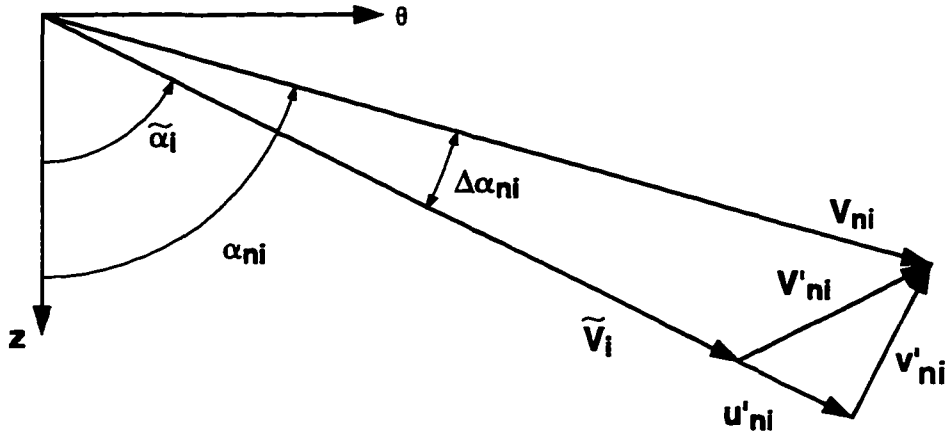


Figure 6.5. Definitions of streamwise and transverse components of fluctuation velocity

verse components. That is to say, $\overline{w'^2}$ in Equations 6.28 and 6.29 is replaced by

$$\frac{1}{2}(\overline{u'^2} + \overline{v'^2})$$

Using the above relationships, the ensemble-averaged distribution and time-averaged value of turbulence intensity are determined from Equations 6.34 and 6.35, respectively. Note that \overline{Tu} is not computed directly from a time average of \tilde{Tu}_i but rather from the time average of the mean-square fluctuations themselves.

$$\tilde{Tu}_i = \frac{\sqrt{\frac{1}{2}(\tilde{u}'^2 + \tilde{v}'^2)}}{\tilde{V}_i} \quad i=1, NPT \quad (6.34)$$

$$\overline{Tu} = \frac{\sqrt{\frac{1}{2}(\overline{u'^2} + \overline{v'^2})}}{\overline{V}} \quad (6.35)$$

In a similar manner, the ensemble-averaged distribution and time-average value of turbulence kinetic energy are computed using Equations 6.36 and 6.37.

$$\tilde{k}_i = \frac{3}{4}(\tilde{u}_i'^2 + \tilde{v}_i'^2) \quad i=1, \text{NPT} \quad (6.36)$$

$$\bar{k} = \frac{3}{4}(\overline{u'^2} + \overline{v'^2}) \quad (6.37)$$

Calculations of turbulence intensity and kinetic energy are carried out with respect to the relative frame of reference as well. Methodology described above as relating to Figures 6.4 and 6.5 is applied again to transform the velocity vectors from the absolute to the relative frame of reference. The components of fluctuation velocity in the relative frame are then determined in a manner analogous to Equations 6.31–6.33.

Before moving on, it is noteworthy to consider the relationship between the turbulence quantities described above and reference frame. The turbulence kinetic energy of a velocity field has the property of being entirely invariant with respect to transformation from one inertial coordinate system to another. Consequently, the numerator of the relationship for turbulence intensity will be identical for both the absolute and relative frames of reference. The value of turbulence intensity, then, will vary from the absolute to relative frame in inverse proportion to the mean velocity associated with each. The invariance of turbulence kinetic energy does *not* imply that the individual fluctuation components themselves (i.e., u' and v') are invariant. On the contrary, their values in general will vary with coordinate system orientation.

6.2.2.2 Integral Length Scale

The integral length scale is a measure of the average size of the energy-containing eddies associated with turbulent motions. It is determined in general by way of a spatial (i.e. two-point) correlation of a given fluctuating quantity as defined by Equation 6.38 (Bradshaw, 1971).

$$\Lambda = \int_0^{\infty} \mathfrak{R}(r) \, dr \quad (6.38)$$

The term, $\mathcal{R}(r)$, is the dimensionless correlation coefficient. It is expressed mathematically as

$$\mathcal{R}(r) = \frac{\overline{u'(x) u'(x + r)}}{\overline{u'^2(x)}} \quad (6.39)$$

The variable “ r ” is the spatial separation in the streamwise direction. The fluctuation quantity in Equation 6.39 is associated with streamwise velocity.

To determine experimentally the spatial correlation defined by Equation 6.39, simultaneous measurements are required from two probes spaced apart by various streamwise distances, r . Because of physical constraints, such measurements were not attainable in the LSRT. Instead, the spatial correlation $\mathcal{R}(r)$ is approximated by employing Taylor’s hypotheses. Provided this approach is valid, the conditions of which are considered in the paragraph that follows, the autocorrelation $\mathcal{R}(\tau)$ of a single time trace obtained at a fixed location, x , will be equal to the spatial correlation from two records obtained at a separation distance, $\overline{V}\tau$ (ibid.). In this manner, Equation 6.38 is rewritten as

$$\Lambda = \overline{V} \int_0^{\infty} \mathcal{R}(\tau) \, d\tau = \overline{V} \mathcal{T} \quad (6.40)$$

where the autocorrelation coefficient is expressed as

$$\mathcal{R}(\tau) = \frac{\overline{u'(t) u'(t + \tau)}}{\overline{u'^2(t)}} \quad (6.41)$$

As indicated in Equation 6.40, integration of the autocorrelation coefficient with respect to time shift τ is equal to the integral time scale, \mathcal{T} , of the turbulent fluctuations. Expressions analogous to Equations 6.39–6.41 can be written for the transverse coordinate direction. Because the integral time scale does not vary with reference frame, it follows from Equation 6.40 that the value of integral length scale will vary in direct proportion to the mean velocity associated with the relative and absolute frames of reference.

With the above analysis established, it is appropriate to consider the validity of invoking Taylor’s hypothesis for unsteady flowfields in turbomachines. Taylor’s hypothesis is based on

the premise that the turbulent eddies do not change appreciably in shape as they convect past a fixed point in space (i.e., “rigid” convection). Implicit to this criterion is that the turbulent fluctuations be “small” relative to the mean flow and that the turbulence field be homogeneous (Hinze, 1975). With regard to the former, Cebeci and Smith (1974) suggest that turbulence intensity should be less than about 1 percent. As will be reported in Chapters 7 and 8, however, intensities in the embedded stages of an LP turbine can be significantly greater than 1 percent. Consequently, some inaccuracies are likely to be introduced. Homogeneity of the turbulence field is a necessary condition in order that the spatial correlation be an even function about zero. This is because the autocorrelation used to approximate the spatial correlation is by definition an even function. Given the ubiquitous mixing processes that occur in turbomachine flowfields, it is likely that this criterion is also not satisfied in the strictest sense. In spite of these shortcomings, Taylor’s hypothesis still represents the most amenable (if not the only) approach to the problem of computing turbulence length scales in turbomachine environments. Hence, it is applied here in a manner similar to other studies (e.g., Camp and Shin, 1994) though appropriate caution is warranted.

For this work, the autocorrelation coefficient, $\mathfrak{R}(\tau)$, that appears in Equation 6.40 is computed for each coordinate direction by way of the inverse Fourier transform of the respective mean square spectral density. For the streamwise coordinate direction, this is expressed mathematically by

$$\mathfrak{R}(\tau) = \frac{1}{u'^2} \int_{-\infty}^{\infty} S(f) e^{2\pi i f \tau} df \quad (6.42)$$

Here, $S(f)$ is the mean square spectral density calculated as

$$S(f) = \lim_{T \rightarrow \infty} \frac{1}{T} |X(f)|^2 \quad \left[\frac{\text{ft}^2/\text{s}^2}{\text{hz}} \right] \quad (6.43)$$

where $X(f)$ is the Fourier transform of the velocity trace.

For the measurements obtained herein, Equations 6.42 and 6.43 are evaluated in a discretized rather than continuous sense. Details of the mathematics are contained in Appendix D while the actual calculation procedure, including examples, is documented in Appendix E.

6.3 Aerodynamics Measurements

6.3.1 Profile Loss Coefficient

Measurements of profile loss were determined at midspan from the circumferential traverses of total and static pressure using Equation 6.44. The numerator of this relationship is the difference between the freestream and mixed-out values of total pressure at the exit measurement plane of the bladerow. The denominator is equal to the freestream dynamic head at the bladerow exit.

$$\omega_p = \frac{\overline{P}_{\text{tex,fs}} - \overline{P}_{\text{tex,mixed}}}{\overline{P}_{\text{tex,fs}} - \overline{P}_{\text{sex}}} \quad (6.44)$$

Predicted values of profile loss coefficient were determined using a 2-D wake mixing analysis similar to that of Denton (1993). Boundary layer quantities at the trailing edge required for this analysis were obtained from 2-D boundary layer calculations. Values of base pressure coefficient recommended by Denton (ibid.) were used.

6.3.2 Velocity Distributions and Airfoil Loading

Velocity along the blade surface was determined from the measured distribution of static pressure. Results were normalized by the bladerow exit velocity as indicated by Equation 6.45.

$$\frac{V_{e_i}}{V_{\text{ex}}} = \sqrt{\frac{\overline{P}_{\text{tex,fs}} - \overline{P}_{s_i}}{\overline{P}_{\text{tex,fs}} - \overline{P}_{\text{sex}}}} \quad (6.45)$$

The subscript “i” denotes the i^{th} static tap.

Airfoil loading is quantified in terms of the Zweifel loading coefficient. This is simply an airfoil lift coefficient tailored to turbine aerodynamics. Its incompressible form, per unit blade height (Glassman, 1972), is given as

$$Z_{\text{inc}} = \frac{\int_0^{c_z} (P_{\text{ps}} - P_{\text{ss}}) dz}{c_z \frac{1}{2} \rho_{\text{ex}} V_{\text{ex}}^2} \quad (6.46)$$

where P_{ps} and P_{ss} are the static pressures acting on the pressure and suction surfaces, respectively, and c_z is axial chord. By considering the conservation of tangential momentum across the bladerow, Equation 6.46 can be recast in terms of axial solidity, σ_z , and flow turning only (Wilson, 1984). Written as Equation 6.47, all flow angles pertain to the reference frame of the bladerow of interest.

$$Z_{\text{inc}} = \frac{2}{\sigma_z} \cos^2 \alpha_{\text{ex}} (\tan \alpha_{\text{in}} - \tan \alpha_{\text{ex}}) \quad (6.47)$$

6.4 Uncertainty Analysis

An uncertainty analysis was carried out to estimate the accuracy of the measured data. The estimated uncertainty intervals of the primary measurement values are listed in Table 6.1a. They were determined statistically from random data samples using 20 to 1 odds. Pressures are given as a fraction of local dynamic pressure.

The propagation of error method (Kline and McClintock, 1953) was used to calculate the uncertainty of the performance parameters and flowfield quantities. Results are listed in Table 6.1b.

Table 6.1. Estimated uncertainty intervals based on 20 to 1 odds

a) measured quantities

Quantity	Uncertainty
Rotational Speed, RPM	± 0.012 rpm (0.003% of measured)
Torque, T	± 3.37 ft•lbf (0.12% of measured)
Temperature, T	± 0.21 °F
Pressures	
– mass flow measurement plane	$\pm 0.003q$
– hub and casing statics	$\pm 0.011q$
– surface statics	$\pm 0.011q$
– probe totals	$\pm 0.002q$
– probe statics	$\pm 0.010q$
X Hot-Film Probe Measurements	
– Velocity, V	± 1.25 %
– Flow Angle, α	$\pm 0.5^\circ$
Surface Hot-Film Measurements	
– zero-flow voltage, E_0	± 0.007 volts
– anemometer output voltage, E	± 0.001 volts

b) computed quantities

Quantity	Uncertainty	(% of Nominal)
Specific Flow, ϕ	± 0.0012	$\pm 0.12\%$
Specific Work, ψ	± 0.0020	$\pm 0.17\%$
Loss Coefficient, ω_p	± 0.0028	$\pm 9.7\%$
Normalized Velocity, V/V_{ex}	± 0.011	$\pm 1.1\%$
Turbulence Intensity, Tu		$\pm 0.04\%$
Quasi Wall Shear Stress, $q\tau_w$		$\pm 10.5\%$

CHAPTER 7. MEASUREMENTS OF BOUNDARY LAYER DEVELOPMENT

Contained in this chapter is a description of the boundary layer development occurring along the LP turbine blading determined from surface hot-film measurements. These measurements constitute the primary focus of this research program. To facilitate the presentation and because of the extensive and lengthy nature of this data set, the chapter is divided into three components. The first component makes up Section 7.1 and consists of a complete description of the test matrix at which the boundary layer measurements were obtained. An overview of the major findings constitutes the second component and makes up Section 7.2. Here, results are presented using simple schematics in a manner similar to Halstead et al. (1995). The objective is to provide the reader with an extended summary of the results in a manner not hindered by the details of the measurements themselves. The third component contains a detailed presentation and interpretation of the experimental measurements used to arrive at those findings. It makes up Sections 7.3–7.6 of this chapter.

7.1 Test Matrix

Test conditions at which the surface hot-film measurements were obtained are given in Figure 7.1 and listed in Table 7.1. The test domain in Figure 7.1 is identical to that presented in Chapter 4. The abscissa is specific flow while the right and left ordinates are stage-averaged Reynolds numbers based on suction surface length and throat width, respectively. The upper and lower shaded regions indicate ranges of takeoff and cruise Reynolds numbers, respectively. It should be noted that the boundaries of these regions are somewhat arbitrary and are drawn here to reflect the LPT turbine family modeled by the LSRT blading.

Each test point on Figure 7.1 and in Table 7.1 is labeled with a letter/number combination. Numbers 5, 6, and 7 are in order of decreasing loading. This numbering convention is used so as to maintain consistency with Halstead et al. (1995). Letters A through E are in order of decreasing Reynolds number. Letters A through C are in the takeoff range of Reynolds number while D and E are in the cruise range.

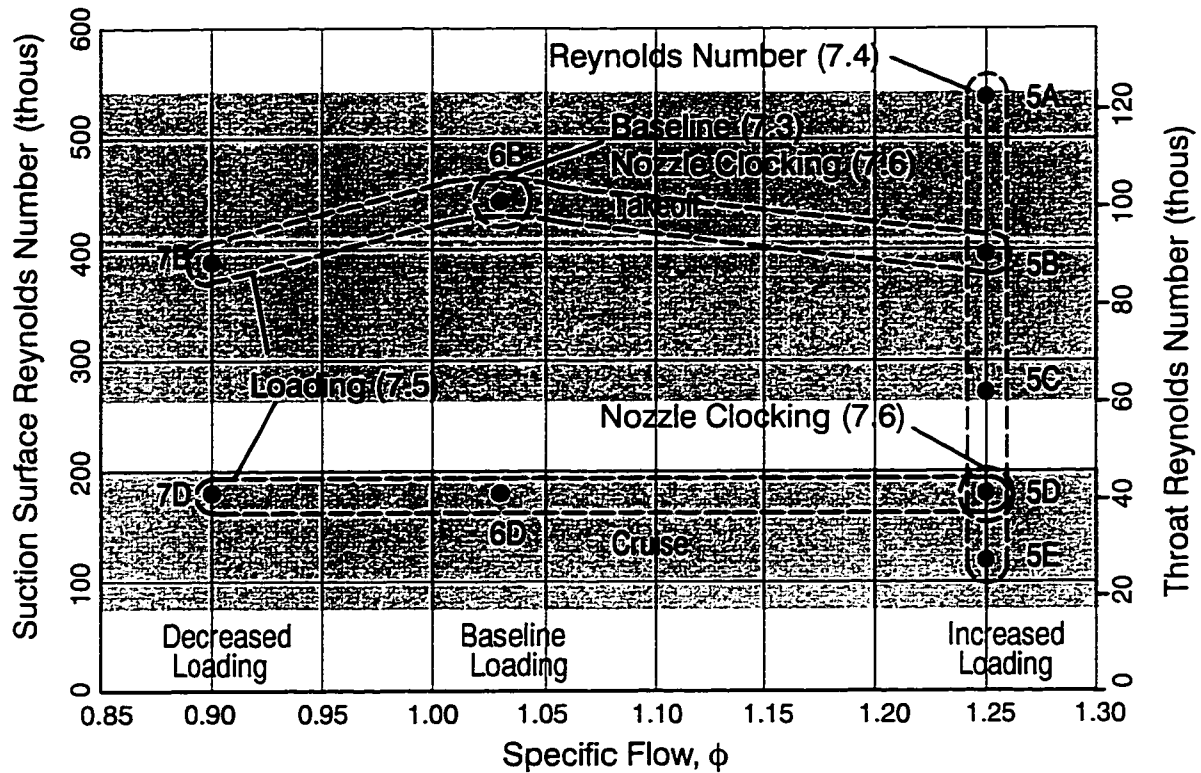


Figure 7.1. Test matrix for boundary layer measurements

Table 7.1. Test conditions for boundary layer measurements

Test Point	Specific Work, ψ	Specific Flow, ϕ	Reduced Freq., k		Zweifel Coef., Z_{inc}		$Re_{ssl} \times 10^{-3}$		
			Nozzle 2	Rotor 2	Nozzle 2	Rotor 2	Stage Ave	Nozzle 2	Rotor2
5A	1.25	1.55	0.619	1.084	0.940	1.010	527	611	443
5B	1.25	1.55	0.619	1.084	0.940	1.010	396	459	333
5C	1.25	1.55	0.619	1.084	0.940	1.010	271	314	228
5D	1.25	1.55	0.619	1.084	0.940	1.010	180	209	151
5E	1.25	1.55	0.619	1.084	0.940	1.010	119	138	100
6B	1.03	1.17	0.751	1.315	0.876	0.937	453	525	381
6D	1.03	1.17	0.751	1.315	0.876	0.937	180	209	151
7B	0.90	1.00	0.859	1.505	0.824	0.880	396	459	333
7D	0.90	1.00	0.859	1.505	0.824	0.880	180	209	151

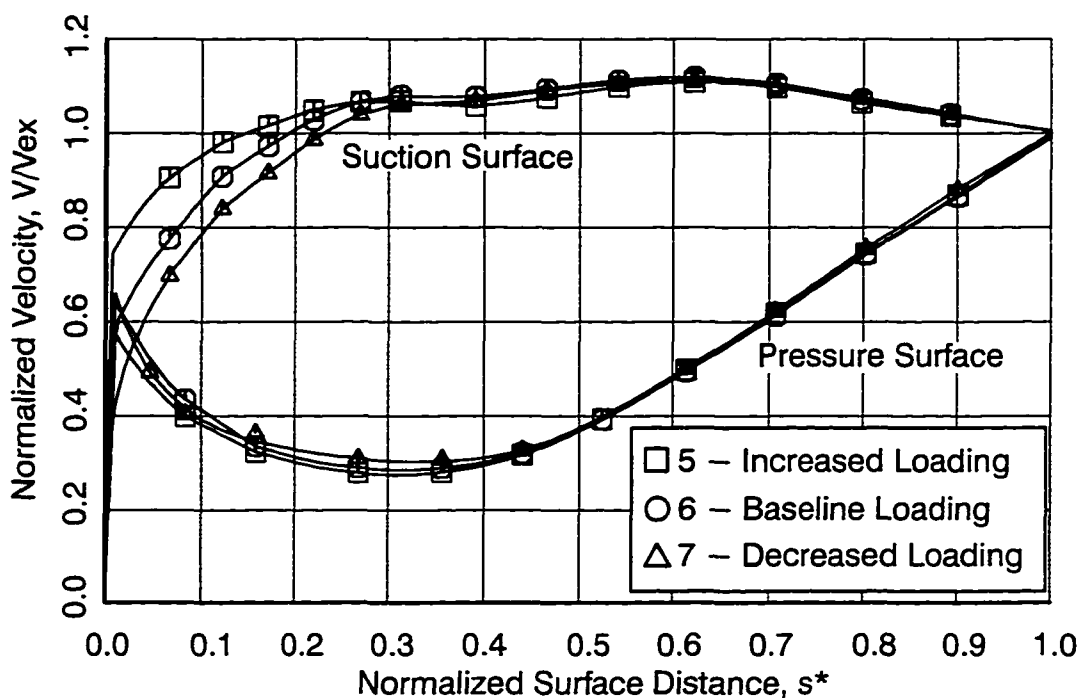
In Table 7.1, three values of Reynolds numbers are provided to facilitate comparison of these data with other turbines. The first is a stage-averaged Reynolds number determined for Stage 2 (the test stage) of the turbine. As noted above, it constitutes the left-hand ordinate of Figure 7.1. The last two columns of the table contain Reynolds numbers of each specific blade-row of the second stage. Their differences are due to differences in bladerow exit velocity and airfoil surface length. All characteristic lengths necessary to convert the Reynolds numbers from surface length based to chord, axial chord, or throat are provided in Table 4.1. The Zweifel loading coefficients and reduced frequencies for the second stage nozzle and rotor are also provided in Table 7.1. They pertain to midspan as calculated using Equation 6.47.

When describing the experimental findings in subsequent sections, reference will be made to single and groups of test points. In Figure 7.1, these are encircled with dashed lines and labeled to indicate the general category of the results and section number in which they are described.

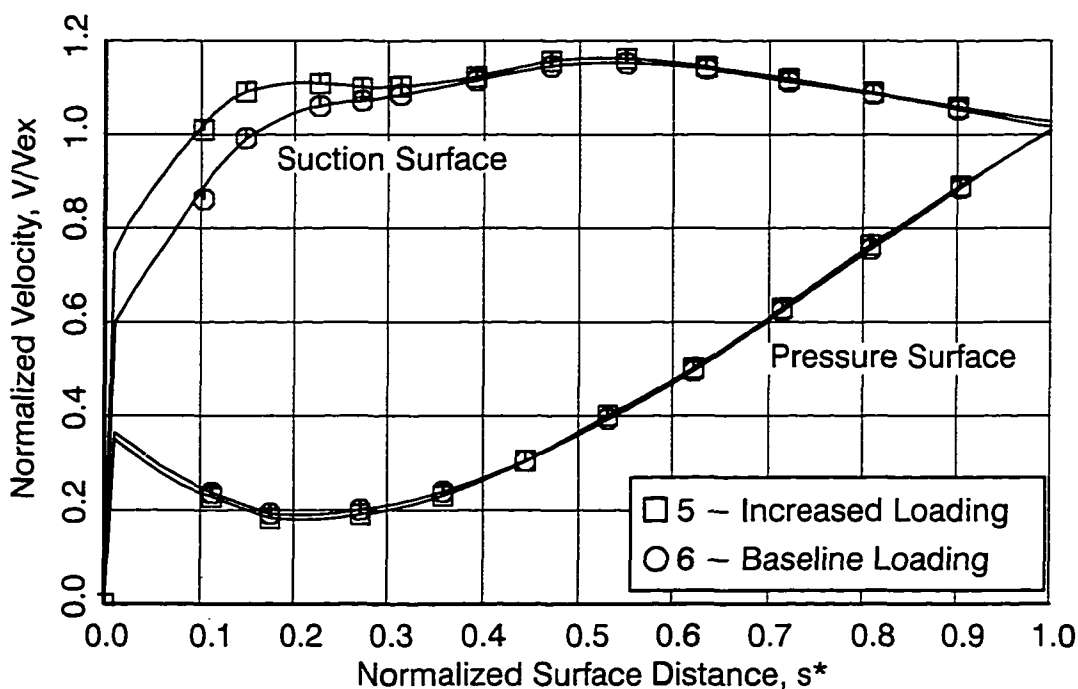
The surface velocity distributions that pertain to the above test conditions appear in Figure 7.2. The abscissa and ordinate are normalized surface distance and velocity, respectively. Velocity has been normalized by the value at the bladerow exit. The symbols, determined from measurements, are labeled by number to correspond with the loading levels identified in Figure 7.1. The effect of Reynolds number on the velocity distributions was not significant for the range tested and hence is not shown explicitly.

In terms of turbine design terminology, both bladerows are “aft-loaded” – that is, maximum velocity along the suction surface is located aft of $0.5s^*$. Maximum velocity occurs at $0.62s^*$ and $0.55s^*$ for the nozzle and rotor, respectively. The associated velocity ratio, V_{\max}/V_{exit} , is equal to 1.12 and 1.15. This is a measure of the amount of suction-side diffusion prior to the trailing edge.

The effect of loading on the velocity distributions is most pronounced along the suction surface. As loading (and, subsequently, incidence angle) increases, the velocity distributions



a) Stage 2 nozzle



b) Stage 2 rotor

Figure 7.2. Normalized surface velocity at midspan for various loading levels (numbers correspond to those in Figures 7.1 and Table 7.1)

“open up” in the leading edge region. This effect extends back to about $0.4s^*$. Of particular interest is that at increased loading (test point 5), the distributions have opened to the point that a region of local diffusion prior to maximum velocity is present along the suction surface of the nozzle and rotor at about $0.3s^*$ and $0.25s^*$, respectively. At baseline loading for the rotor (test point 6) and decreased loading for the nozzle (test point 7), continuous acceleration is maintained along the suction surface to maximum velocity. As will be shown in Section 7.5, this subtle difference in velocity distribution can influence significantly the location of boundary layer transition.

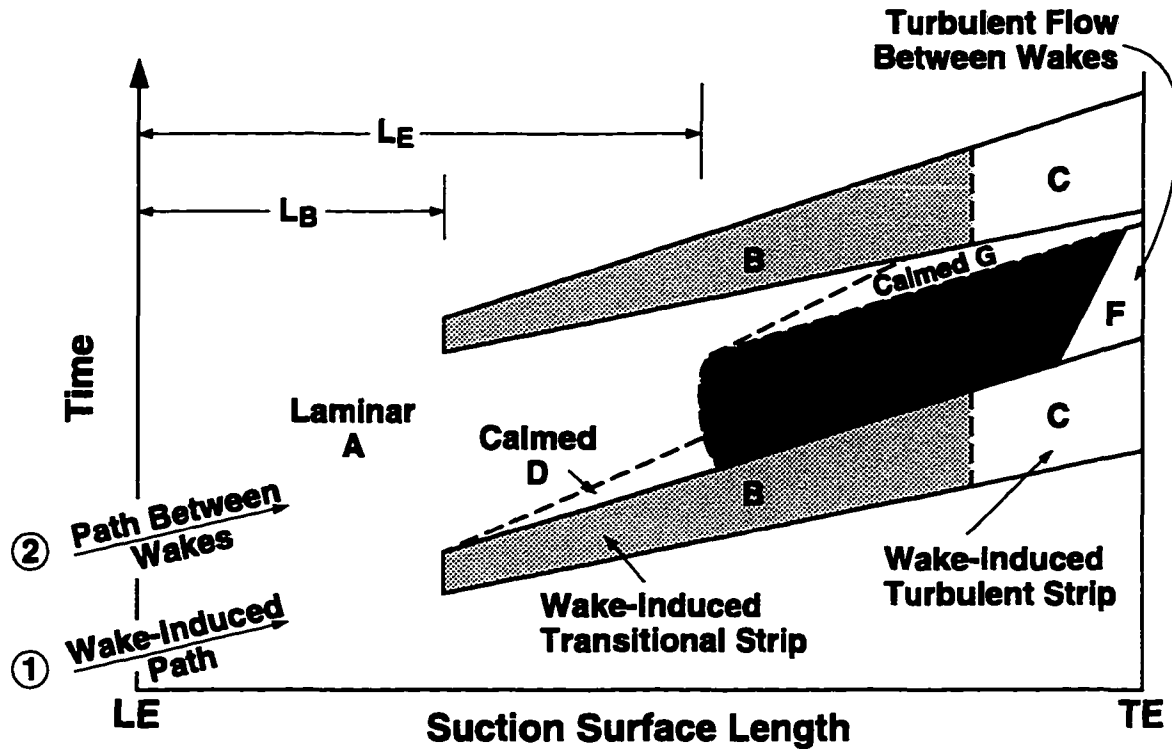
Along the pressure surface, flow diffusion occurs downstream of the leading edge followed by a strong acceleration back to the trailing edge. At decreased loading, the cross-over of the velocity distribution near the leading edge for the nozzle is an indication of negative incidence.

7.2 Summary of Major Findings

Contained in this section is an extended summary of the major findings of how boundary layers develop along LP turbine blading of the LSRT. To this end, simplified $s-t$ diagrams are introduced to identify unique regions of boundary layer development along the airfoil suction surfaces. After a discussion of the baseline test condition, we will consider the effects of Reynolds number, loading, and nozzle clocking.

7.2.1 Baseline Test Condition

The $s-t$ diagram of boundary layer development for the baseline test condition of the LSRT is given in Figure 7.3a. The experimental measurements used to construct this schematic will be presented in Section 7.3. The test point for this turbine operating condition is 6B which pertains to intermediate loading and high, takeoff Reynolds number. It was chosen as a convenient reference point to which results from the rest of the test matrix are compared.



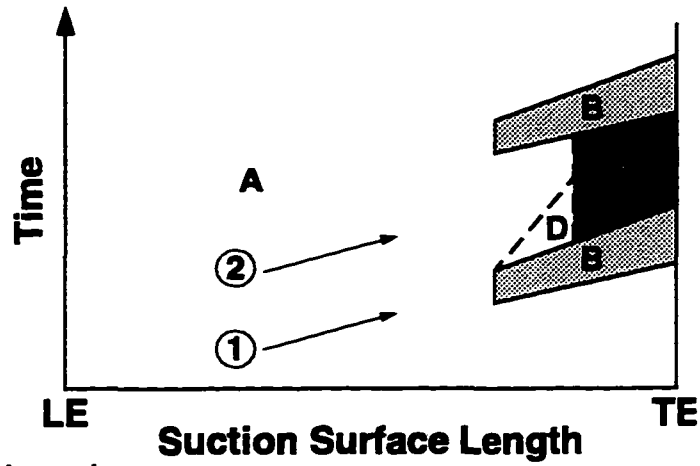
a) baseline test condition, takeoff Reynolds number

Figure 7.3. S-t diagram schematics of boundary layer development for LSRT

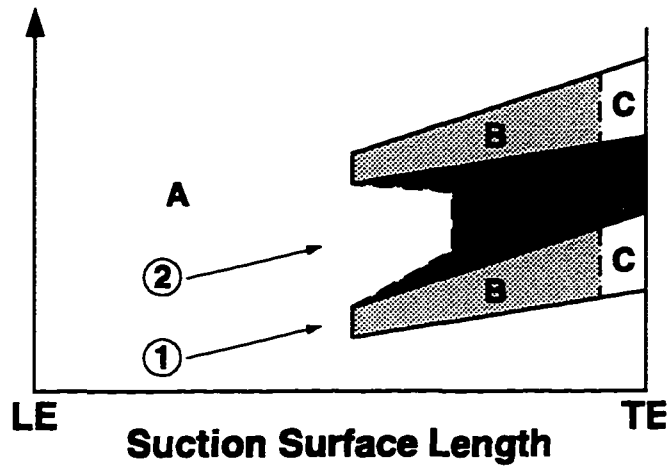
The s-t diagram is drawn in a manner analogous to that for the turbulent spot in Figure 6.2b. The abscissa is now suction surface distance extending from leading to trailing edge. The ordinate is equal to time.

For the baseline test condition, the suction surface boundary layer is observed to develop along two distinct paths. They are identified in Figure 7.3a as the wake-induced path and the path between wakes. The characteristics of each are described below. Specific regions of boundary layer development are identified as regions A through G.

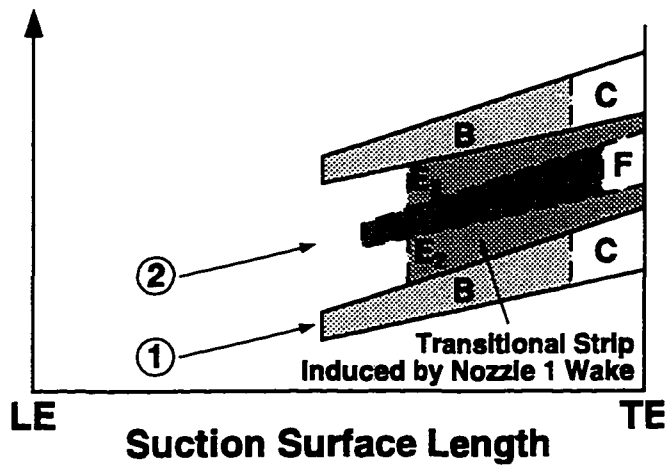
In a multi-stage turbine, wakes from upstream airfoils periodically wash over the surfaces of the downstream airfoils. These wakes are characterized by a deficit in velocity and by increased turbulence intensity. Influence of the wake flow on the developing airfoil boundary



b) low, cruise Reynolds number



c) decreased loading



d) Nozzle 1 clocking

Figure 7.3. continued

layer gives rise to the wake-induced path. For the baseline test condition, in Figure 7.3a, the wake-induced path is seen to consist of three regions – A, B, and C. Downstream of the leading edge and beneath the wake, the boundary layer remains laminar (albeit in a disturbed state) in spite of the increased wake turbulence intensity. This portion of the path is labeled laminar region A. Only at a distance L_B downstream of the leading edge is the disturbance level convecting with the wake sufficient to initiate boundary layer transition. Here, the instantaneous time traces from the hot-films reveals the formation of individual turbulent spots. As the turbulent spots convect downstream, they grow and merge, forming the wake-induced transitional strip labeled region B. From Figure 7.3a, we see that this strip remains narrow, occupying only about 25 percent of the blade-passing period. The surface hot-film data further reveal that the leading and trailing boundaries of strip B are approximately equal to those of an individual turbulent spot. As a result, the strip increases in temporal and streamwise extent with increasing surface distance in the manner drawn. When transition along B is completed, a region of turbulent boundary layer flow, labeled “C,” extends to the trailing edge.

The second path of boundary layer development is identified in Figure 7.3a as the path between wakes. Along this path, the laminar region A extends further aft owing to the lower turbulence intensity between wakes. For the baseline test condition, the region of transition between wakes, region E, commences aft of mid surface distance. Transition is completed prior to the trailing edge where a region of turbulent flow is identified, labeled “F.”

Two additional regions also appear along the path between wakes in Figure 7.3a. Labeled D and G, they are associated with regions of calmed flow. As described in Appendix A, calmed regions form behind turbulent spots. Across these regions, wall shear stress decays from a turbulent level at the trailing boundary of the spot to the laminar level of the background flow some distance behind the spot. For the baseline test condition of this turbine, calmed regions are observed behind the turbulent spots of the wake-induced transitional strip B, forming calmed region D, and behind the spots of transitional region E, forming calmed region G. It will be

shown in Section 7.3 that region G is especially unique. Here, the elevated shear stress of the calmed flow effectively suppresses separation in the region of adverse pressure gradient prior to the trailing edge. As a consequence, intermittent regions of attached, non-turbulent flow persists to the trailing edge.

In summary, the boundary layer along the suction surface at this baseline test condition develops along two distinct paths in response to the time-varying flow entering the bladerow. Along the path beneath the convecting wake, transition occurs earliest. Between wakes, laminar flow extends past mid surface length. Along both paths, large extents of laminar and transitional flow are present. Most surprising was the fact that, for the LSRT at this high Reynolds number condition, fully turbulent boundary layer flow is observed only along the latter 10 to 15 percent of the airfoil surface.

7.2.2 Effects of Reynolds Number

The detailed experimental measurements documenting the effects of Reynolds number are given in Section 7.4. An s - t diagram pertaining to a low, cruise Reynolds number in Figure 7.3b summarizes the findings. Most apparent is that laminar region A now extends very far downstream. The surface hot-film measurements will show, in addition, that the laminar boundary layer itself varies periodically due to interaction with the passing wakes. Transition along the wake-induced path did not begin until well into the region of diffusion along the aft portion of the airfoil and continued to the trailing edge.

Along the path between wakes, the periodicity of the laminar boundary layer coupled with the effect of calming appears to suppress separation between wakes. This enables a significant region of attached, transitional flow to persist to the trailing edge. That flow separation did not occur is especially noteworthy since, as will be shown in Chapter 9, conventional boundary layer calculations predicts laminar separation to occur upstream of the attached-flow transition in region E.

7.2.3 Effects of Loading

The effects of loading on boundary layer development are documented experimentally in Section 7.5. In general, as loading of the LSRT increases, the location of wake-induced transition moves toward the leading edge relative to the baseline condition of Figure 7.3a. At takeoff Reynolds numbers and increased loading, the actual location of onset along the wake path coincides with the small local diffusion in the velocity distribution near 30 percent surface length.

Because of its different character, the s - t diagram for decreased loading is shown in Figure 7.3c. At this test condition, continuous flow acceleration is maintained from the leading edge to maximum velocity. As a result, wake-induced transition is postponed significantly in comparison to the baseline condition, occurring aft of mid surface length. Transition along the path between wakes is postponed to a degree as well relative to that for increased loading.

7.2.4 Effects of Nozzle Clocking

The relative clocking of bladerows of the same reference frame is found to impact substantially the boundary layer development and aerodynamic loss of the downstream bladerow. The surface hot-film measurements documenting this interaction are contained in Section 7.6.

For the LSRT, very different time-varying distributions of turbulence intensity entering Nozzle 2 are measured for different relative clocking locations of Nozzle 1. That these differences occur indicates that the wake of Nozzle 1 has not mixed out by the inlet plane to Nozzle 2.

The impact of clocking Nozzle 1 on the boundary layer of Nozzle 2 is illustrated by comparing the s - t diagram of Figure 7.3d with that of part a. The diagrams pertain to the identical baseline test condition with the exception that Nozzle 1 was at two different clocking positions. In part d, wakes from Rotor 1 still produce wake-induced transitional/turbulent strips as indicated. However, the wake segments from the upstream Nozzle 1 create an additional transitional strip E/F. An interesting consequence of this interaction is that periodic variations of the boundary layer at the trailing edge occur at twice blade-passing frequency. The implications

of nozzle clocking on aerodynamic loss are found to be important as well and are documented in Chapter 9.

7.2.5 Pressure Surface

Along the pressure surface for all test conditions, laminar–turbulent transition occurs near the leading edge in the region of adverse pressure gradient. Dependent upon loading, transition takes place via either a laminar separation bubble or by attached–flow means. Downstream of minimum velocity, the strong flow acceleration extending back to the trailing edge produces a partial relaminarization of the turbulent boundary layer. Development of the pressure surface boundary layer in the LSRT does not vary significantly with Reynolds number.

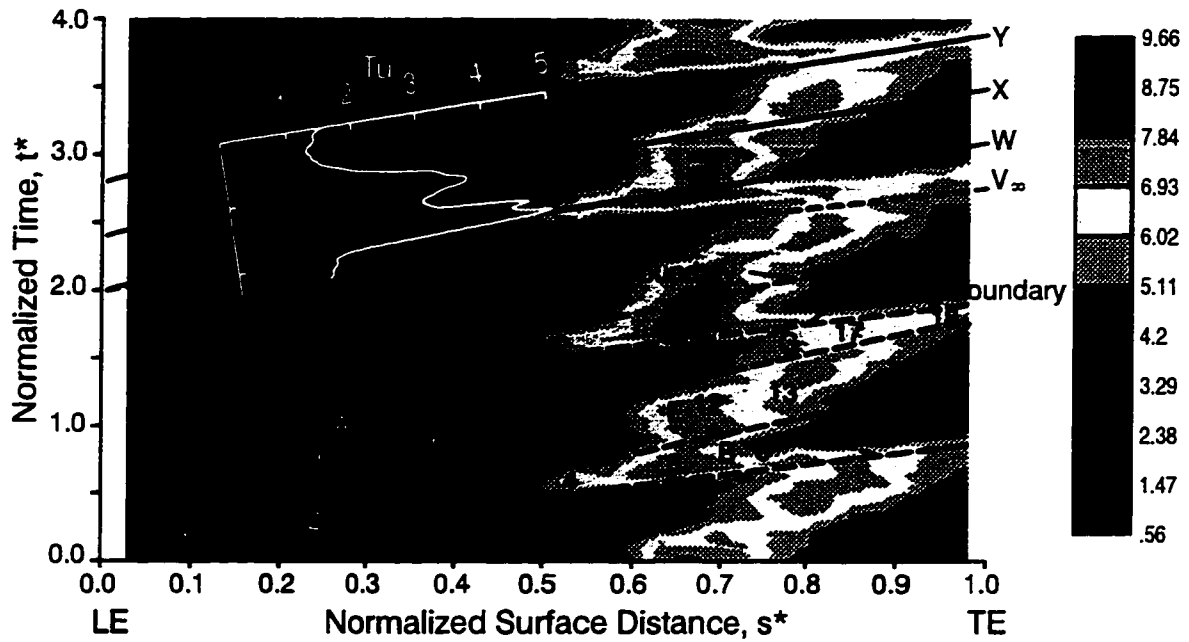
7.3 Boundary Layer Development for Baseline Test Point

This section contains a detailed description of the boundary layer measurements from along the second stage nozzle and rotor at the baseline test point. Results will be presented for the suction and pressure surfaces of each airfoil. The test condition is identified as point 6B on Figure 7.1 and Table 7.1. Coinciding with the design point of the turbine, it pertains to a baseline loading and takeoff Reynolds number condition. Here, the turbine operates near peak efficiency.

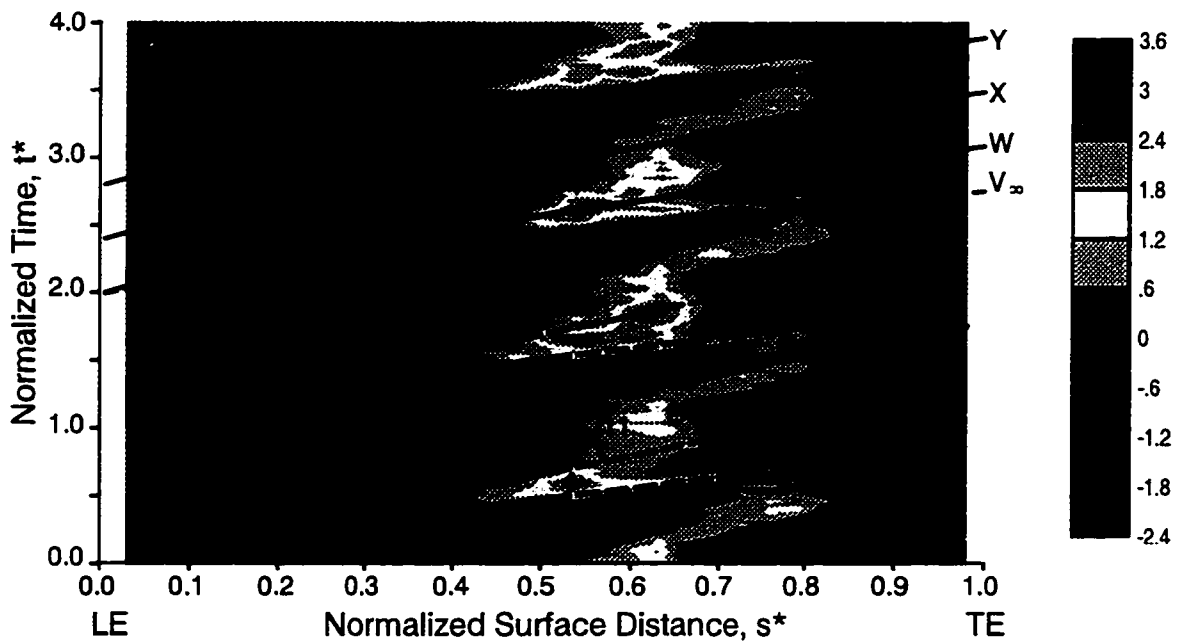
7.3.1 Nozzle Suction Surface

The time history of the boundary layer development is described first using s – t diagrams showing color contours of ensemble–averaged quantities and line plots of time–averaged quantities. Determined from the surface hot–film measurements, two such color contour plots are shown in Figure 7.4 for the nozzle suction surface. The contours are of random unsteadiness and skew, respectively. The abscissa of each is normalized surface distance, s^* , with 0.0 corresponding to the leading edge and 1.0 to the trailing edge. The ordinate is time normalized by the blade–passing period of the upstream rotor.

The color contours consist of 10 colors with the lowest value equal to blue and the highest to red. The color legend to the left of each contour plot provides the range and increment of varia-



a) random unsteadiness ($Q_0=0.56, Q_{10}=9.66$)



b) skew ($Q_0=-2.4, Q_{10}=3.6$)

Figure 7.4. Ensemble-averaged shear stress characteristics along suction surface of Nozzle 2, test point 6B

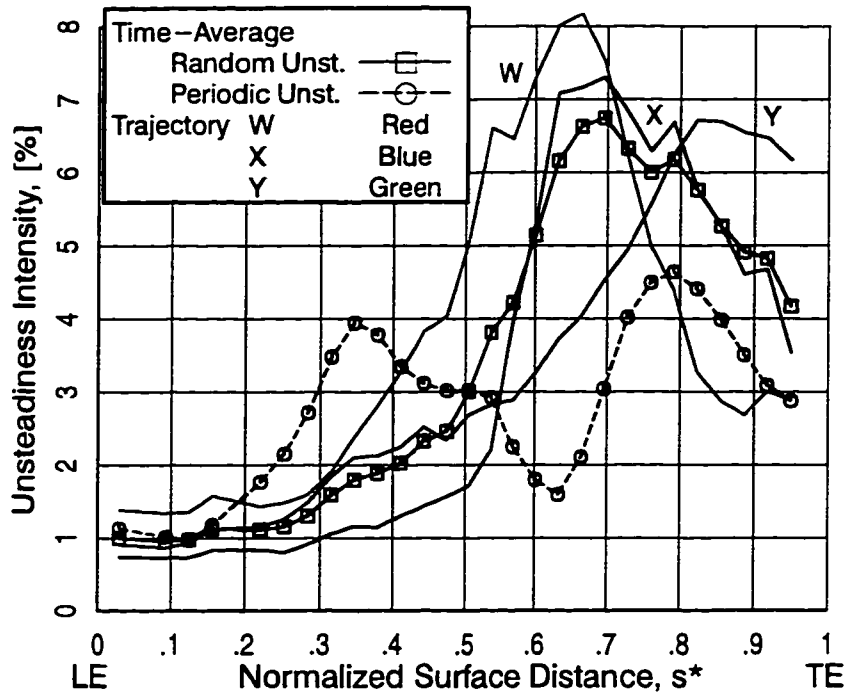
tion. For all subsequent contour plots, the color legend will not be repeated unless a different number of contours are used. Instead, the minimum and maximum values of the range will be provided as Q_0 and Q_{10} , respectively.

Three trajectories labeled W, X, and Y are superimposed onto the contours. They are drawn to correspond to a speed of $0.7V_\infty$. This was found to be the average convective velocity of “events” moving along the blade surface as determined using cross-correlation analysis of neighboring hot-film traces. In general, the trajectories are not straight lines since the freestream velocity varies through the bladerow. For these and all subsequent s-t diagrams, trajectory W is drawn through the wake-induced path while all other trajectories extend along paths between regions effected by the wakes. The trajectory drawn as a dashed line corresponds to the free-stream convective velocity, V_∞ .

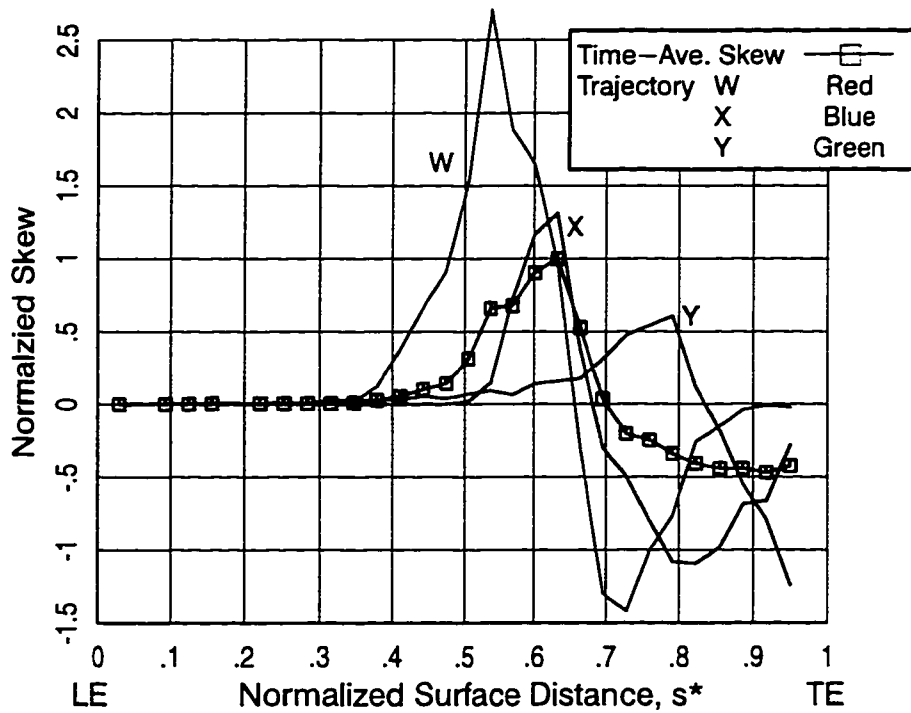
Important regions of boundary layer development are labeled from A through G. They are equivalent to those introduced in Section 7.2 in reference to Figure 7.3a. Points of specific interest are numbered 1, 2, 3, etc.

A line plot of the ensemble-averaged distribution of turbulence intensity, measured at the inlet of Nozzle 2, has been superimposed onto the s-t diagram of random unsteadiness in Figure 7.4a. Its coordinate axes are labeled. As indicated, the higher levels of intensity extend to the right. Though this form of presentation is not conventional, it illustrates conveniently the correlation of the inlet disturbance environment convecting into the bladerow with the boundary layer development along the blade. Over the course of this work, it was found that the turbulence distribution at the inlet to Nozzle 2 was influenced significantly by the circumferential clocking location of the upstream Nozzle 1. For the measurements presented in this section, the relative clocking of Nozzles 1 and 2 were chosen so that this influence was minimized. A complete description of nozzle clocking effects is reserved for Section 7.6.

Line plots of random unsteadiness and skew along the suction surface are given in Figure 7.5. The solid and dashed black lines of Figure 7.5a correspond to time-averaged random and



a) random and periodic unsteadiness



b) skew

Figure 7.5. Time-averaged shear stress characteristics along suction surface of Nozzle 2, test point 6B

periodic unsteadiness, respectively. The colored lines indicate the distributions of random unsteadiness occurring along trajectories W, X, and Y. The ordinate of Figure 7.5a is unsteadiness intensity, in terms of percent, calculated using Equations 6.9 and 6.11. In an analogous fashion, the black and colored lines of Figure 7.5b refer to time-averaged skew and skew along the trajectories, respectively

The boundary layer development along the nozzle suction surface was described in conjunction with the schematic of Figure 7.3a as developing along two separate but coupled paths. The wake-induced path consisted of regions A, B, and C while the path between wakes was made up of regions A, E, and F. The paths were coupled by regions of calmed flow denoted by letters D and G. A detailed description of each path as well as the calmed regions is given below.

7.3.1.1 Wake-Induced Path

As wakes from the upstream bladerow convect along the surface of the downstream airfoil, the local boundary layer beneath these wakes develops along what is called the wake-induced path. This path is traced out by trajectory W on Figure 7.4. It lags slightly behind that of the wake itself which, being away from the airfoil surface and outside the boundary layer, convects at freestream velocity.

The wake-induced path begins at the leading edge near point 1 in Figure 7.4. In spite of the high turbulence intensity of the incoming rotor wake, equal to nearly 5 percent, the boundary layer in the vicinity of the leading edge remains laminar. Consequently, this region is labeled as the laminar region A. At points 1 and 2 along trajectory W, the random unsteadiness remains low and skew is near zero. This is further evident from the red lines in Figure 7.5. These characteristics were shown in Section 3.3.2 to be indicative of laminar flow.

From points 2 to 3 along trajectory W, the random unsteadiness increases as the thickening laminar boundary layer responds to the high turbulence intensity of the wake. Up until $0.35s^*$, skew along W remains near zero as evident from Figure 7.5b. This suggests the increased random unsteadiness remains symmetric about the mean and hence is not the result of

turbulent spot formation. In total then, the laminar region A along the wake-induced path extends from the leading edge to about $0.4s^*$.

Downstream on point 3 of Figure 7.4 and along trajectory W (see also red lines of Figure 7.5), random unsteadiness and skew increase significantly in value. The instantaneous time traces from this location, which are considered later in this section, indicate the formation of individual turbulent spots. These changes denote the onset of wake-induced transition. We see from Figure 7.2a that this commencement of transition coincides with the slight, local diffusion in the surface velocity distribution near $0.35s^*$.

The subsequent region of transitional boundary layer flow along trajectory W is called the wake-induced transitional strip and is identified as “B” in Figure 7.4. It occurs in phase with the high turbulence intensity from the wake of Rotor 1. From points 4 to 5 in Figure 7.4, the random unsteadiness increases to its maximum value. As described in Section 3.3.2, this maximum in random unsteadiness occurs near the midpoint of transition (i.e., intermittency is ~ 0.5). Here the fluctuating wall shear stress resides an equal amount of time at laminar and turbulent levels. Values of skew reach a maximum at point 4 followed by a decrease. At point 5 near $0.65s^*$, skew crosses zero. Coinciding with the location of peak random unsteadiness, this is a further indication that transition is near its midpoint.

From points 5–6–7 along trajectory W, random unsteadiness decreases monotonically. Skew in turn reaches a negative minimum and subsequently increases back toward zero as transition nears completion. The latter is evident especially from the red line of Figure 7.5b.

Along the wake-induced path then, boundary layer transition extends from near point 3 at $0.4s^*$ to approximately point 7 at $0.85s^*$. The width of this transition strip remains narrow—equal to nominally 25 percent of the wake-passing period. The leading and trailing boundaries of the strip are drawn for speeds of $0.9V_\infty$ and $0.5V_\infty$, respectively. These coincide with the convective velocities associated with individual turbulent spots as described in Section 6.1.3. Because of these differing convective velocities, the strip increases in spatial and temporal extent

as one moves in the streamwise direction. From the variation in contours in Figure 7.4, the boundaries between the wake-induced and neighboring non-wake regions are seen to be very distinct. This suggests there is little variation in phase of the transitional activity initiated by each passing wake.

Region C occurring along the trajectory W prior to the trailing edge is identified as the wake-induced turbulent strip. It begins near $0.85s^*$ and extends through points 7 and 8. As indicated by the red line in Figure 7.5a, random unsteadiness is maintained at a near constant value in region C and at a level much lower than that for the transitional flow but significantly higher than that for the laminar flow near the leading edge. Again, a similar signature was found in Figure 3.5 for boundary layer transition with a steady mean flow. Values of skew through region C (red line, Figure 7.5b) are near zero indicating that the turbulent fluctuations are symmetric about the mean. The leading and trailing boundary for Region C are drawn for the identical speeds as for the wake-induced transitional strip B.

It is noteworthy that the leading edge of the wake-induced strip convects at a velocity ($0.9V_\infty$) that is lower than the wake itself ($1.0V_\infty$). This implies that an overhang exists as the wake-induced strip forms beneath the wake. Schubauer and Klebanoff (1956) observed such an overhang for individual turbulent spots. That additional wall turbulence does not form beneath this overhang is due to the time required by the turbulence to propagate inward across the boundary layer (ibid.).

7.3.1.2 Path Between Wakes

We will now consider the boundary layer development taking place between the wakes convecting along the nozzle suction surface. This was described in Section 7.2 as the “path between wakes.” In Figure 7.4, trajectories X and Y extend along this path and lag Trajectory W in phase by $0.4 t^*$ and $0.8 t^*$, respectively.

As was found along the wake-induced path, the boundary layer between wakes is initially laminar downstream of the leading edge. However, because the turbulence intensity between

wakes is significantly lower as indicated by the superimposed distribution, the laminar region A extends further downstream. Through points 9, 9', and 10, random unsteadiness remains low, and skew is near zero. Along trajectory X, which corresponds to the blue lines in Figure 7.5, transition onset occurs near point 11 at $0.55s^*$, about seven percent surface length prior to maximum velocity. This marks the beginning of region E which identifies the region of transition between wakes. It correlates with the local maximum in turbulence intensity of 3.5% that occurs between rotor wakes. As will be shown in Section 7.6 and in Chapter 8, this is the turbulence signature of the Nozzle 1 wake segment which as yet has not mixed out completely.

Along trajectory X in region E, transition reaches its midpoint near point 12. Here, random unsteadiness has peaked, and skew has decreased through zero as indicated by the blue lines in Figure 7.5. From points 13 to 14, transition in Region E nears completion. Random unsteadiness (blue line of Figure 7.5a) decreases continually to the last measurement location prior to the trailing edge. Skew, after having reached a negative minimum at $0.82s^*$, increases back toward zero (Figure 7.5b).

A small region F is drawn on Figure 7.4 directly downstream of point 14. This is the region of turbulent flow between wakes. As the color contours of Figure 7.4 and the blue lines of Figure 7.5 indicate, this region is very short — at most about five percent surface length. Along trajectory X between wakes then, the boundary layer is non-turbulent for approximately 95 percent of the surface length for this high, takeoff Reynolds number condition.

7.3.1.3 Calming Regions

Two additional and very interesting regions also appear along the path between wakes in Figure 7.4. Labeled D and G, they are associated with regions of calmed flow. As described in Appendix A, calmed regions form behind convecting turbulent spots. Through these regions, wall shear stress decays asymptotically from a turbulent level at the trailing boundary of a turbulent spot to the laminar level of the background flow.

Calmed region D occurs behind the turbulent spots formed in the wake-induced transitional strip B. The decaying wall shear stress extends into laminar region A. The trailing boundary of the region D in Figure 7.4 is drawn at a speed of $0.3V_\infty$. This was determined from instantaneous time traces.

In anticipation of results presented later in this chapter, it is worth noting that for this particular test case, calmed region D does not extend far into the laminar region A. This likely results for two reasons. The first is related to the inlet turbulence distribution. Between wakes, the highest turbulence occurs, in a temporal sense, soon after that from the rotor wake. Consequently, transition between wakes is initiated in the same proximity as region D. Turbulent spots formed near point 11 will overtake and engulf quickly much of the calmed flow. In addition, as shown in Figure 17a of Halstead et al. (1995), turbulent spots can form on occasion in regions of calmed flow provided the background disturbance is of sufficient amplitude.

A second reason that region D lacks prominence is related to the reduced frequency. Defined in Section 6.1.3 as

$$k = \frac{f_{bp} s_{tot}}{V_{ex}} = \frac{\tau_{conv}}{\tau_{bp}}$$

reduced frequency is simply the ratio of convective to periodic time scales. The time scale, τ_{conv} , is a measure of the residence time of a fluid particle convecting along the suction surface. For the normalized s - t diagrams in Figure 7.4, the residence time is approximately equal to the time-period between successive wakes — in other words, $k \approx 1$. For higher values of reduced frequency, fluid particles move through the bladerow more slowly. That is to say, the slopes of the trajectories will be inclined more from horizontal in s - t space. In a normalized sense, then, the regions have more time to grow.

Region G in Figure 7.4 also is characterized by calming effects and possesses rather unique characteristics. To describe region G, we consider the flow development along trajectory Y where the turbulence intensity of the incoming flow is at its lowest level. From points 15 and

16, random unsteadiness increases gradually. At $0.70s^*$ however, the line plots in Figure 7.5a reveal significantly lower RMS along trajectory Y (green) than along W (red) and X (blue). At $0.83s^*$ near point 17, the random unsteadiness along Y reaches a peak, and skew has decreased from a positive maximum to a value near zero. Just prior to the trailing edge, the green line plots indicate a decreasing level of random unsteadiness and a decreasing level of negative skew. Taken together, the distributions of random unsteadiness and skew from points 16 to 18 are indicative of transition, albeit more protracted than what was found along trajectories W and X.

It is important to remember that the contour plots of Figure 7.4 and line plots of Figure 7.5 provide only an “average” picture of the boundary layer development. With this in mind, we will see shortly from the instantaneous traces that region G is composed of calmed, non-turbulent flow extending to the trailing edge for some wake-passing events while for others it is more turbulent in nature. On *average* then, we find the picture as suggested in Figures 7.4 and 7.5.

7.3.1.4 Instantaneous Time Traces

We will now consider a set of instantaneous traces that were used in part to discern aspects of boundary layer development. These traces proved very useful for the study of individual flow features such as turbulent spots and calmed regions (i.e., instantaneous events). Such insight can not be gained from ensemble-averaged data alone.

Instantaneous time traces of instantaneous, quasi wall shear stress are given in Figure 7.6 for test point 6B. This grouping represents one out of the 400 that make up the complete ensemble. Twenty-four of the 31 sensors were operated simultaneously allowing individual events to be tracked along the surface. The sensor locations are indicated along the right-hand side of the figure. The traces are presented in an AC-coupled format, determined using Equation 6.16, and extend for five wake-passing periods. Trajectories W, shown in red, are drawn for successive wake-passing periods and are identified with numerical subscripts. Areas of importance

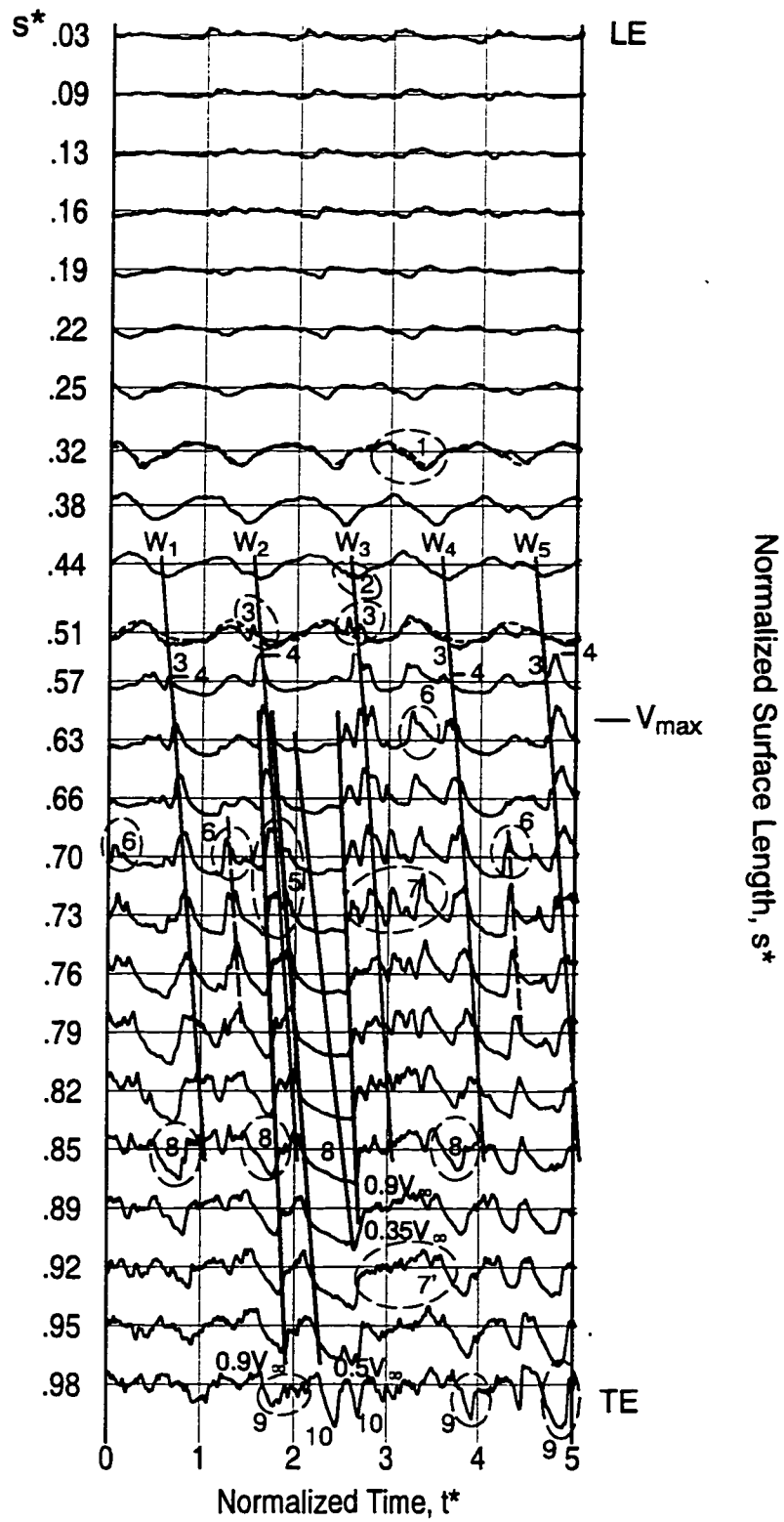


Figure 7.6. Instantaneous time traces of quasi wall shear stress along suction surface of Nozzle 2, test point 6B

are encircled and identified by number. Discussion of these traces is given in conjunction with the regions of boundary layer development identified above.

The first nine time traces downstream of the leading edge pertain to the perturbed laminar region A of Figure 7.4. Near the leading edge, an example being the trace at $0.09s^*$, the fluctuations in wall shear stress remain low in amplitude. This is indicative of a thin, low Reynolds number boundary layer responding to the background turbulence. From the fifth time trace at $0.19s^*$ to the ninth at $0.38s^*$, the amplitude of wall shear variation increases markedly. For comparison, the ensemble average is superimposed as a dashed line at $0.32s^*$. The close agreement between the two indicates that the variations are strongly periodic and not random in nature. Such periodic variation, a specific example being the encircled area 1, is associated with the jet-wake effect as will be described later in this section.

The earliest evidence of transition onset in this set of time traces occurs along the wake trajectories W, coinciding with the wake-induced transitional strip B. At $0.51s^*$ and $0.57s^*$, we find distinct spikes in wall shear stress indicated by areas 3. These spikes signify the passing of turbulent spots over the sensors as wall shear stress switches abruptly from laminar to turbulent levels. From the ensemble-averaged distribution superimposed at $0.51s^*$, it is evident that transition onset along the wake-induced path is initiated near the trough of the periodically-varying wall shear. The streamwise convection of the turbulent spots, on average, follows the W trajectories which are drawn for a convective velocity of $0.7V_\infty$.

Along trajectory W_3 , we find that the turbulent events at $0.51s^*$ are preceded by low-amplitude, discrete oscillations at $0.44s^*$ (area 2). The frequency of these oscillations corresponds approximately to that of a Tollmien-Schlichting instability wave as determined using the method of Walker (1989). Interrogation of numerous additional sets of traces from this ensemble indicates further presence of such oscillations though they occur infrequently. Far more likely is the direct appearance of turbulent spots in a manner consistent with bypass transition.

Along trajectories W_1 – W_4 , the turbulent events occur very much in phase with wake passing. For W_5 however, the spot lags by about 15 percent of blade–passing period. Similar observations were made from other sets of traces. Hence, it is apparent that the width of the transitional strip B of Figure 7.4 is due in part to the variation in time period between successive wake–induced spots as well as to the finite width of the spots themselves.

It is worth noting that for a given time trace, the heights of the spikes in wall shear vary considerably from event to event along the W trajectories. Examples are indicated by the numbers 4 at $0.57s^*$. Halstead et al. (1995) employed a spanwise array of surface hot–films to show that this difference is attributed to the spanwise variation in the formation and development of turbulent spots. Recall that from overhead, spots are approximately triangular in shape and grow in a self–similar fashion as they convect downstream. Because newly–created spots are small in size, it is likely they will cover only a portion of a given surface hot–film sensor as they move over it. The anemometer output from an individual sensor, however, is simply an average of what occurs across the entire sensor. This will produce the different levels of shear stress that are especially evident at the beginning of transition.

Further evidence of this spanwise development is seen from area 5. Along W_2 at $0.7s^*$, a second turbulent event with a lower peak value appears behind the initial spot that first appeared at $0.51s^*$. By $0.73s^*$, the peak levels of both spots are similar in magnitude. The second spot likely formed at a different spanwise location and/or streamwise location. It then spread laterally such that it covered a portion of the sensor at $0.70s^*$ and much of the sensor at $0.73s^*$. A similar interaction of multiple, wake–induced spots is visible along W_3 from $0.51s^*$ to $0.63s^*$.

Along W_2 , the wake–induced turbulent event clearly exhibits the growth and convective characteristics of a conventional turbulent spot. Its leading and trailing boundaries are indicated by the blue lines which correspond to convective velocities of 0.9 and $0.5 V_\infty$, respectively. The gradual decay of shear stress that characterizes the calmed region is observed behind the W_2 event. The trailing boundary of this calmed region is approximated by the green line. It is drawn

for $0.35V_{\infty}$ as determined from the traces. A third blue line, commencing at $0.63s^*$, delineates the leading boundary of the next turbulent event following *behind* that of W_2 . Because of the difference in convective velocities, the trailing spot (along W_3) closes on the W_2 spot ahead of it. By about $0.85s^*$, the calm region extends completely across the between-wake region to the leading boundary of the W_3 turbulent event. It follows from these propagation characteristics of turbulent spots that the non-turbulent flow eventually is consumed.

Evidence of the onset of transition between wake-influenced regions is indicated by areas 6. Consistent with Figure 7.4, the earliest evidence of transition occurs just prior to maximum velocity. The average convection velocity of two of these events occurring between wakes is noted from the trajectories drawn at $0.7V_{\infty}$. Interestingly, by $0.73s^*$, discrimination between wake and non-wake induced turbulent spots is virtually impossible. From here to the trailing edge, the spots grow and merge together, an example being areas 7 and 7'.

The last 20 percent of the nozzle suction surface is characterized by intermixed regions of turbulent and calmed flow. At $0.85s^*$, a number of the latter regions are identified as areas 8. In all cases, the shear stress in the calmed regions is still decreasing up to the leading boundary of the following turbulent event. As a result of this elevation in wall shear, these regions of non-turbulent, calmed flow can persist in the adverse pressure gradient all the way to the trailing edge without incurring separation.

At $0.98s^*$, three calmed regions are identified as areas 9. These are significant as they coincide with the calmed region G of Figure 7.4a. Examination of other groups of traces also reveals this phase-wise biasing. As indicated by areas 10, some non-turbulent regions did occur between regions G, albeit in a more random fashion. In a time-averaged sense then, the boundary layer at the trailing edge for this high, takeoff Reynolds number case is still transitional in nature.

The results presented thus far constitute much of the basis from which the features of boundary layer development were determined. For the balance of the discussion of this test case,

additional data are presented that further substantiate the picture described above and provide additional insight into the transition process.

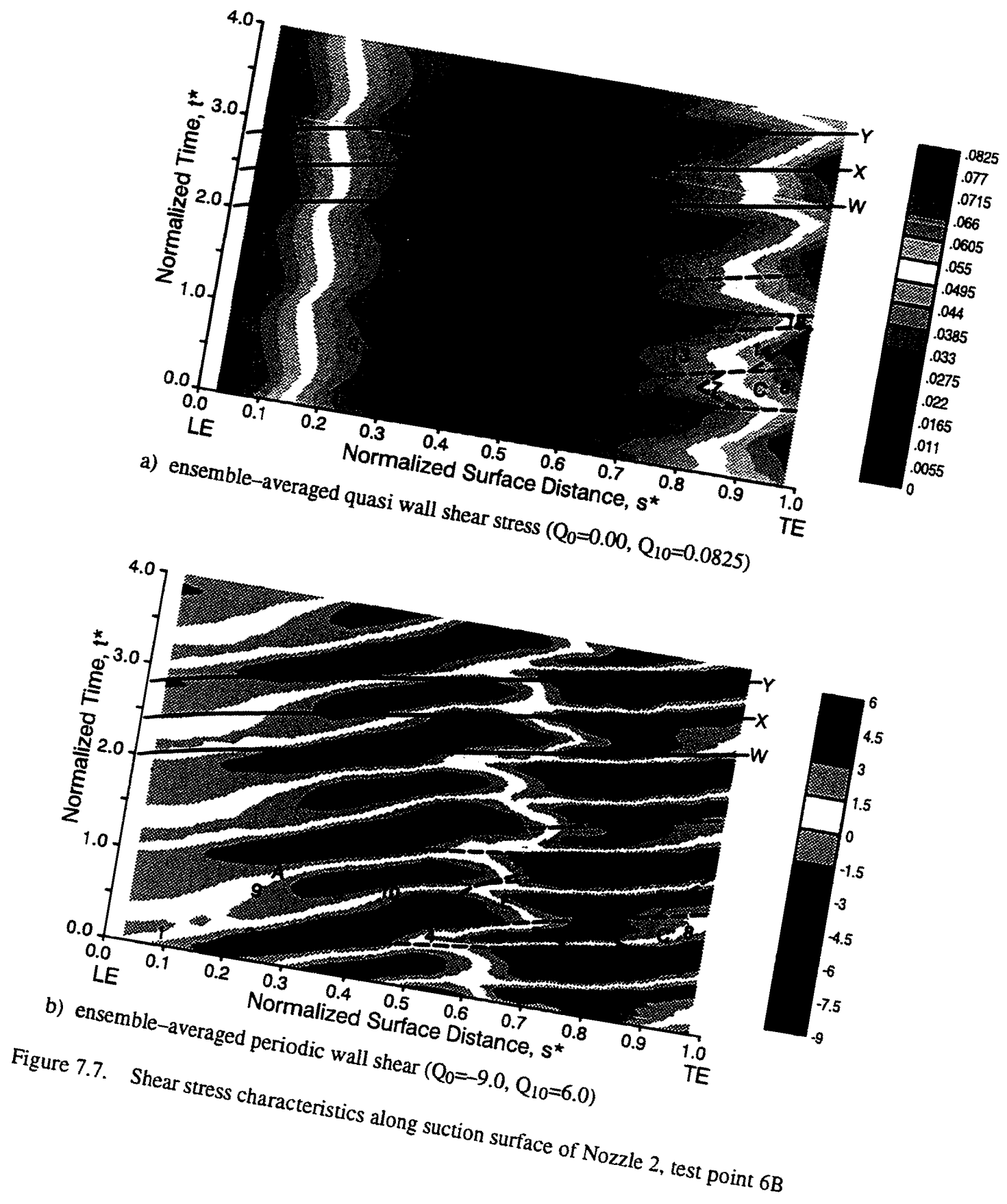
7.3.1.5 Mean Quasi Wall Shear and Periodic Unsteadiness

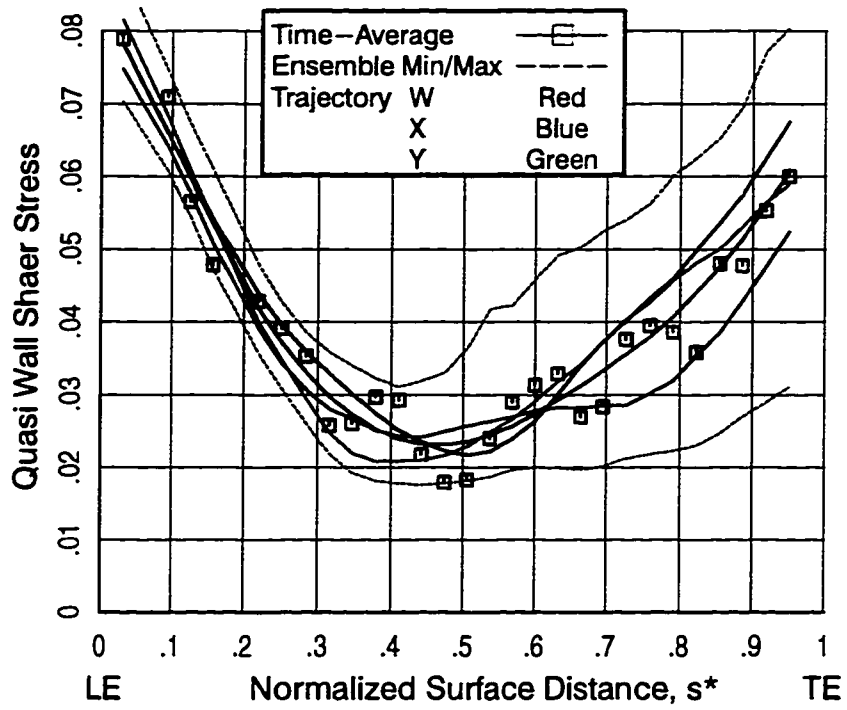
Space–time diagrams of quasi wall shear stress and periodic unsteadiness are given in parts a and b of Figure 7.7. The ensemble–averaged distributions used to construct the contours were calculated using Equations 6.3 and 6.5. The abscissa and ordinate of each plot is identical to that of Figure 7.4. To facilitate interpretation, the regions of boundary layer development and points of interest introduced in Figure 7.4 are overlaid onto these contours. For Figure 7.7a, fifteen color contours are employed as identified with the color legend.

In Figure 7.7c, line plots of $q\tau_w$ along the nozzle suction surface are given. The symbols denote time–averaged values at each sensor location. The solid black line is a least–squares fit of those measurements. The dashed lines are a measure of the minimum and maximum values occurring in each ensemble, $q\tau_{w,ni}$, along the surface. The colored lines are distributions of $q\tau_w$ along trajectories W, X, and Y.

The overall variation of quasi wall shear stress along the nozzle suction surface is readily apparent from parts a and c of Figure 7.7. Shear stress initially decreases downstream of the leading edge, reaches a minimum in the vicinity of transition onset near mid–surface length, and then increases back to the trailing edge. Along the entire surface, the minimum values of wall shear (lower dashed line of part c) remain well above zero indicating that no flow separation occurs.

The s–t diagram in Figure 7.7b is a measure of the periodic variation of $q\tau_w$ about the time mean. Hence the red and blue contours indicate regions of high and low wall shear, respectively, relative to the mean. Near the leading edge then, we find the periodic unsteadiness to be, in a relative sense, low in amplitude. From points 2/9 to 3/9', periodicity increases significantly. From the dashed line in Figure 7.5a, we see that periodic unsteadiness reaches a local maximum here at 0.35s*. Note from Figure 7.7b that this periodicity develops in region A and hence is





c) time-averaged quasi wall shear stress

Figure 7.7. continued

indicative of an unsteady laminar boundary layer. It is *not* attributable to boundary layer transition. An example of an individual ensemble distribution from this region was presented in Figure 7.6 as the dashed line at $0.32s^*$. That these perturbations result from the jet-wake effect will be considered shortly.

In this region of increased periodicity, the maximum values of local wall shear occur from 9–9'–15 along the non-wake induced path while a trough of minimum $q\tau_w$ develops from points 2 to 3. It is precisely in this trough at point 3 that the onset of wake-induced transition is observed.

Because the onset of transition occurs at different streamwise locations along the wake and non-wake paths, the unsteady variation of $q\tau_w$ changes in an interesting but predictable fashion further downstream. Along the wake-induced path from points 3 to 6, the wall shear stress in region B increases in a manner reflective of transition from laminar to turbulent boundary layer flow. This is evident in both parts a and b of Figure 7.7 but especially for the latter as we see the color contours change from blue at point 3 to red at point 6. It is noteworthy that at $0.52s^*$, the wall shear associated with the transitional boundary layer at point 4 is still less than that of the laminar boundary layer at point 15. Downstream of transition onset along trajectory X, we again observe a continual rise in wall shear from points 11 to 13 as flow in region E undergoes transition. Because transition along trajectories W and X takes place earlier than along Y, a distinct phase reversal in periodic wall shear occurs near $0.6s^*$. From the contour plot in Figure 7.7b, we see that the wall shear of transitional boundary layers along points 5–6 and 12–13 has now risen above that which occurs along trajectory Y. In fact, from about $0.65s^*$ back to the trailing edge, a trough in local wall shear now occurs along Y and coincides with region G. In Figure 7.7c, this phase reversal also is evident near $0.6s^*$ where the red and blue lines cross over the green.

In light of these findings, it should be noted that other researchers (e.g., Hodson, Huntsman, and Steele, 1994, and Schroder, 1991) have observed similar phase reversals in wall shear

stress along LP turbine blading. In both cases, it was attributed to separated–flow transition that was claimed to occur in conjunction with a laminar separation bubble. Clearly, the results in Figure 7.7 show that such a phase reversal is not a sufficient condition to conclude that separation has taken place. Rather, whether boundary layer transition takes place in an attached or separated mode, the phase change simply reflects the periodicity in boundary layer development that is driven by passing wakes.

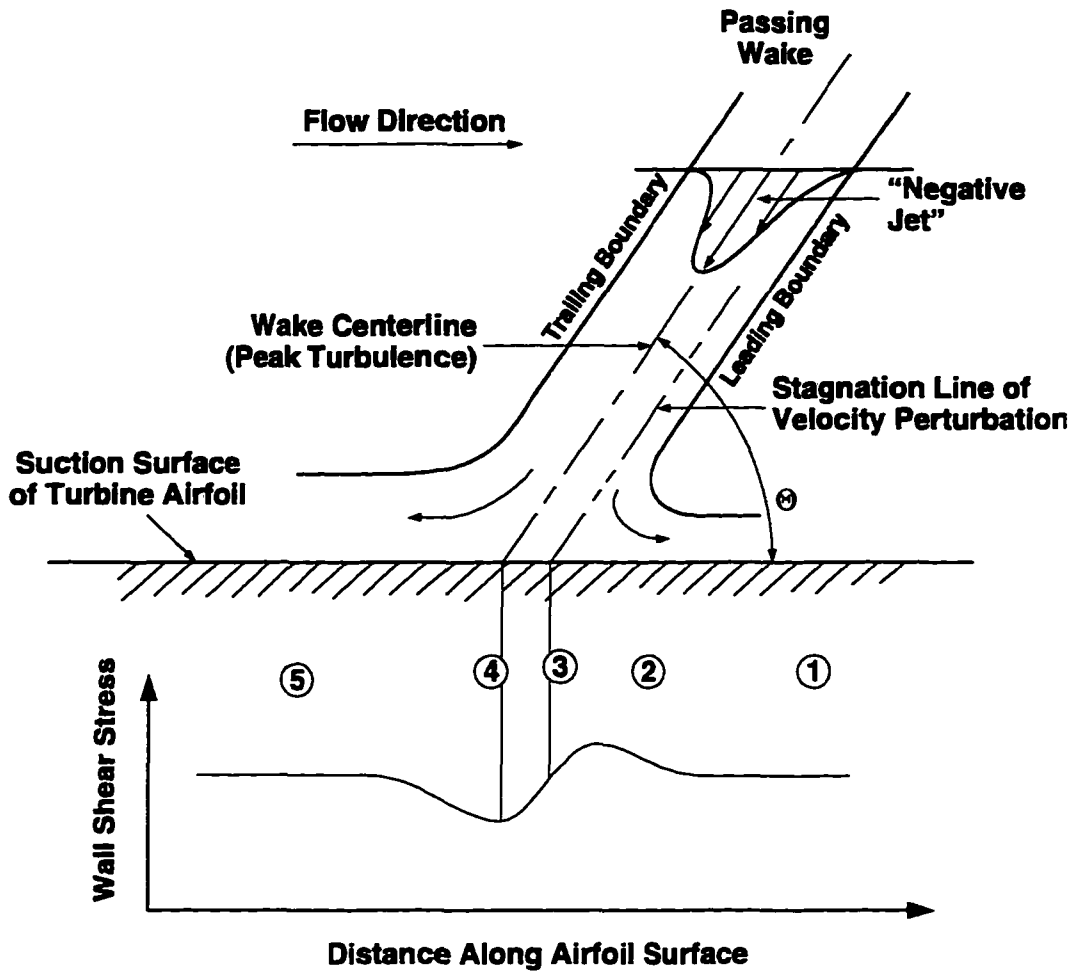
One final point with regard to Figures 7.7b and c is noteworthy. It is evident that along trajectory X from points 13 to 14+, the local wall shear has increased in level above that found along the wake–induced path from points 7 to 8. This is a consequence of the boundary layer along W being transitional and turbulent earlier along the airfoil surface. Hence it is closer to a fully mature turbulent state where shear stress will again decrease with surface length.

To summarize then, the contour plots of $q\tau_w$ and the periodic variation of $q\tau_w$ show significant complexity of the developing boundary layer. While useful in discerning features of this development, these contours by themselves are not adequate to discern the distinct regions of boundary layer development. Only when interpreted in conjunction with random unsteadiness and skew is a consistent picture formed.

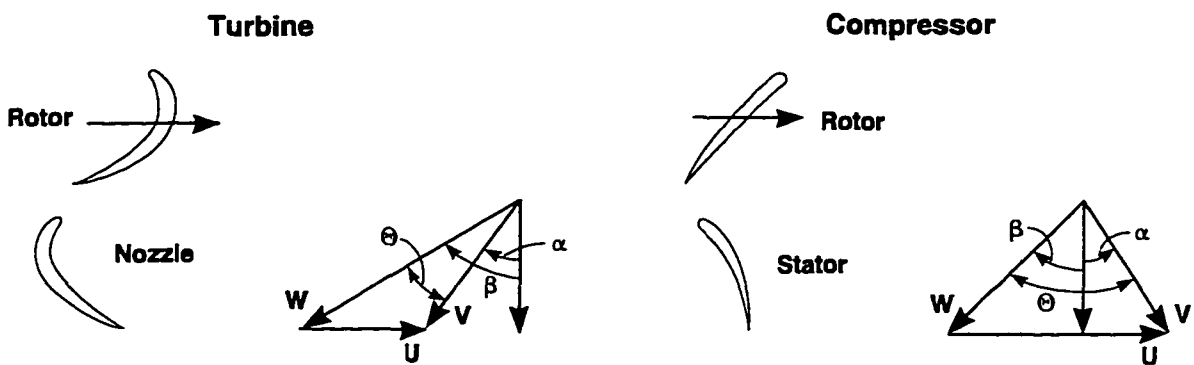
7.3.1.6 Boundary Layer Development and the Jet–Wake Effect

As described in conjunction with Figure 7.7b, significant periodic variation in wall shear stress was observed in laminar region A prior to the onset of boundary layer transition. This periodicity is attributed to the so–called jet–wake effect. The early analytic investigation of Meyer (1958) showed that interaction of a wake with the downstream airfoil brings about a migration of wake fluid relative to the airfoil surface. This migration, termed the jet–wake effect, is in the direction of the wake deficit. For a turbine, the result is a convection of wake fluid toward the suction surface as illustrated in Figure 7.8.

For the schematic in Figure 7.8, flow along the airfoil is from left to right. The center line of the wake is identified. Traveling with the wake, one would observe that the effect of the



a) interaction of wake with airfoil surface



b) vector diagrams for a turbine and compressor

Figure 7.8. The jet-wake effect along the suction surface of a turbine airfoil

wake deficit is to produce a “negative jet” which transports fluid in the direction toward the suction surface as indicated. This fluid accumulates along the suction surface and is pushed in upstream and downstream directions. In the reference frame of the airfoil then, this flow perturbation produces a local flow acceleration at the leading boundary of the wake and a deceleration at the trailing boundary.

The nature of jet–wake interaction is influenced by the angle made between the wake center line and airfoil surface. As shown by the vector diagrams in Figure 7.8b, this angle, Θ , is equal approximately to the difference between the absolute and relative flow directions (α and β , respectively). For conventional LP turbines, Θ is much less than 90° , and for this turbine was equal to about 20° . In comparison the vector diagram for a compressor shows that Θ nominally is equal to 90° . Consequently, in a compressor the downstream bladerow slices directly through the wake, whereas in an LP turbine this action is much more skewed.

From Figure 7.8a, it is apparent that if the wake is perpendicular to the surface, the flow perturbation produced by the jet–wake effect will be nominally symmetric about the wake center line. In the case of this turbine, where Θ is much less than 90° , more fluid is directed upstream than downstream, as illustrated. Consequently, the stagnation line of the impinging flow does not coincide with, but instead leads, the wake center line.

The variation in shear stress at the wall that results from the jet–wake effect was identified earlier in conjunction with area 1 of Figure 7.6. In the lower portion of Figure 7.8a, it is redrawn schematically in spatial rather than temporal terms. The abscissa is distance along the airfoil surface. Far downstream of the wake, at point 1, the wall shear stress is equal to that of the undisturbed, developing boundary layer. At point 2, wall shear has increased since the perturbation flow moves in the same direction as the mean flow. This, in turn, increases the velocity gradient at the wall. Continuing upstream, wall shear reaches a peak and then decreases as one moves toward the stagnation point of the perturbation, located at point 3. Further upstream (e.g., point 4), wall shear has decreased to levels below that of the undisturbed boundary layer. This

results from the opposing directions of the mean and perturbation flows. Finally, far upstream of the wake, at point 5, wall shear stress is back to the level of the background, undisturbed boundary layer. A measurement of the perturbation velocity made just off the surface in the boundary layer would look similar to that shown for wall shear.

An important question to consider at this point is whether the velocity perturbation produced by the jet–wake effect influences the location of transition onset. From the studies of transition along a flat plate in oscillating, non–reversing flows, Obremski and Fejer (1967) found the onset of transition to be dependent on the non–steady Reynolds number

$$Re_{NS} = \frac{\Delta V L}{2\pi\nu} = \frac{\Delta V}{V} \frac{V^2}{2\pi f_{oscill}}$$

where L = length traveled by a fluid particle during one cycle of the imposed oscillation
 $= V/f_{oscill}$
 V = amplitude of oscillation
 f_{oscill} = frequency of oscillation

For non–steady Reynolds numbers of greater than about 26000, they found transition onset occurred periodically in time at the frequency of the freestream oscillation. The initial breakdowns in the boundary layer occurred in the trough of the velocity perturbations at a streamwise location significantly upstream of that for the equivalent steady flow. This mode of transition was termed “periodic.”

In oscillating flows with Re_{NS} less than 26000, transition onset was not related directly to the freestream disturbance. However, they did observe transition occurring somewhat earlier than for the steady flow case. Also, transition showed some biasing to the imposed oscillation. That is, turbulent breakdowns were more prevalent during some parts of the cycle and less during others. They termed this “aperiodic” transition.

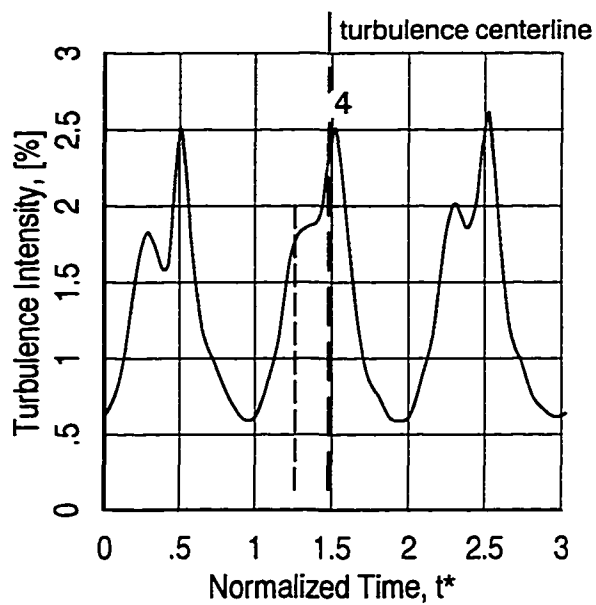
For flows in turbines, Addison and Hodson (1989) estimated Re_{NS} in terms of the velocity deficit, produced by the incoming wake, which occurs periodically at blade–passing frequency. It must be noted, however, that this application of Obremski and Fejer’s non–steady Re-

ynolds number is approximate. First, as pointed out by the above-mentioned authors, the velocity perturbation in a turbomachine convects with the flow, whereas for the experiments of Obremski and Fejer just described, the oscillation was a standing wave. Secondly, transition along a turbine airfoil occurs under the influence of a pressure gradient. Regarding the latter, the pressure gradients in the vicinity of transition onset for test case 6B are mild ($\lambda_\theta \leq 10.021$) and likely have only a second order effect on Re_{NS} .

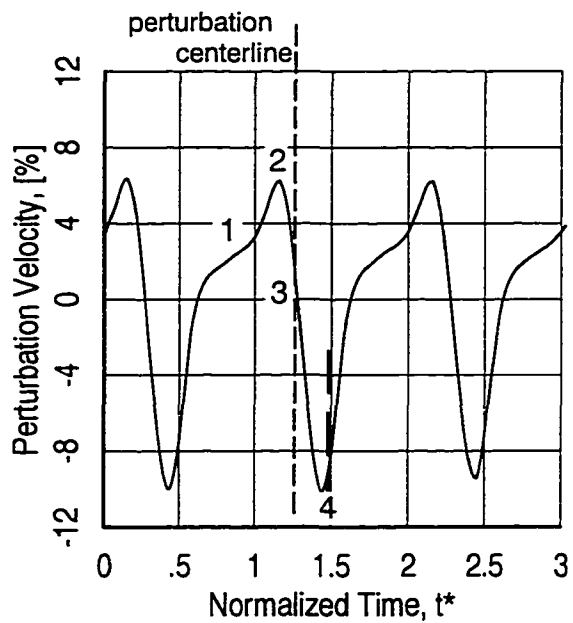
For test point 6B of the LSRT, the non-steady Reynolds number calculated as proposed by Addison and Hodson(1989) is less than 10000. This suggests the velocity perturbation played, at most, an indirect role regarding the location of transition onset. This at first appears to contradict surface hot-film data for this test point. In Figure 7.7b, the contours of periodic unsteadiness clearly show that the onset of wake-induced transition occurs in the trough of the shear stress perturbation. This is just what was observed by Obremski and Fejer (1967) for the case of periodic transition. However, in the turbine, the wake is also characterized by increased turbulence intensity with peak turbulence occurring in the vicinity of the wake center line. Because of the inclination of the wake to the airfoil surface for this turbine as shown in Figure 7.8, the wake center line (point 4), and hence peak turbulence, occur upstream of the stagnation line of the velocity perturbation, point 3. Consequently, the highest turbulence, which promotes earlier transition, coincides with the trough of the velocity/shear perturbation.

Measurements that confirm this phase-wise orientation of wake turbulence intensity and velocity perturbation were acquired as part of the Halstead et al. (1995) study. Results are shown in Figure 7.9. The measurements were made near the edge of the boundary layer at a streamwise location of $0.5s^*$ using a boundary layer hot-wire probe. Further details of the instrumentation are given in Halstead et al. (ibid.).

Included in Figure 7.9 are ensemble-averaged distributions of perturbation velocity and turbulence intensity. Perturbation velocity is reported as percent of the time mean. Both distributions are consistent with our previous discussion. In between wakes at point 1, turbulence



a) turbulence intensity



b) velocity perturbation, percent of time mean

Figure 7.9. Variation of turbulence intensity and velocity at edge of boundary layer along nozzle suction surface, $0.5s^*$

intensity is lowest. A flow acceleration (point 2) then occurs as the leading boundary of the wake passes the probe. This is followed by a decrease in velocity through the stagnation point of the perturbation, designated point 3. At point 4, we find that the region of flow deceleration that occurs on the trailing side of the velocity perturbation coincides exactly with the wake center line, identified as peak turbulence in Figure 7.9a. Similar observations are reported in Funazaki (1996).

To summarize then, the value of non-steady Reynolds number for this test case suggests that the velocity perturbation caused by the jet-wake effect plays a secondary role in initiating transition. Rather, transition onset correlates closely with the time-varying turbulence environment. Specifically, transition along the wake-induced path occurs earliest owing to the higher wake turbulence intensity. Because the wake is inclined with the airfoil surface as it moves through the bladerow, the peak turbulence, marking the wake center line, lags behind the velocity/shear stress perturbation.

7.3.1.7 Frequency-Averaged Spectra

Lastly, we consider the normalized RMS spectra of the surface hot-film measurements. This is given as a contour plot in Figure 7.10. As with the previous contour plots, the abscissa is equal to normalized distance, s^* , along the nozzle suction surface. The ordinate is frequency normalized by that of blade-passing, f_{bp} . Consequently, components of periodic unsteadiness appear in Figure 7.10 as horizontal lines at integer multiples of f^* . The color contours are that of normalized, root mean square spectral density, given in decibels, as determined using Equation 6.17.

The variation in spectral density is consistent with the previously-described nature of the boundary layer. From near the leading edge at area 1 to about $0.3s^*$ (area 2), the energy associated with random unsteadiness reduces in amplitude. As noted previously, this is due to the thickening laminar boundary layer being less influenced by the freestream disturbance environment. Near $0.35s^*$ at point 3, the energy content at blade-passing frequency ($f^*=1$) reaches

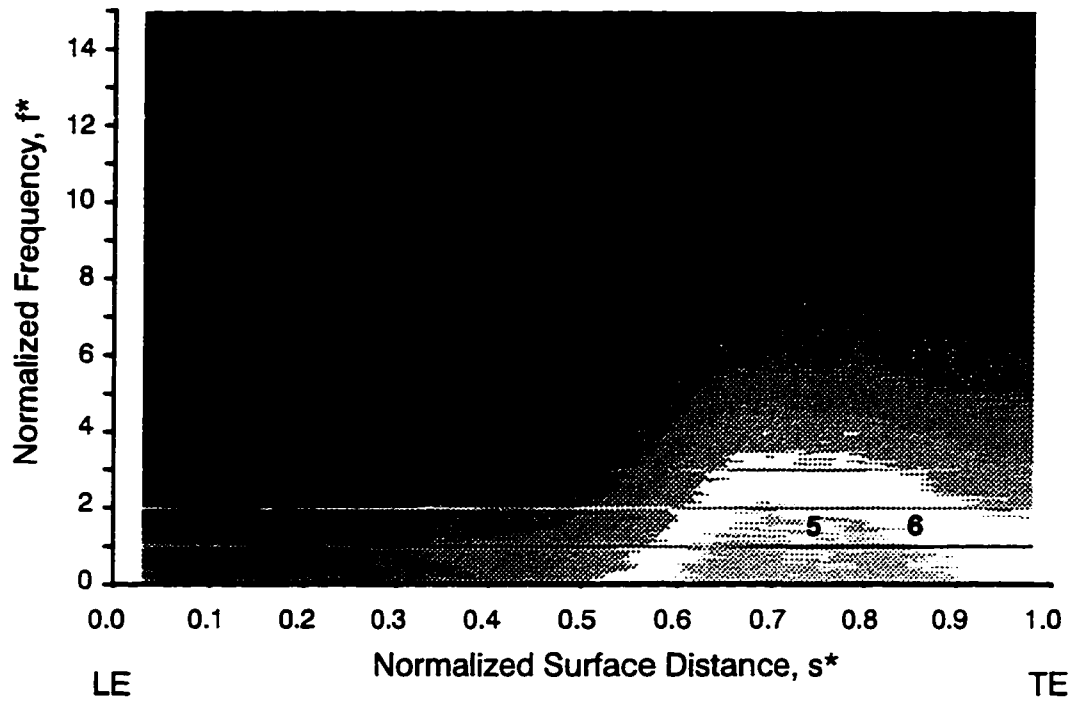


Figure 7.10. Frequency-averaged spectra of hot-film sensor output along suction surface of Nozzle 2, test point 6B, ($Q_0=-95$, $Q_{15}=-50$)

a local maximum. This coincides with the large, periodic variations in wall shear observed in Figures 7.7b and attributed to the jet–wake effect.

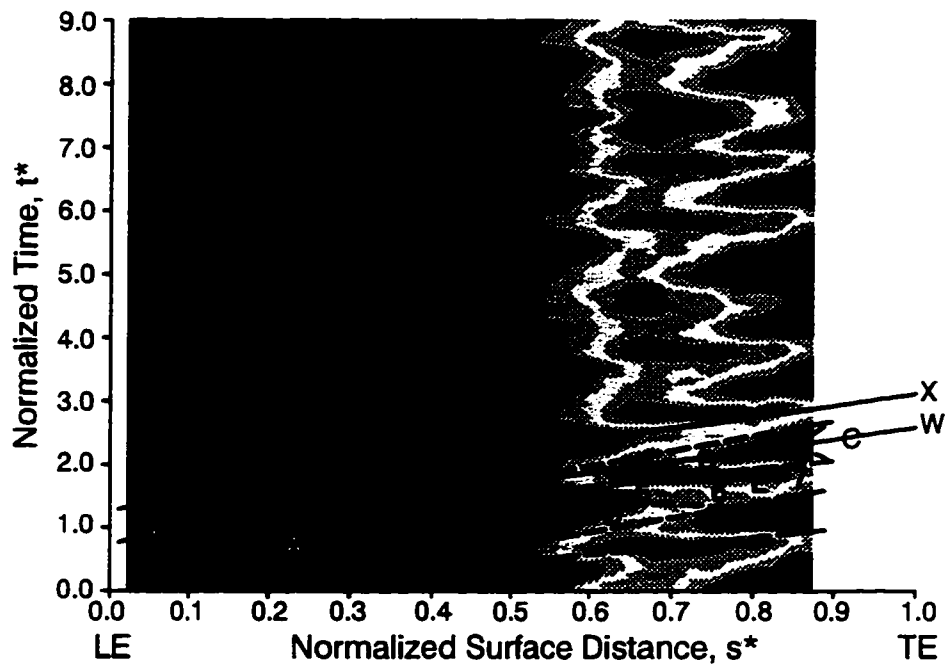
Downstream of wake–induced transition onset, the energy of random unsteadiness increases in amplitude and extends into higher frequencies (area 4). The peak integrated energy across the frequency domain occurs at $0.75s^*$, area 5. This is consistent with the time–averaged midpoint of transition as noted previously from the square symbols in Figure 7.5a. As transition nears completion (area 6), the random energy of especially the lower frequencies decrease in amplitude. This reflects the gradual diminishing of switching in wall shear between laminar and turbulent levels as intermittency approaches one. At frequencies above about eight times blade–passing, the amplitude of the turbulent fluctuations continues to increase. Along the entire suction surface, the predominant periodic component of frequency occurs at blade–passing frequency.

Certainly, it is evident from this discussion that Figure 7.10 provides only an overall, averaged look at the distribution of energy. While this itself is informative, we can not, for example, discriminate the time–varying nature of the boundary layer development.

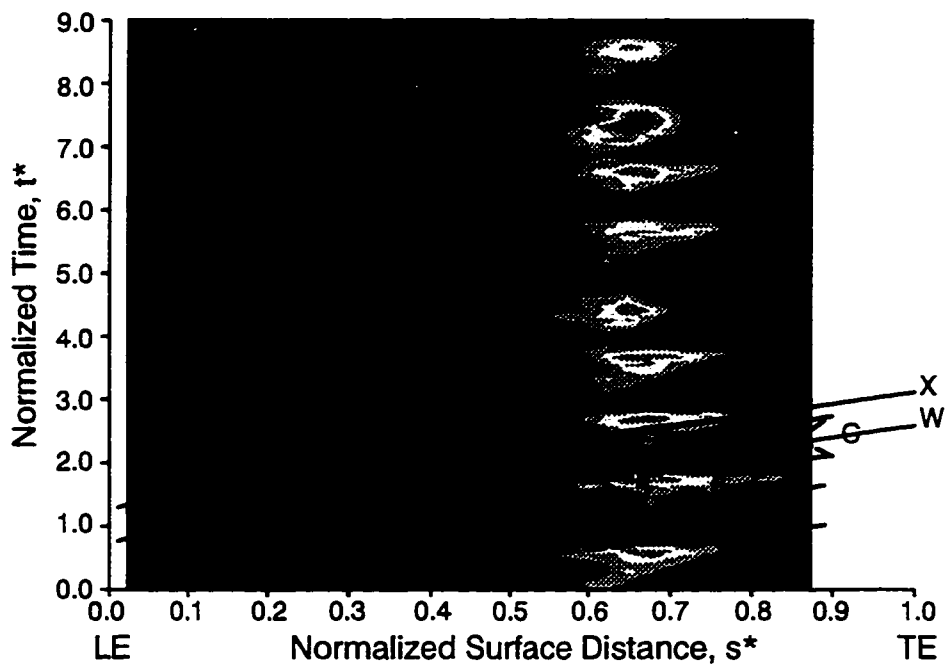
7.3.2 Rotor Suction Surface

We will now consider boundary layer development along the suction surface of Rotor 2 for the identical test point 6B. Measurements from the surface hot–film sensors are presented in Figures 7.11–15. For consistency, the figures are given in the identical sequential order as for the nozzle results of the previous section.

An important feature that will differentiate boundary development along Rotor 2 with that of Nozzle 2 relates to differences in the disturbance environment entering each bladerow. In the LSRT, the Nozzle 1 and 2 bladerows upstream of Rotor 2 have differing blade counts. In the rotor frame of reference then, the circumferential orientation of individual Nozzle 1 and 2 airfoils varies around the turbine. Because the wakes from Nozzle 1 are not mixed out by the inlet to Rotor 2 (direct evidence of this is presented in Chapter 8), the disturbance environment

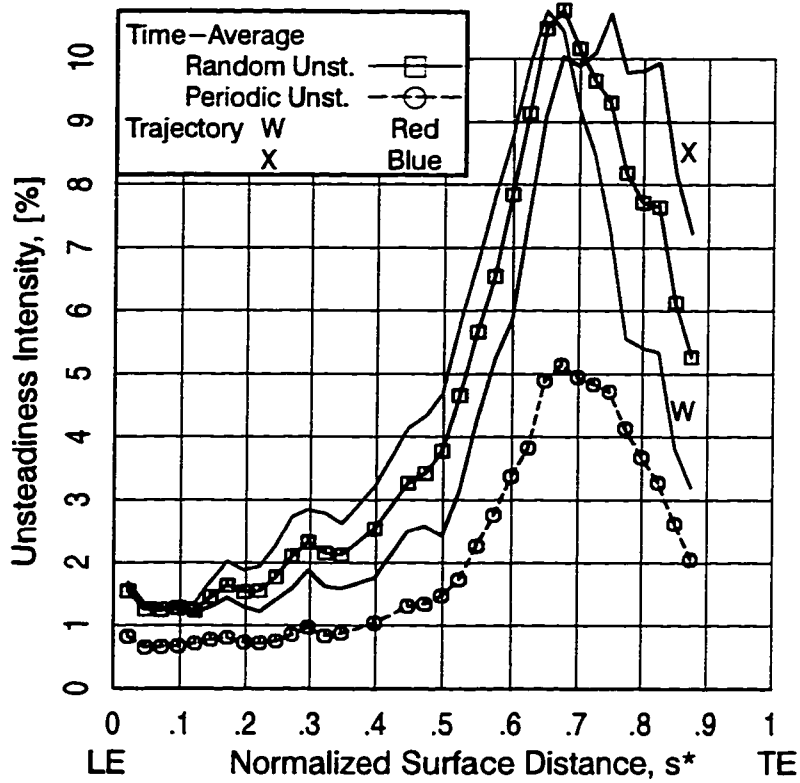


a) random unsteadiness ($Q_0=0.83$, $Q_{10}=13.23$)

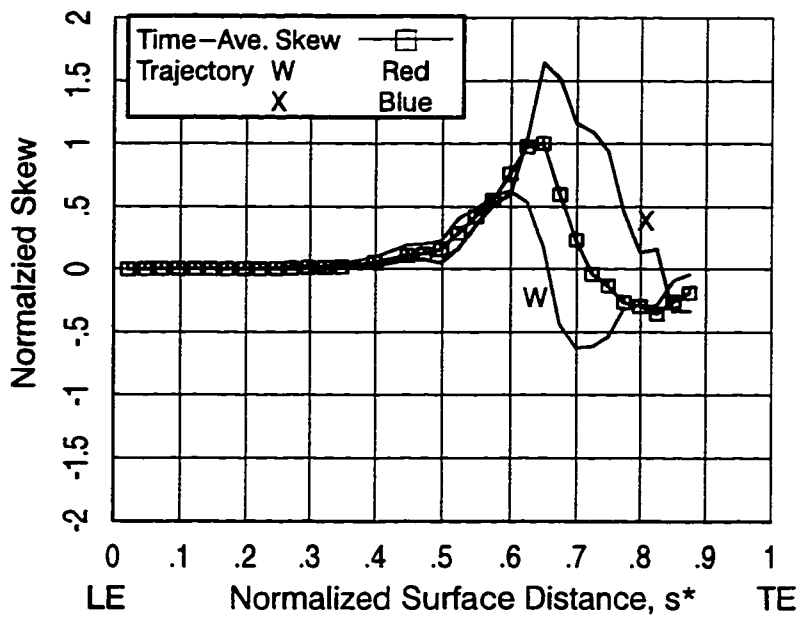


b) skew ($Q_0=-1.5$, $Q_{10}=3.5$)

Figure 7.11. Ensemble-averaged shear stress characteristics along suction surface of Rotor 2, test point 6B



a) random and periodic unsteadiness



b) skew

Figure 7.12. Time-averaged shear stress characteristics along suction surface of Rotor 2, test point 6B

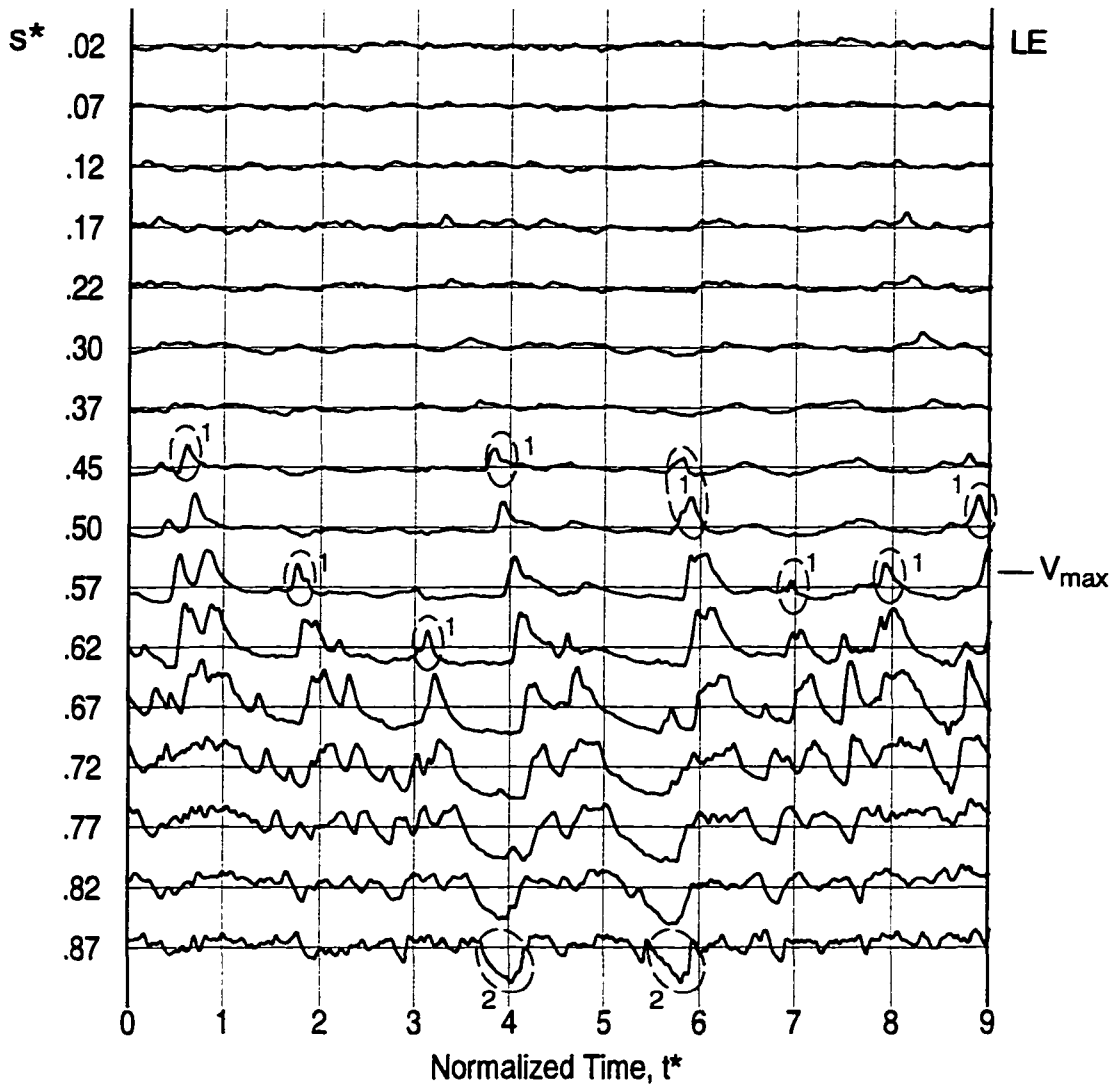
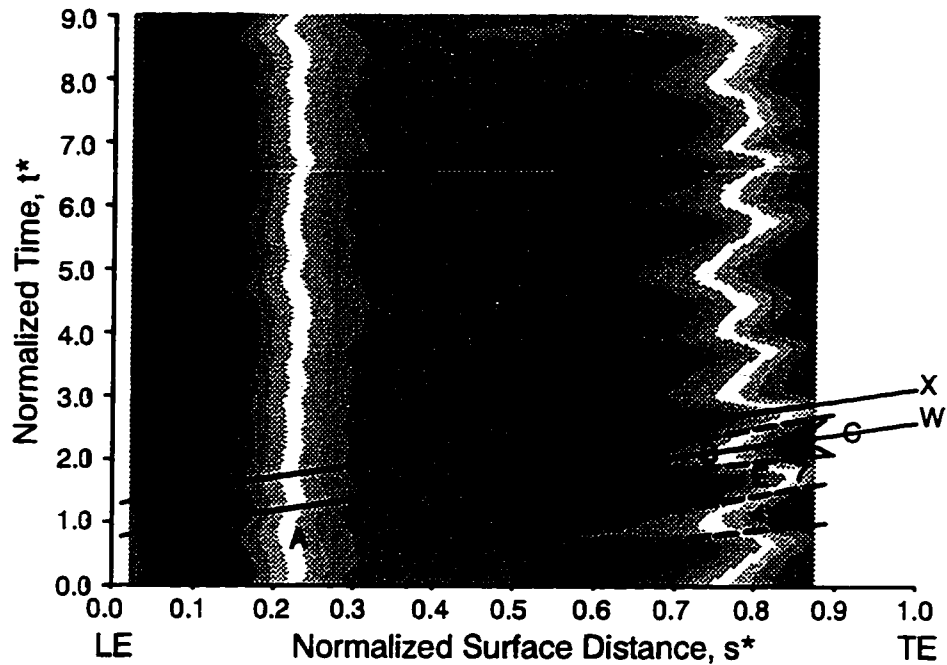
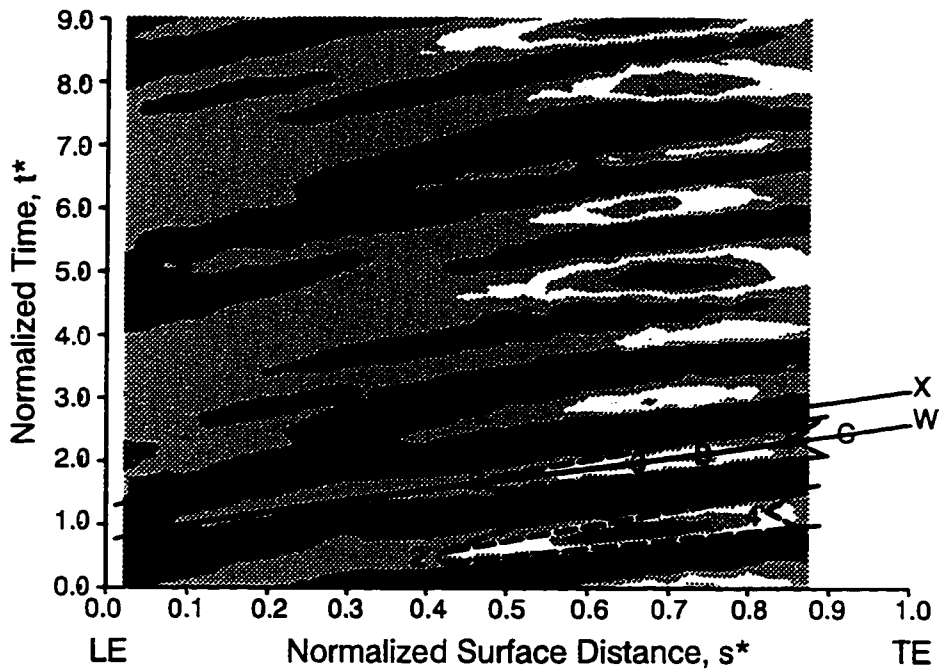


Figure 7.13. Instantaneous time traces of quasi wall shear stress along suction surface of Rotor 2, test point 6B

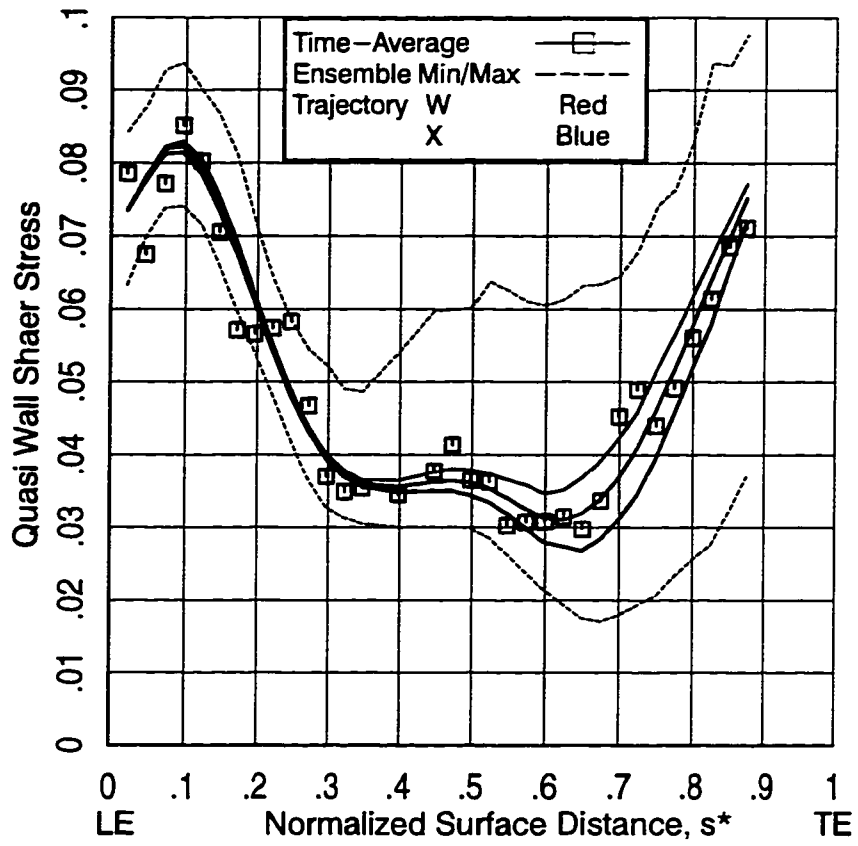


a) ensemble-averaged quasi wall shear ($Q_0=0.00$, $Q_{10}=0.0855$)



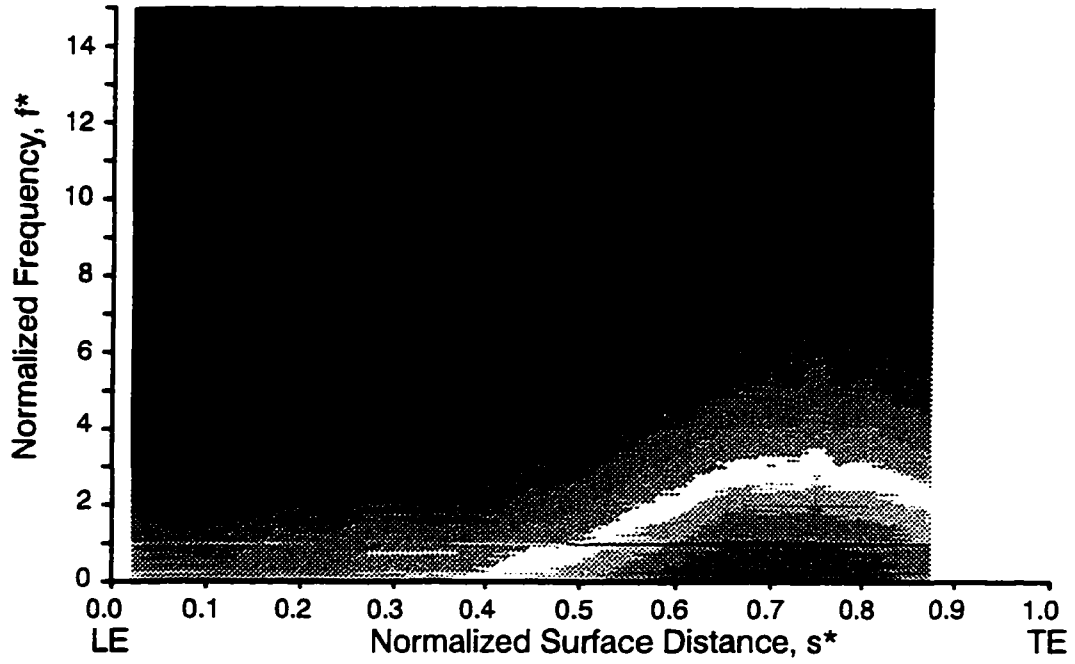
b) ensemble-averaged periodic wall shear ($Q_0=-11.0$, $Q_{10}=11.0$)

Figure 7.14. Shear stress characteristics along suction surface of Rotor 2, test point 6B



c) time-averaged quasi wall shear stress

Figure 7.14. continued



a) space-frequency diagram

Figure 7.15. Frequency-averaged spectra of hot-film sensor output along suction surface of Rotor 2, test point 6B, ($Q_0=-95$, $Q_{15}=-50$)

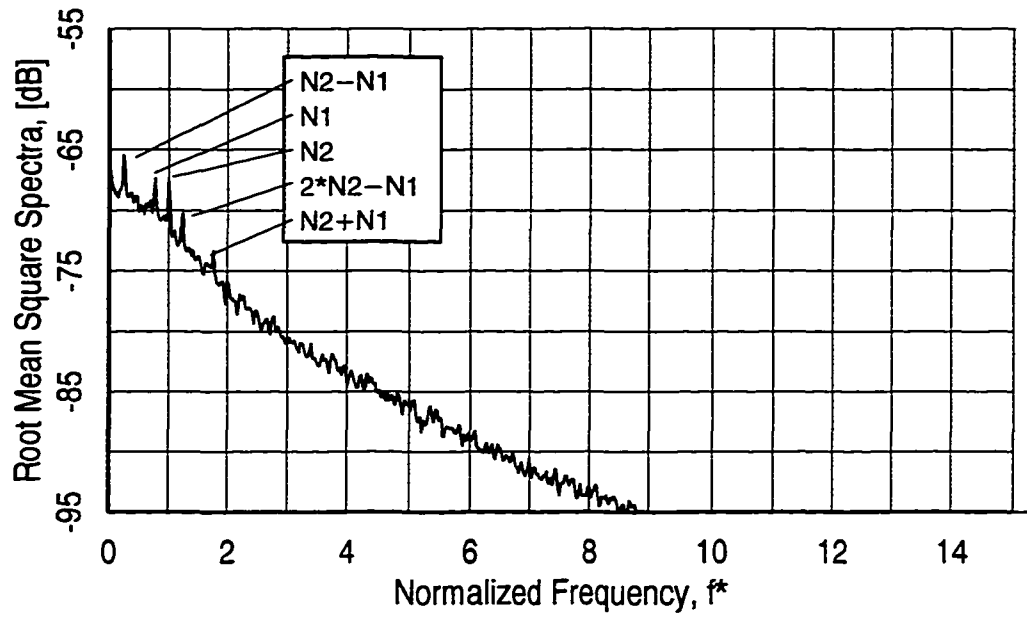
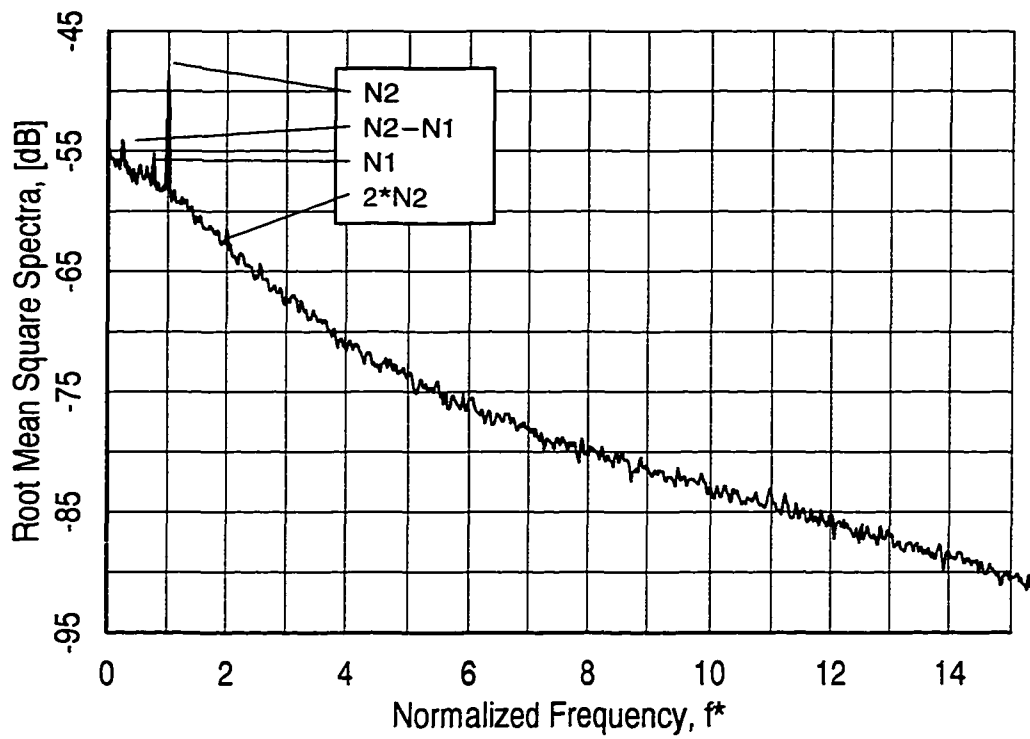
b) individual spectrum, $0.35s^*$ c) individual spectrum, $0.72s^*$

Figure 7.15. continued

entering Rotor 2 also will vary circumferentially. For the LSRT, the pattern of Nozzle 1/2 orientation is repeated every 4+ blade pitches of Nozzle 2. Hence, the s-t diagrams of these rotor measurements extend in time for nine blade passing periods of Nozzle 2 in order to show two of these cycles.

7.3.2.1 Wake and Non-Wake Paths

The basic picture of boundary layer development along the rotor is similar qualitatively to that seen along the nozzle with a few notable differences. In an overall sense, development is dominated by the presence of wake-induced and non-wake induced paths.

The s-t diagrams in Figure 7.11a reveal that, along the wake-induced path, the boundary layer is again laminar downstream of the leading edge. Along trajectory W, the laminar region A extends from points 1 to 2. The line plots in Figure 7.12 for W indicate low levels of random unsteadiness and near zero values of skew. The onset of wake-induced transition occurs at 0.48s* in a region of favorable pressure gradient just upstream of maximum velocity (Figure 7.2b). Consistent with the nozzle results, random unsteadiness increases and skew becomes positive downstream of transition onset. The peak in random unsteadiness and zero crossing of skew that identifies the midpoint of transition occurs at point 3. As transition along W nears completion at point 4, random unsteadiness decreases and skew, after attaining a negative minimum, increases back toward zero. The red line plots in Figure 7.12 indicate further that transition along W is nearly completed by the last sensor located at 0.88s*. Because the size of the hot-film array was dictated by the surface length of the rotor at the trunnion, it was not possible to place sensors closer to the trailing edge.

The path between wakes is shown in Figure 7.11 to consist of a calmed region D and transitional region E. As before, the calmed region develops behind the wake-induced region B. Unlike what we observed for the nozzle, this calmed region appears more effectively to suppress transition along trajectory X. This effectiveness, however, varies significantly from one wake-passing period to the next and likely is influenced by the circumferentially-varying disturbance

environment. Just downstream of region D demarcated in Figure 7.11, transition onset between wakes occurs first at point 5 where calming is weakest. Further aft, in region E, increased random unsteadiness signifying transition onset extends from point 5 to 6. In Figure 7.12, the line plots of random unsteadiness and skew along trajectory X indicate that transition has not been completed by the last sensor location at point 7.

7.3.2.2 Additional Observations

From the s - t diagram of random unsteadiness in Figure 7.11a, it is evident that the differing Nozzle 1 / Nozzle 2 blade counts produce a “beating” pattern in the development of the boundary layer. This is especially apparent along successive wake-induced paths where the locations of transition onset are seen to vary by about 10 percent surface distance (e.g., points 2, 2', and 2''). Likewise, the end of transition (e.g., points 4 and 4') are influenced as well. Whereas distinct regions of calming D occur behind the wake-induced strips such as 2 and 2', they are less prevalent or not apparent at all behind wake-induced paths such as the 2'' path. Additional evidence of beating is noted by considering the successive regions of high random unsteadiness (red contours). Tick marks have been placed at increments of blade-passing period corresponding to these regions in Figure 7.11a. Using this reference, we see that the periodic spacing, temporal width, and streamwise length vary from period to period.

The contour plot of random unsteadiness illustrates also an important point relating to the interpretation of these measurements. It is quite common to use such contours to infer convective velocities (i.e., trajectories in s - t space) of various features of boundary layer development (e.g., Hodson, Huntsman, and Steele, 1994, Schroder, 1991). In Figure 7.11a, the general shape of the red contour regions suggest a nearly infinite convective velocity. That is, for example, the boundary from points 5 to 7 is nearly horizontal. As noted in the above discussion, however, this characteristic was attributed to the fact that transition between wakes occurred first at a location just adjacent to the following wake-induced strip (i.e., point 5). Further aft, transition onset occurred along a line from 5 to 6 where the effects of calming were least. Hence, we see

that the *apparent* convection velocity inferred from the contours is simply a by-product of the averaging process. To determine convection velocities accurately then, one must analyze the instantaneous traces themselves.

7.3.2.3 Instantaneous Time Traces

A set of instantaneous time traces from along the rotor are given in Figure 7.13. In the rotating frame of reference, traces could be obtained simultaneously from 16 sensors. They are shown for nine blade-passing periods.

The traces from the leading edge to $0.37s^*$ are associated with the laminar region A. The first turbulent events occur along the wake-induced paths as identified by areas 1. The streamwise location at which the spots first appear varies significantly. Some are apparent as early as $0.45s^*$ while others do not appear until $0.62s^*$. This likely is due to two reasons. First, because transition onset occurs in a favorable pressure gradient, the production rate of turbulent spots will be lower than for along the nozzle where transition commenced in a region of local adverse pressure gradient (Gostelow, Blunden, and Walker, 1994). Consequently, a longer streamwise distance is required for spots formed at different spanwise locations to spread so that they pass over a sensor. Secondly, because of the Nozzle 1 / Nozzle 2 interaction, the disturbance environment (i.e., turbulence intensity and length scale) along successive wake-induced paths will differ. This in turn produces a variation in the streamwise location where transition begins.

By $0.67s^*$, significant regions of calmed flow are evident. In fact, it appears that no “conventional” laminar flow (i.e., regions of approximately constant wall shear following a calmed region) remains. Turbulent spots between wake-induced paths appear at various times in the blade-passing period. Such variability is expected given the differences observed in the contours of random unsteadiness that are attributed to the circumferentially-varying disturbance environment.

Consistent with Figures 7.11 and 7.12, transition is not completed at the last sensor given the occurrence of non-turbulent, calmed flow (e.g., areas 2).

7.3.2.4 Mean Quasi Wall Shear and Periodic Unsteadiness

As evident from Figures 7.14a and c, wall shear stress decreases downstream of the leading edge, reaches a minimum near the location of transition onset, and increases through the region of transition. A similar variation was noted for the nozzle. The minimum wall shear is again clearly greater than zero implying attached boundary layer flow.

From the s - t diagram of Figure 7.14b, we find only very low amplitude periodic unsteadiness in laminar region A prior to transition onset. This is further born out by considering the line plot of time-averaged periodic unsteadiness. For the nozzle result given in Figure 7.5a, a clear local peak occurs at $0.35s^*$ prior to boundary layer transition. No such peak prior to transition occurs along the rotor suction surface as evident from Figure 7.12a. This suggests, in contrast to what was observed along the nozzle, the jet-wake effect had no perceptible influence on the developing laminar boundary layer. The reason for this is not entirely clear at this time. The loading level of the nozzle and rotor airfoils are similar given that their respective Zweifel coefficients differ by less than 10 percent. The primary difference between Nozzle 2 and Rotor 2 in the LSRT is the disturbance environment entering each bladerow. Possibly the enhanced mixing that characterizes the flow entering Rotor 2 attenuates the jet-wake interaction. The centrifuging of the lower-momentum wake flow may play a role also.

In Figure 7.14b, the strongest variation in periodic unsteadiness is found downstream of transition onset. The highest levels of wall shear stress occur in region B where transition occurs earliest. In contrast, the lowest levels are found along the non-wake path where transition occurs latest. By the last sensor at $0.88s^*$, the amplitude of this periodic variation diminishes considerably as transition along both paths is near completion. Incidentally, in the region of transitional flow, the beat frequency corresponding to the difference in blade counts of Nozzle 1 and 2 is very apparent in Figure 7.14b. As mentioned previously, the time period of this beating is just over 4 times the blade-passing frequency of Nozzle 2.

7.3.2.5 Frequency–Averaged Spectra

Characteristics of the normalized RMS spectra of the hot–film measurements are provided by way of an s – f diagram in Figure 7.15a and individual spectra in Figures 7.15b–c. In an overall sense, the energy distribution of random unsteadiness in the s – f diagram varies in a manner similar to that noted for the nozzle. The energy level downstream of the leading edge and up to where transition begins is, in a relative sense, low in amplitude. After transition begins, energy shifts to higher frequencies. A peak in energy content occurs near $0.7s^*$ where transition is near its midpoint.

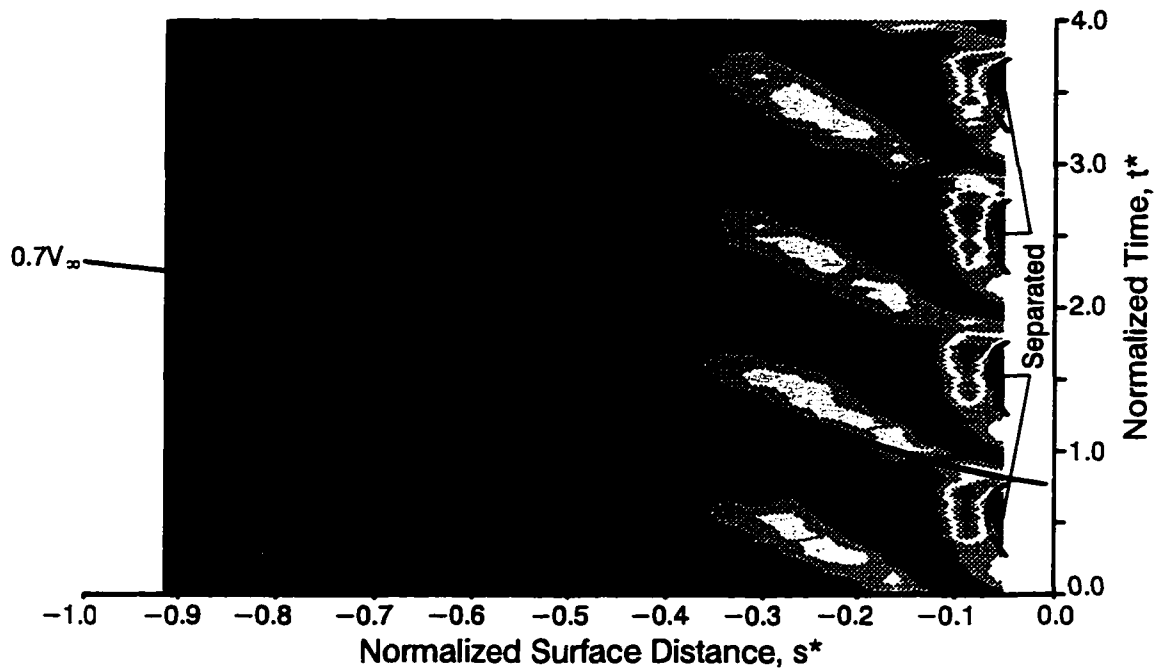
The individual spectra in parts b and c of Figure 7.15 provide direct evidence of the beating phenomenon. From the spectrum obtained at $0.35s^*$, five periodic components are identified. Interestingly, the component at the fundamental beat frequency (corresponding to the difference in Nozzle 1 / Nozzle 2 blade count) is highest in amplitude. Additionally, components corresponding to Nozzle 1 and Nozzle 2 blade passing are equal in amplitude.

The second spectrum, shown in part c, was obtained at $0.72s^*$ near the midpoint of transition. Here, the blade–passing frequency of Nozzle 2 is most prominent. Through the region of transition, then, periodicity of the boundary layer development is driven most strongly still by the upstream Nozzle 2. As noted, components at the fundamental beat frequency and Nozzle 1 blade passing are still present.

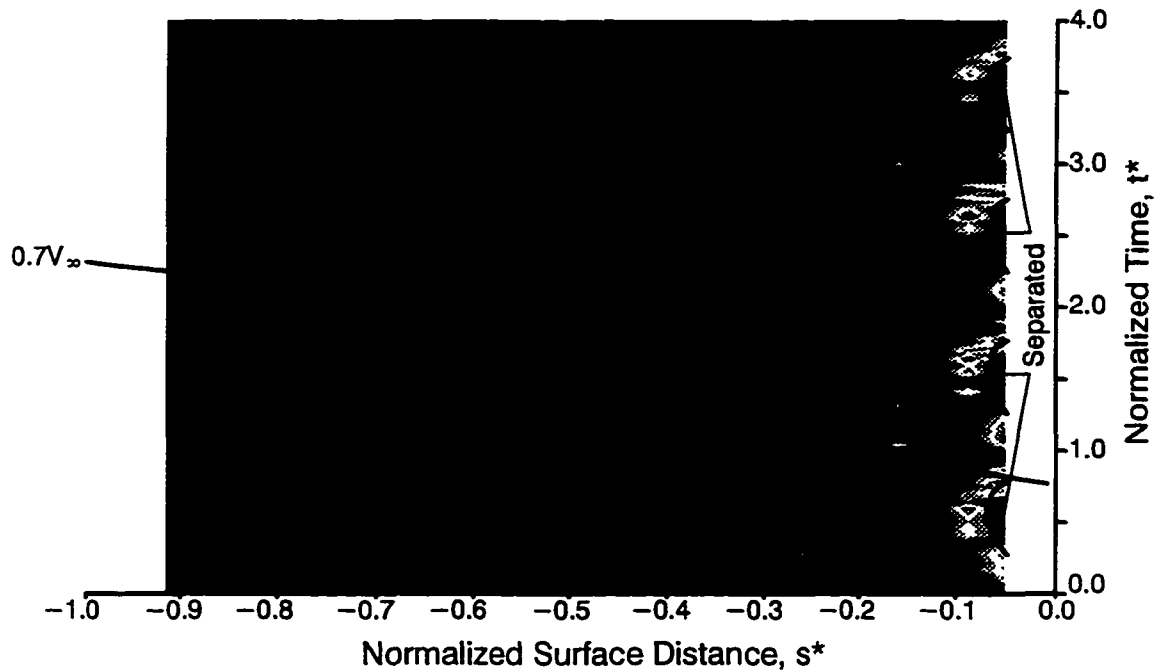
7.3.3 Nozzle Pressure Surface

Surface hot–film measurements from the pressure surface boundary layer along Nozzle 2 are given in Figures 7.16–20. The format of data presentation is identical to that employed in the previous sections. Rather than considering each group of figures in a sequential fashion as done above, particular flow features will be pointed out using the figures that most apply.

For the baseline test condition, boundary layer development along the pressure surface is influenced greatly by the presence of a leading–edge separation bubble. In the discussion be-

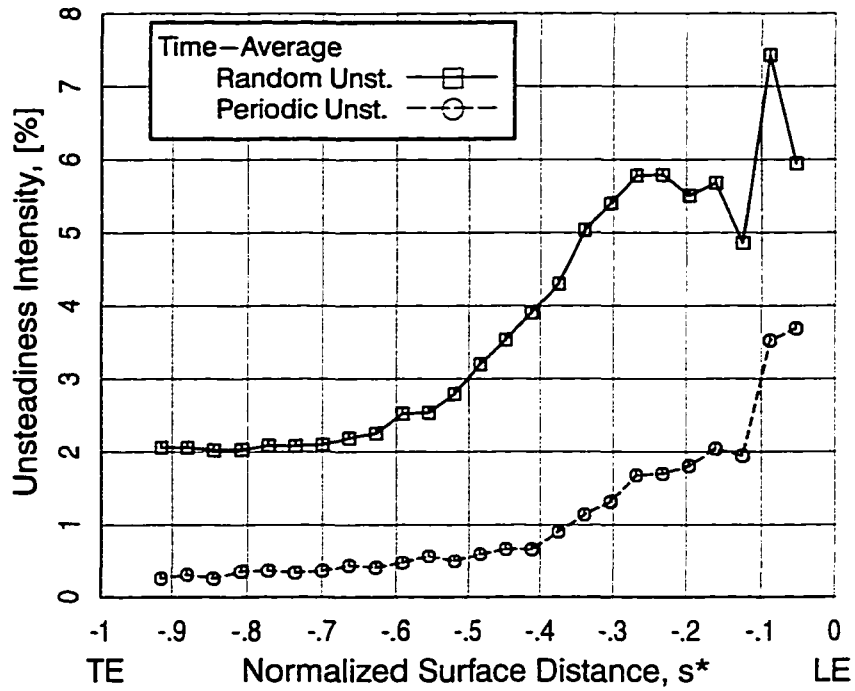


a) random unsteadiness ($Q_0=1.55, Q_{10}=10.35$)

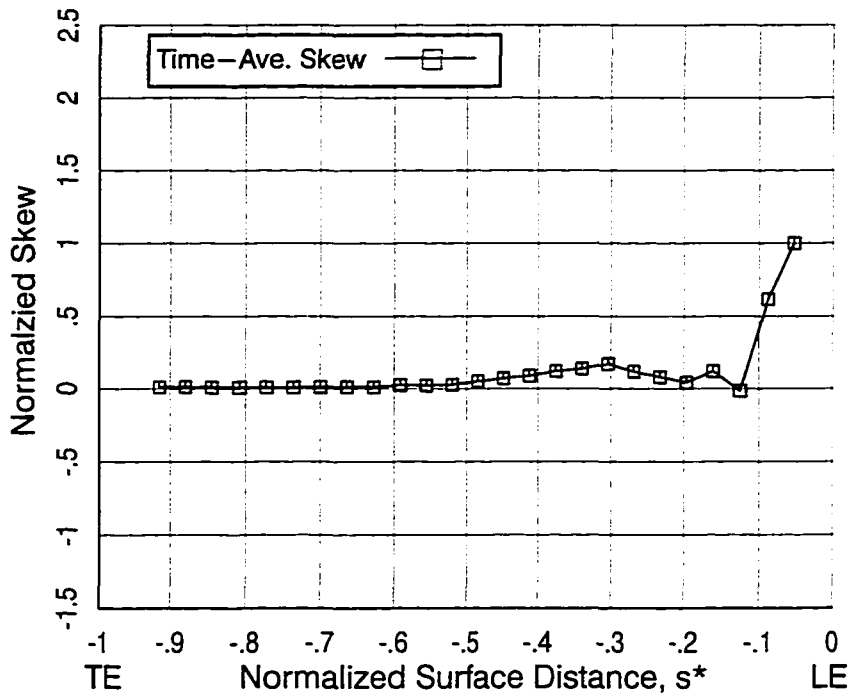


b) skew ($Q_0=-0.7, Q_{10}=2.8$)

Figure 7.16. Ensemble-averaged shear stress characteristics along pressure surface of Nozzle 2, test point 6B



a) random and periodic unsteadiness



b) skew

Figure 7.17. Time-averaged shear stress characteristics along pressure surface of Nozzle 2, test point 6B

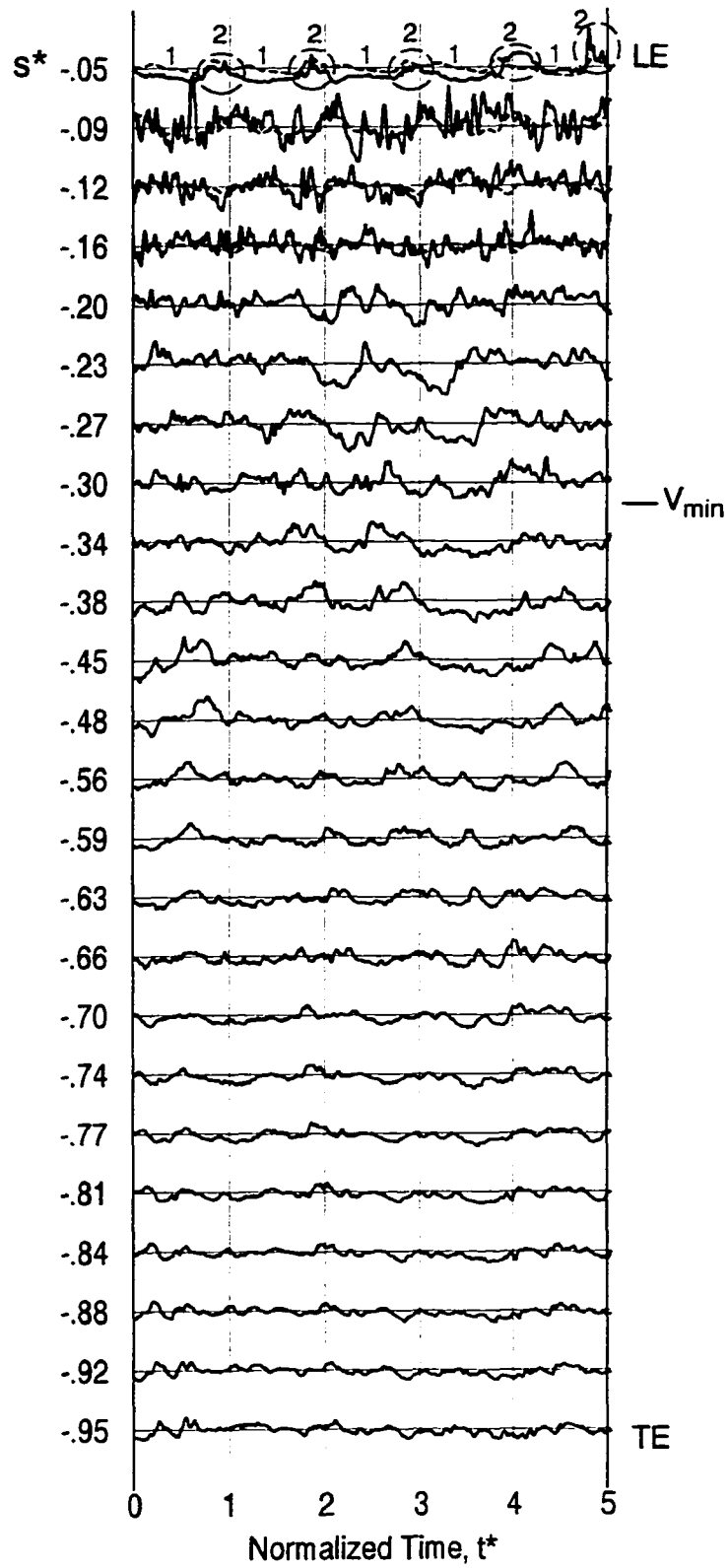
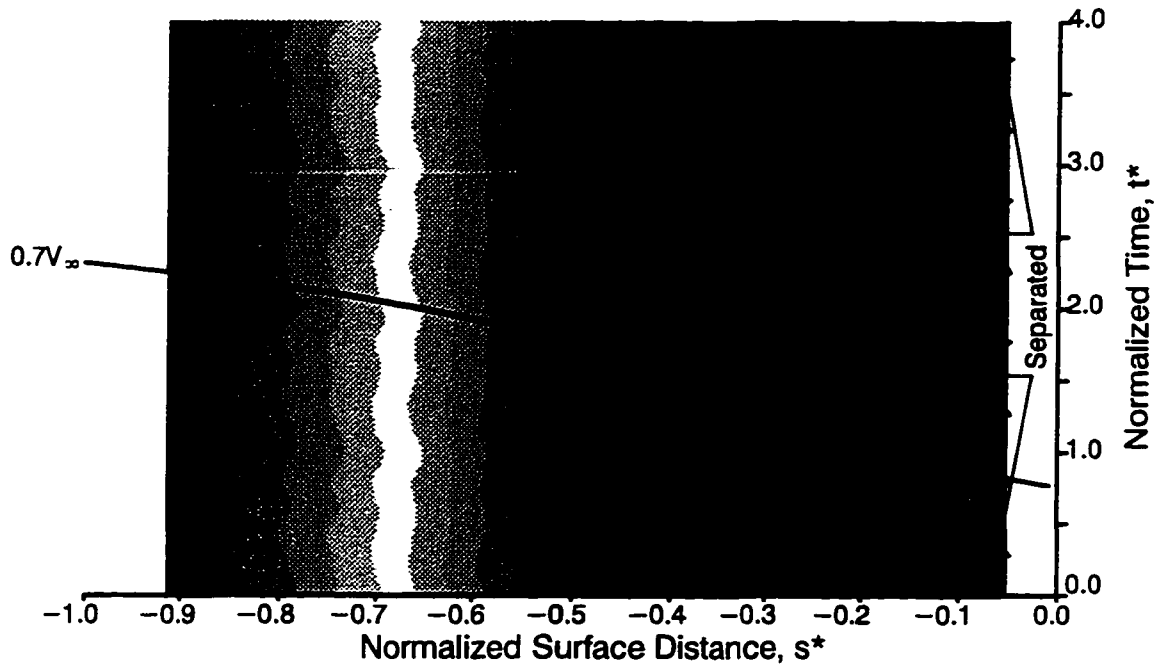
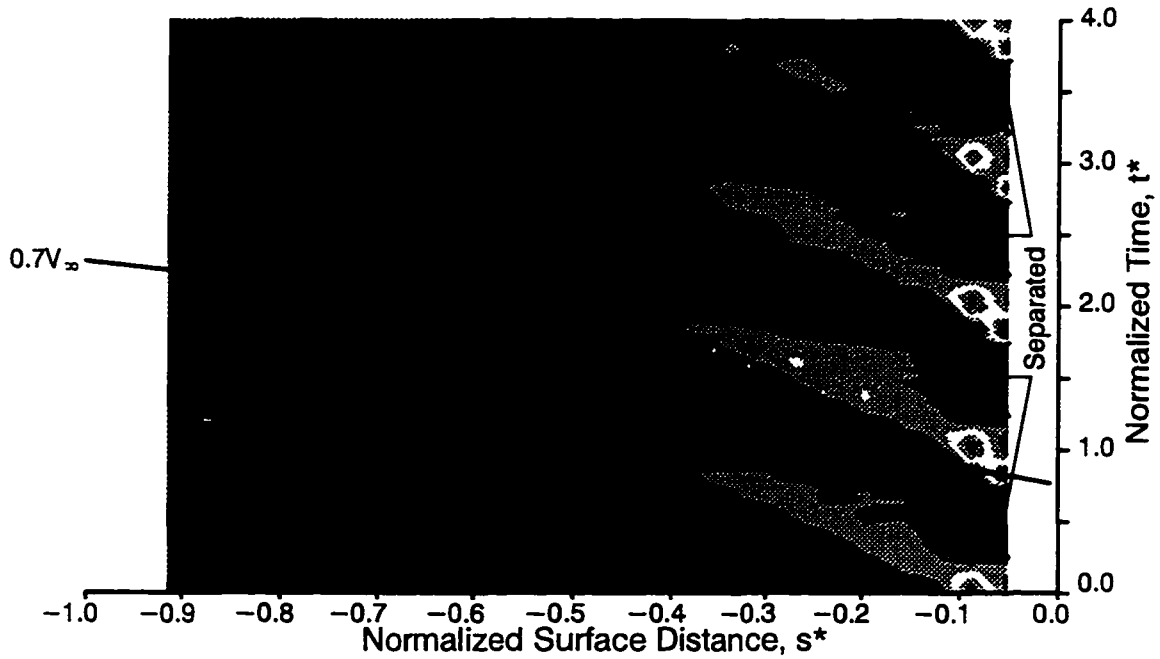


Figure 7.18. Instantaneous time traces of quasi wall shear stress along pressure surface of Nozzle 2, test point 6B

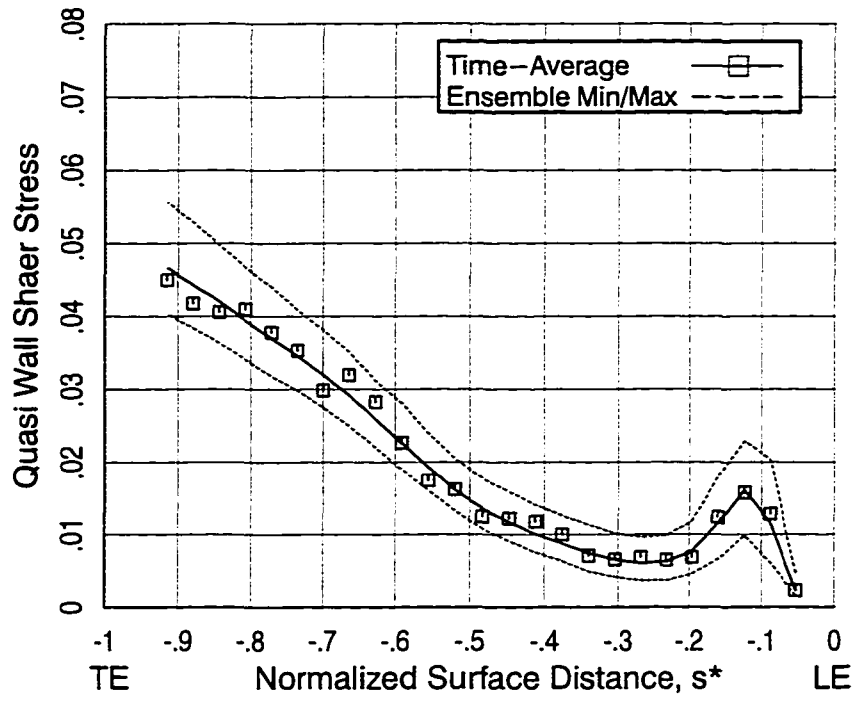


a) ensemble-averaged quasi wall shear stress ($Q_0=0.00$, $Q_{10}=0.048$)



b) ensemble-averaged periodic wall shear ($Q_0=-6.0$, $Q_{10}=9.0$)

Figure 7.19. Shear stress characteristics along pressure surface of Nozzle 2, test point 6B



c) time-averaged quasi wall shear stress

Figure 7.19. continued

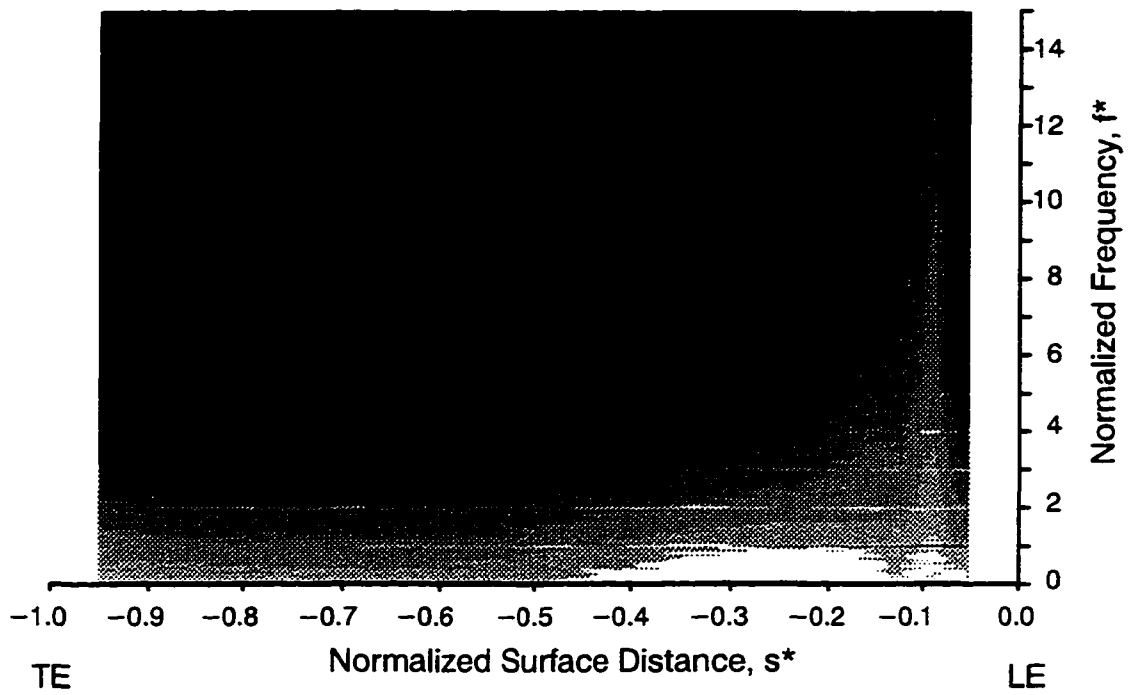


Figure 7.20. Frequency-averaged spectra of hot-film sensor output along pressure surface of Nozzle 2, test point 6B, ($Q_0=-95$, $Q_{15}=-50$)

low, we will first consider the flow characteristics in the vicinity of the separation and secondly the flow characteristics downstream of reattachment.

7.3.3.1 Separation and Transition near the Leading Edge

From the distributions of random unsteadiness and skew in Figures 7.16–17, it is evident that the boundary layer develops in a manner very different from that observed along the suction surface. In Figure 7.16a, a region of separated flow is identified near the leading edge. This coincides with the strong adverse pressure found in the velocity distribution of Figure 7.2a.

A detailed look at the characteristics of the separation is available from the instantaneous time traces in Figure 7.18. The trace closest to the leading edge at $0.05s^*$ contains two distinct regions. Areas 1 are characterized by low amplitude fluctuations and the lowest overall level of wall shear. Between are regions influenced by the passing wakes. Designated areas 2, they are characterized by higher amplitude fluctuations and higher overall levels of shear stress. The actual amplitude of $q\tau_w$ at $0.05s^*$ can be seen in Figure 7.19c. As before, the square symbols denote time-averaged values of $q\tau_w$. The lower dashed line, determined from the minimum values of the ensemble, is close to zero at this first sensor location suggesting the presence of separated flow for at least a portion of the wake-passing period.

By the second sensor at $0.09s^*$, the character of the instantaneous time trace has changed dramatically. It is now composed entirely of high frequency and large amplitude fluctuations. The corresponding time-mean and minimum ensemble values of $q\tau_w$ from Figure 7.19c are now well above zero indicating that the boundary layer at $0.09s^*$ is attached at all times. The instantaneous traces at 0.12 and $0.16s^*$ contain turbulent-like fluctuations similar to those at $0.09s^*$, albeit at a lower amplitude. Though these traces were acquired simultaneously, there is little visible correlation in the fluctuations from one trace to the next. This suggests the existence of a rapidly changing boundary layer characterized by length scales much smaller than the spacing between sensors from which these traces were acquired.

From the above considerations, it is concluded that complete reattachment of a separated flow occurs between sensors at 0.05 and 0.09s*. Certainly, by 0.09s*, the level of quasi wall shear stress is well above zero. At 0.05s* however, the low level of shear stress occurring between wake-influenced regions (i.e., areas 1) suggests that flow separation has already occurred. Note that, for this work, it is not possible to discriminate between forward or reversed flow as both produce a positive value of $q\tau_w$. The wake-influenced regions identified by areas 2 at 0.05s* are thought to be attached given the higher levels of wall shear as compared to areas 1. Because of the uncertainty as to the exact extent of the leading edge separation, the region is indicated by the dashed lines on the s-t diagrams.

The change in energy distribution of the fluctuations occurring downstream of the leading edge is evident from the normalized spectra in Figure 7.20. From 0.05–0.09s*, there is a dramatic shift in energy to higher frequencies. As will be discussed below, the fluctuation energy diminishes in amplitude downstream of 0.09s* as the attached boundary layer develops.

In the vicinity of the leading edge, distributions of skew provide little insight into the flow development. In Figures 7.16b and 7.17b, we find the maximum values of skew at the first sensor. This is consistent with the instantaneous time trace from this location which contained primarily positive spikes in wall shear stress. High positive skew also occurs up to and just beyond reattachment at 0.09s* as evident from the s-t diagram of Figure 7.16b.

As expected, the contour plot of periodic unsteadiness indicates that the highest local wall shear at the first sensor locations pertains to the wake-influenced path.

7.3.3.2 Development of the Reattached Boundary Layer

Downstream of reattachment, the amplitude of the random unsteadiness diminishes as one moves back toward the trailing edge. This is visually apparent from the instantaneous traces in Figure 7.18 as well as from the normalized spectra in Figure 7.20. For the latter, energy at frequencies above two times blade-passing dissipates rapidly. From 0.32s* back to the trailing edge, the acceleration factor is greater than 3×10^{-6} which promotes further dissipation (i.e., rela-

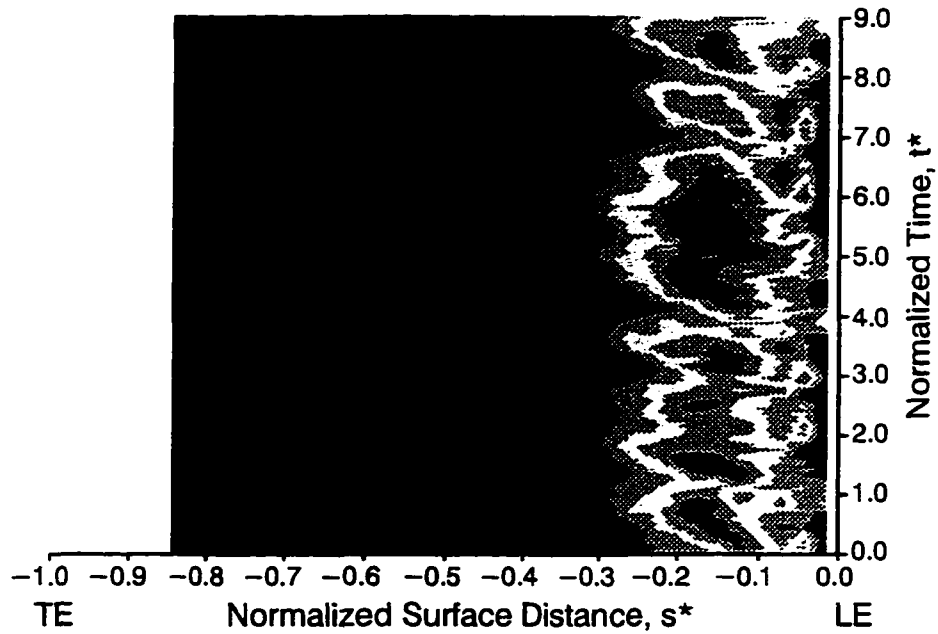
minarization per Schlichting, 1979). For the last 30–40 percent surface distance prior to the trailing edge, the frequency spectra (Figure 7.20) and time-averaged values of random unsteadiness (Figure 7.17a) remain nearly unchanged, suggesting a balance between production and dissipation of turbulent energy. In addition, the instantaneous time traces from Figure 7.18 possess an increasing degree of correlation from trace to trace downstream of minimum velocity. Hence dissipation of the higher frequency unsteadiness leads to larger length scales in the boundary layer as expected.

Regarding wall shear stress, we see from parts a and c of Figure 7.19 that a local maximum occurs at $0.12s^*$ just after reattachment. This is followed by a decrease to a local minimum near minimum velocity. As the flow accelerates back to the trailing edge, $q\tau_w$ increases monotonically. Unlike what was observed along the suction surface, almost no periodic variation in wall shear stress is evident downstream of $0.35s^*$ in Figure 7.19b. The same is generally true for the s - t diagram of random unsteadiness and skew in Figure 7.16.

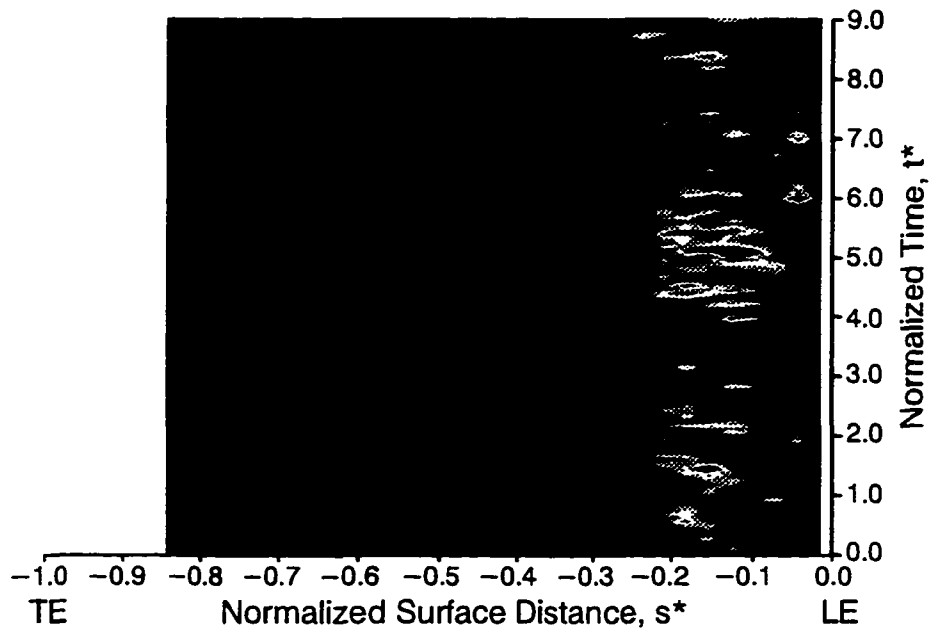
In summary then, the boundary layer along the pressure surface develops in a far less structured fashion than along the suction surface. Directly downstream of the leading edge, in the region of flow deceleration, transition of the boundary layer is initiated abruptly as a result of a separation bubble. Following transition, little periodicity is retained in the developing boundary layer. Along the latter 65 percent of the airfoil, high frequency fluctuations in the turbulent boundary dissipate in response to the strong flow acceleration extending back to the trailing edge.

7.3.4 Rotor Pressure Surface

Measurements of boundary layer development along the pressure surface of Rotor 2 for test point 6B are contained in Figures 7.21–25. For completeness and consistency, results are presented in the same sequence as for the previously-discussed data sets. Measurements were obtained from 29 sensors extending from 0.02 to $0.85s^*$. A group of sixteen sensors was operated simultaneously to acquire instantaneous traces.

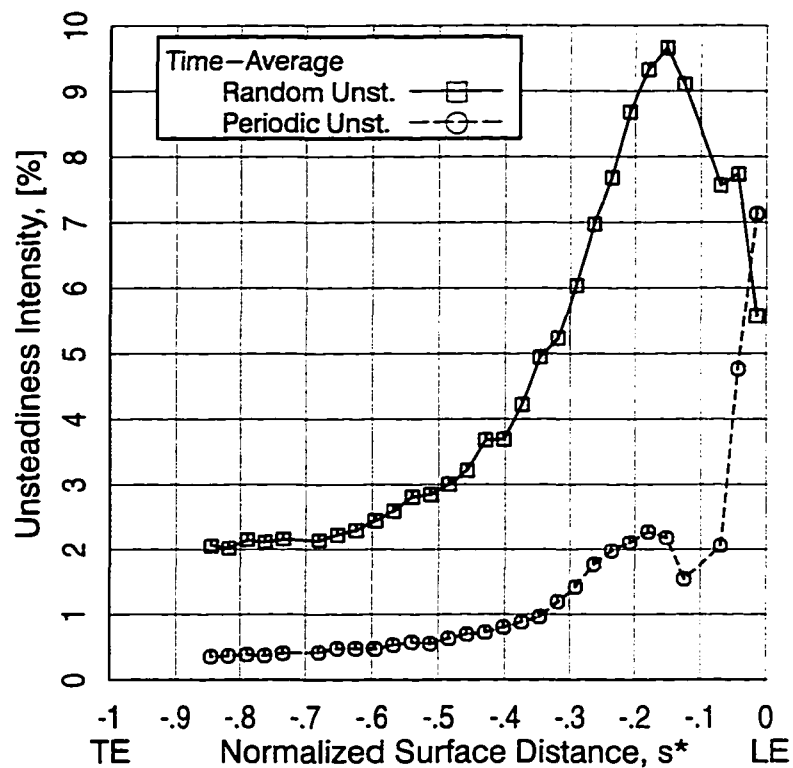


a) random unsteadiness ($Q_0=1.6, Q_{10}=11.8$)

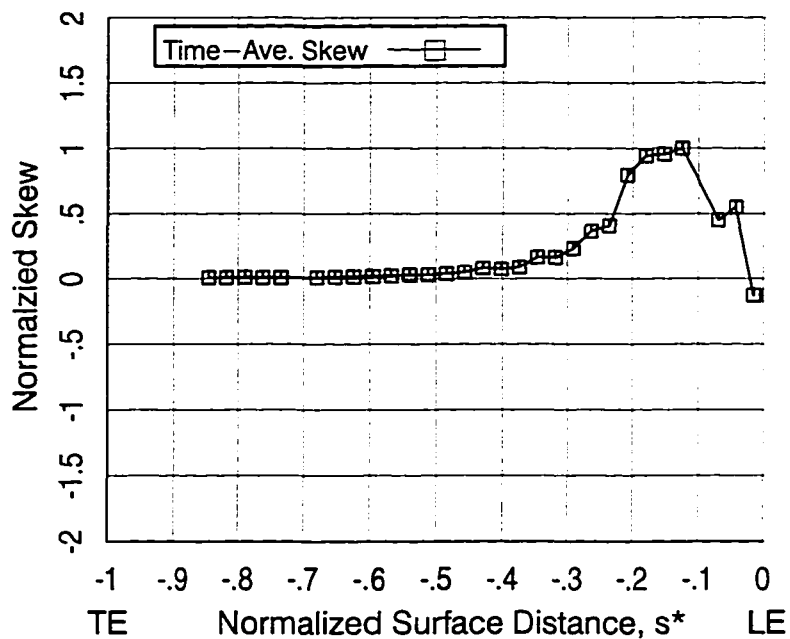


b) skew ($Q_0=-1.0, Q_{10}=4.0$)

Figure 7.21. Ensemble-averaged shear stress characteristics along pressure surface of Rotor 2, test point 6B



a) random and periodic unsteadiness



b) skew

Figure 7.22. Time-averaged shear stress characteristics along pressure surface of Rotor 2, test point 6B

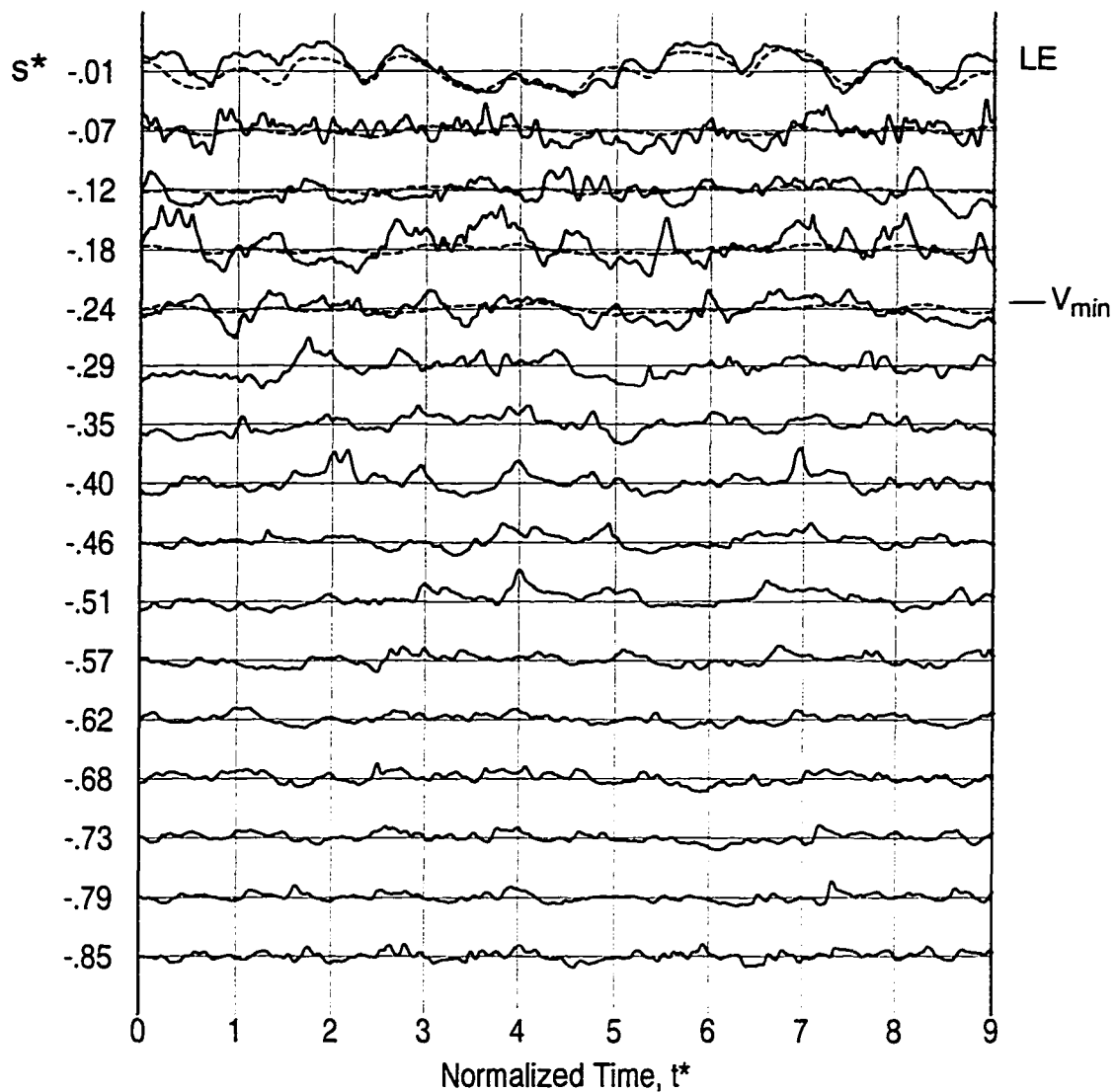
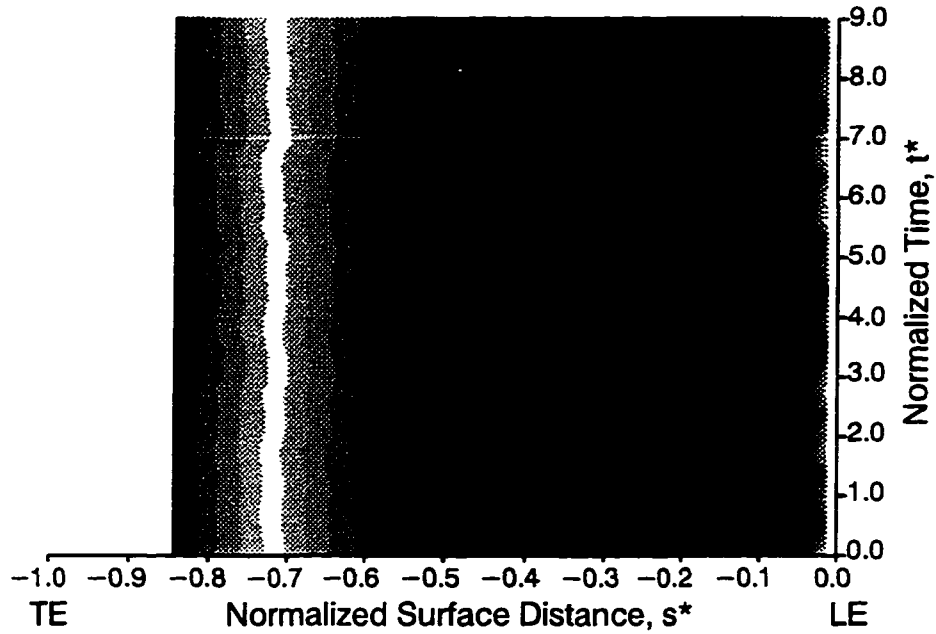
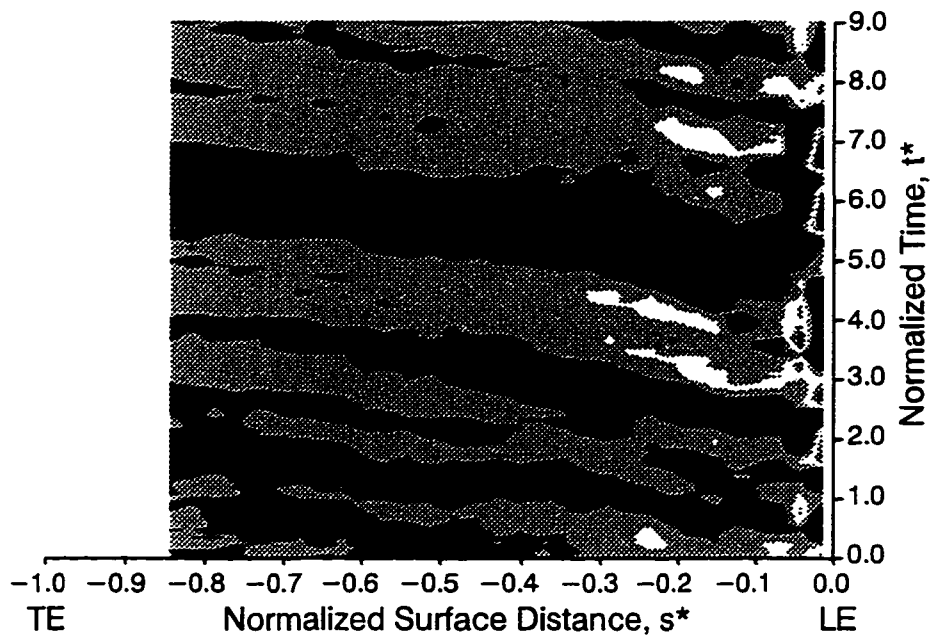


Figure 7.23. Instantaneous time traces of quasi wall shear stress along pressure surface of Rotor 2, test point 6B

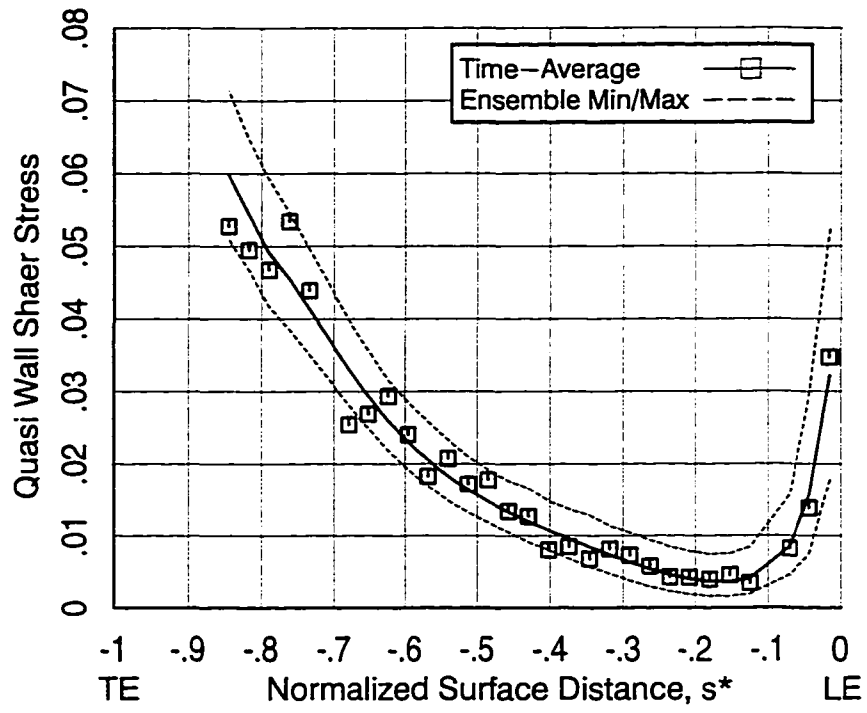


a) ensemble-averaged quasi wall shear stress ($Q_0=0.00$, $Q_{10}=0.0615$)



b) ensemble-averaged periodic wall shear ($Q_0=-13.0$, $Q_{10}=13.0$)

Figure 7.24. Shear stress characteristics along pressure surface of Rotor 2, test point 6B



c) time-averaged quasi wall shear stress

Figure 7.24. continued

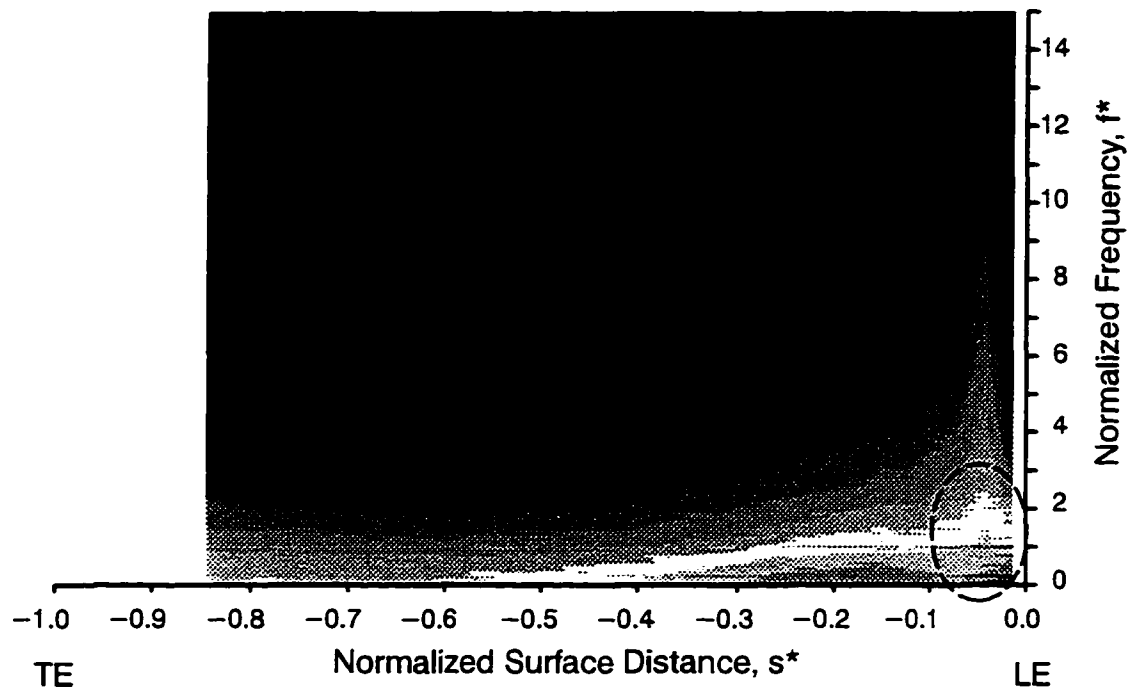


Figure 7.25. Frequency-averaged spectra of hot-film sensor output along pressure surface of Rotor 2, test point 6B, ($Q_0=-95$, $Q_{15}=-50$)

As observed along the nozzle pressure surface, the instantaneous time traces and frequency spectra (Figures 7.23 and 7.25, respectively) suggest a very rapid transition downstream of the leading edge. At $0.02s^*$, superposition of the instantaneous and ensemble-averaged traces in Figure 7.23 reveals that the fluctuations are primarily periodic in nature — albeit complex. By the second trace at $0.07s^*$, the fluctuations are very turbulent in nature. In a consistent manner, we see from the frequency spectra in Figure 7.25 a substantial shift in energy to higher frequencies downstream of the first sensor.

The distribution of quasi wall shear stress near the leading edge, however, is quite different from that found along the nozzle pressure surface. Given in Figure 7.24c, time-averaged and minimum values of $q\tau_w$ are seen to decrease along the initial 10+ percent surface length and remain above zero. This suggests the boundary layer remains attached through the region of transition. That the flow along the rotor pressure surface is more apt to remain attached in comparison to the nozzle follows for two reasons. First, the adverse pressure gradient at the rotor leading edge is less severe than for the nozzle. Secondly, the local turbulence intensity influencing the boundary layer is higher. Not only is the inlet turbulence higher for the rotor, as will be documented in Chapter 8, but additional augmentation results from the lower local velocity ratio downstream of the leading edge.

Following transition, the boundary layer development is similar to that of the nozzle. In Figures 7.21a and 7.22a, contours of maximum random unsteadiness occur from 0.1 to $0.2s^*$. This is due in part to the low values of $q\tau_w$ in this region which is used for normalization. Aft of $0.2s^*$, random unsteadiness steadily decreases reaching a near constant level from $0.7s^*$ back to the trailing edge. The s - t diagram of skew in Figure 7.21b shows even less periodic structure than along the nozzle. The only significant non-zero values of skew coincide with the contours of maximum random unsteadiness. Aft of $0.4s^*$, skew is near zero indicating symmetry in the turbulent fluctuations.

The only significant periodic unsteadiness found in Figure 7.24b occurs along the rotor pressure surface within 5 percent surface distance of the leading edge. The periodic components of frequency, noted by the encircled area in Figure 7.25, are identical to those observed along the suction surface in Figure 7.15b and pertain to both upstream nozzle bladerows. Downstream of about $0.1s^*$, only minor vestiges of periodic frequency components are found.

As with the nozzle data set, both the instantaneous traces and frequency spectra exhibit a dissipation of random energy downstream of transition. This dissipation abates by $0.5-0.6s^*$, consistent with the variation in random unsteadiness noted above.

In summary then, boundary layer development along the pressure surface of Rotor 2 is very similar to that of Nozzle 2 with one exception. That is, it appears for Rotor 2 that flow attachment is maintained through the region of transition downstream of the leading edge. For either case (nozzle or rotor), transition occurs very rapidly.

7.4 Effects of Reynolds Number

To document the effects of Reynolds number on boundary layers of the LSRT blading, measurements were acquired at constant loading for five Reynolds numbers ranging from high takeoff to low cruise values. The corresponding test points are designated 5A through 5E and appear in Figure 7.1 and Table 7.1. It was decided early in this test program to acquire these data in increased loading to reduce the negative incidence at the leading edge. By acquiring the data sets at a constant value of specific flow, the normalized vector diagrams remained unchanged as Reynolds number was varied.

In this section, selected boundary layer measurements obtained along the nozzle suction surface will be presented for test points 5A, 5C, and 5E. To simplify the discussion, each test case is described separately with similarities and contrasts drawn between them when significant. Figures containing the same measured quantities from the three Reynolds numbers are grouped together, however, to facilitate visual comparison.

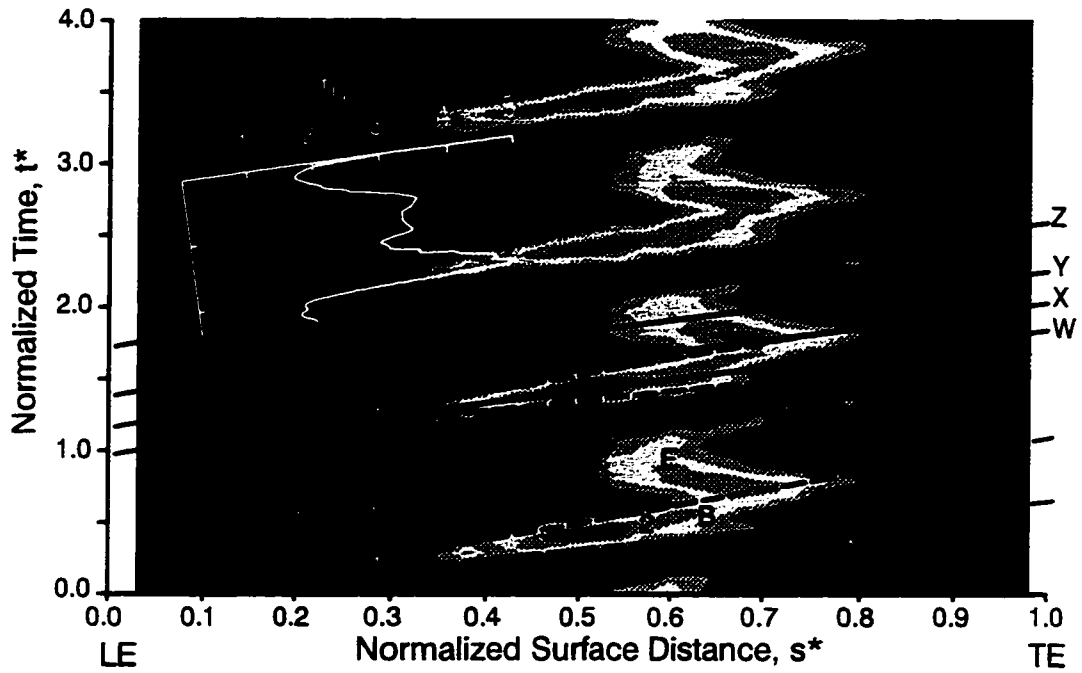
Results from the rotor were similar to those of the nozzle and hence are not included. A description of the boundary layer development along the pressure surface is deferred to Section 7.5 where one set of measurements for this loading level is presented — the reason being that the results did not vary significantly with Reynolds number.

The surface velocity distribution along the nozzle for increased loading is given by the square symbols in Figure 7.2a. The primary difference with that of baseline loading occurs along the front portion of the airfoil. At increased loading, a distinct region of local diffusion extends from $0.32s^*$ to $0.38s^*$. At the lower, baseline loading, this diffusion is less perceptible. The maximum to exit velocity ratio along the suction surface is equal to 1.12 as it was for the baseline condition.

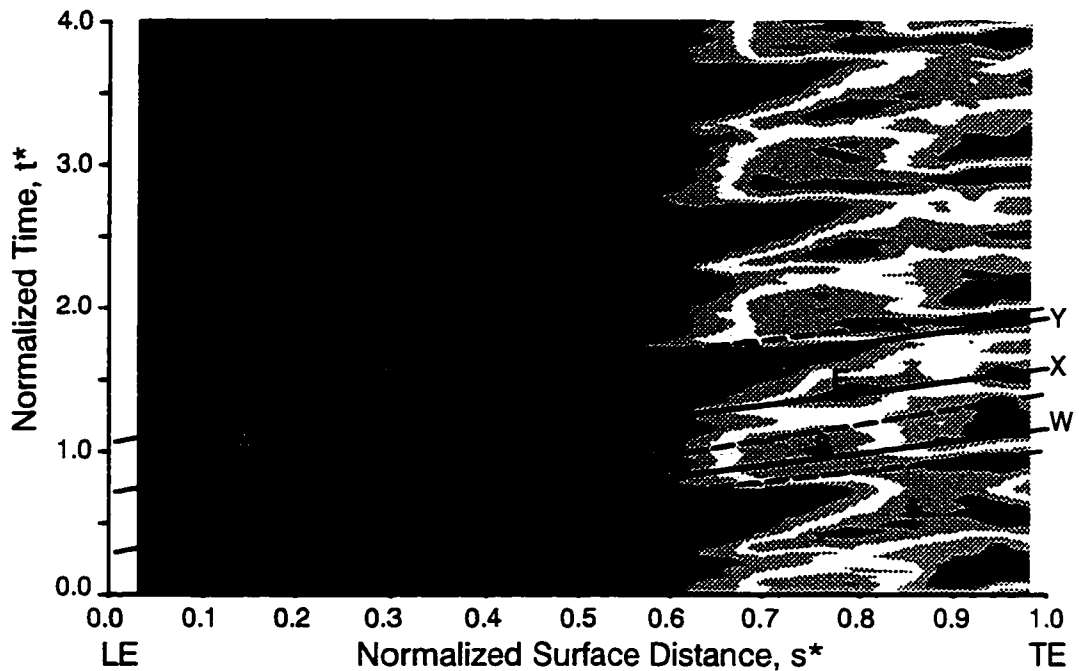
7.4.1 High (Takeoff) Reynolds Number

Boundary layer development for test point 5A is qualitatively similar to that observed along the nozzle suction surface at the baseline test condition. The specific regions of development are delineated on the contour plots of random unsteadiness and skew in Figures 7.26a and 7.27a. In a manner described previously, the distribution of turbulence intensity measured at the inlet to the nozzle is superimposed onto the contour plot in Figure 7.26a.

As with the baseline test case, the boundary layer develops along the distinct wake and non-wake paths. Along the wake-induced path (trajectory W), the boundary layer is again laminar downstream of the leading edge. Transition onset along W occurs at $0.32s^*$ (point 1) which is coincident with the local diffusion in the velocity distribution. In comparison, transition onset for the baseline case was located at $0.4s^*$. Downstream of $0.32s^*$, the wake-induced transitional strip B develops. From the line plots of random unsteadiness and skew (red lines in Figures 7.28a and 7.29a, respectively), we see that transition reaches a midpoint at $0.57s^*$ and is completed by about $0.8s^*$. These are marked points 2 and 3, respectively, on the s - t diagrams. Following the completion of transition along W, wake-induced turbulent region C extends to the trailing edge.

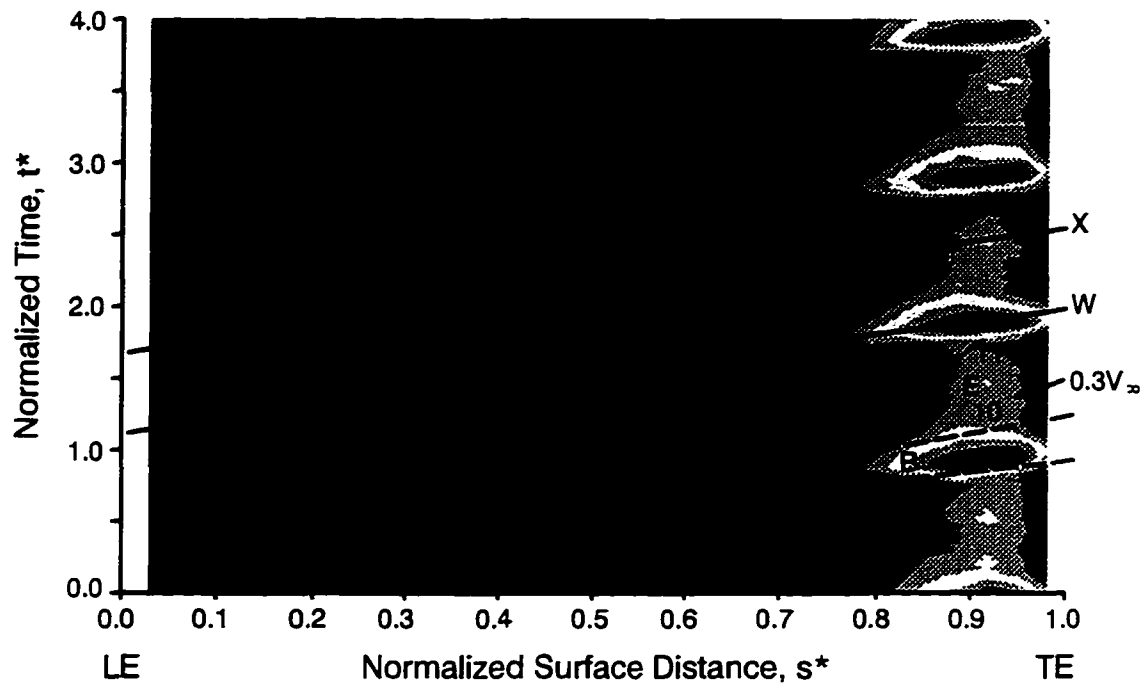


a) test point 5A, $\overline{Re}_{ssl}=5.27 \times 10^5$ ($Q_0=0.66$, $Q_{10}=9.66$)



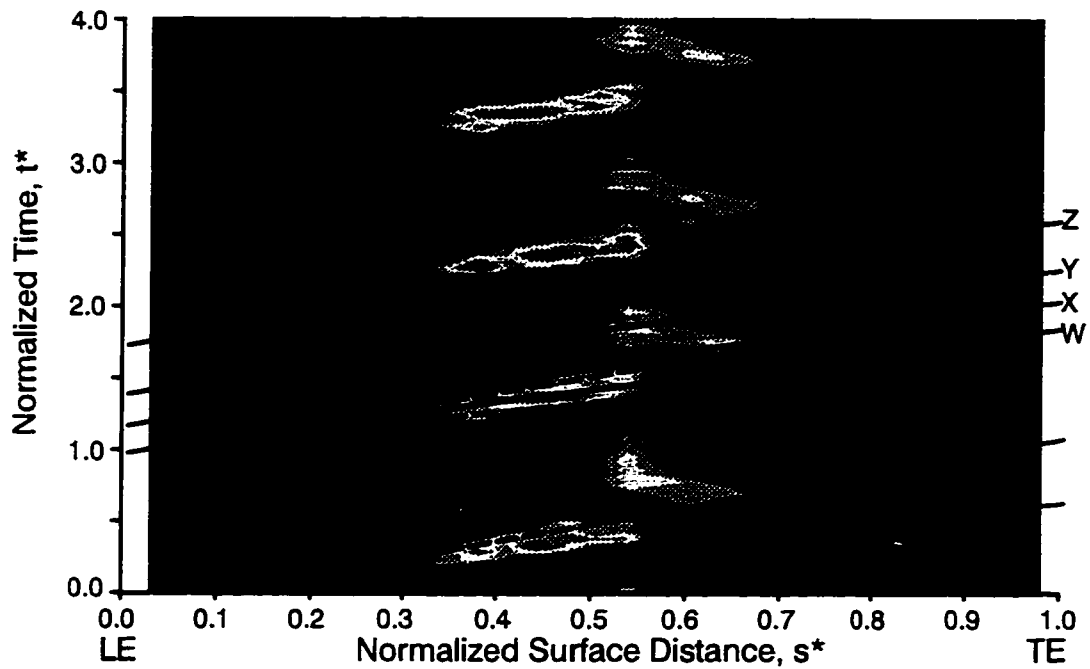
b) test point 5C, $\overline{Re}_{ssl}=2.71 \times 10^5$ ($Q_0=1.20$, $Q_{10}=11.20$)

Figure 7.26. Space-time diagrams of random unsteadiness along suction surface of Nozzle 2

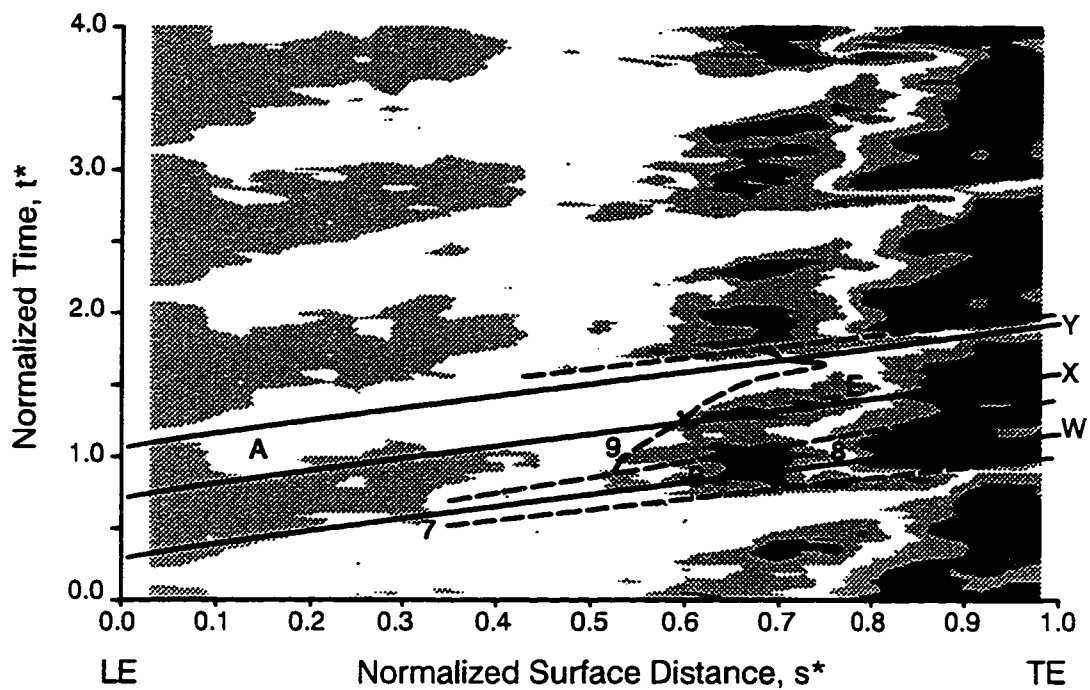


c) test point 5E, $\overline{Re}_{ssl}=1.19 \times 10^5$ ($Q_0=1.13$, $Q_{10}=23.73$)

Figure 7.26. continued

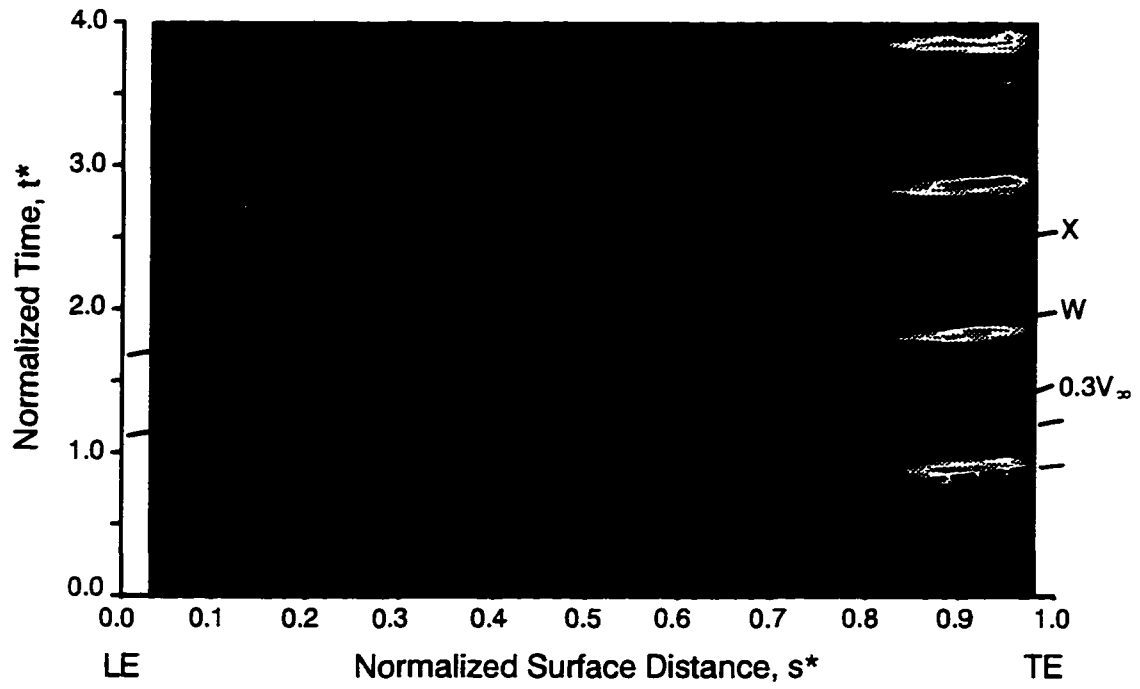


a) test point 5A, $\overline{Re}_{ssl} = 5.27 \times 10^5$ ($Q_0 = -1.5$, $Q_{10} = 3.5$)



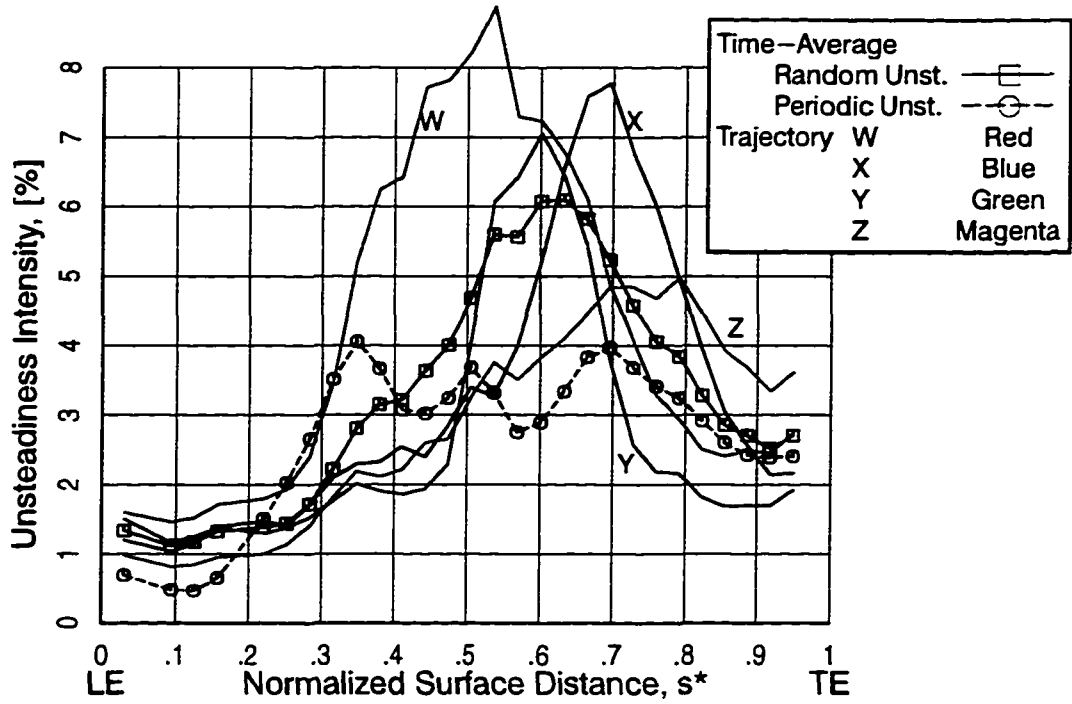
b) test point 5C, $\overline{Re}_{ssl} = 2.71 \times 10^5$ ($Q_0 = -2.4$, $Q_{10} = 1.6$)

Figure 7.27. Space-time diagrams of skew along suction surface of Nozzle 2

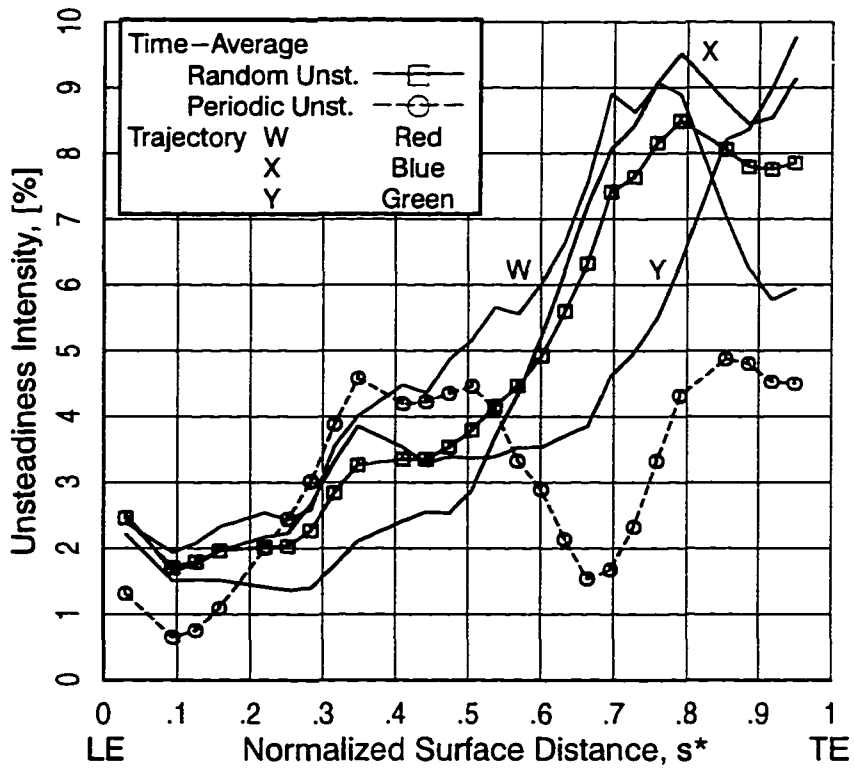


c) test point 5E, $\overline{Re}_{ss1} = 1.19 \times 10^5$ ($Q_0 = -2.0$, $Q_{10} = 8.0$)

Figure 7.27. continued

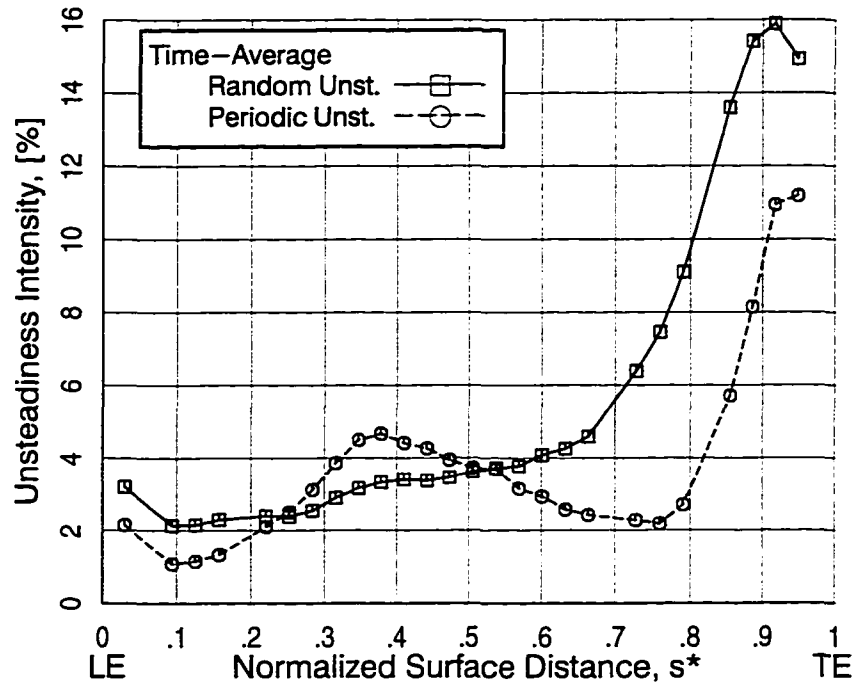


a) test point 5A, $\overline{Re}_{ssl}=5.27 \times 10^5$



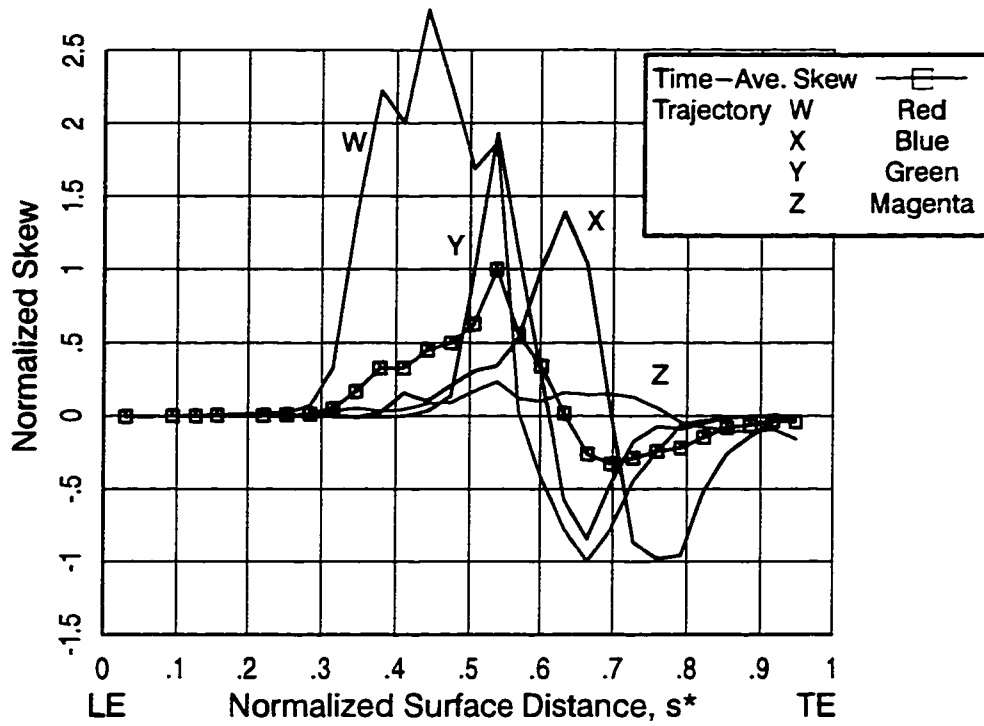
b) test point 5C, $\overline{Re}_{ssl}=2.71 \times 10^5$

Figure 7.28. Time-averaged distributions of random and periodic unsteadiness along suction surface of Nozzle 2

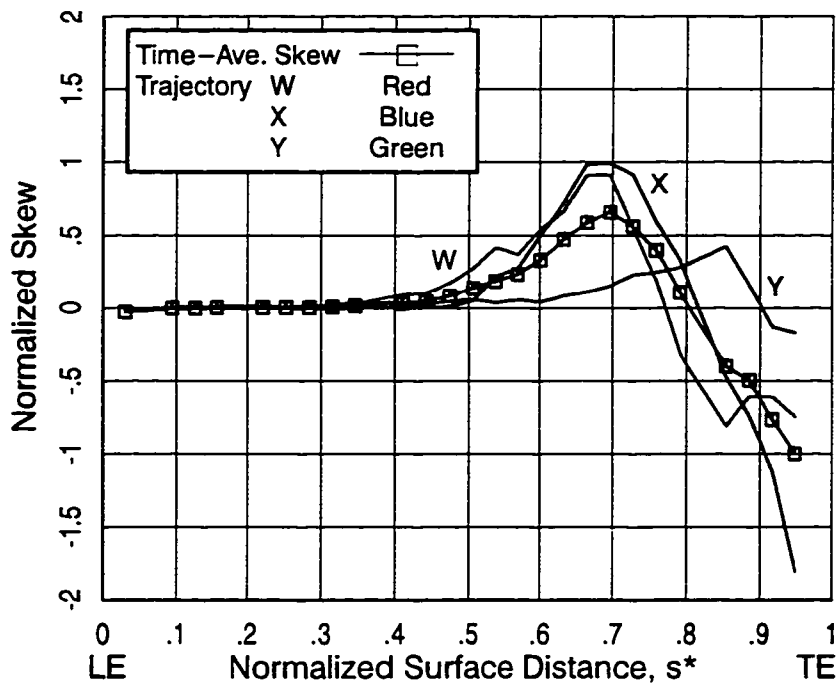


c) test point 5E, $\overline{Re}_{ssl} = 1.19 \times 10^5$ ($Q_0 = -2.0$, $Q_{10} = 8.0$)

Figure 7.28. continued



a) test point 5A, $\overline{Re}_{ssl}=5.27 \times 10^5$



b) test point 5C, $\overline{Re}_{ssl}=2.71 \times 10^5$

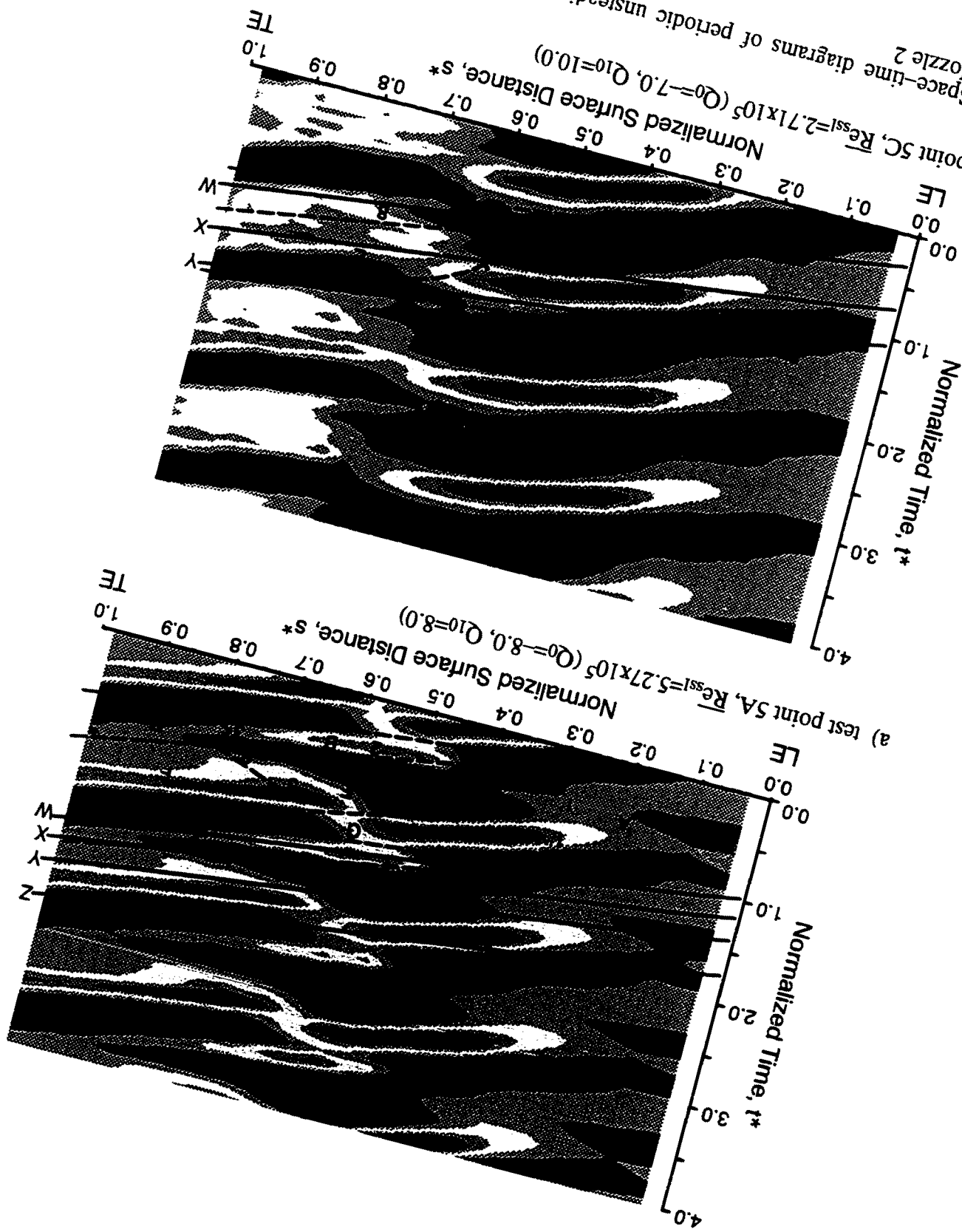
Figure 7.29. Time-averaged distributions of skew along suction surface of Nozzle 2

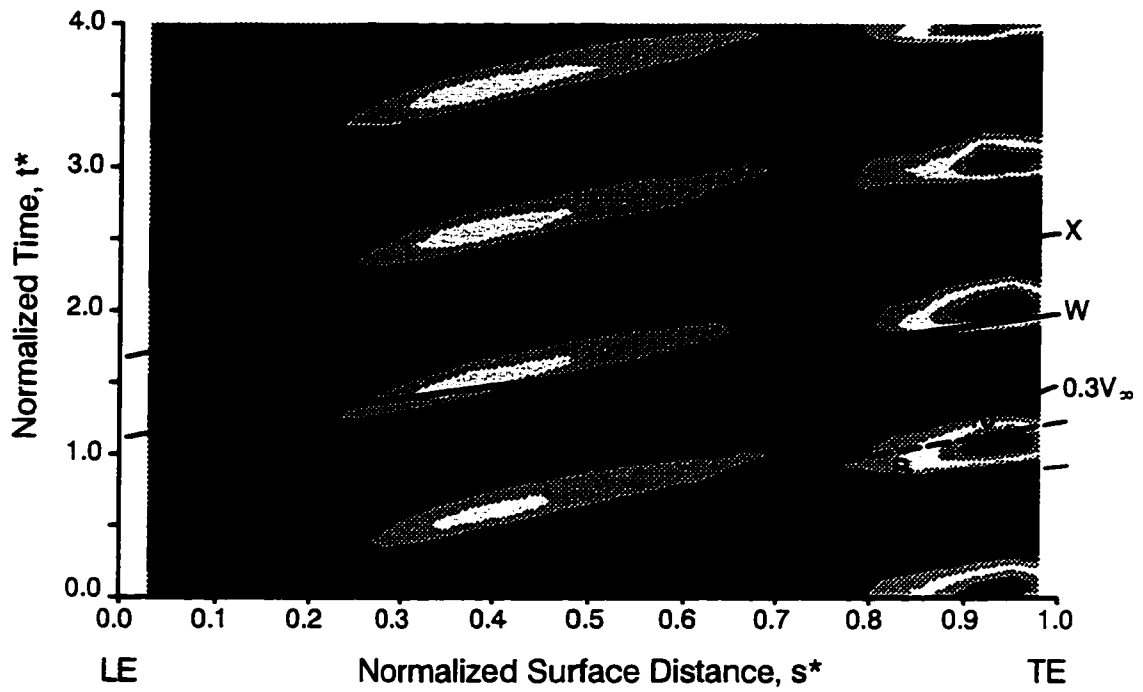
The path between wakes consists of a laminar region A, transitional region E, turbulent region F, and, as with the baseline case, two calmed regions D and G. The onset of transition between wake paths occurs earliest at $0.5s^*$ (point 4) and marks the beginning of region E. The completion of transition extends from 0.70 – $0.75s^*$ (points 5 to 6). Line plots of random unsteadiness and skew along trajectories X, Y, and Z are provided in Figures 7.28a and 7.29a. They document, in a time-averaged fashion, specific features of boundary layer development along the path between wakes. Most notable are that transition occurs furthest aft along trajectory Z and is far from completion at the trailing edge. This corresponds to calmed region G of the s - t diagrams in Figures 7.26a and 7.27a.

The contours of periodic unsteadiness for test point 5A appear in Figure 7.30a. Taken as a whole, the variation exhibits an orderly but complicated structure. At $0.3s^*$, the temporal variation in wall shear stress is again indicative of the jet-wake effect. A region of nearly constant wall shear (green contours, point 1') is followed first by a local maximum (red contours, point 1'') corresponding to the leading boundary of the wake and then a local minimum (blue contours, point 1) corresponding to the trailing boundary. The onset of wake-induced transition occurs in the trough of wall shear stress at point 1 in the same manner as observed for the baseline case. By the midpoint of transition at point 2 in figure 7.30a, the highest levels of local shear stress are found in the wake-induced strip, region B. As flow in region E undergoes transition further aft, its wall shear becomes the maximum periodic value (e.g., point 5). Along the last 30 percent of the nozzle, the lowest wall shear coincides with the calmed region G where transition occurs furthest aft.

Distributions of time-averaged, quasi wall shear stress for the three Reynolds number test cases are shown together in Figure 7.31. To enable the distributions to be plotted on identical scales, it was necessary to take into account the differences in Reynolds number. This was done by scaling the magnitude of quasi wall shear stress, $q\tau_w$, by $Re^{3/2}$. Consequently, the normalized quantity plotted in Figure 7.31 is proportional to $c_f Re^{1/2}$. For test case 5A, minimum values of

Figure 7.30. Space-time diagrams of periodic unsteadiness along suction surface of Nozzle 2





c) test point 5E, $\overline{Re}_{ssl}=1.19 \times 10^5$ ($Q_0=-14.0$, $Q_{10}=21.0$)

Figure 7.30. continued

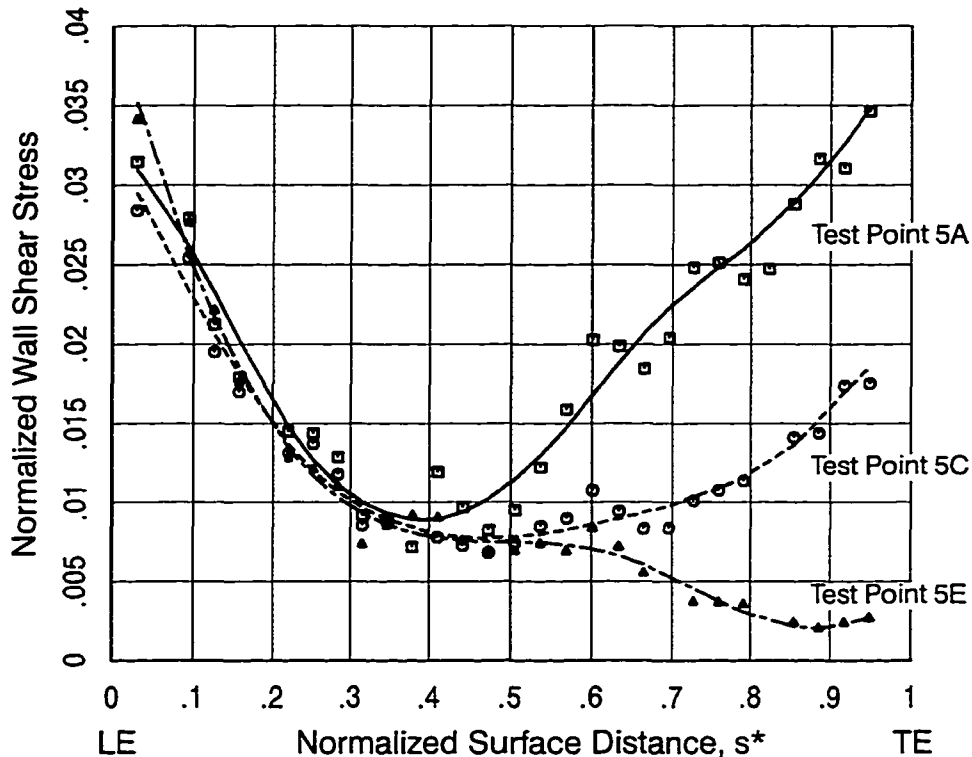


Figure 7.31. Distributions of normalized quasi wall shear stress along suction surface of Nozzle 2

wall shear occur near $0.4s^*$ which coincides with the beginning of boundary layer transition. The overall level of wall shear for 5A indicates that no boundary layer separation takes place along the suction surface.

The instantaneous time traces for this test case are contained in Figure 7.32a. No turbulent events appear in the first five traces. By $0.25s^*$, periodic fluctuations characteristic of the jet-wake effect are evident. An example is noted by area 1. Turbulent events, marked "2," first appear along the wake trajectories W. As before, the events are seen to both lead and lag the equally-spaced wake trajectories. An example of a calmed region developing behind a wake-induced spot is identified as area 3.

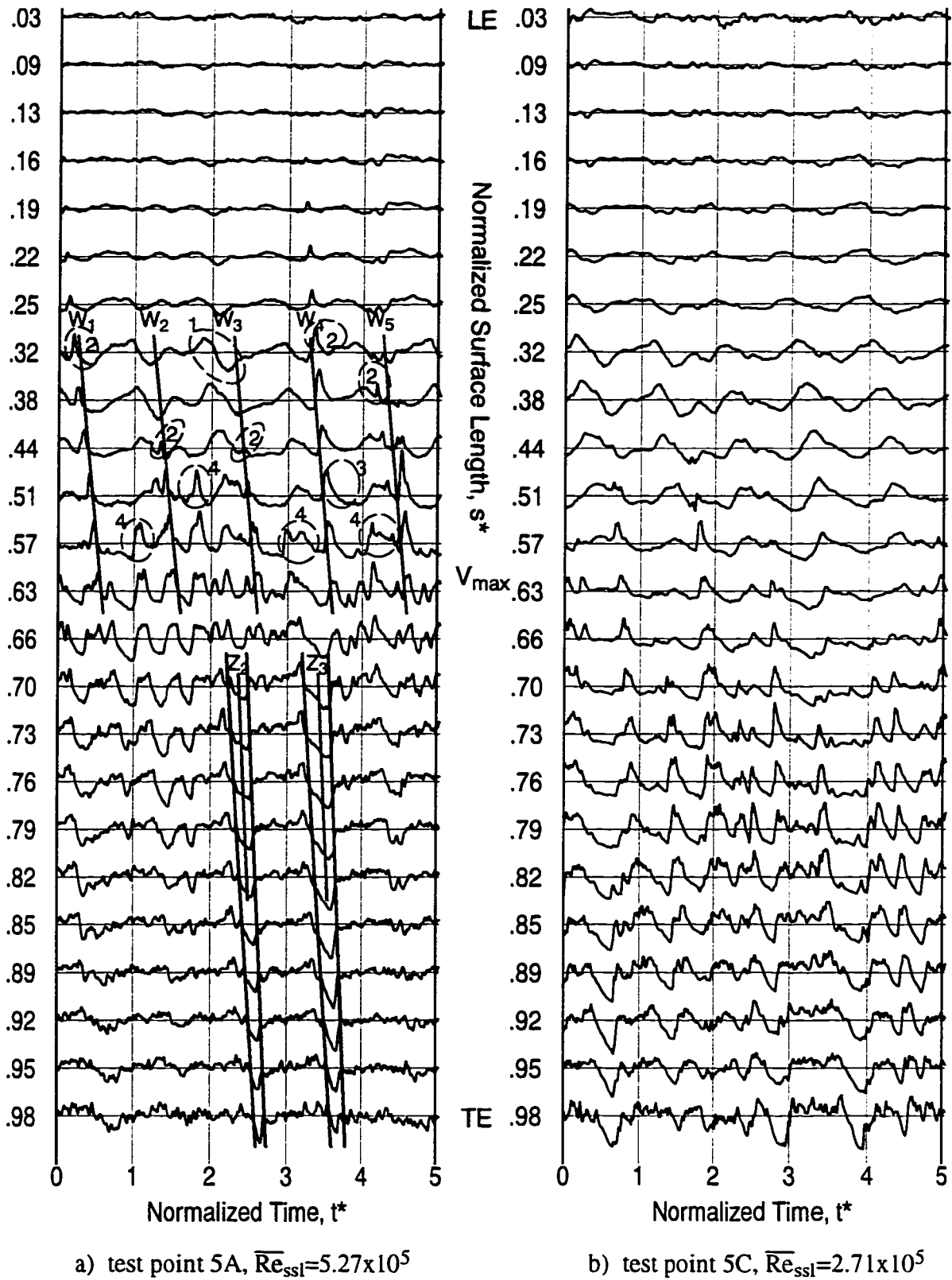
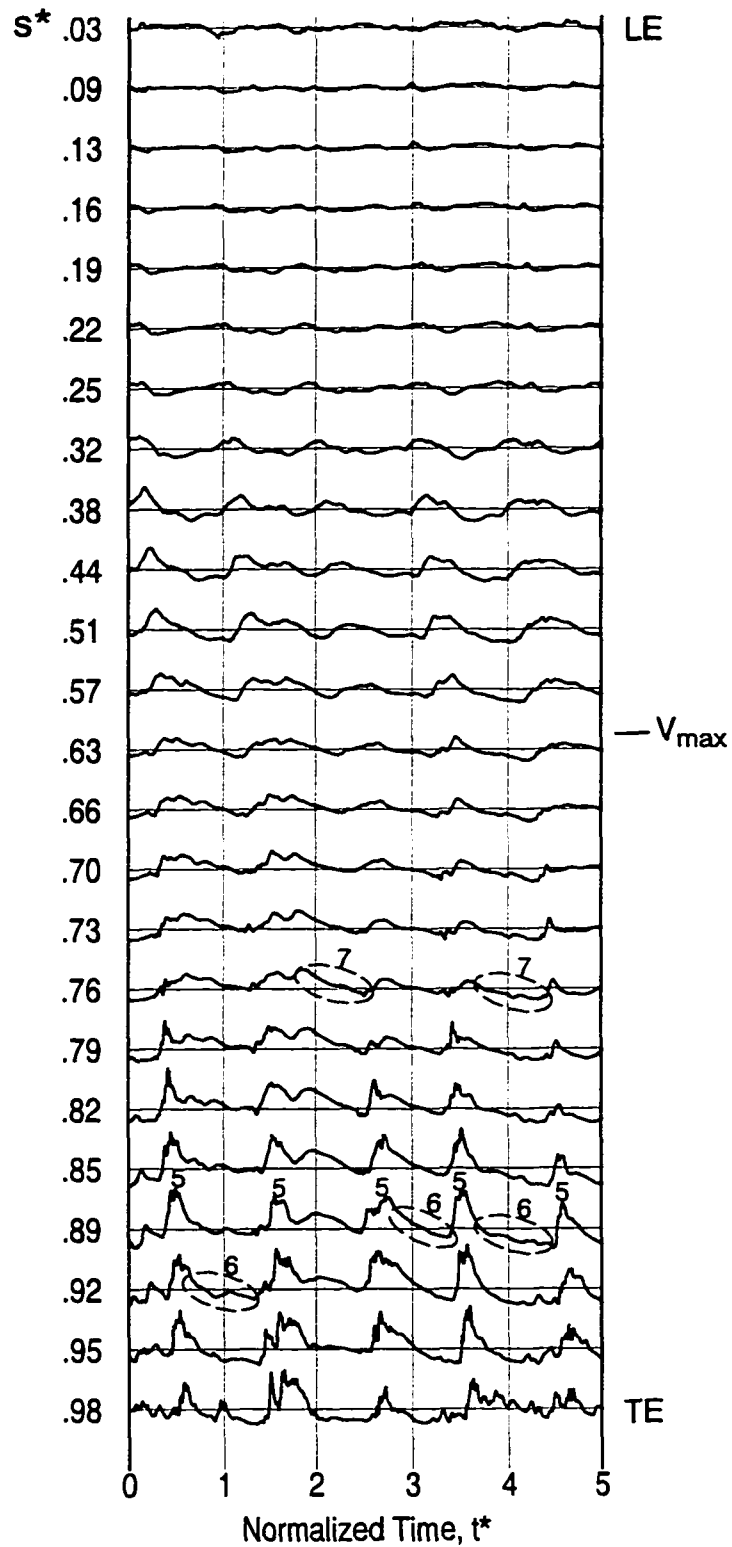


Figure 7.32. Instantaneous time traces along suction surface of Nozzle 2



c) test point 5E, $\overline{Re}_{ssl} = 1.19 \times 10^5$

Figure 7.32. continued

Evidence of transition onset between wakes is found at $0.51s^*$ and $0.57s^*$ prior to maximum velocity. These events are labeled “4.” At $0.63s^*$, which is just aft of maximum velocity, the instantaneous traces consist almost entirely of wake and non-wake induced turbulent spots and their associated calmed regions. Little or no conventional laminar flow is apparent. Also, it is not possible to discriminate between wake and non-wake induced spots from the single trace alone.

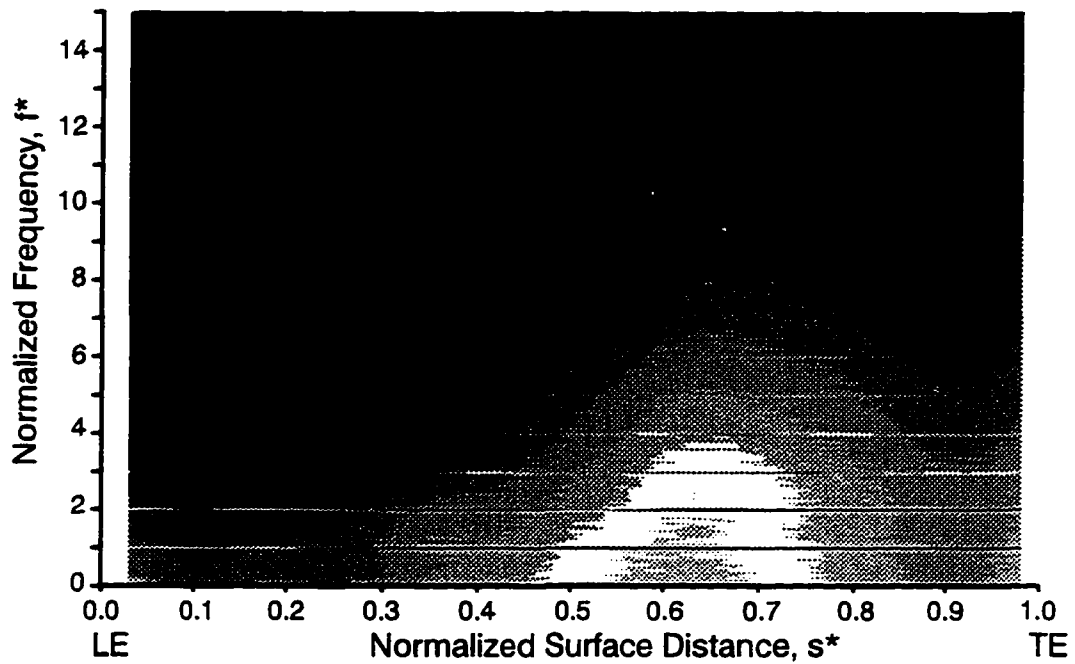
From $0.63s^*$ to the trailing edge, the boundary layer is characterized by the growth and merging of turbulent spots. The calmed regions are consumed, for the most part, though some non-turbulent flow persists to the trailing edge. Examples of the latter are identified along trajectories Z_2 and Z_3 . They coincide with the calmed region G identified on the contour plots.

The contour plot of normalized RMS spectra in Figure 7.33a provides little additional insight into the boundary layer development over and above that just described. It is qualitatively identical to that for the baseline result and is included here to enable comparison with the lower Reynolds number results.

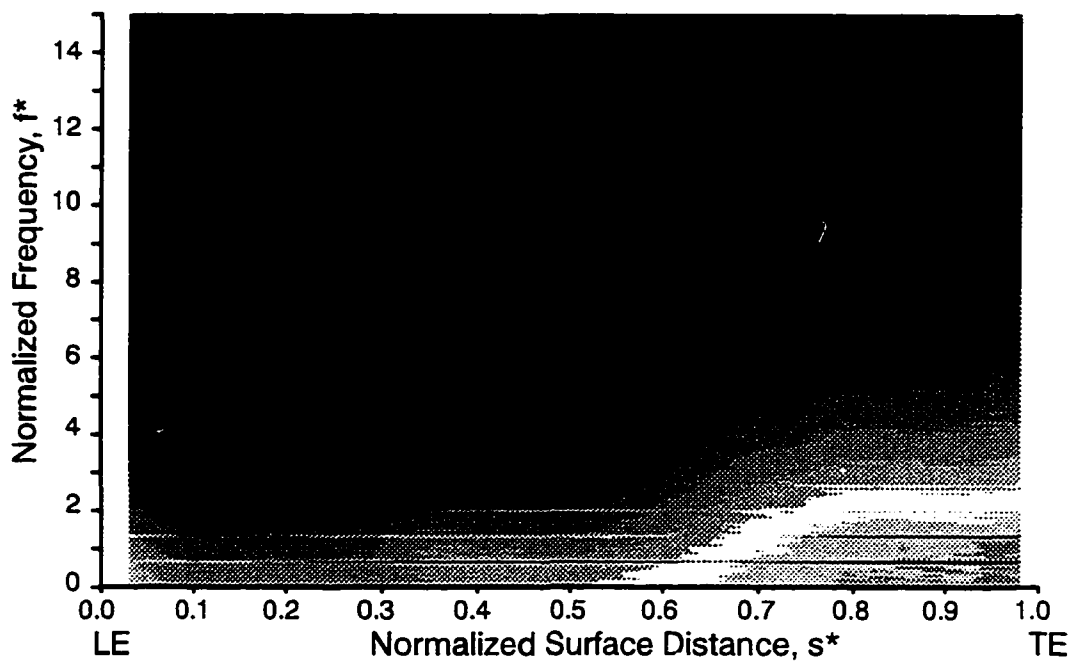
7.4.2 Intermediate Reynolds Number

Measurements from the intermediate Reynolds number at test point 5C make up part b of Figures 7.26–7.33.

The contour plots of random unsteadiness and skew for test case 5C appear in Figures 7.26b and 7.27b, respectively. As before, regions of boundary layer development are demarcated. From a comparison with the results of 5A, it is apparent that transition along the wake-induced path initially is much weaker at this lower Reynolds number. Transition onset still occurs in the region of local diffusion (point 7 of Figure 7.26b), but the contours of random unsteadiness remain green in color until after maximum velocity at $0.62s^*$. The contours of skew in Figure 7.27b substantiate further the less-pronounced behavior along this portion of the wake-induced strip. (Note that the differences in dominant colors of the contours of skew in parts a and b of Figure 7.27 result from different zero locations on the scale.)

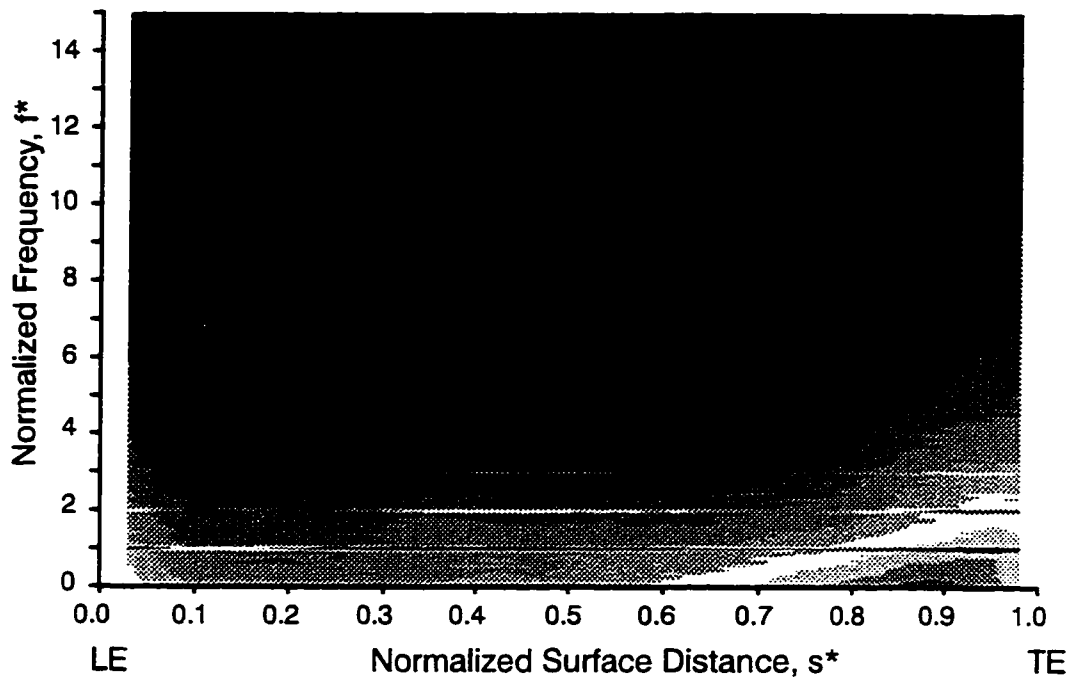


a) test point 5A, $\overline{Re}_{ssl}=5.27 \times 10^5$ ($Q_0=-95.0$, $Q_{10}=-50$)



b) test point 5C, $\overline{Re}_{ssl}=2.71 \times 10^5$ ($Q_0=-95.0$, $Q_{10}=-50.0$)

Figure 7.33. Space-frequency diagrams of normalized RMS spectra along suction surface of Nozzle 2



c) test point 5E, $\overline{Re}_{ssl}=1.19 \times 10^5$ ($Q_0=-95.0$, $Q_{10}=-50.0$)

Figure 7.33. continued

The line plots of random unsteadiness and skew along trajectory W (red lines of Figures 7.28b and 7.29b) indicate the half-way point of transition to be near $0.75s^*$ (point 8 of the contour plots) and that transition along the wake-induced path is not completed at the trailing edge. Clearly, the entire transition process along W is more protracted than for test case 5A.

Transition between wakes also occurs further aft as compared to the high Reynolds number test case. It follows from the weakness of transitional strip B that little calming occurs behind it. Consequently, transition between wakes first occurs at point 9. From the contour plots of random unsteadiness and skew as well as from the line plots along trajectories X and Y (Figures 7.28b and 7.29b), it is evident that transition between wakes does not approach completion prior to the trailing edge. It is worth noting for emphasis that *no* turbulent regions C or F occur at this intermediate Reynolds number.

Characteristics of the periodic unsteadiness, shown in Figure 7.30b, are similar to those for the high Reynolds number case just described. Onset of wake-induced transition occurs at point 7 in the wall shear stress trough. Along the final 35 percent surface distance, the highest levels of shear stress occur in regions B and E where transition occurred earliest.

From Figure 7.31, we see that for this test case, the minimum value of normalized, quasi wall shear stress occurs further aft in a manner consistent with the shift in transition. Also, wall shear remains above zero along the entire suction surface.

Instantaneous time traces are provided in Figure 7.32b. Consistent with the discussion above, turbulent events first appear at locations further aft than for the higher Reynolds number. For this particular group of traces, little transitional activity occurs upstream of $0.51s^*$. For the traces from $0.57s^*$ to $0.66s^*$, it is actually quite difficult to discriminate between the wake- versus non-wake-induced turbulent events. As expected, significant transitional activity is evident back to the trailing edge. For about the last five traces, all patches of non-turbulent flow exhibit the shear stress variations characteristic of calming.

7.4.3 Low (Cruise) Reynolds Number

Results of boundary layer development at test point 5E for a cruise Reynolds number constitute part c of Figures 7.26–7.33.

The contour plot of random unsteadiness in Figure 7.26c is now markedly different from those of the two previous, higher Reynolds number cases. The laminar region A is seen to extend along more than 70 percent of the nozzle suction surface. Transition occurs first along the wake-induced path at $0.73s^*$ in a region of decelerating flow. This is about 10 percent surface distance aft of maximum velocity. Whereas for the higher Reynolds number boundary layers, wake-induced transition is triggered in the region of local diffusion near $0.35s^*$, at this lower Reynolds number, the boundary layer remains stable through this region.

Between wakes, the boundary layer develops in a very interesting manner. From the instantaneous traces in Figure 7.32c, we find that distinct turbulent events have developed at increments of blade passing by $0.89s^*$ (areas 5). Behind each event is a region of decreasing shear stress that extends across to the following turbulent event. Examples are noted in the figure by encircled areas 6. Unlike previous explanations, however, this elevation of shear stress between turbulent events can *not* be attributed to calming effects alone. As the trajectory drawn at $0.3V_\infty$ in Figure 7.26c implies, the calmed regions created behind turbulent spots of region B will extend only partially into the region between wakes.

Further interrogation of the instantaneous traces provides an alternative explanation. Prior to the appearance of individual turbulent spots, periodicity in the disturbed, laminar boundary layer is evident (e.g., areas 7 of the trace at $0.76s^*$ in Figure 7.32c). Further aft, turbulent events appear such that these regions of decreasing shear present in the disturbed laminar flow occur between the events. Consequently, the elevation of shear stress between turbulent events is due both to calming and to the boundary layer periodicity that existed *prior* to transition onset. The end result is that the shear stress of the non-turbulent flow is elevated such that it does not separate.

The dashed line extending across region E in Figure 7.26c approximately demarcates the extent of this elevated shear region. In an ensemble-averaged sense, this variation of wall shear across region E is evident from the periodic variation of $q\tau_w$ in Figure 7.30c. Following behind region B in time, wall shear decreases continuously from points 10 to 11, the latter occurring just prior to the next wake-induced strip.

Comparison of the time-averaged distribution of normalized $q\tau_w$ in Figure 7.31 indicates that at this low Reynolds number, shear stress decreases continuously along much of the surface distance. Low, near-zero levels of wall shear persist through the region of transitional flow prior to the trailing edge.

Before concluding this discussion, a few comments with regard to skew are worth considering. Consistent with previous interpretation, the contours of skew in Figure 7.27c remain near zero in laminar region A. In region B, high positive skew occurs at the leading boundary of the strip, while at the trailing boundary, skew is negative. This likely results from phase-wise “jitter” between individual turbulent events and the ensemble average. For this case, if fewer than half the events occur early in time relative to the average, the result would be just what appears in region B of Figure 7.27c — that is, positive skew at the leading boundary and negative skew at the trailing boundary of B. This brings to light another point of caution regarding the interpretation of unsteady measurements such as these. In an ensemble-averaged sense, jitter between successive periodic events, turbulent fluctuations, and laminar/turbulent switching contribute to skew and random unsteadiness.

The frequency spectra for the three test conditions are given in Figure 7.33. As expected from the above discussion, we find the signature of transition, that being the shifting of energy to higher frequencies, occurring further aft as Reynolds number is reduced.

7.5 Effects of Loading

In this section, the effect of loading level on boundary layer development is evaluated. Airfoil loading in the LSRT was varied by changing the flowrate through the turbine. At in-

creased loading, flow turning across the bladerows is increased and vice versa for decreased loading. Results are presented from the suction surface of the nozzle and rotor and from the pressure surface of the nozzle. For the test cases considered, Reynolds number was held fixed while loading was varied unless otherwise noted.

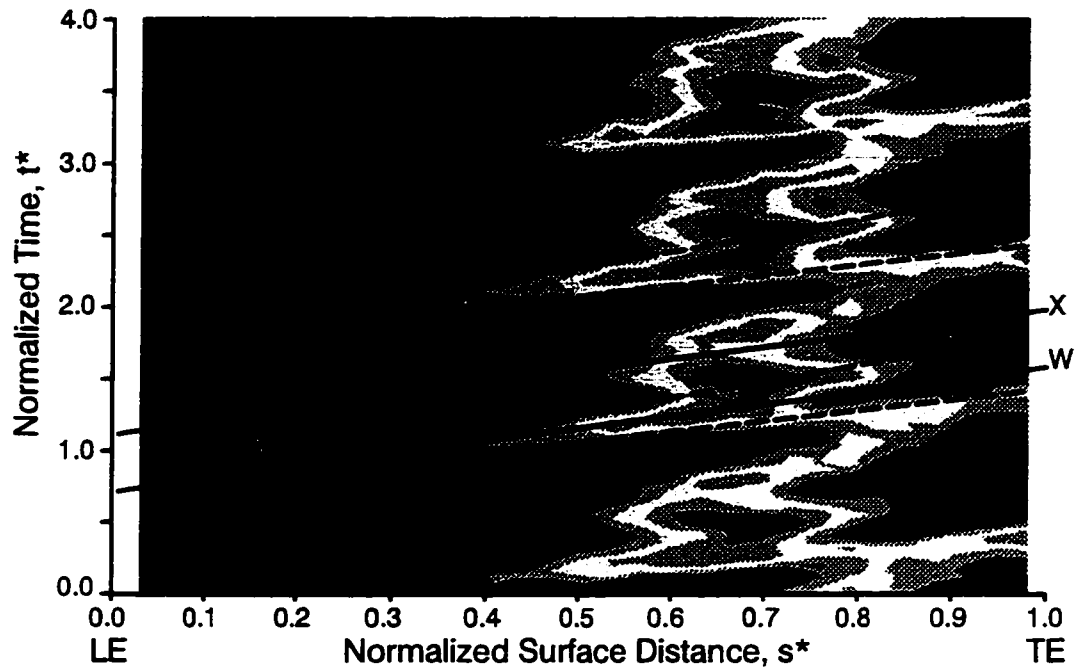
7.5.1 Nozzle Suction Surface

Measurements of boundary layer development along the nozzle suction surface are documented in Figures 7.34–7.38. They were obtained at increased and decreased loading and correspond to test points 5B and 7B, respectively. The Reynolds number, being equal to 3.96×10^5 for both, is for a takeoff condition. It should be noted that test point 5B was obtained at the same increased loading condition as the data sets from Section 7.4 that addressed Reynolds number effects and hence can be compared to those results accordingly.

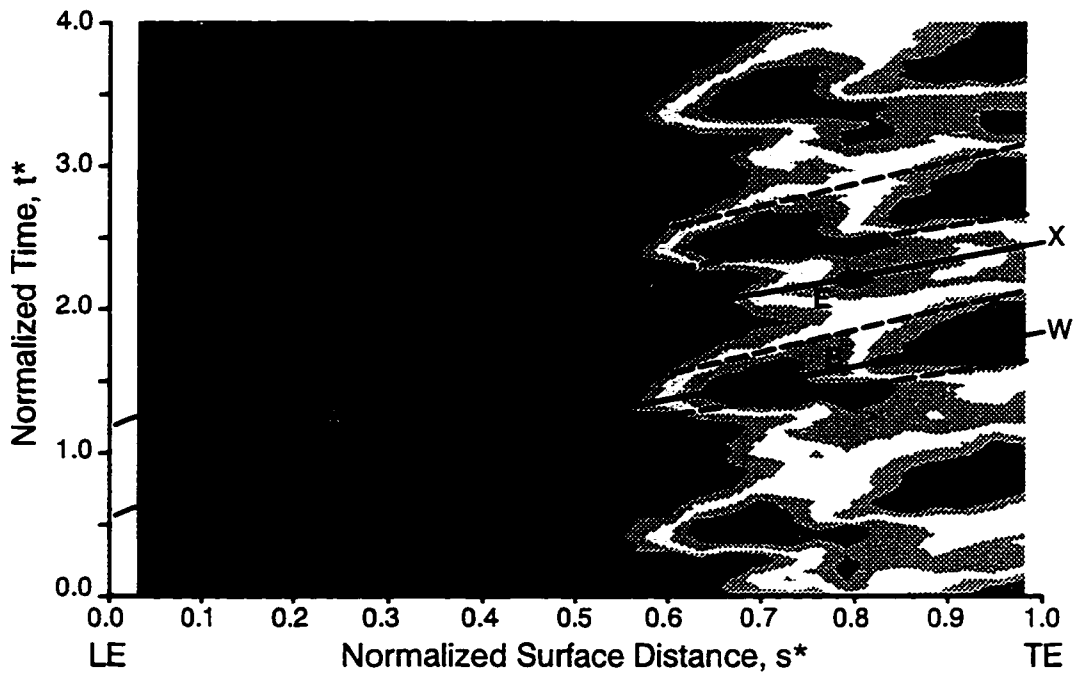
The velocity distributions along the nozzle for test points 5B and 7B are given in Figure 7.2a. The only significant differences occur along the initial 40 percent of the suction surface. As noted previously, a region of local diffusion occurs near $0.35s^*$ at increased loading. For decreased loading, however, continuous acceleration is maintained from the leading edge to maximum velocity at $0.62s^*$.

Boundary layer development at increased loading is similar to that observed at the take-off Reynolds number condition, test point 5A, described in the previous section. In Figures 7.34a and 7.35a, we see that wake-induced transition commences at $0.33s^*$ at the region of local diffusion. The line plots along trajectory W, shown in Figures 7.36a and 7.37a, show the transitional strip B extending to $0.87s^*$. Between wakes, transition in region E is shown in the color contour plots extending from $0.52s^*$ to $0.85s^*$. Turbulent regions C and F extend along the wake-induced and non-wake-induced paths back to the trailing edge. Calmed regions D and G are identified as well with the latter also extending to the trailing edge.

A different picture of boundary layer development emerges at decreased loading. The contour plot of random unsteadiness in Figure 7.34b shows a larger extent of laminar region A.

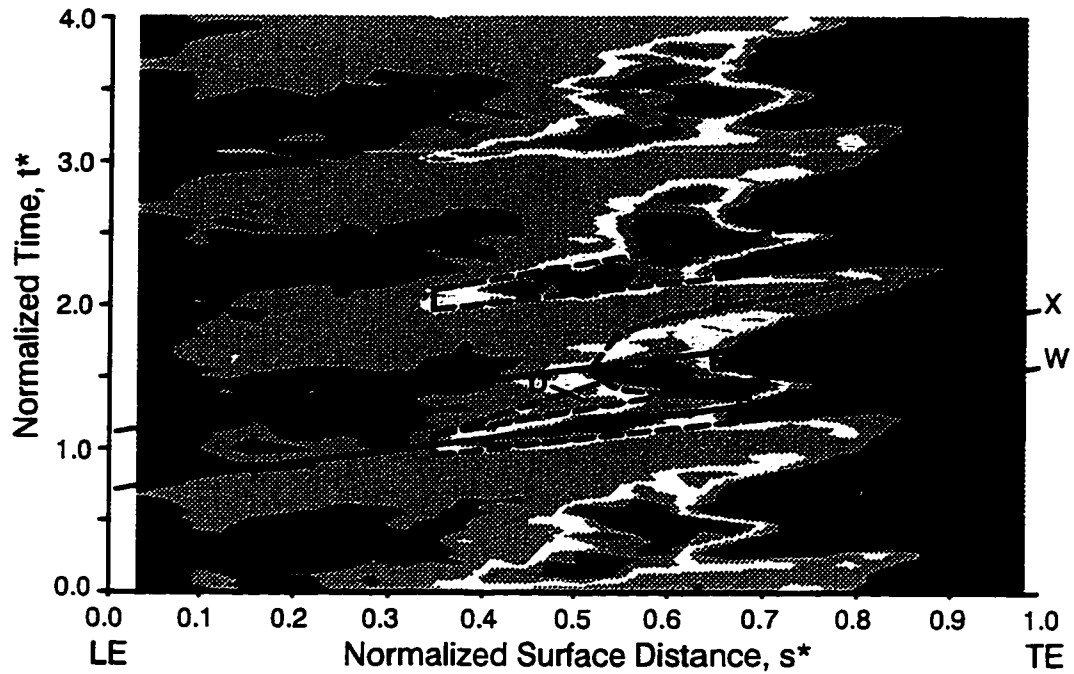


a) test point 5B, increased loading ($Q_0=0.88$, $Q_{10}=9.48$)

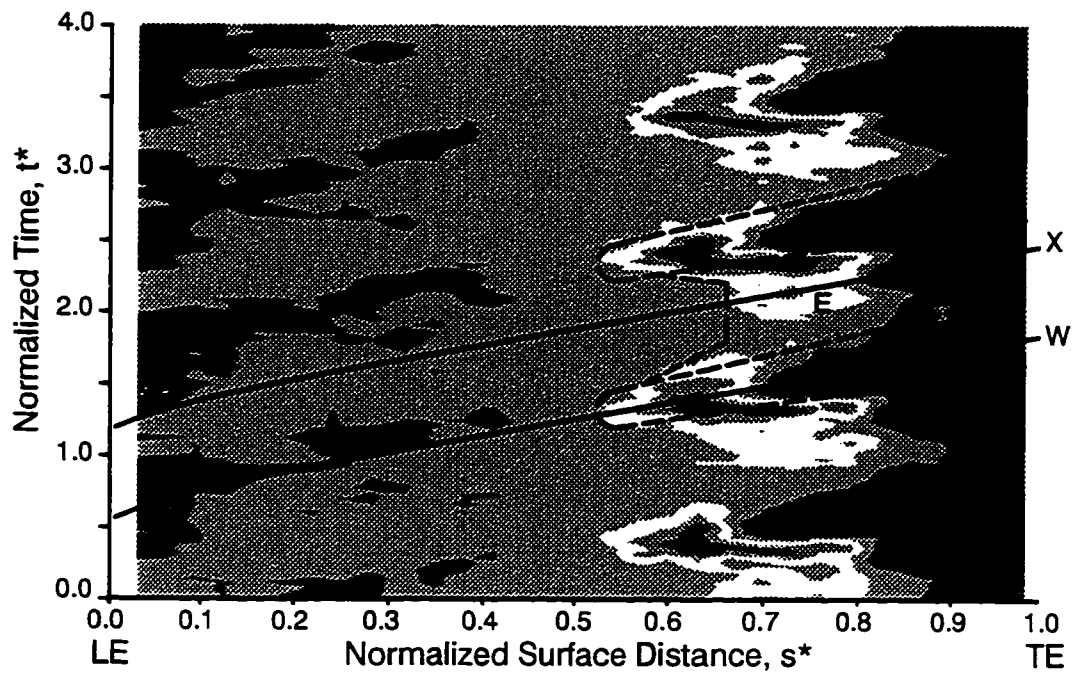


b) test point 7B, decreased loading ($Q_0=0.64$, $Q_{10}=10.54$)

Figure 7.34. Space-time diagrams of random unsteadiness along suction surface of Nozzle 2

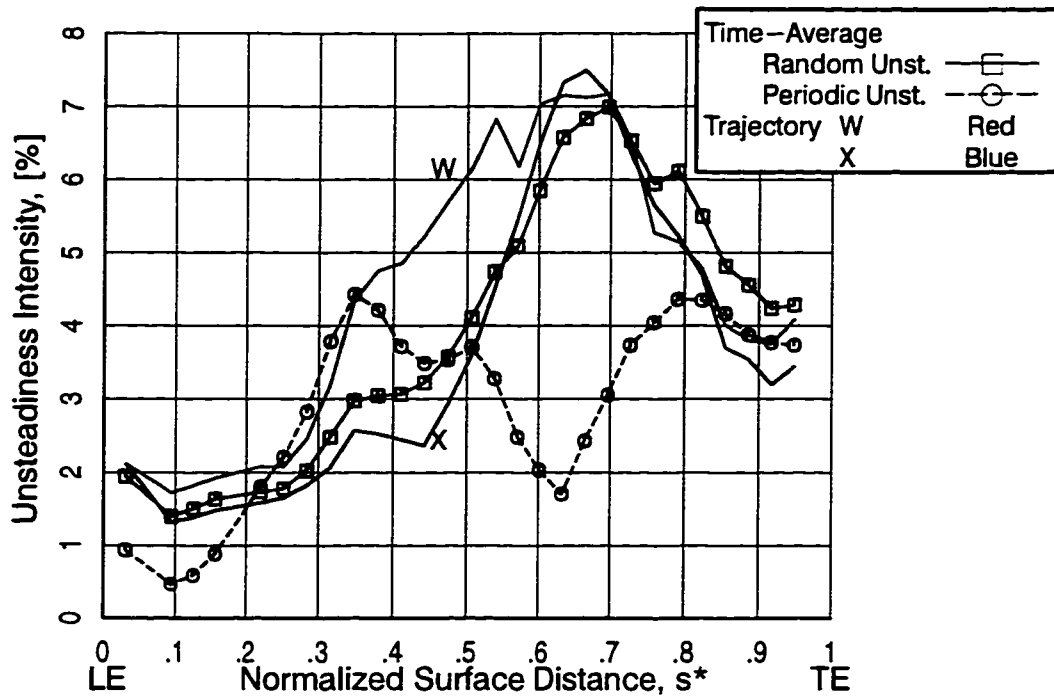


a) test point 5B, increased loading ($Q_0=-2.3$, $Q_{10}=2.3$)

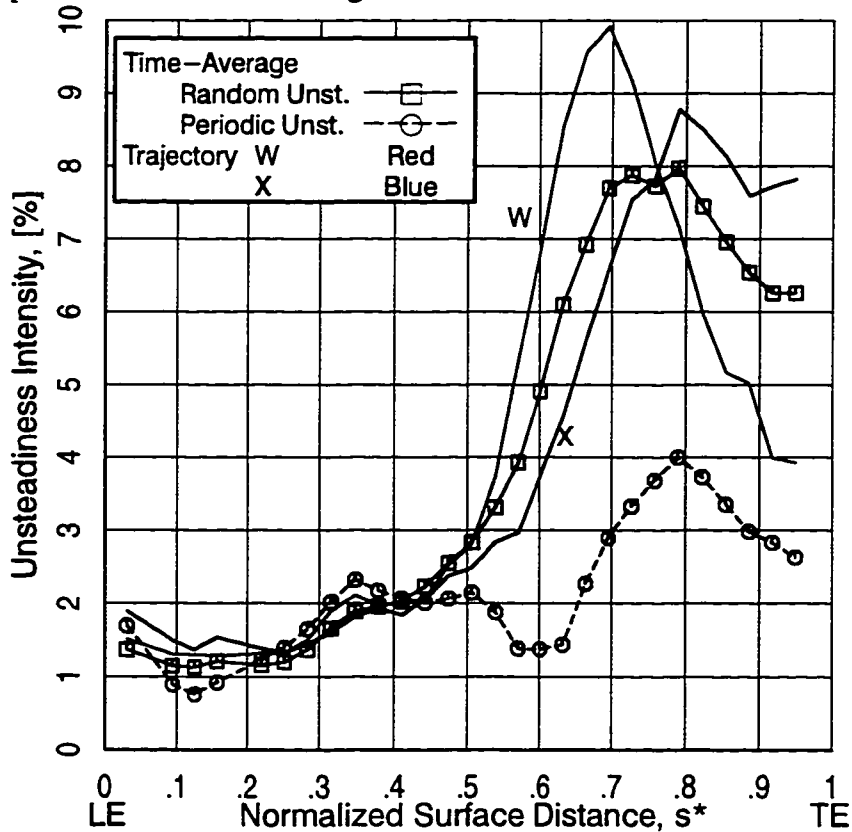


b) test point 7B, decreased loading ($Q_0=-3.0$, $Q_{10}=3.0$)

Figure 7.35. Space-time diagrams of skew along suction surface of Nozzle 2

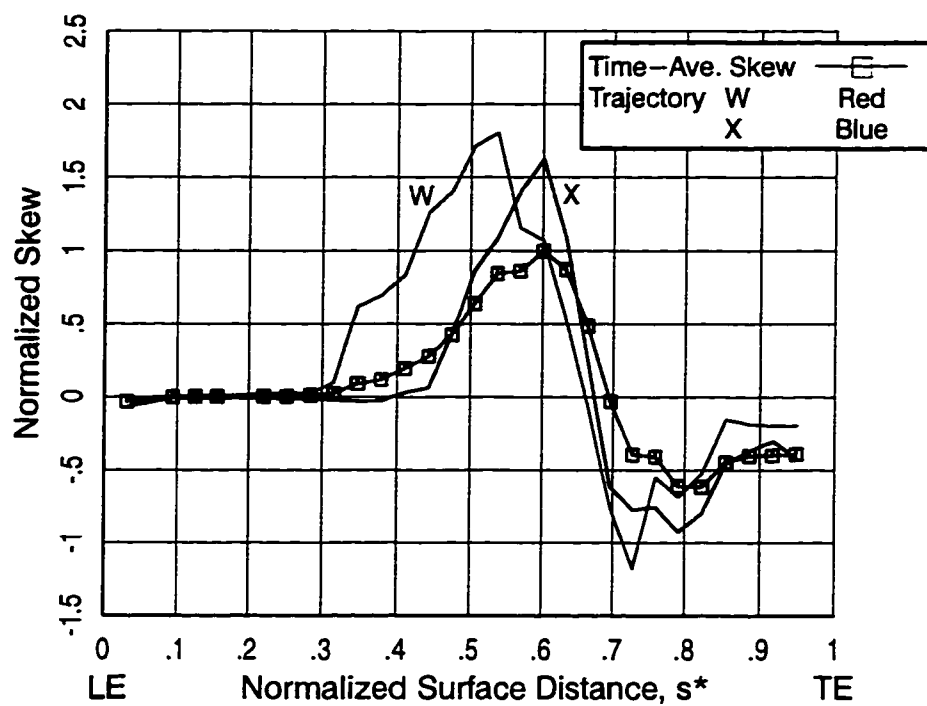


a) test point 5B, increased loading

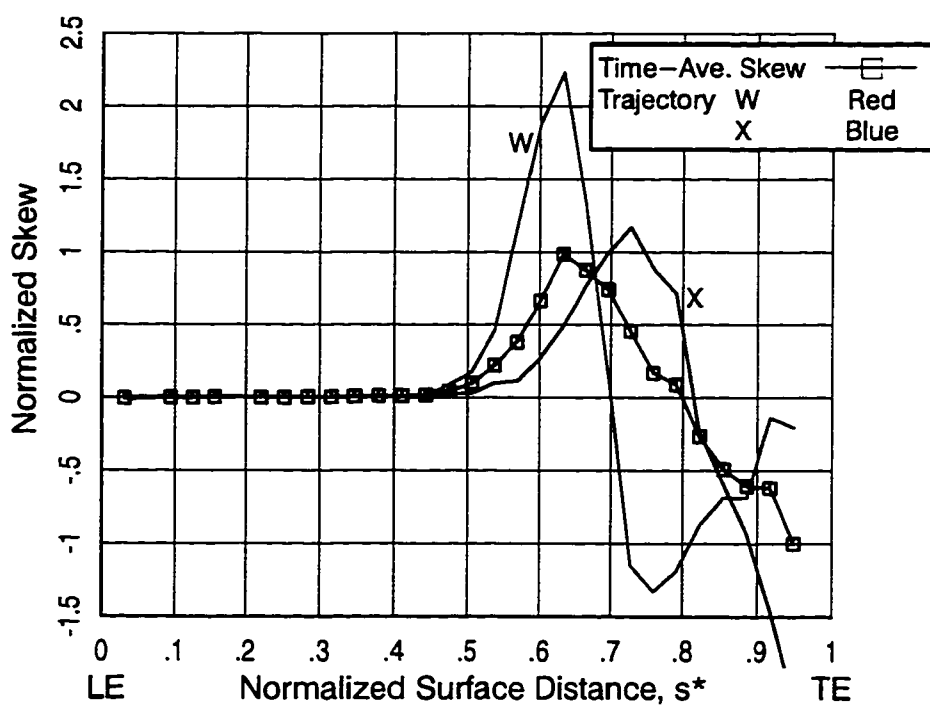


b) test point 7B, decreased loading

Figure 7.36. Time-averaged distributions of random and periodic unsteadiness along suction surface of Nozzle 2



a) test point 5B, increased loading



b) test point 7B, decreased loading

Figure 7.37. Time-averaged distributions of skew along suction surface of Nozzle 2

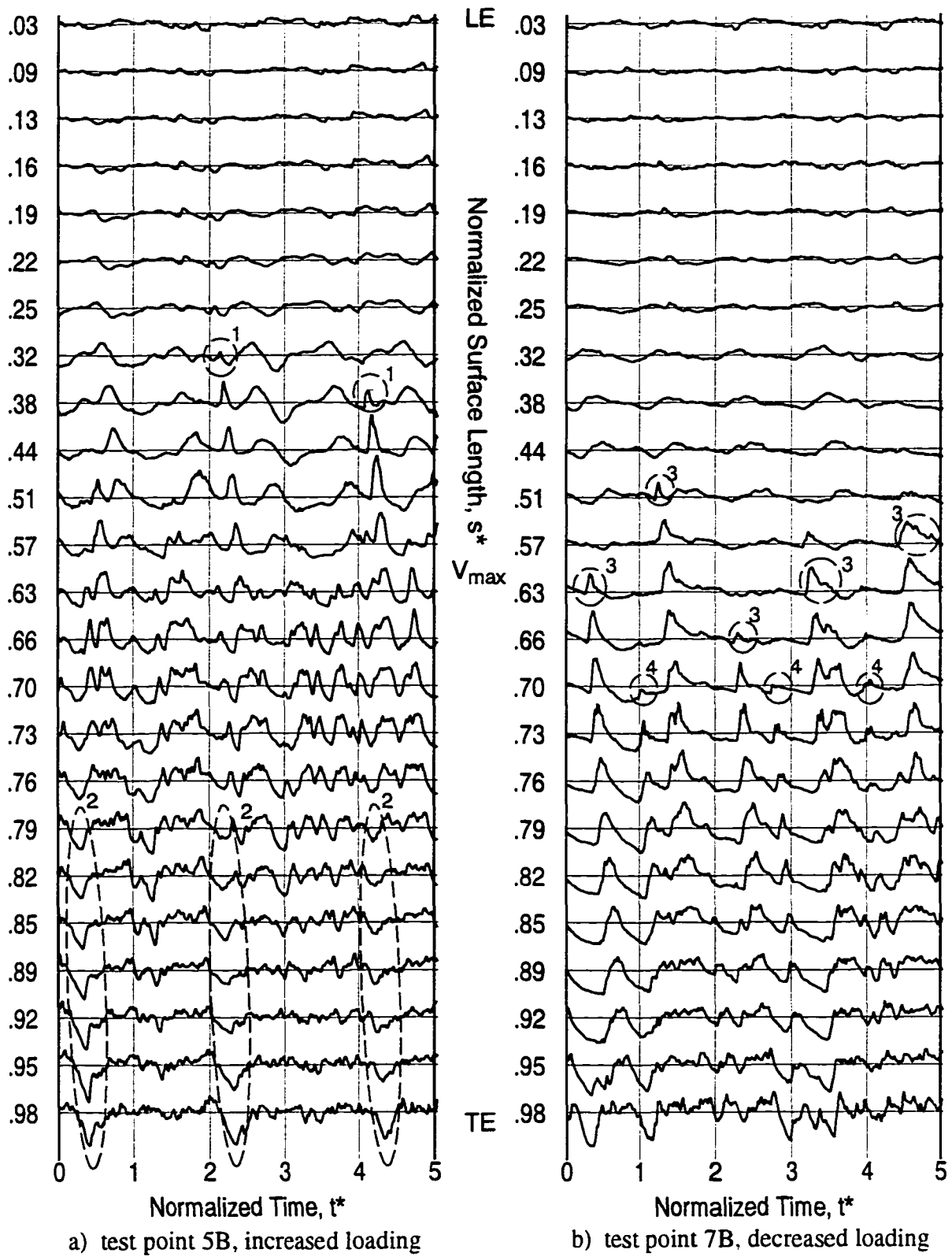


Figure 7.38. Instantaneous time traces along suction surface of Nozzle 2

The earliest evidence of wake-induced transition has shifted from $0.33s^*$ at increased loading to $0.53s^*$. This is evident from the now familiar signatures of random unsteadiness and skew in Figures 7.34b and 7.35b, respectively. The line plots of random unsteadiness and skew along trajectory W (Figures 7.36b and 7.37b, respectively) reveal that transition of the wake-induced strip is completed just prior to the trailing edge — about 10 percent aft of that at increased loading. Between wakes, transition begins from 0.60 – $0.65s^*$. No evidence of specific calming regions is apparent. From the s - t diagrams, we see that transition in region E is about three-quarters complete at the trailing edge. It is noteworthy that transition onset between wake paths occurs just at or downstream of maximum velocity for this takeoff Reynolds number condition.

Lastly, we consider a set of instantaneous traces from each test point as given in Figure 7.38. At increased loading, examples of wake-induced transition onset are identified by areas 1 in Figure 7.38a. That turbulent events do not appear in the traces for each passing wake in this region is consistent with the long transition length along W — almost 50 percent surface distance. At $0.57s^*$, the instantaneous traces exhibit transitional flow between wake paths. The distinct calmed regions extending back to the trailing edge (encircled regions 2) coincide with region G of Figures 7.34a and 7.35a.

Consistent with the contour plot of random unsteadiness, wake-induced turbulent events for decreased loading (Figure 7.38b) appear first at $0.51s^*$. Examples of a number of wake-induced events are labeled “3.” By $0.7s^*$, turbulent events are established between wake-induced paths as indicated by areas 4.

7.5.2 Rotor Suction Surface

Results obtained from the rotor suction surface are presented to further illustrate the influence of the airfoil velocity distribution on boundary layer development. Measurements for the rotor were obtained at baseline and increased loading, test points 6B and 5B, respectively. The Reynolds number for the latter was about 13 percent lower than for 6B. Based on the results presented in Section 7.4, this difference is not significant for this comparison.

The effect of loading on the velocity distribution of the rotor is more pronounced than for the nozzle. As noted previously in reference to Figure 7.2b, continuous acceleration from the leading edge to maximum velocity is maintained at intermediate loading. At increased loading, a region of local diffusion occurs near $0.25s^*$ that is more pronounced than that for the nozzle.

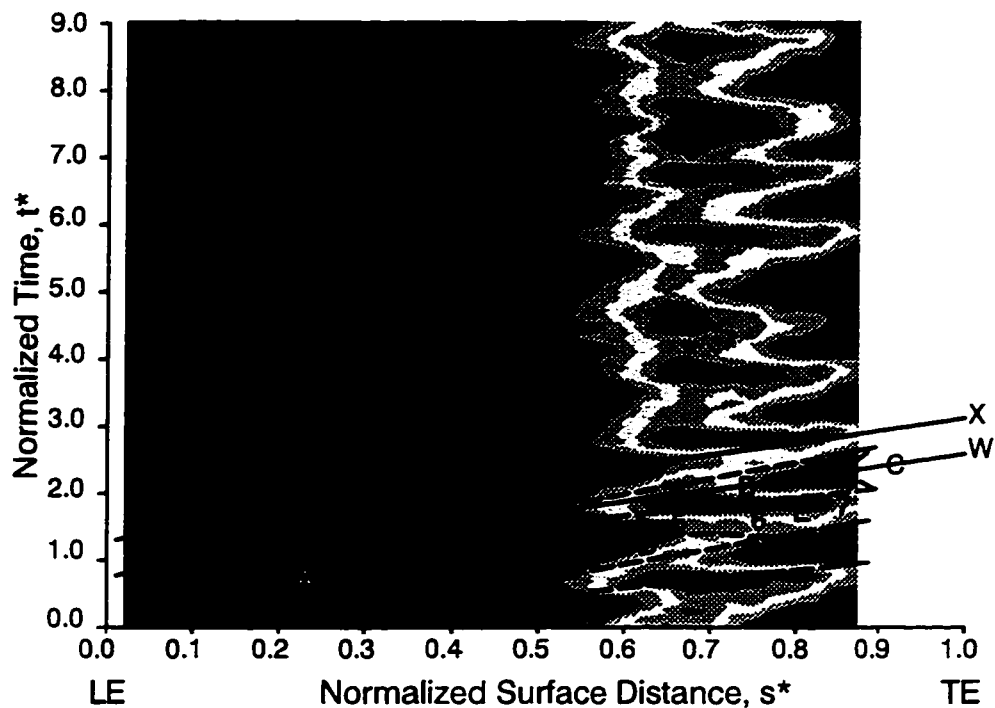
Selected shear stress characteristics for the two test conditions appear in Figure 7.39 and 7.40. Those from test point 6B pertain to the baseline results described in Section 7.32 and are repeated here to facilitate comparison.

Differences in boundary layer development are very apparent. For intermediate loading (Figure 7.39), we observed previously that transition onset along the wake-induced (trajectory W) and non-wake-induced (trajectory X) paths occurred at about 0.48 and $0.55s^*$, respectively. The distribution of skew in part b indicates that transition is just completed along W and is near its midpoint along X at the last sensor location.

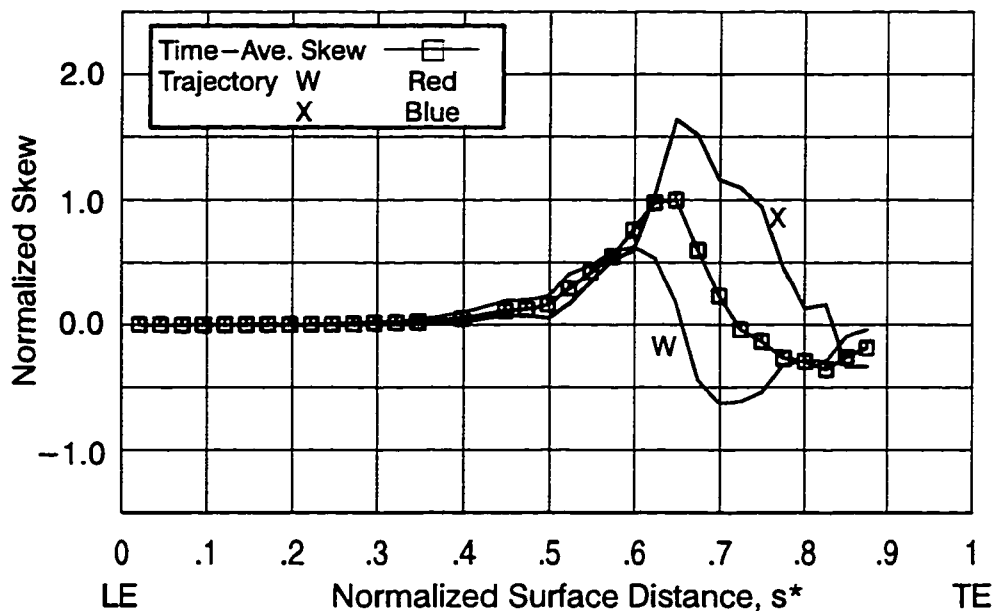
At increased loading in Figure 7.40, transition along W begins at $0.26s^*$ in the region of local diffusion. From the distribution of skew in part b, we see that transition along W reaches the midpoint at $0.42s^*$ – about 5 percent surface distance upstream of the transition onset location at intermediate loading. Between wakes, transition at increased loading commences at $0.5s^*$ and is about three-fourths complete at the last sensor.

In both $s-t$ diagrams of random unsteadiness, periodicity associated with the beat frequency from the upstream nozzles is evident.

In summary, boundary layer development along the suction surfaces is influenced significantly by the airfoil velocity distribution. For the cases considered here, regions of local diffusion prior to maximum velocity were sufficient to initiate boundary layer transition far upstream of where it would occur had constant acceleration been maintained.

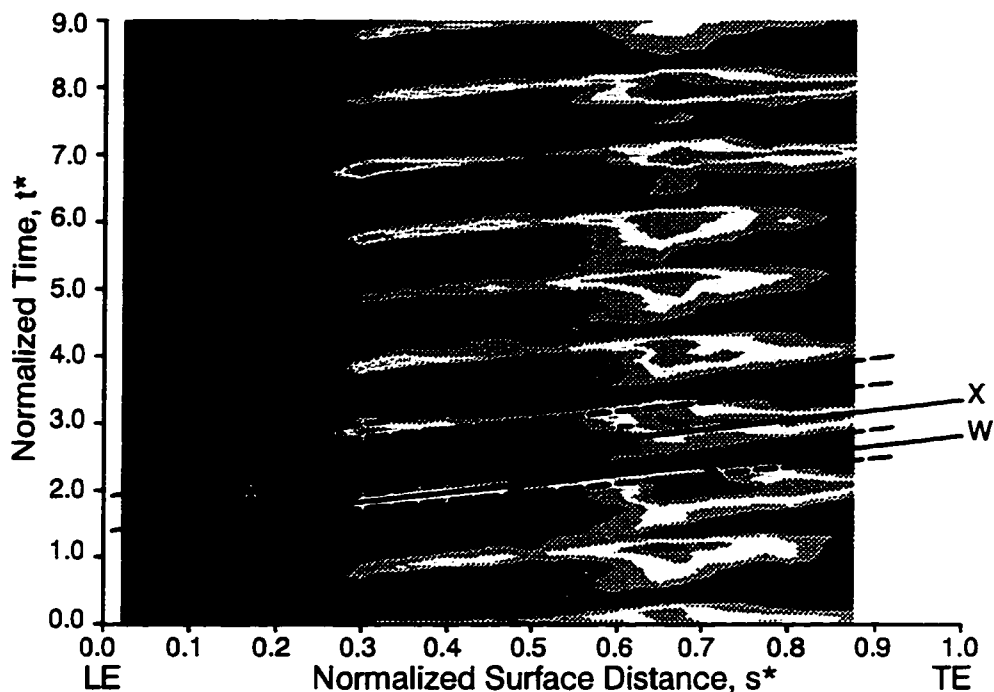


a) ensemble-averaged random unsteadiness ($Q_0=0.83, Q_{10}=13.23$)

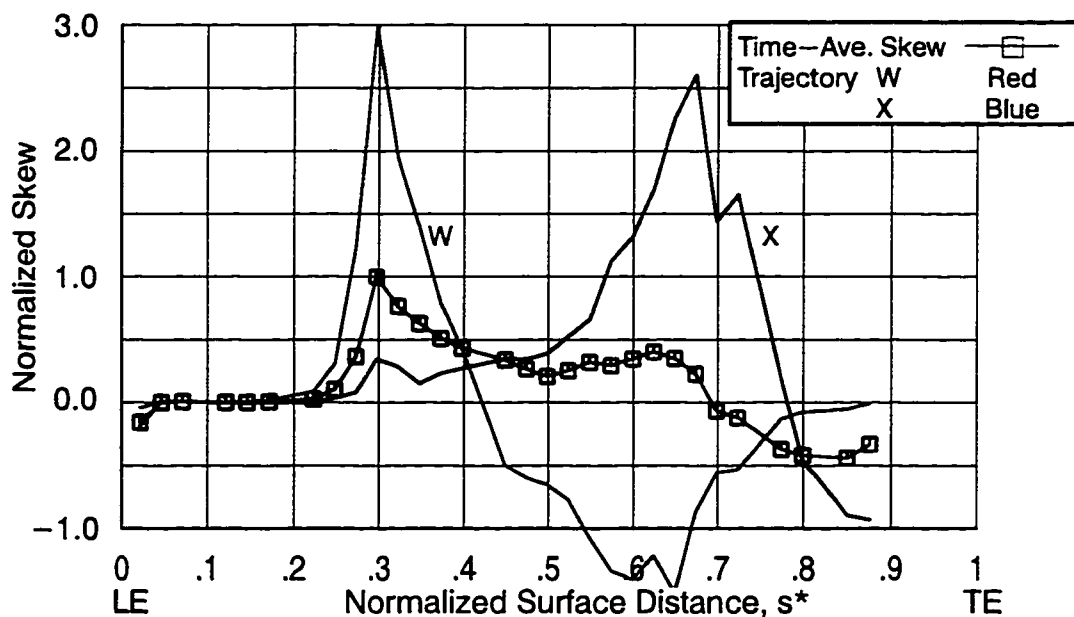


b) skew

Figure 7.39. Shear stress characteristics along suction surface of Rotor 2 at baseline loading, test point 6B



a) ensemble-averaged random unsteadiness ($Q_0=0.69, Q_{10}=11.99$)



b) skew

Figure 7.40. Shear stress characteristics along suction surface of Rotor 2 at increased loading, test point 5B

7.5.3 Nozzle Pressure Surface

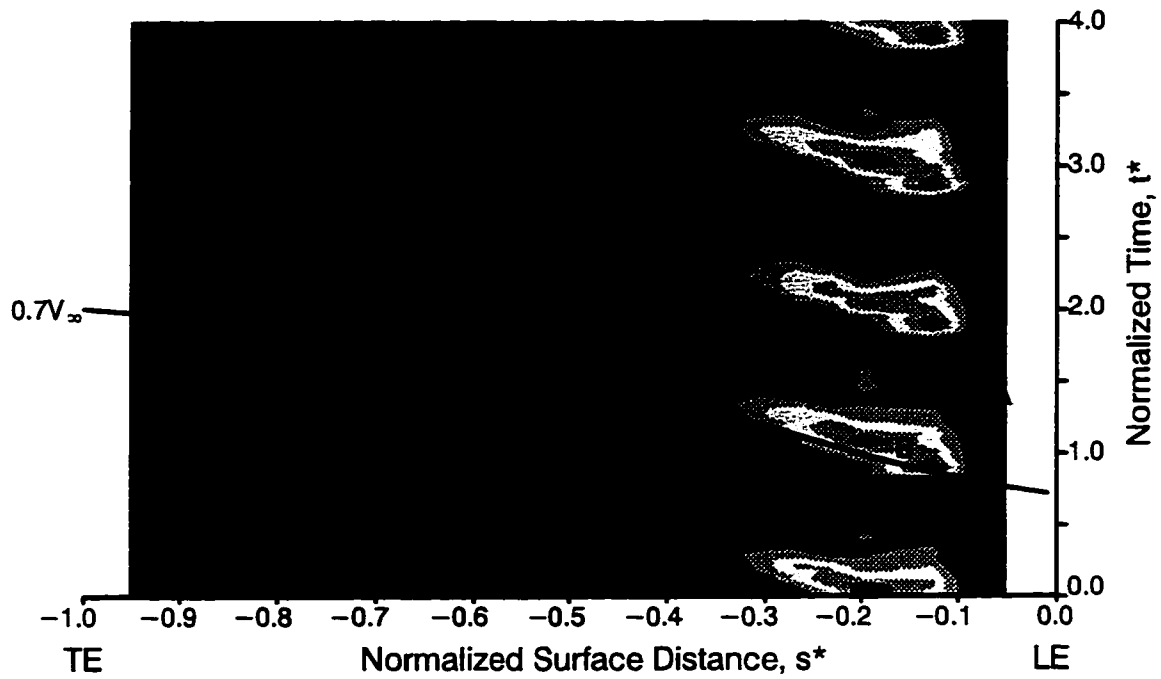
We will conclude the discussion on the effects of loading by considering results from along the nozzle pressure surface. Measurements from increased loading (test point 5D) and decreased loading (test point 7D) are compared. Both data sets were acquired at the cruise Reynolds number of 1.80×10^5 . During the course of the test program, it was determined that the pressure surface boundary layer did not vary significantly with Reynolds number. Consequently, complete data sets were acquired for each loading level at the cruise Reynolds number only.

At increased loading, the incidence angle becomes less negative relative to the baseline condition. From the contour plot in Figure 7.41a, we find that random unsteadiness is initially low at the first sensor locations indicating the presence of laminar-like flow (region A). This is confirmed from the instantaneous time traces in Figure 7.42a. By the third sensor at $0.12s^*$, distinct turbulent events are present at intervals of wake-passing. These are labeled "1" and correspond to region B of Figure 7.41a.

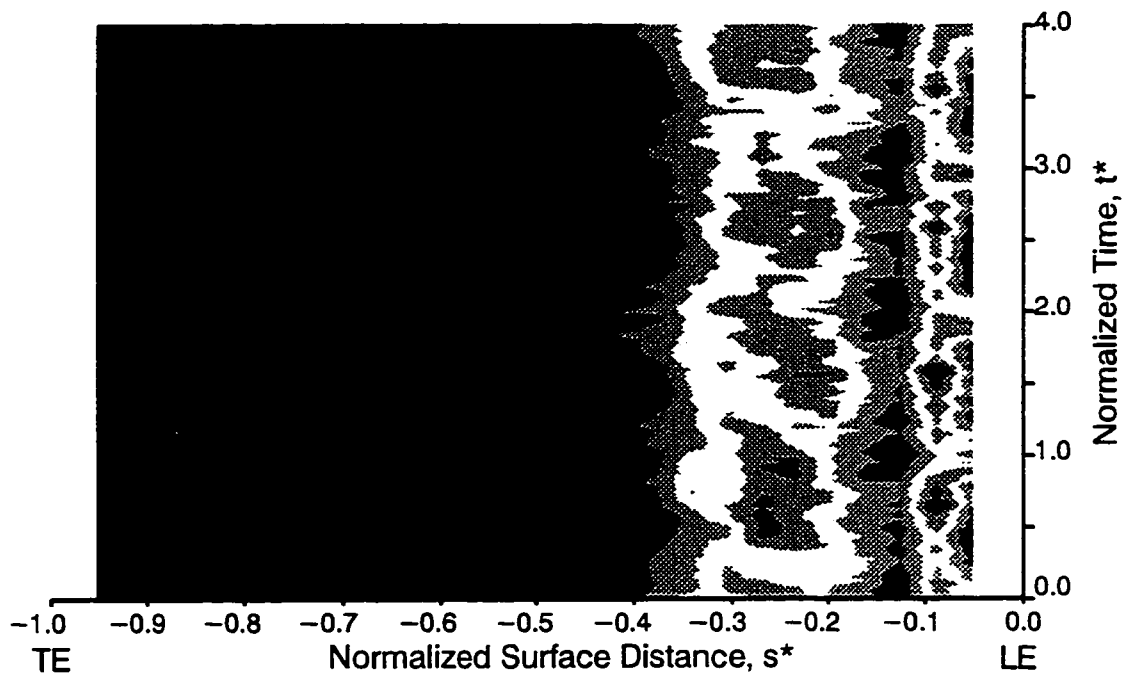
Between the wake-induced paths, the fluctuations in shear stress identified as areas 2 in Figure 7.42a are indicative of disturbed, laminar flow. By 0.16 and $0.20s^*$, transition of this flow is well underway as indicated by areas 3 in Figure 7.42a and region E in Figure 7.41a. By $0.27s^*$, the instantaneous traces contain no evidence of conventional laminar flow though a periodic character of the shear stress variation is maintained.

From the contour plot of frequency spectra in Figure 7.43a, we see energy extending to higher frequencies downstream of $0.1s^*$ as a result of boundary layer transition. This is followed by energy dissipation as transition is completed and the flow undergoes acceleration.

For test point 7D at decreased loading, the nozzle is subjected to a higher degree of negative incidence. Here, the s - t diagram of random unsteadiness in Figure 7.41b indicates that transition occurs abruptly and close to the leading edge. The instantaneous trace at $0.05s^*$ in Figure 7.42b reveals high amplitude fluctuations at intervals of blade passing with lower amplitude fluctuations between. By $0.09s^*$, the fluctuations in the trace are much more turbulent in charac-

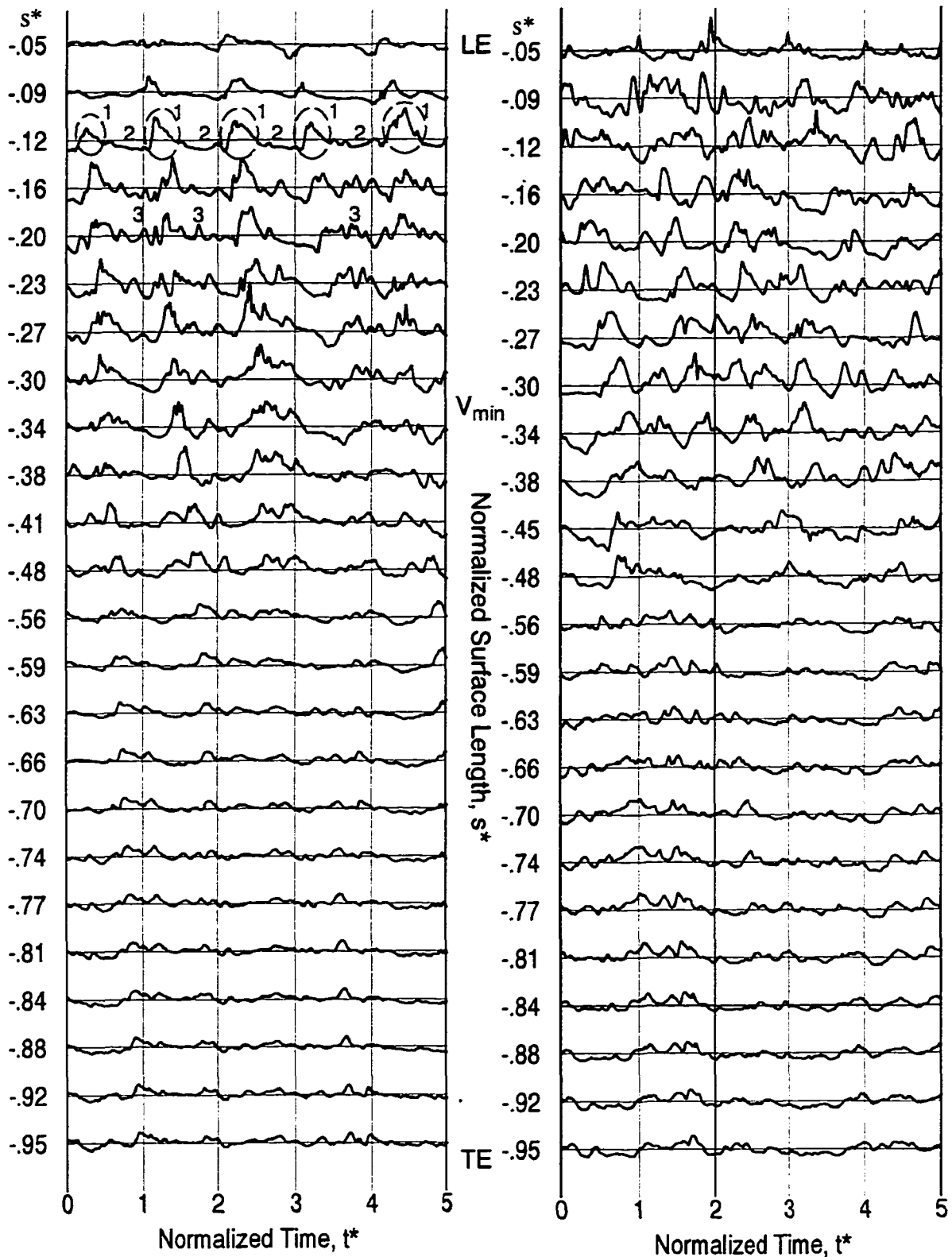


a) test point 5D, increased loading ($Q_0=1.29$, $Q_{10}=19.09$)



b) test point 7D, decreased loading ($Q_0=2.24$, $Q_{10}=17.54$)

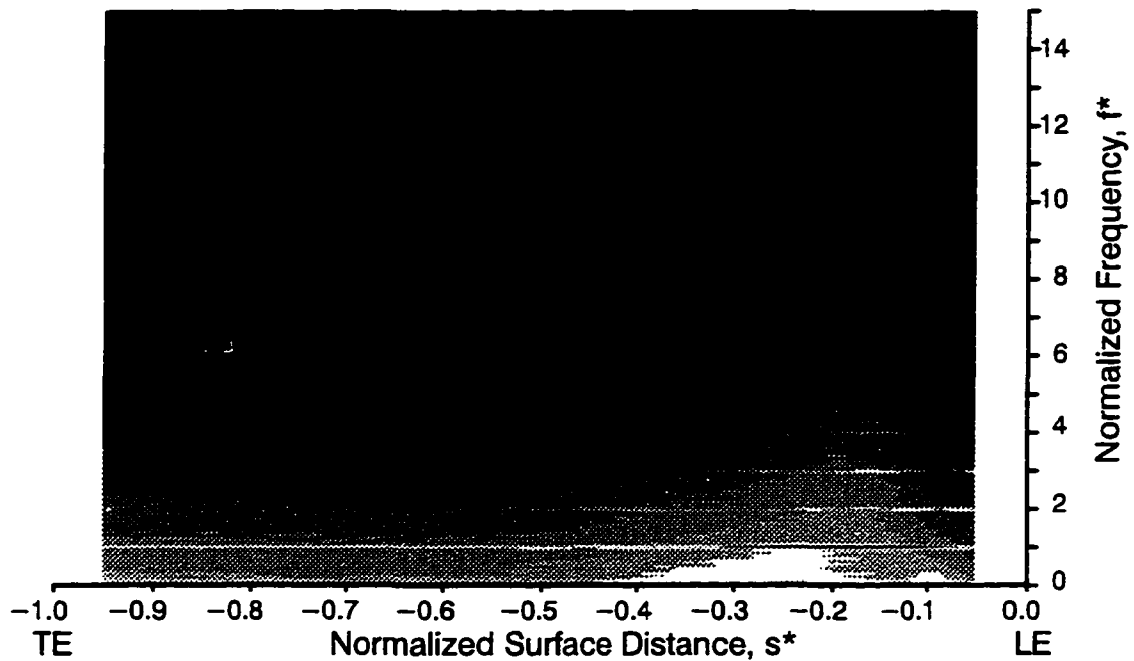
Figure 7.41. Space-time diagrams of random unsteadiness along pressure surface of Nozzle 2



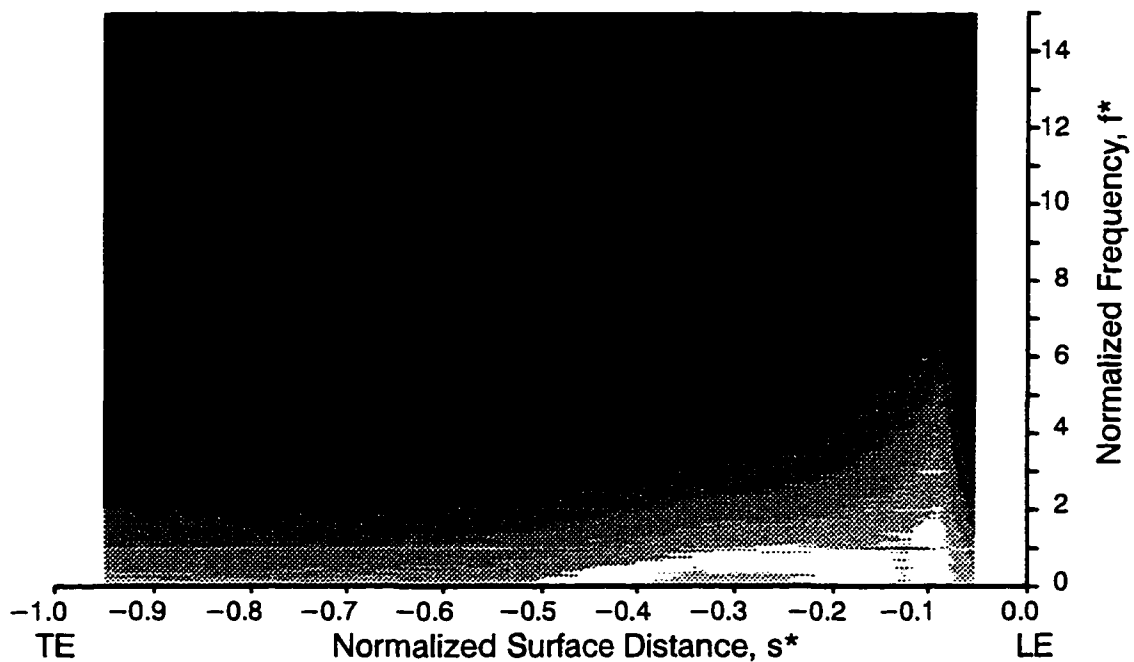
a) test point 5D, increased loading

b) test point 7D, decreased loading

Figure 7.42. Instantaneous time traces along pressure surface of Nozzle 2



a) test point 5D, increased loading ($Q_0=-95.0$, $Q_{10}=-50.0$)



b) test point 7D, decreased loading ($Q_0=-95.0$, $Q_{10}=-50.0$)

Figure 7.43. Space-frequency diagrams of normalized RMS spectra along pressure surface of Nozzle 2

ter. Unlike for test point 5D, no visible correlation is present between traces from the second and third sensors. As was concluded in Section 7.3, it is likely that transition has occurred in a separated shear layer with complete reattachment taking place prior to $0.09s^*$. As expected, the normalized RMS spectra of Figure 7.43b show a very abrupt shift of energy to higher frequencies at a location upstream of that for test point 5D.

7.6 Effects of Nozzle Clocking

In this section, the effect of clocking Nozzle 1 relative to Nozzle 2 on boundary layer development is considered. The variation of profile loss of Nozzle 2 with Nozzle 1 clocking will be presented in Chapter 9. For the Nozzle 2 suction and pressure surfaces, measurements were acquired at the baseline test point 6B and increased loading test point 5D, respectively. Complete sets of surface hot-film data were taken for five circumferential orientations of Nozzle 1 relative to Nozzle 2. To this end, Nozzle 1 was indexed at increments of 20 percent pitch from 0 percent to 80 percent. It should be emphasized that over the course of which these measurements were obtained, the test condition of the turbine was held constant. The only change was the location of Nozzle 1. The surface velocity distribution for Nozzle 2 did not vary perceptibly for the different clocking positions of Nozzle 1.

Results contained in this section were taken from two of the five clocking orientations and were chosen to illustrate the widest range of variation observed. Contour plots from each data set are plotted using the same color scales to allow direct comparison.

Distributions of turbulence intensity at the inlet to Nozzle 2 were obtained for the same five Nozzle 1 clocking positions described above. The two distributions that pertain to the surface hot-film data described below are plotted in Figure 7.44. These are ensemble-averaged distributions, hence the abscissas are normalized time. Only a cursory description of these measurements is given here. A more extensive treatment is reserved for Chapter 8. The peak levels of turbulence in each distribution of Figure 7.44 are identified as being associated with the wake from Rotor 1 (the bladerow immediately upstream of the X probe and Nozzle 2). They are la-

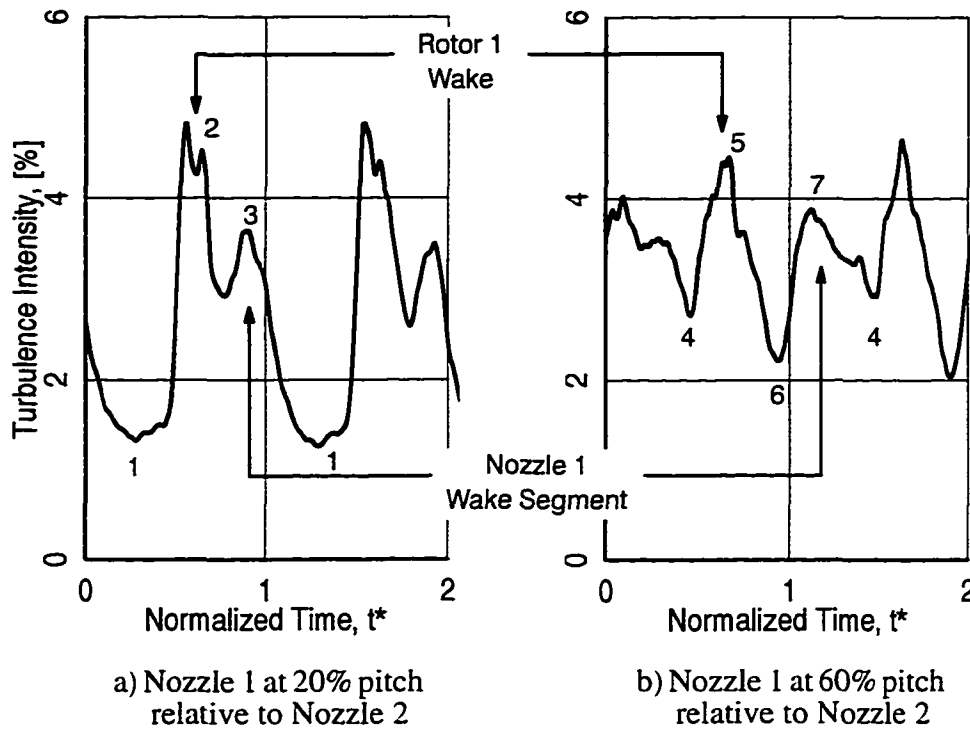
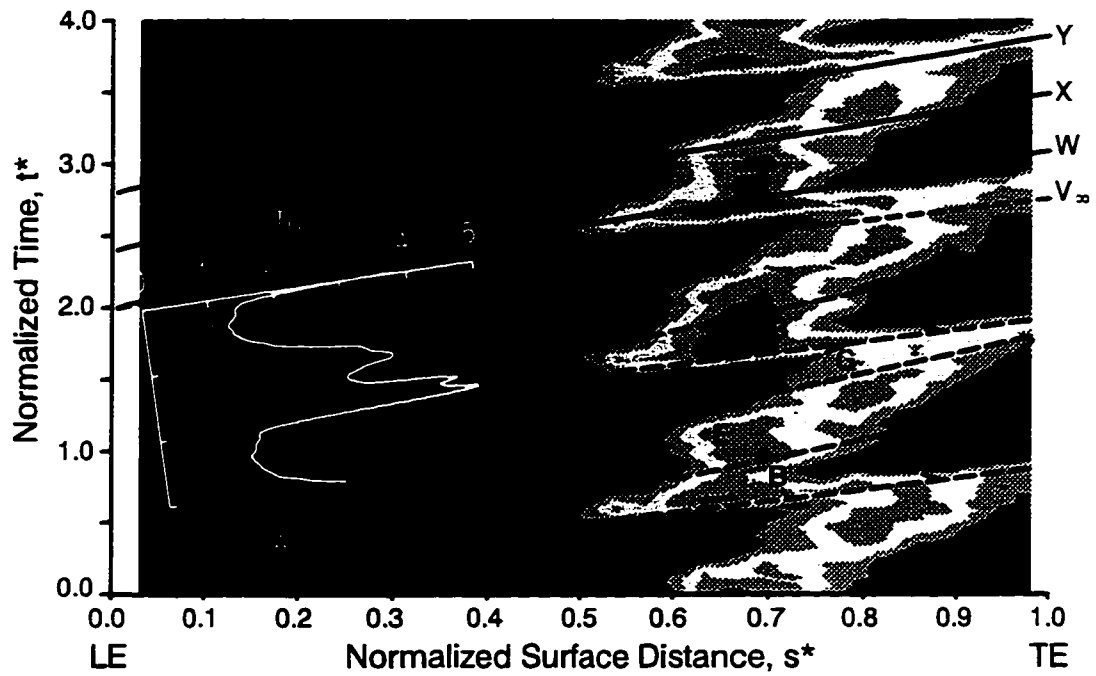


Figure 7.44. The effect of Nozzle 1 clocking on turbulence intensity at inlet to Nozzle 2

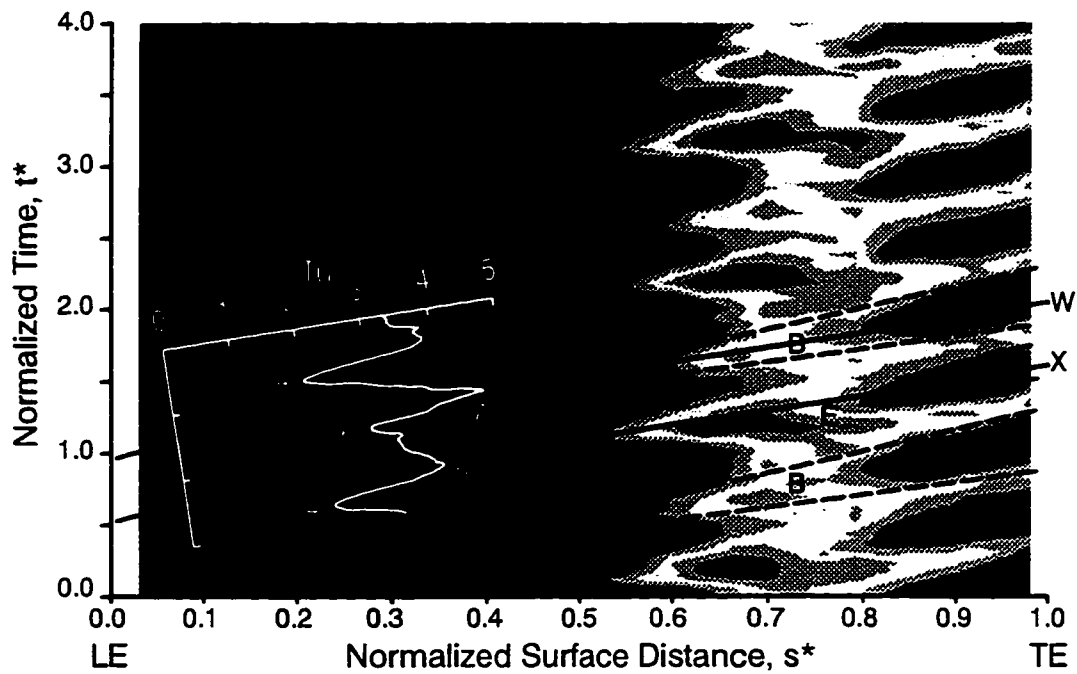
beled points 2 and 5. Between rotor wakes, a second local peak is observed in the distributions. They are identified by points 3 and 7 and pertain to the wake segment of Nozzle 1. Again, substantiation of this interpretation is given in Chapter 8.

7.6.1 Nozzle Suction Surface

The effect of nozzle clocking on the suction surface boundary layer of Nozzle 2 is documented in Figures 7.45–7.47. Part a of each figure is from the baseline data set described in Section 7.3.1 and are repeated here for comparison purposes. The clocking position of Nozzle 2 for these data was 20 percent relative pitch. The contour plot of random unsteadiness along with the identified regions of development make up Figure 7.45a. As before, the associated distribution of turbulence is superimposed onto the plot. From the interpretation described in Section 7.3.1, transition was found to occur first along the wake-induced path W where turbulence intensity is highest (points 2 of Figure 7.45a). Between wake paths, transition occurs earliest in conjunction with points 3. Again, this second local maximum is attributed to the wake segment of



a) Nozzle 1 at 20 percent pitch relative to Nozzle 2



b) Nozzle 1 at 60 percent pitch relative to Nozzle 2

Figure 7.45. Space-time diagrams of random unsteadiness along suction surface of Nozzle 2, test point 6B ($Q_0=0.56$, $Q_{10}=9.66$)

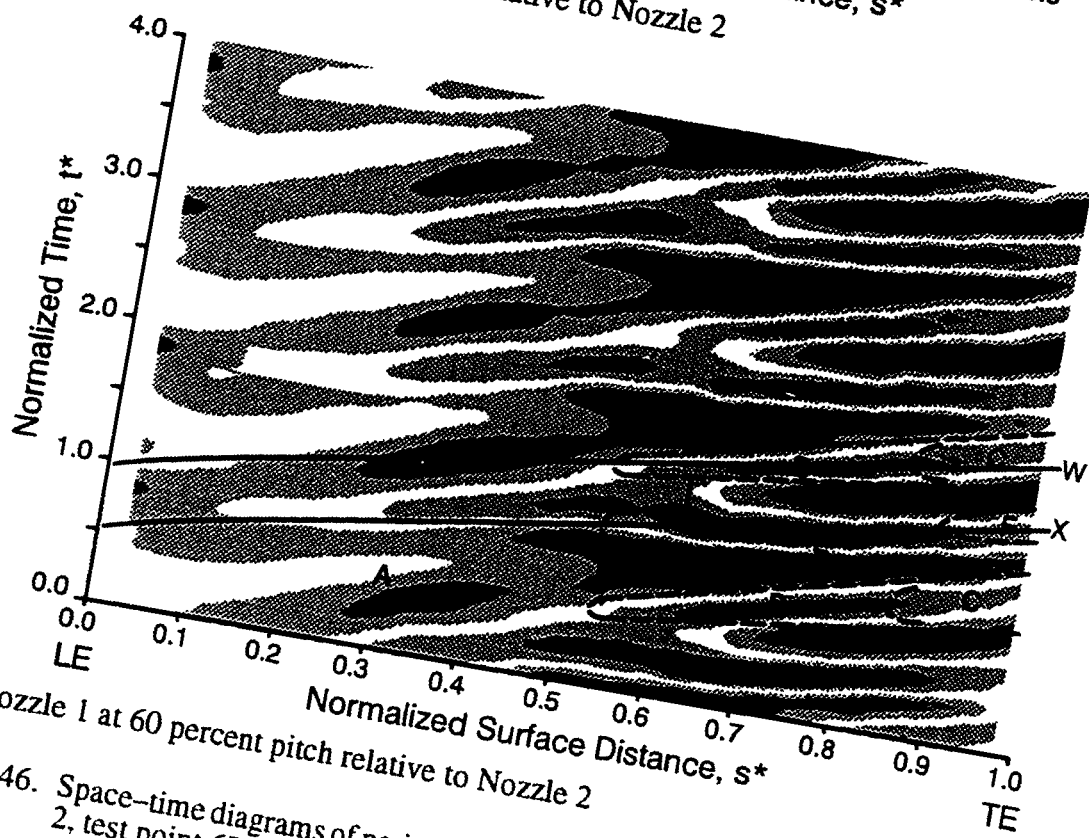
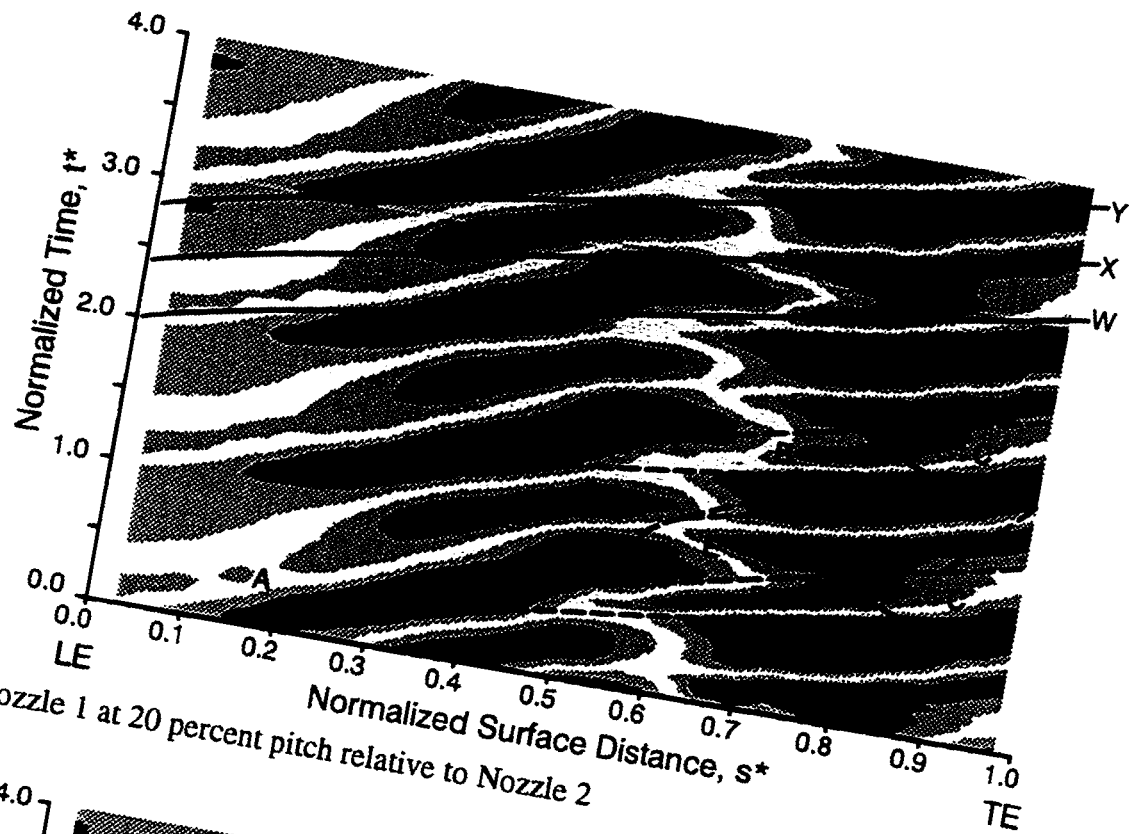
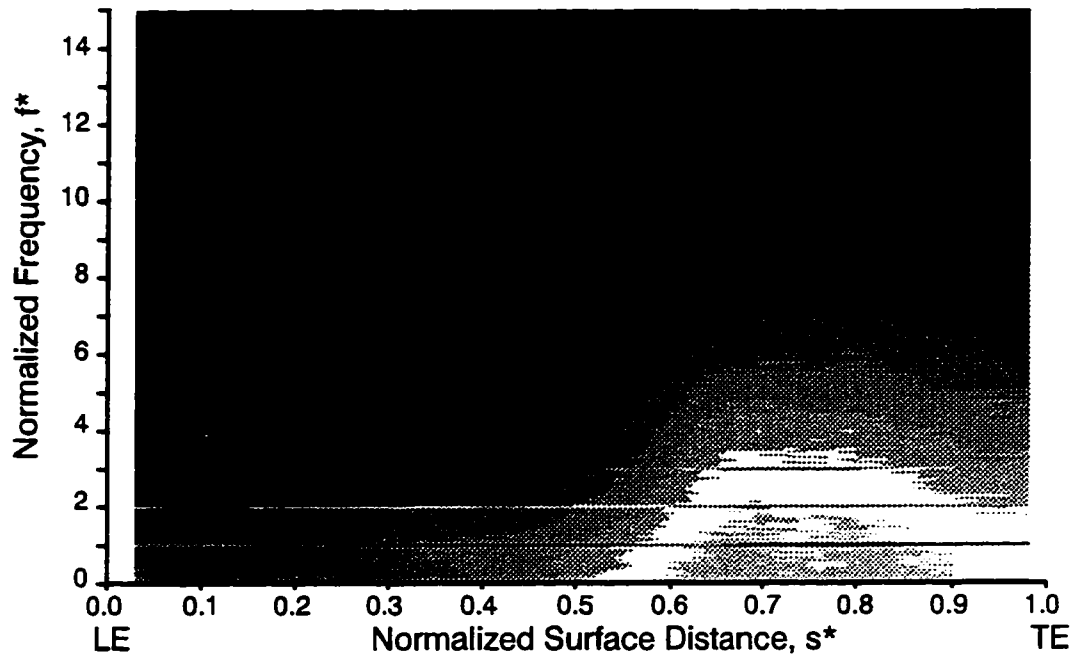
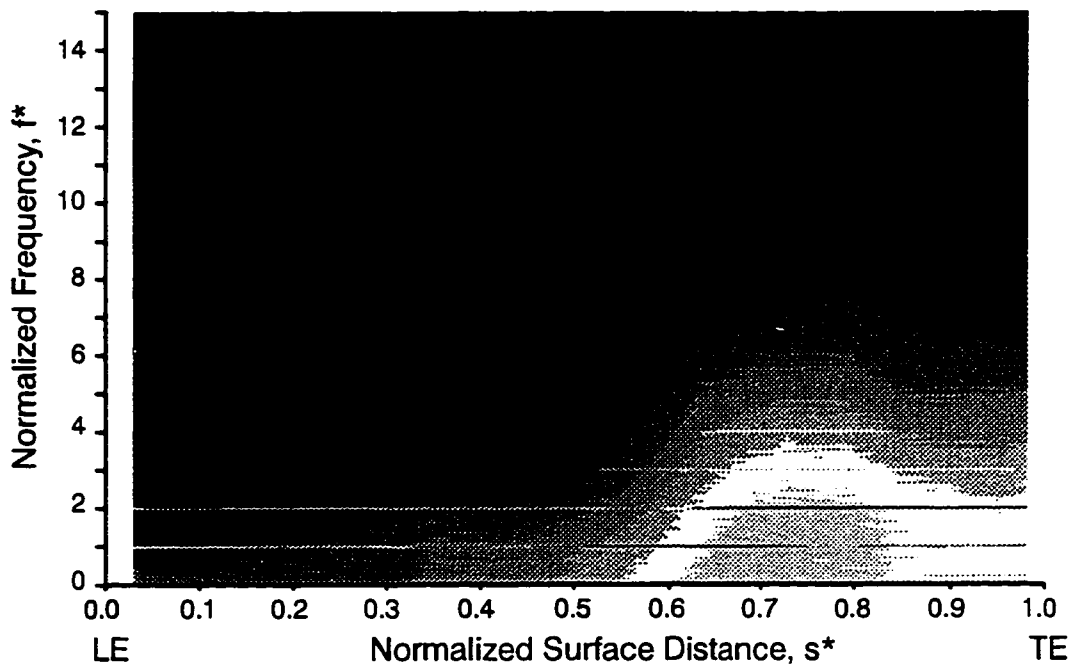


Figure 7.46. Space-time diagrams of periodic unsteadiness along suction surface of Nozzle 2, test point 6B ($Q_0 = -9.0$, $Q_{10} = 6.0$)



a) Nozzle 1 at 20 percent pitch relative to Nozzle 2



b) Nozzle 1 at 60 percent pitch relative to Nozzle 2

Figure 7.47. Space-frequency diagrams of normalized RMS spectra along suction surface of Nozzle 2, test point 6B ($Q_0=-95$, $Q_{15}=-50$)

Nozzle 1. Where the inlet turbulence is lowest along points 1, transition occurs furthest aft, commencing at $0.6s^*$.

A significantly different picture of boundary layer development occurs with Nozzle 2 at 60 percent relative pitch. The contour plot of random unsteadiness in Figure 7.45b shows the development of two distinct transitional/turbulent strips per wake-passing period. The distribution of inlet turbulence for this data set that is overlaid onto the contour plot shows a clear correlation with the strips. One strip occurs along the wake-induced path W. This is in phase with the wake turbulence of Rotor 1, identified by points 7. Here, transition begins near $0.53s^*$ and is completed by $0.85s^*$. Turbulent region C then extends back to the trailing edge. The second strip results from increased turbulence of the Nozzle 1 wake segment, point 5. Along this path (i.e., trajectory X), transition extends from about 0.53 to $0.90s^*$. This is followed by the turbulent region F. As a result of this development, periodic variations in random unsteadiness occur at twice blade-passing frequency at the trailing edge.

Predictably, the periodic unsteadiness of $q\tau_w$, given figure 7.46, shows differing development for the two data sets. The description for Nozzle 1 at 20 percent relative pitch (part a) was provided in Section 7.3.1. With Nozzle 1 at 60 percent pitch (part b), downstream of transition onset, the highest levels of shear stress are found along the strips where transition occurs earliest. Between strips, shear stress is lowest. Periodicity of $q\tau_w$ at twice blade-passing clearly develops downstream of transition onset. This latter point is demonstrated further by the contour plots of normalized RMS spectra. For Nozzle 1 at 60 percent, the largest amplitude of periodic unsteadiness along the latter 30 percent surface distance is that of two times blade-passing frequency. With Nozzle 1 at 20 percent, the fundamental blade-passing frequency is the dominant periodic component along almost the entire suction surface.

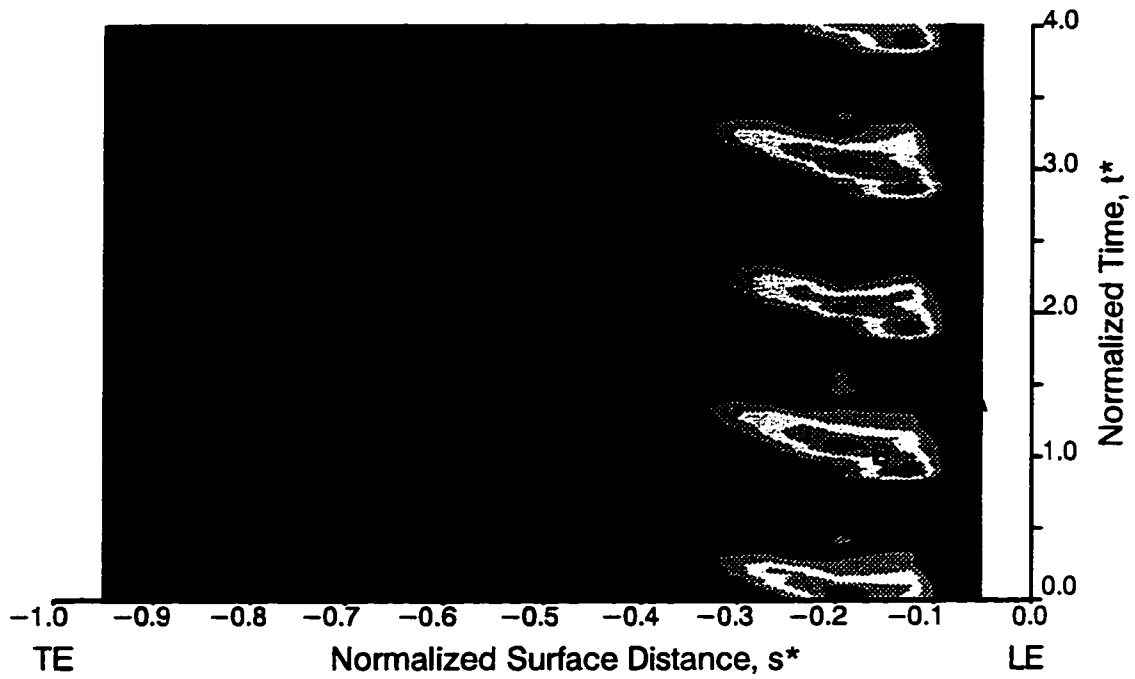
7.6.2 Nozzle Pressure Surface

An abbreviated set of results documenting clocking effects on the boundary layer of the Nozzle 2 pressure surface is given in Figures 7.48 and 7.49. The measurements were obtained

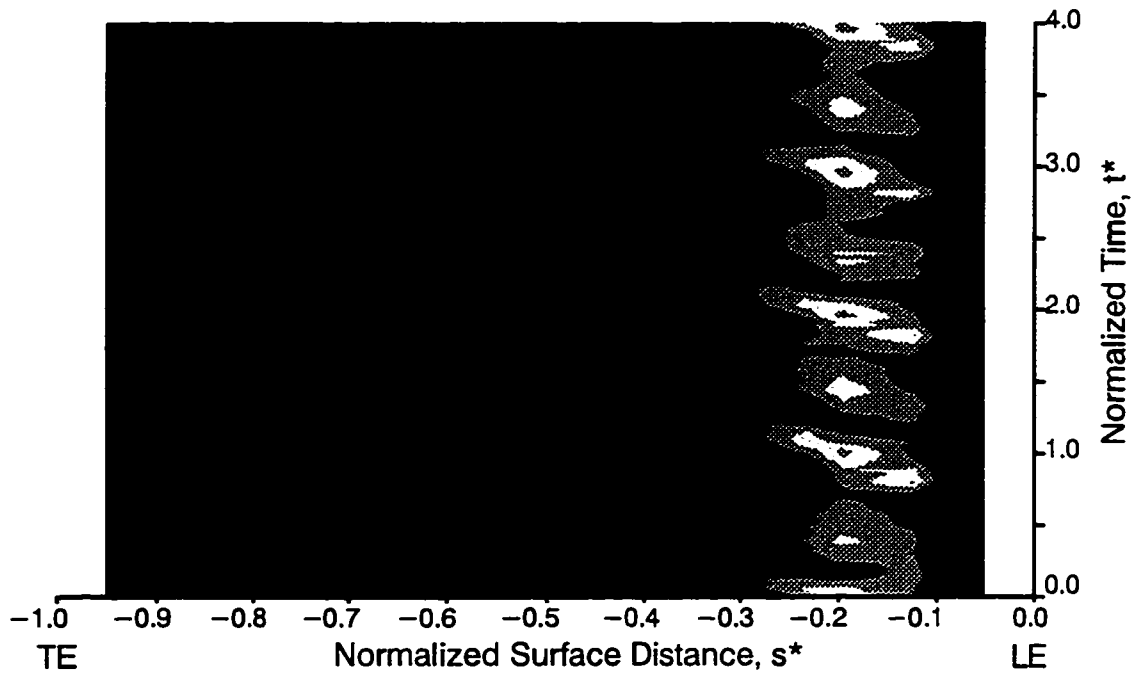
at test condition 5D corresponding to a cruise Reynolds number and increased loading. The increased loading condition was chosen so that the effects of clocking were not masked by the leading edge separation that occurred at the lower loadings. Also, due to time constraints, data sets from the pressure surface were obtained at this test condition only for differing locations of Nozzle 1.

Measurements with Nozzle 1 at 20 percent relative pitch, constituting parts a of Figures 7.48 and 7.49, are from the identical data set considered in Section 7.5.3 as part of the study of loading effects. As noted in the accompanying discussion, transition occurred first along a wake-induced path (region B) and then a non-wake path (region E). From Figure 7.49a, we see that shear stress is highest along region B where transition occurs first.

With Nozzle 1 at 60 percent relative pitch, the contour plot in Figure 7.48b contains regions of elevated random unsteadiness along the wake and non-wake paths that are similar in amplitude. Additionally, the periodic variation of $q\tau_w$ in Figure 7.49b contains a phase change near the leading edge. This phase change may be due in part to the time-varying nature of the velocity field as well as the turbulence field. This is considered in more detail in the following chapter. For both data sets, it is apparent that by 0.3–0.4s*, the only remaining periodic unsteadiness occurs at blade-passing frequency and is low in amplitude.

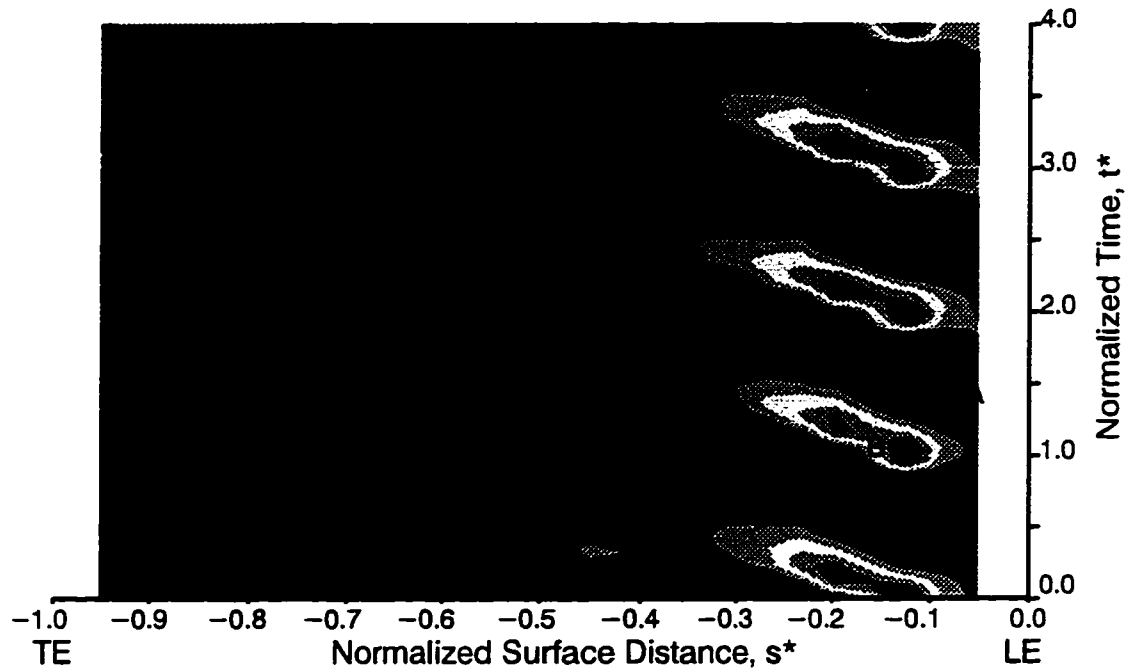


a) Nozzle 1 at 20 percent pitch relative to Nozzle 2

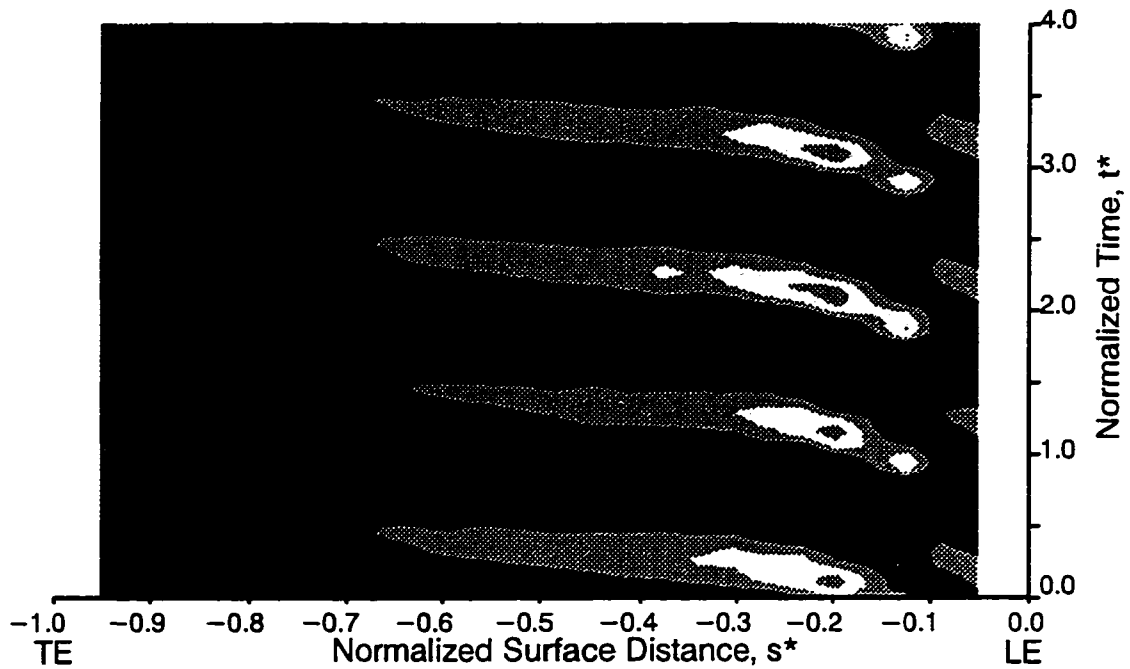


b) Nozzle 1 at 60 percent pitch relative to Nozzle 2

Figure 7.48. Space-time diagrams of random unsteadiness along pressure surface of Nozzle 2, test point 5D ($Q_0=1.29$, $Q_{10}=19.09$)



a) Nozzle 1 at 20 percent pitch relative to Nozzle 2



b) Nozzle 1 at 60 percent pitch relative to Nozzle 2

Figure 7.49. Space-time diagrams of periodic unsteadiness along pressure surface of Nozzle 2, test point 5D ($Q_0 = -12.0$, $Q_{10} = 18.0$)

CHAPTER 8. FLOWFIELD UNSTEADINESS AND WAKE INTERACTION

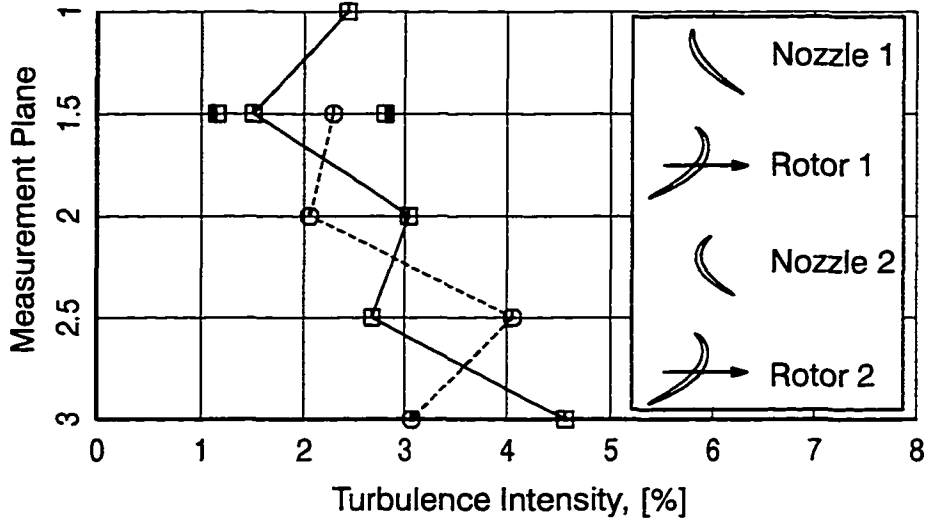
Flowfield unsteadiness was shown in the previous chapter to have a major influence on boundary layer development in LP turbines. In turbomachines, unsteadiness can be decomposed into random and periodic components. For this work, the random component is categorized as that which does not correlate with shaft rotational frequency or blade-passing frequency. It is referred to herein as turbulence. Periodic unsteadiness is any unsteadiness that correlates with shaft or blade-passing frequency. It is caused primarily by airfoil wakes and potential flow effects.

In this chapter, detailed measurements of the inter-bladerow flowfield obtained using the X hot-film probe are presented. Contained in the first section are circumferential and time-averaged measurements of turbulence characteristics from the five measurement planes of the turbine. Next, a general discussion of wake interaction in LP turbines is given. In the third section, measurements of the time-varying flowfield are presented that describe the interaction of rotor and nozzle wakes as they convect through the two-stage turbine of the LSRT.

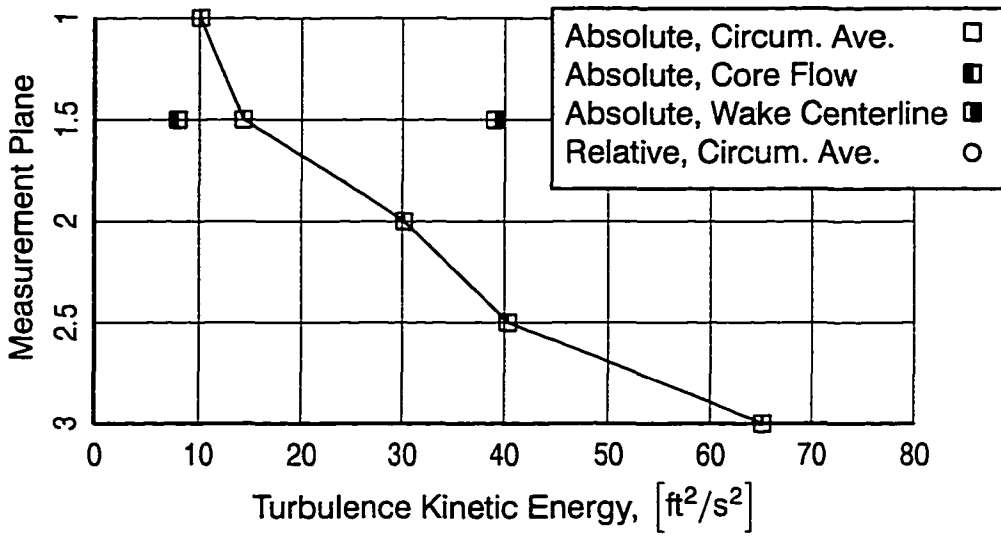
8.1 Average Turbulence Characteristics

Circumferential-averaged measurements of turbulence intensity, kinetic energy, and length scale obtained from the inlet to exit of the LSRT are shown in Figures 8.1a-c. The ordinate of each figure is measurement plane number. For reference, a schematic of the blading is shown along the right-hand side of Figure 8.1a.

All symbols are defined in the legend of Figure 8.1b. Quantities denoted by open symbols were computed from circumferential averages along one blade pitch with the exception of the turbine inlet (Plane 1.0) where the flowfield was circumferentially uniform. Measurements obtained from Planes 1.5 – 3.0 are reported with respect to the absolute frame of reference, given by the square symbols, and the relative frame of reference, given by the circular symbols. Because turbulence kinetic energy is invariant with reference frame, its values are given in Figure 8.1b using square symbols only. The partially filled symbols indicate values obtained along the

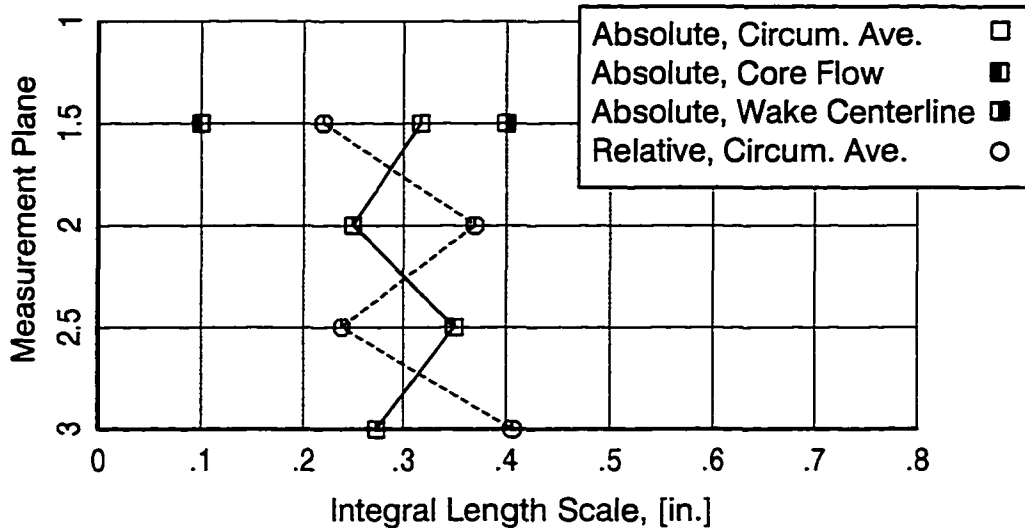


a) turbulence intensity



b) turbulence kinetic energy

Figure 8.1. Circumferential-averaged turbulence characteristics of the LSRT at midspan



c) integral length scale

Figure 8.1. continued

wake center line and values obtained between wakes of the upstream bladerow. For this discussion, the latter is termed the “core flow” region.

8.1.1 Plane 1.0

The inlet measurement plane of the turbine is located approximately 9 in. downstream of the flow-conditioning screen and more than three axial chords (6.6 in.) upstream of the stage 1 nozzle. Turbulence intensity at this location is equal to 2.4% (Figure 8.1a). The mean square streamwise and transverse components of fluctuation velocity differed by less than 5 percent suggesting the turbulence is very nearly isotropic. The integral length scales in the streamwise and transverse directions are 0.31 and 0.15 in., respectively. This also is consistent with isotropic turbulence theory which predicts that the transverse scale should be equal to one-half the streamwise value (Baines and Peterson, 1951).

8.1.2 Plane 1.5

Measurements at Plane 1.5 were obtained with the X probe positioned axially at a location midway between the stage one nozzle and rotor bladerows. For the exit air angle from

Nozzle 1, the Plane 1.5 measurement station is at a streamwise distance of about 30 percent surface length downstream from the nozzle trailing edge.

The change in turbulence intensity across Nozzle 1 is apparent from Figure 8.1a. In the absolute frame of reference, the circumferential-averaged level of turbulence has decreased to 1.5%. The highest level of turbulence, measuring 2.8%, occurs along the wake center line while in the core flow region between Nozzle 1 wakes, it is just 1.15%. In the relative frame of reference, the circumferential-averaged turbulence intensity is 2.3% (open circular symbol in Figure 8.1a). Its value is greater than that of the absolute frame by the ratio of absolute to relative velocity at Plane 1.5.

The decrease in core flow turbulence across Nozzle 1 results from two factors: flow acceleration across the bladerow and turbulence dissipation. The former is simply a kinematic effect as turbulence intensity is inversely proportional to velocity. For Nozzle 1, this effect is significant as the inlet-to-exit velocity ratio is equal to 0.54 at midspan. From flow acceleration alone then, one would expect the core flow turbulence to decrease from 2.4% at the inlet to 1.3% at the exit.

The second factor relates to turbulence dissipation. Its role is evident from measurements of turbulence kinetic energy (TKE) reported in Figure 8.1b. In the core flow at Plane 1.5, TKE has decreased by 20 percent compared to its value at Plane 1.0. This results from turbulence dissipation occurring between the measurement planes which are separated by a streamwise distance of 11.0 in. (about 40–50 times the average integral length scale). This decrease in magnitude of core flow TKE is consistent with the decay of isotropic turbulence predicted using the empirical relationship of Baines and Peterson (1951). In contrast to the change in core flow TKE, the circumferential-averaged level of turbulence kinetic energy, indicated by the open symbol at Plane 1.5, actually increases by 40 percent across the nozzle bladerow. Along the wake center line, TKE has increased by nearly a factor of four. In a circumferential-averaged sense then, dissipation of core flow turbulence between Planes 1.0 and 1.5 is more than offset

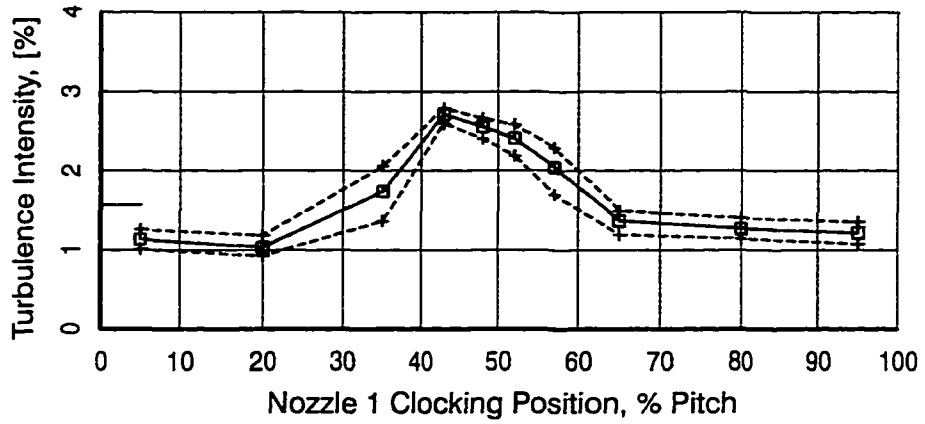
by turbulence production associated with the airfoil boundary layers and trailing edge mixing of Nozzle 1.

Circumferential-averaged values of turbulence length scale at Plane 1.5 are given in Figure 8.1c. In the absolute frame of reference, the average length scale at the exit of Nozzle 1 measured 0.32 in. It is noteworthy that the variation of length scale in the circumferential direction is substantial. The largest scales, measuring 0.4 in., are found in the core flow between wakes. This increase in size relative to that found at Plane 1.0 follows directly from the associated turbulence dissipation (*ibid.*). The smallest scales occur in the wake of Nozzle 1 and measure about 0.1 in. These latter values are of the same order as the trailing edge blockage (i.e., the sum of the blade thickness and displacement thickness of the boundary layers at the trailing edge).

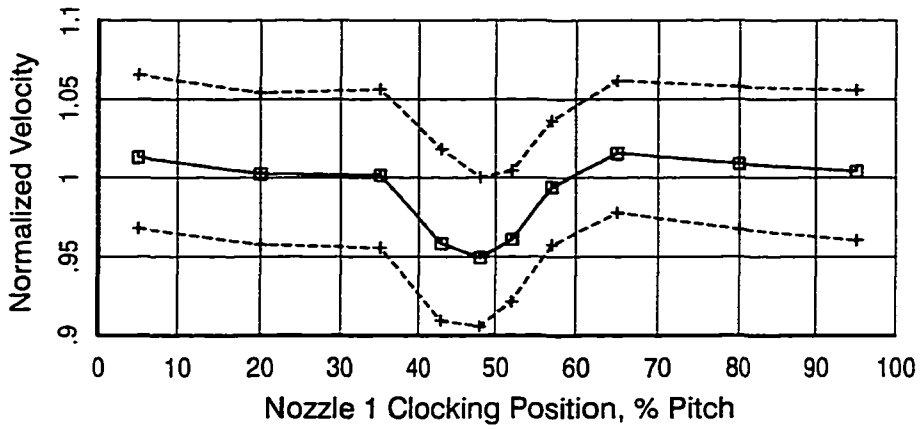
Length scales in the rotor and nozzle frames of reference are directly proportional to the ratio of relative to absolute flow velocity. For conventional LP turbines, this ratio is less than one at nozzle exit planes and vice versa for rotor exit planes. For Plane 1.5 then, the length scale in the rotor frame of reference is proportionally less than the corresponding absolute frame value.

The circumferential variation of the flowfield at the exit on Nozzle 1 is given in Figure 8.2. The abscissa is Nozzle 1 clocking position in percent pitch. Absolute velocity in part b is normalized by the circumferential-averaged value. The symbols connected with the solid lines are time-averaged values. The dashed lines in the figure indicate the average minimum and maximum excursions in periodic unsteadiness. They are determined from ensemble-averaged distributions at each location. For this traverse, the wake center line of Nozzle 1 is near 50 percent pitch.

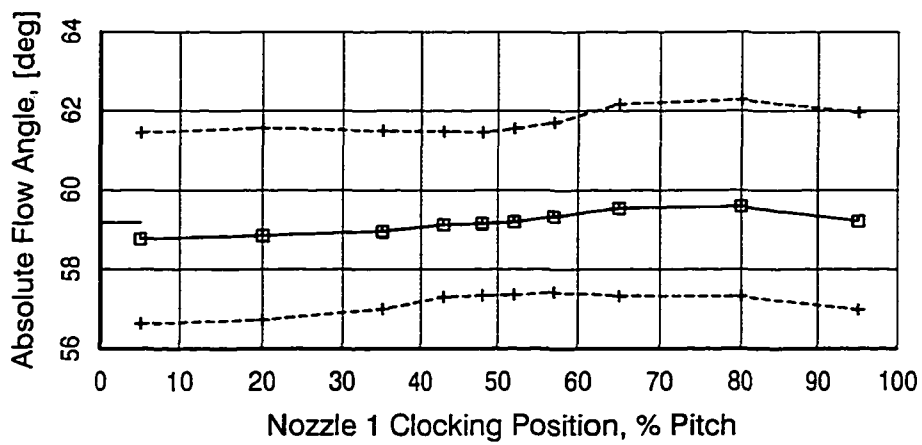
The time-averaged values (solid lines) in Figure 8.2 indicate a conventional behavior of the Nozzle 1 exit flowfield. The highest turbulence intensity occurs at the wake center line. The velocity defect of the wake is equal to 5.8 percent. The variation in flow angle across the wake is not significant.



a) turbulence intensity



b) normalized absolute velocity



c) absolute flow angle

Figure 8.2. Circumferential variation of flowfield at exit of Nozzle 1

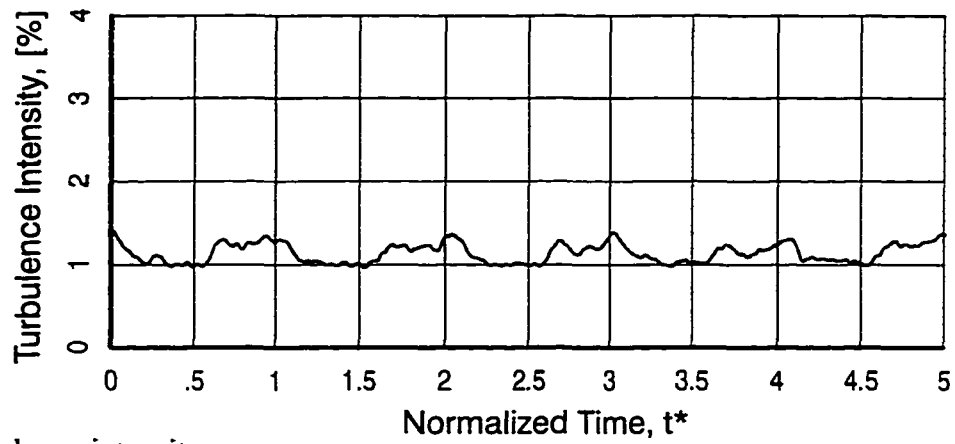
The magnitude of periodic unsteadiness at the Nozzle 1 exit is indicated by the minimum/maximum envelopes (dashed lines) of Figure 8.2. For the sake of example, the set of ensemble-averaged distributions used to determine the envelopes in Figure 8.2 at 5 percent pitch is given in Figure 8.3. The distributions are shown for five blade-passing periods of the downstream Rotor 1. The ordinate scales are identical to those of Figure 8.2 to facilitate comparison. Velocity is normalized by its time-averaged value.

The only source of periodic unsteadiness at Plane 1.5 is potential flow interaction from the downstream Rotor 1. The distributions in Figure 8.3 show that the periodic variation of the velocity field is nearly sinusoidal. The amplitude of the velocity fluctuations in Figure 8.2b is about 5 percent of the time mean and was found not to be a function of Nozzle 1 location. Flow angle varies about 2° from the mean. The minimum/maximum envelopes for turbulence intensity, given in Figure 8.2a, simply reflect the time variation in velocity which is the denominator of turbulence intensity. Had Nozzle 1 been tested as an isolated annular cascade, no discrete periodic variations of the flowfield would be expected with the possible exception of vortex shedding from the trailing edge.

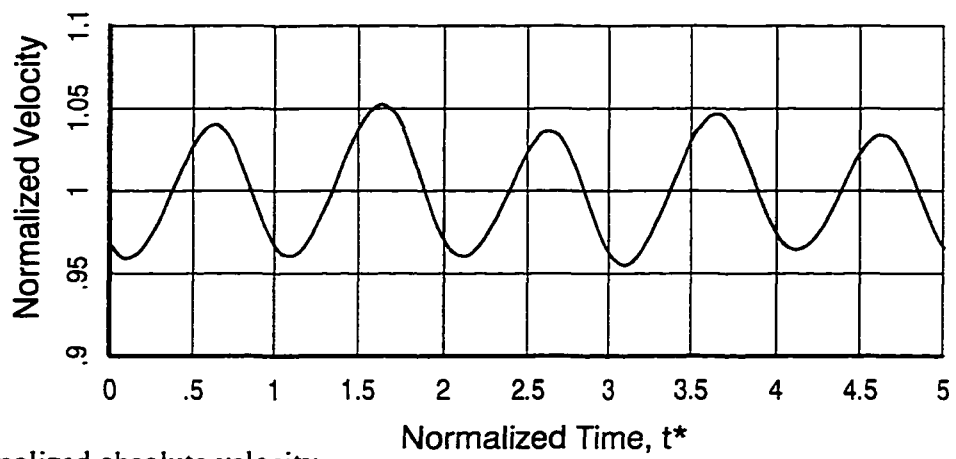
8.1.3 Plane 2.0

Across Rotor 1 and at the inlet to the second stage nozzle, the circumferential-averaged turbulence intensity in the absolute frame of reference has increased to 3.0% (Figure 8.1a). This increase is due to both the reduction in absolute velocity and to turbulence production occurring across Rotor 1. Turbulence kinetic energy across the rotor has increased by more than a factor of two (Figure 8.1b). From Figure 8.1c, we see that the average length scale in the absolute frame has decreased to a value of 0.25 in. which, again, is due in part to the reduction in absolute velocity.

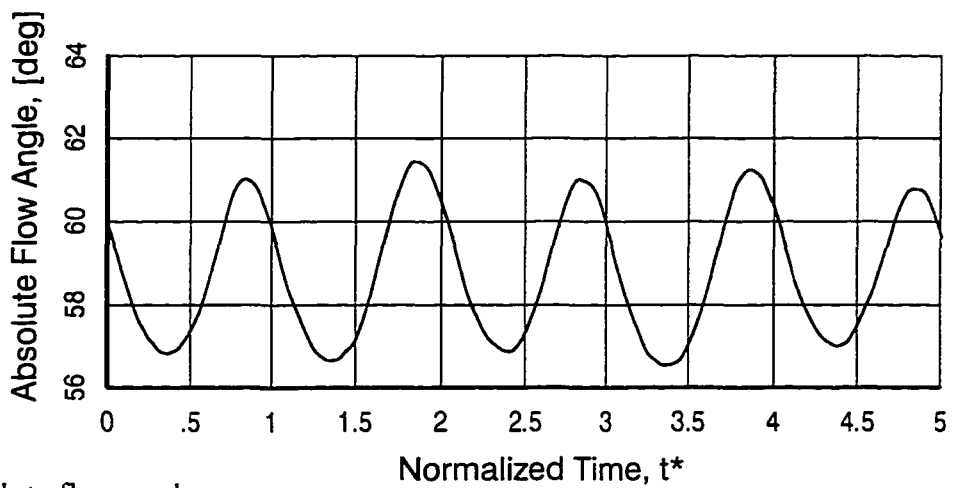
The circumferential variation of the exit flowfield from Rotor 1 is given in Figure 8.4 as a function of Nozzle clocking position. While acquiring these Plane 2.0 data, Nozzles 1 and 2 were both indexed. As before, the solid and dashed lines are drawn through the time average



a) turbulence intensity

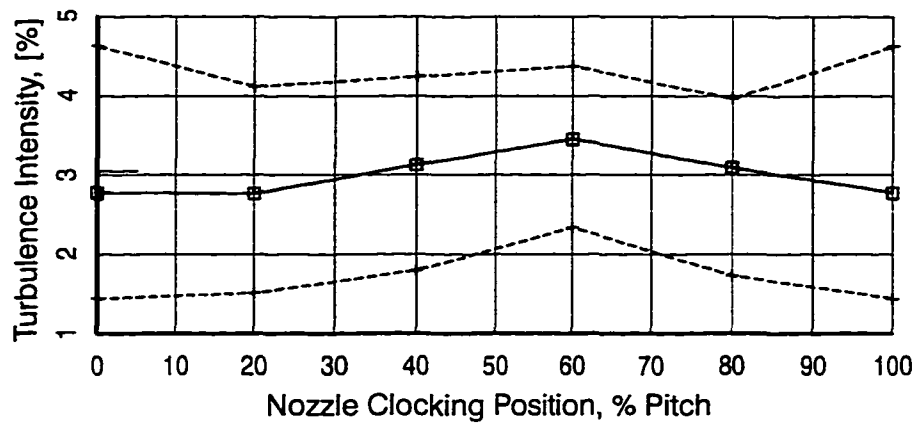


b) normalized absolute velocity

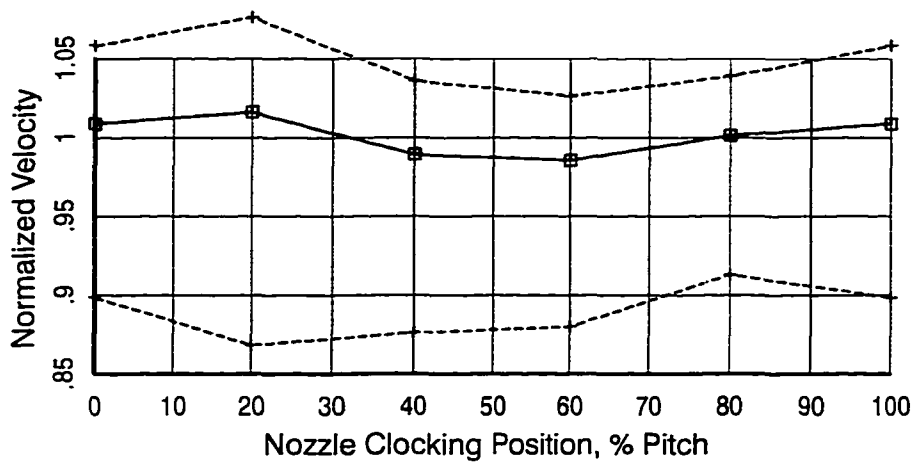


c) absolute flow angle

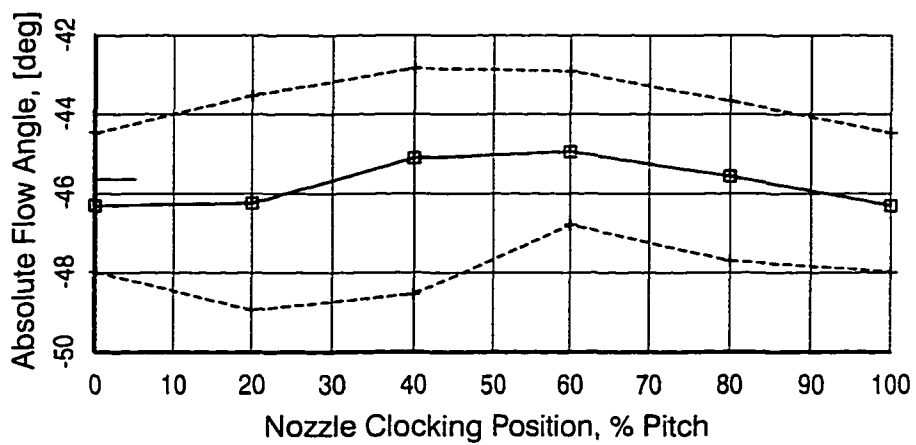
Figure 8.3. Time varying flowfield at exit of Nozzle 1, 5 percent pitch



a) turbulence intensity



b) normalized absolute velocity



c) absolute flow angle

Figure 8.4. Circumferential variation of flowfield at exit of Rotor 1

and minimum/maximum envelopes determined from the ensemble-averaged distributions. Because of their interesting characteristics, these latter distributions are presented below in Section 8.3 where they are described in detail.

Much of the the circumferential variation exhibited in Figure 8.4 is due to potential flow effects from the downstream Nozzle 2. For the most part, the envelopes of minimum/maximum variation trend with the time average. As will be shown in Section 8.3, the minimum and maximum levels of turbulence indicated by the envelopes correlate with the core flow region between wakes and along the center line of the Rotor 1 wake, respectively.

8.1.4 Stage 2

As evident from Figure 8.1, variations of turbulence quantities through the second stage are similar to those of Stage 1. Turbulence intensity continually increases at each subsequent measurement plane. In the relative frame of reference, the turbulence level entering Rotor 2 (Plane 2.5) is 4.0%. At the exit plane of the LSRT (which represents the inlet plane of the next downstream nozzle bladerow if it were present), turbulence intensity in the absolute frame has increased to 4.6%. Note this is substantially higher than that measured at the Nozzle 2 inlet.

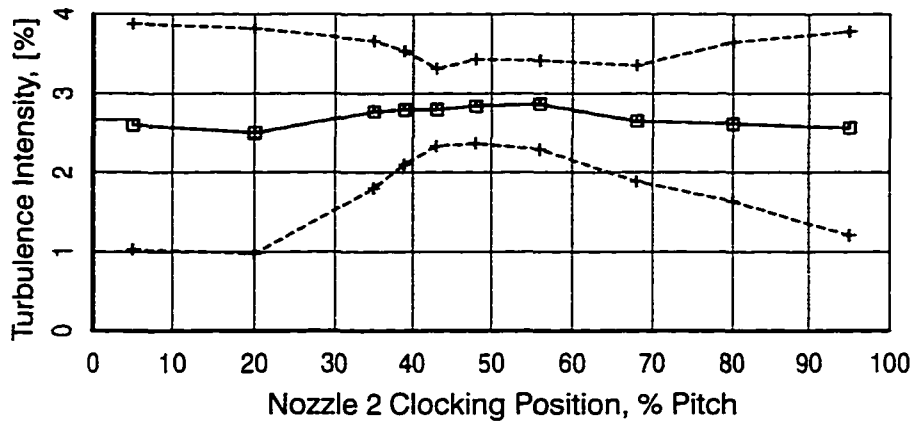
The increase in turbulence kinetic energy across the bladerows of the second stage is notably greater than that for the first stage and is attributed to two factors. First, additional mixing of the wakes shed from the Stage 1 blading will occur as these wake segments convect through the second stage. This is considered further in Section 8.3 where time-unsteady measurements are presented. Secondly, Stage 2 of this turbine is loaded about 10 percent higher than the first stage due to the decrease in density that occurs through the machine. This likely will produce higher levels of aerodynamic loss (and hence turbulence production) in the second stage.

The integral length scales associated with Stage 2 are similar in magnitude to those from Stage 1. Changes in scale from one plane to the next result primarily from the change in velocity across bladerows.

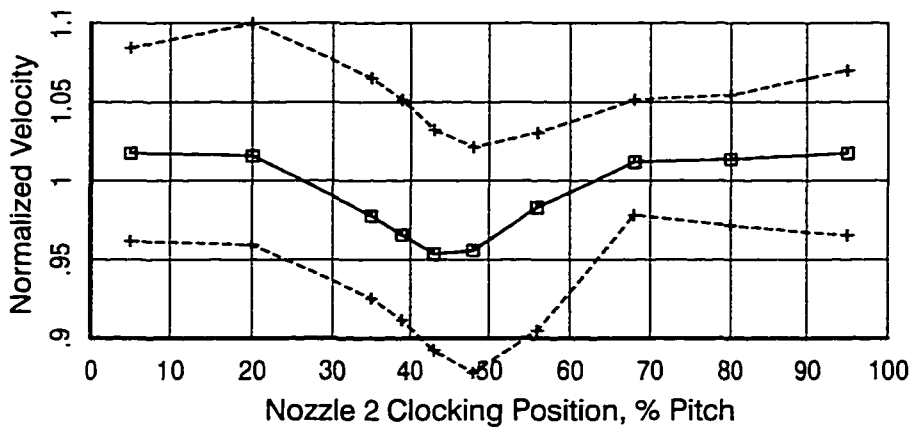
The circumferential variations of the flowfield at the exit of Nozzle 2 and Rotor 2 are given in Figures 8.5 and 8.6, respectively. At the exit of Nozzle 2, the variation of velocity and flow angle is similar to that observed for Nozzle 1 (Figure 8.2b–c). The velocity defect of the wake is 6.0 percent. The amplitude of the periodic velocity fluctuations is about 5–10 percent of the time mean. Flow angle varies about 3° to 4° from the mean — slightly more than observed at the exit of Nozzle 1. For this traverse, the wake center line is near 45 percent pitch.

The circumferential variation in turbulence intensity at the exit of Nozzle 2 is very different than expected, however. From Figure 8.5a, we find the time-averaged values in the wake of Nozzle 2 only slightly greater than for the core flow. In fact, it is not possible to distinguish the wake at all from the variation in time-average values alone. The envelopes of minimum and maximum ensemble variation show a modulation across the nozzle pitch. In the core flow region between Nozzle 2 wakes, both the lowest and highest levels of turbulence are found. The high levels are associated with wakes generated by bladerows upstream of Nozzle 2 while the lowest levels occur between those wakes. In the region of the Nozzle 2 wake, centered at about 45 percent pitch in Figure 8.5, the minimum envelop values of turbulence are greater in magnitude and maximum values lower in magnitude than for the core flow. All told, the character of the turbulence unsteadiness at the Nozzle 2 exit is far different from the more conventional characteristics observed at the exit of Nozzle 1. The primary difference between the two is that Nozzle 1 operates with a steady inlet flowfield while Nozzle 2 is embedded in an unsteady, multi-stage environment.

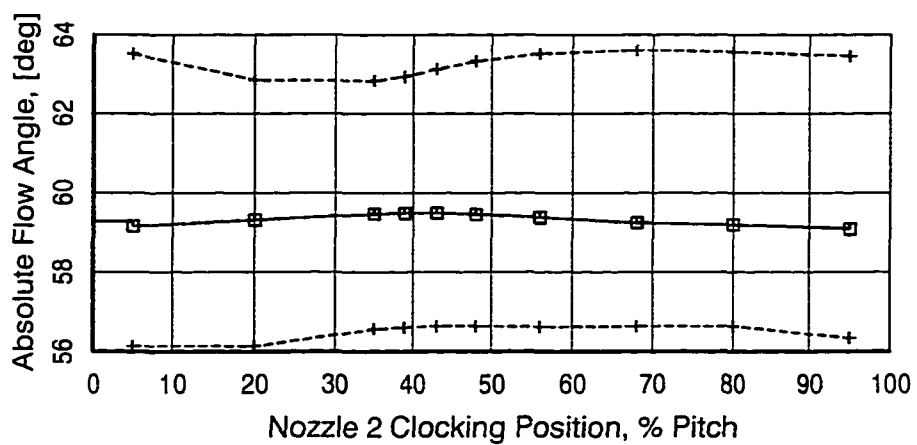
The circumferential variation of the Rotor 2 exit flowfield is shown in Figure 8.6. The character is similar to that observed behind Rotor 1 (Figure 8.4). The time-averaged values of turbulence intensity, velocity, and flow angle are only weakly dependent on the clocking position of the upstream nozzles.



a) turbulence intensity

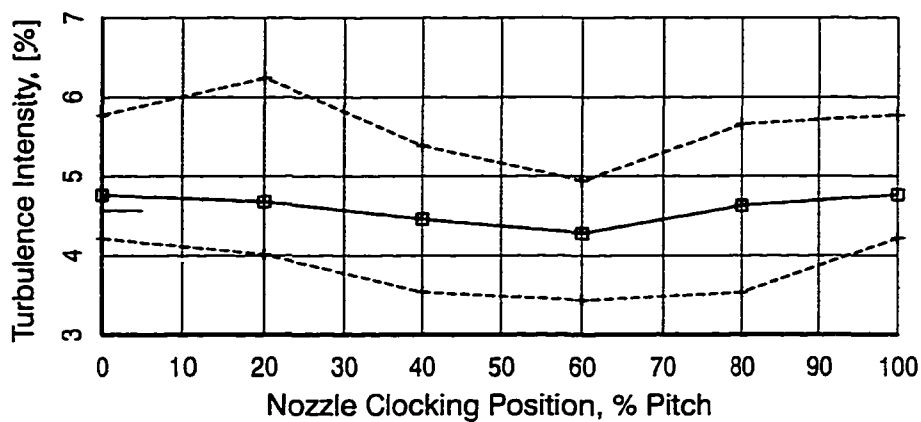


b) normalized absolute velocity

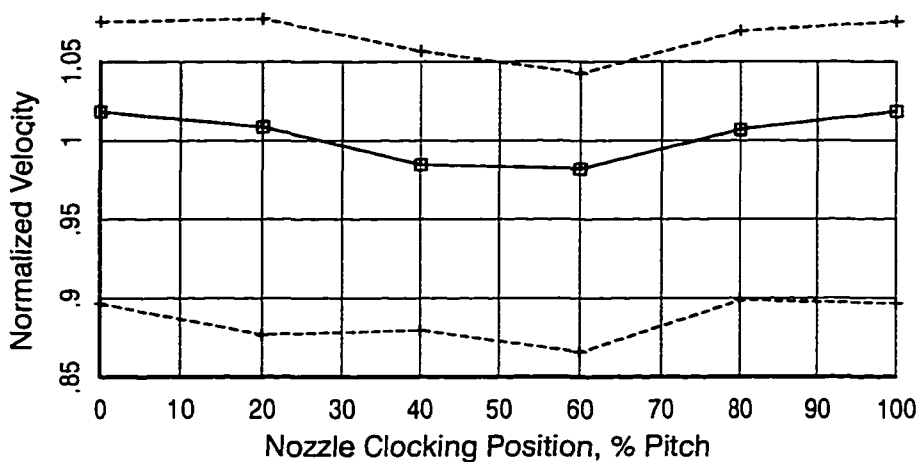


c) absolute flow angle

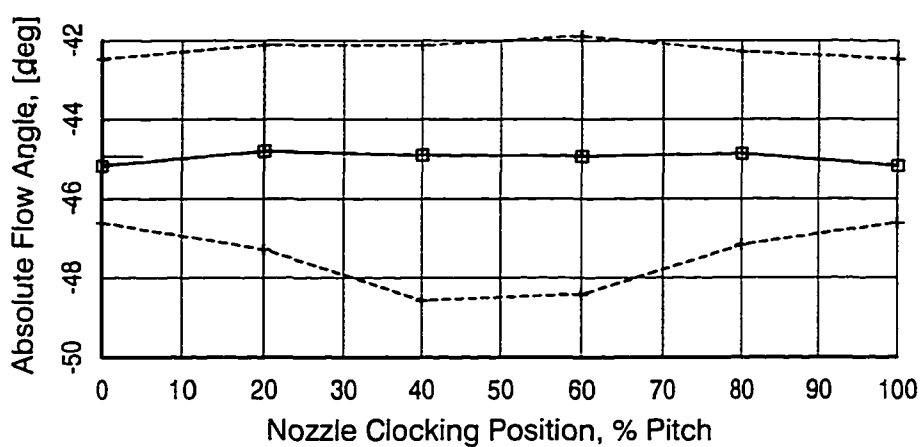
Figure 8.5. Circumferential variation of flowfield at exit of Nozzle 2



a) turbulence intensity



b) normalized absolute velocity



c) absolute flow angle

Figure 8.6. Circumferential variation of flowfield at exit of Rotor 2

8.1.5 Additional Observations

From Figure 8.1, we observe that the levels of turbulence intensity and kinetic energy increase continuously from the inlet to exit of the two-stage LSRT. Extrapolation of these trends implies a further rise in values across subsequent stages. For a true “repeating stage environment,” however, we would expect turbulence kinetic energy to remain more nearly constant across stages, indicating a balance in production and dissipation of turbulence. That this was not found suggests the LSRT configuration *does not* achieve a repeating stage environment by the second stage — at least in terms of its turbulence characteristics. This may result in part from maintaining a “clean” inlet upstream of Nozzle 1. Installation of a grid to augment turbulence levels upstream of the turbine inlet may produce higher and more constant levels of turbulence across the turbine itself. This may model the engine environment more closely as the LP turbine is located downstream of the combustor and high pressure turbine. Because no other quantitative measurements from a multi-stage LP turbine have been published, questions remain as to what the exact turbulence level is and what the characteristics are in the actual engine component. Certainly though, the LSRT in its present configuration adequately simulates the most important aspects of the unsteady flowfield to make it a viable research vehicle for these boundary layer studies.

Secondly, non-dimensionalization of the integral length scales was carried out in order to extend the applicability of these results to LP turbines in general. Given the geometry of blade passages in LP turbines, it is proposed that the most appropriate characteristic length for normalization is throat width, d_0 , as defined in Figure 4.3. Given the high aspect ratios of modern LP turbine blading, this is the most restrictive dimension of the flow path. Using throat width then, the integral length scales of Figure 8.1c have been recast into a normalized form in Figure 8.7. At each measurement plane, the length scale is normalized by the throat width of the bladerow directly upstream of it and, for consistency when specifying inlet conditions, is given with respect to the reference frame of the downstream bladerow. In this manner, only a single value

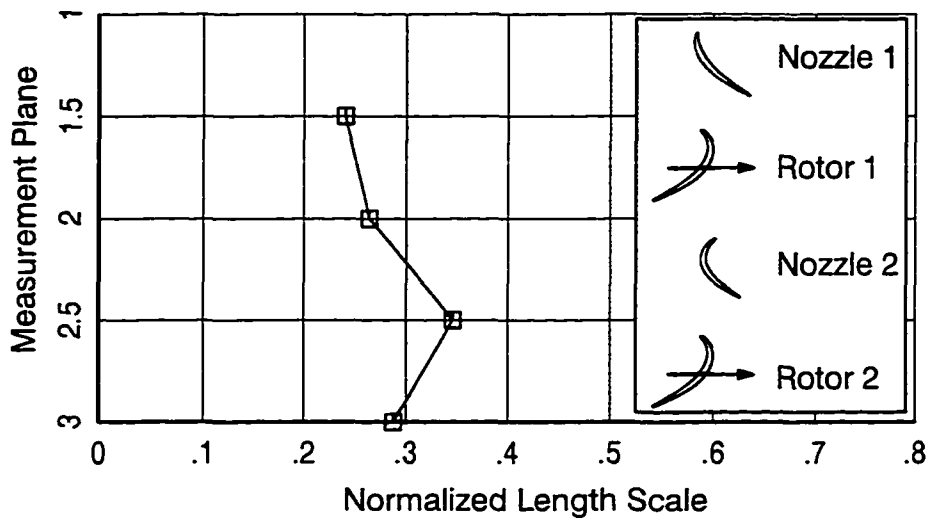


Figure 8.7. Normalized integral length scale of the LSRT at midspan

of normalized scale appears for each measurement plane. For example then, at the inlet to Rotor 2 (Plane 2.5), the length scale is normalized by the throat width of the second stage nozzle and plotted in terms of the rotating (i.e., rotor) reference frame.

From Figure 8.7, we find that the normalized integral length scale across the turbine at midspan is equal to approximately 30 percent of the throat width of the upstream bladerow. Because these are the only known measurements of turbulence length scale from a multi-stage LP turbine, additional data are needed to substantiate these results.

8.2 Wake Interaction in LP Turbines

Before interrogating the time unsteady measurements, it is useful to consider the current understanding of wake interaction in LP turbines. A description is provided in this section.

Complex wake interaction takes place in LP turbines as upstream wakes convect through downstream bladerows. This situation is illustrated in Figure 8.8 as it pertains to the first stage of the two-stage LSRT. It is based in part on general numerical simulations (e.g., Denton, 1993, and Hodson, 1985b) and experimental measurements (e.g., Arndt, 1993, and Hodson, 1985a).

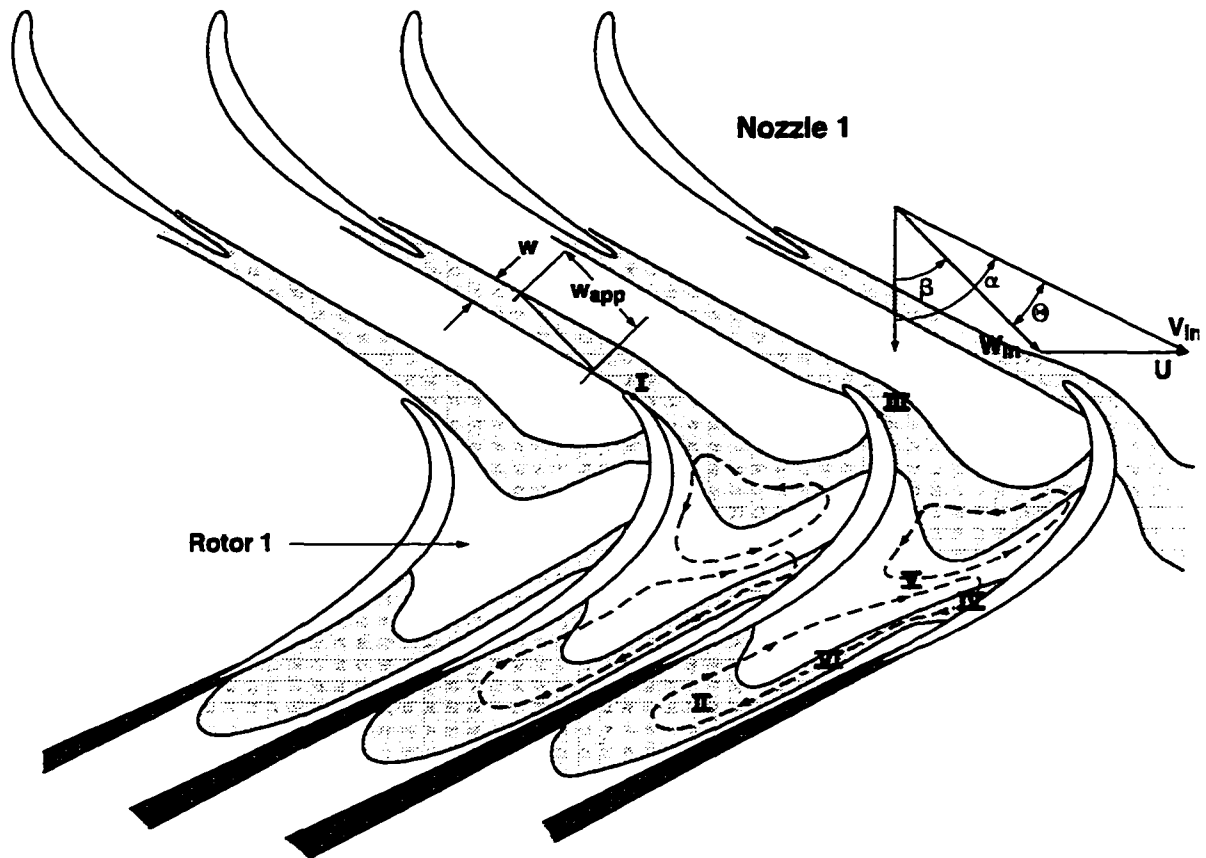


Figure 8.8. Wake interaction in a multi-stage LP turbine

The wakes produced by the Nozzle 1 bladerow are lightly shaded in the figure. The darker shaded regions delineate Rotor 1 wakes. The airfoil pitch ratio is identical to that for the Stage 1 nozzle and rotor of the LSRT.

As illustrated in Figure 8.8, wakes shed from Nozzle 1 convect into the downstream rotor bladerow. In the rotor frame of reference, the wakes are encountered in the flow direction indicated by the velocity vector, W_{in} . The angle of inclination of the wake with respect to the relative inlet flow direction, Θ , was defined in Section 7.3.1.6 as " $\alpha - \beta$ ". To reiterate, Θ was equal to about 20° for this turbine. Consequently, the nozzle wake impacts first along the suction side of the rotor, labeled with Roman numeral I in Figure 8.8. As it convects into the rotor passage and moves past the leading edge, the wake is chopped, producing a wake segment (e.g., II) that

extends across the blade passage. The bowing of this segment in the streamwise direction is a result of higher mid–passage velocities.

Along the rotor suction surface near the leading edge, the streamwise extent of the wake segment increases substantially as indicated by III. This is caused by two phenomena (Hodson, 1985b). First, the downstream portion of the nozzle wake segment that initially impacts the suction surface undergoes flow acceleration as it convects along the leading edge. By the time the upstream portion of the wake (which is convecting at a lower velocity) reaches the blade leading edge, the downstream portion has moved away, resulting in a streamwise spreading. The amount of spreading is related to the *apparent* wake thickness, w_{app} , relative to the downstream blade-row. As illustrated schematically in Figure 8.8, it is simply the thickness of the wake in the rotor frame of reference as determined from Equation 8.1. The greater the apparent thickness of the wake, the greater is the difference in the convective velocities from the upstream to downstream interface of the wake. Because of the small angle between relative and absolute directions for this turbine, w_{app} is nearly three times that of the wake thickness, w , in the absolute frame.

$$w_{app} = \frac{w}{\sin(\alpha - \beta)} \quad (8.1)$$

A second contributor to the increased wake spreading along the rotor suction surface results from the jet–wake effect. Consistent with the description in Section 7.3.1.6, the interaction of the Nozzle 1 wake as it moves through Rotor 1 will result in a migration of wake fluid toward the rotor suction surface. Along the suction surface then, the wake fluid tends to accumulate, further increasing its streamwise extent. The opposite is true along the pressure surface where, because the jet–wake effect is coupled with flow deceleration downstream of the leading edge, the wake segments remain much narrower (e.g., region IV of Figure 8.8).

Hodson found from both measurements (1985a) and computations (1985b) that the jet–wake effect additionally will bring about the formation of large–scale, counter–rotating vortices extending across the blade passage. The orientation and direction of rotation of these vortices are illustrated by the dashed lines labeled V in the figure. As will be shown later using measure-

ments of the periodically varying flowfield, these vortices are evident from the existence of over- and under-turning occurring between bladerows.

Aerodynamic circulation produces further distortion of the wake segments as they pass through the blade passage. For this LP turbine, the residence time for fluid particles moving through the rotor passage is more than two times greater along the pressure surface than along the suction surface. Consequently, the nozzle wake segment is rotated and stretched significantly before emerging from the downstream side of the bladerow. Conservation of vorticity dictates that this stretching will bring about a thinning of the wake segment (Smith, 1966), such as labeled VI in Figure 8.8.

8.3 Time-Varying Flowfield

Wake interaction in multi-stage turbines, similar to that just described, has been shown to produce significant temporal and spatial variations of flowfield quantities (Arndt, 1993, Huber et al., 1995). For the present investigation, ensemble-averaged distributions determined from phase-locked measurements are used to assess wake interaction phenomena in the LSRT. Results from Stage 2 (Planes 2.0, 2.5, and 3.0) are presented below.

8.3.1 Plane 2.0

Variation of the inlet flowfield to Nozzle 2, in the form of ensemble-averaged distributions of turbulence intensity, absolute velocity, and absolute flow angle, are presented in Figure 8.9a-e. Measurements were acquired for five clocking locations of the Nozzle 1 bladerow, labeled from 0 percent to 80 percent, as indicated, with the X probe located at Plane 2.0. The top row of the figure contains the distributions of turbulence intensity for each location. The middle and bottom rows consist of velocity and flow angle, respectively, pertaining to the absolute frame of reference. Velocity is normalized by its time-averaged value. Flow angle is referenced from axial with the negative direction being opposite rotor rotation. The abscissa of each distribution is normalized time extending for three blade-passing periods of the rotor.

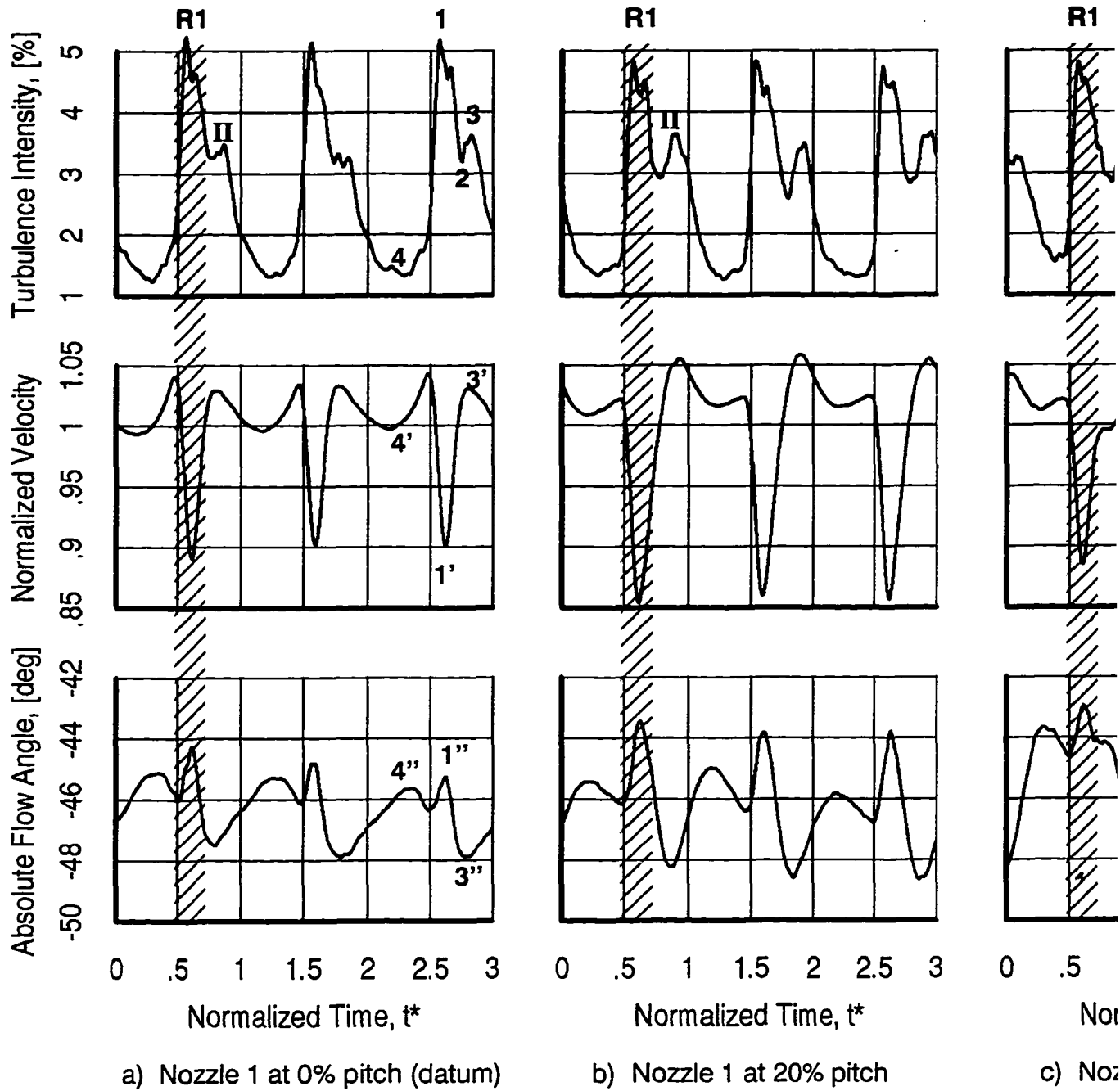
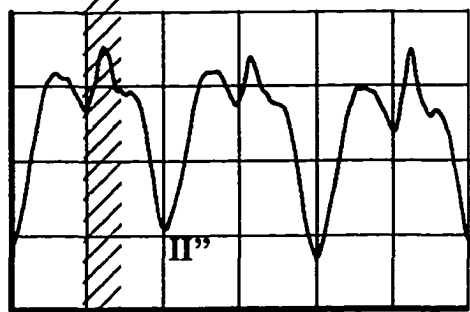
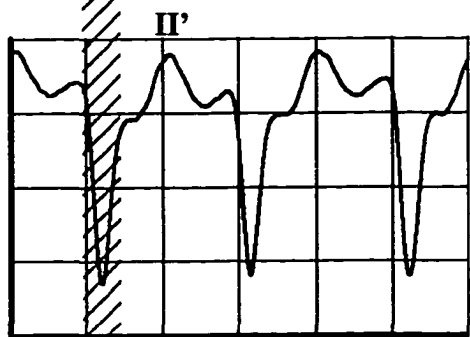
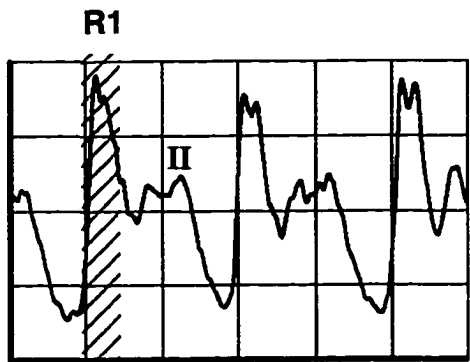


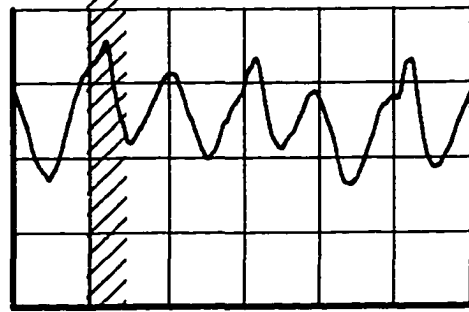
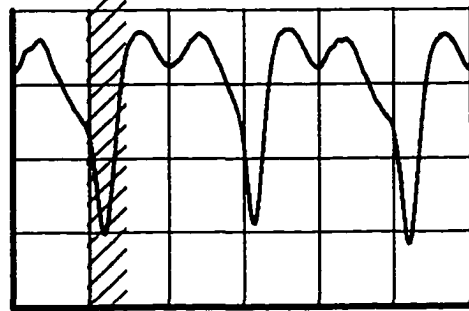
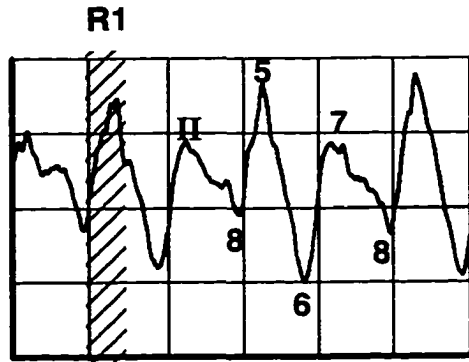
Figure 8.9. Measurements of unsteady flowfield at inlet to Nozzle 2 (Plane 2.0)





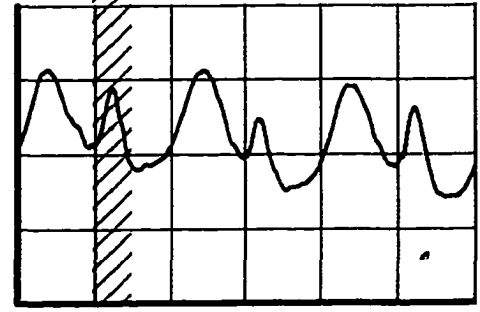
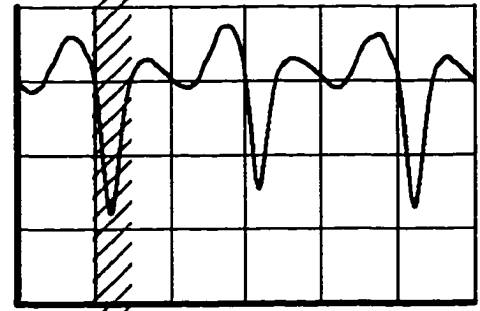
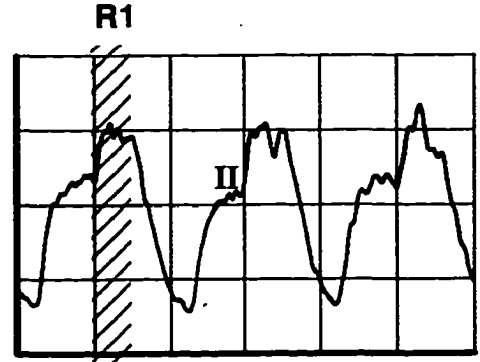
0 .5 1 1.5 2 2.5 3
Normalized Time, t^*

c) Nozzle 1 at 40% pitch



0 .5 1 1.5 2 2.5 3
Normalized Time, t^*

d) Nozzle 1 at 60% pitch



0 .5 1 1.5 2 2.5 3
Normalized Time, t^*

e) Nozzle 1 at 80% pitch



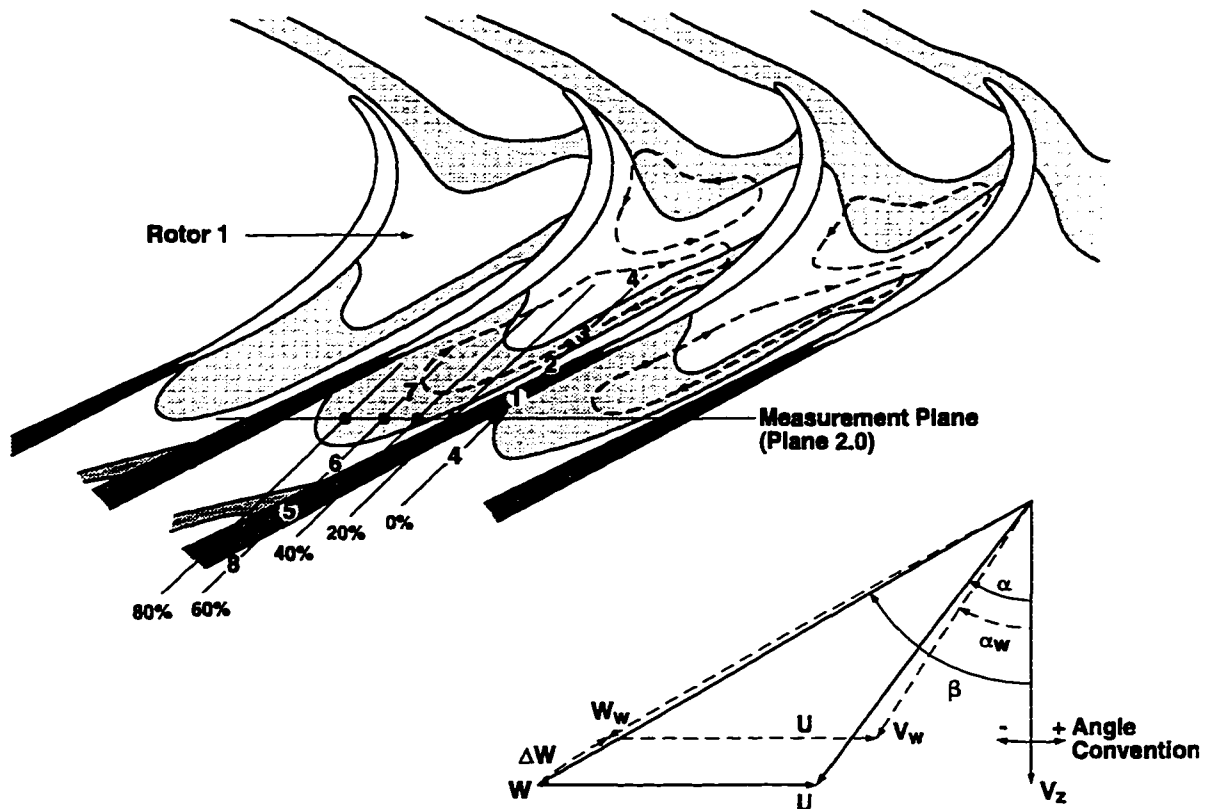


Figure 8.10. X probe measurement locations at Plane 2.0 relative to Nozzle 1

To facilitate interpretation of these measurements, a portion of the schematic from Figure 8.8 is redrawn in Figure 8.10. The vector diagram for Plane 2.0 is also shown. The five relative clocking locations of the X probe with respect to Nozzle 1 are identified by the filled circles and labeled from 0% to 80%. The line extending through each measurement location is oriented in the absolute flow direction and hence gives the flow trajectory in relation to the X probe (and to the downstream Nozzle 2). For simplicity only, Figure 8.10 is drawn in a manner that suggests the X probe was moved relative to Nozzle 1. As explained previously, the probe remained at a fixed location during acquisition of the data sets and, instead, the Nozzle 1 bladerow was indexed circumferentially at 20 percent increments of its airfoil spacing.

The ensemble-averaged distributions associated with the 0 percent clocking position of Nozzle 1 constitute the left-most column of Figure 8.9. The hatched region denoted “R1” identifies the signature of the Rotor 1 wake. It is also labeled point 1 in both Figures 8.9 and 8.10. From Figure 8.9a, we see that the rotor wake flow is characterized by increased turbulence intensity, exceeding 5% at the wake center line. In the absolute frame of reference, the rotor wake also brings about a decrease in both absolute velocity (point 1') and flow turning (point 1'') as shown in the middle and lower distributions of Figure 8.9a (note that a change in flow angle towards axial is termed a “decrease” for this discussion). That a decrease in flow turning should occur in the wake is evident from the vector diagram in Figure 8.10. Here, the relative and absolute velocity vectors are given by the components $\{W, \beta\}$ and $\{V, \alpha\}$, respectively. Subscript “w” refers to the wake fluid. As illustrated, the relative flow angle, β , remains nearly constant across the rotor wake. Consequently, the rotor wake deficit, ΔW , produces a decrease in both velocity and flow angle in the absolute frame of reference.

Looking again at the distribution of turbulence intensity in Figure 8.9a, we find a second local maximum occurring in time just after that from the Rotor 1 wake. It is identified as point 3. In Figure 8.10, we see that point 3 coincides with the wake segment from Nozzle 1. Along the trajectory extending through the 0 percent measurement location, the wake segment occurs in a streamwise sense just upstream of the Rotor 1 wake (point 1) and is quite narrow. Both absolute velocity and flow angle associated with point 3 in Figure 8.9a have increased in value. This is consistent with the relative motion of wake fluid within the segment as described by the jet-wake effect and denoted in Figure 8.10 by the dashed lines. The increase in flow turning past the time mean is referred to commonly as overturning. Between the regions of wake-influenced flow, identified by point 2 in the figures, the turbulence intensity is at a local minimum. Following the N1 wake segment in time, the turbulence intensity in Figure 8.9a decreases monotonically to a minimum at point 4 prior to the next wake from Rotor 1. In Figure 8.10, point 4 identifies that portion of the cross-passage vortex that transports fluid back toward the pressure surface.

This produces a local minimum in absolute velocity and a small degree of underturning (points 4' and 4'' of Figure 8.9a, respectively) in a manner consistent with the vector diagram.

The unsteady flowfield for Nozzle 1 at 20 percent pitch, given in Figure 8.9b, is similar to that just described. In a temporal sense, the ensemble-averaged distributions show that the lag of the wake segment from Nozzle 1, labeled II in the figure, has increased relative to the Rotor 1 wake. This is consistent with the flow trajectory for 20 percent in Figure 8.10. With Nozzle 1 positioned at 40 percent pitch from datum, the distribution of turbulence intensity in Figure 8.9c documents the presence of a wider Nozzle 1 wake segment that lags further behind the wake of Rotor 1. As with the first two clocking locations of Nozzle 1, local underturning in the Rotor 1 wake (R1) and overturning in the Nozzle 1 segment (II' and II'') is evident from periodic variations on velocity and flow angle in Figure 8.9c.

With Nozzle 1 at 60 percent relative pitch, the turbulence intensity from the Nozzle 1 wake segment (point 7 of Figures 8.9d and 8.10) is nearly equal in magnitude to that of the Rotor 1 wake (point 5). The segment now lags the Rotor 1 wake in time by about one-half the blade-passing period. Consequently, a Nozzle 2 airfoil positioned along a streamline corresponding to this flow trajectory will encounter a disturbance environment that exhibits a very strong periodic component at two times blade-passing frequency. As we found in Section 7.6, the resulting boundary layer development is influenced duly. From Figures 8.9 and 8.10, we see that point 6 corresponds to the cross-flow vortex occurring between the rotor wake and nozzle wake segment (i.e., region V of Figure 8.8). The low turbulence intensity occurring just prior to the next rotor wake is labeled point 8 in the figures.

The last set of measurements were obtained with Nozzle 1 at 80 percent from its datum. As characterized by the turbulence distribution of Figure 8.9e and the schematic of Figure 8.10, the Nozzle 1 segment along this streamline is adjacent to the suction side of the rotor wake. Peak turbulence within the rotor wake has decreased to about 4% and may be due in part to interaction and mixing of the rotor wake and nozzle wake segment.

Note that for all five sets of measurements in Figure 8.9, the phase of the rotor wake with respect to the trigger pulse (i.e., $t^*=0.0$) does not change.

In summary, we see from Figure 8.9 that the unsteady flowfield along a given streamline entering Nozzle 2 depends directly on the relative clocking location of Nozzle 1. The variation in unsteadiness observed at the inlet to Nozzle 2 agrees well with the wake interaction model illustrated in Figures 8.8 and 8.10. This being the case, we should note that the variation in associated *time-averaged* quantities, presented in Figure 8.4, was not large.

8.3.2 Plane 2.5

Some interesting features regarding the variation of turbulence kinetic energy (TKE) occur across Nozzle 2. Shown in Figure 8.11 are two distributions of ensemble-averaged TKE obtained at the inlet and exit of the bladerow. For reference, the distribution from the inlet was obtained with Nozzle 1 at 0 percent pitch and thus pertains to the flow condition of Figure 8.9a described above. The lower distribution was obtained with the probe positioned in the core-flow region between wakes on Nozzle 2. Minimum and time-averaged values of TKE are indicated to the right of each distribution.

As denoted in Figure 8.11, the maximum levels of ensemble-averaged turbulence kinetic energy characterize the wake unsteadiness from Rotor 1. Across Nozzle 2, these levels actually increase by about 20 percent. This suggests that continued mixing (i.e., turbulence production) of the Rotor 1 wakes takes place within the passage of Nozzle 2. In contrast, the minimum levels of TKE, which pertain to flow between Rotor 1 wakes, remain about constant. For this portion of the flow then, which is equivalent to region V of Figure 8.8, turbulence dissipation across Nozzle 2 is negligible. In contrast, we see that the time-averaged level of TKE in the core flow region increased by about 50 percent across Nozzle 2.

8.3.3 Plane 3.0

Characteristics of the time-varying flowfield at the Rotor 2 exit plane are shown in Figure 8.12. The presentation format is identical to that of Figure 8.9. During acquisition of these

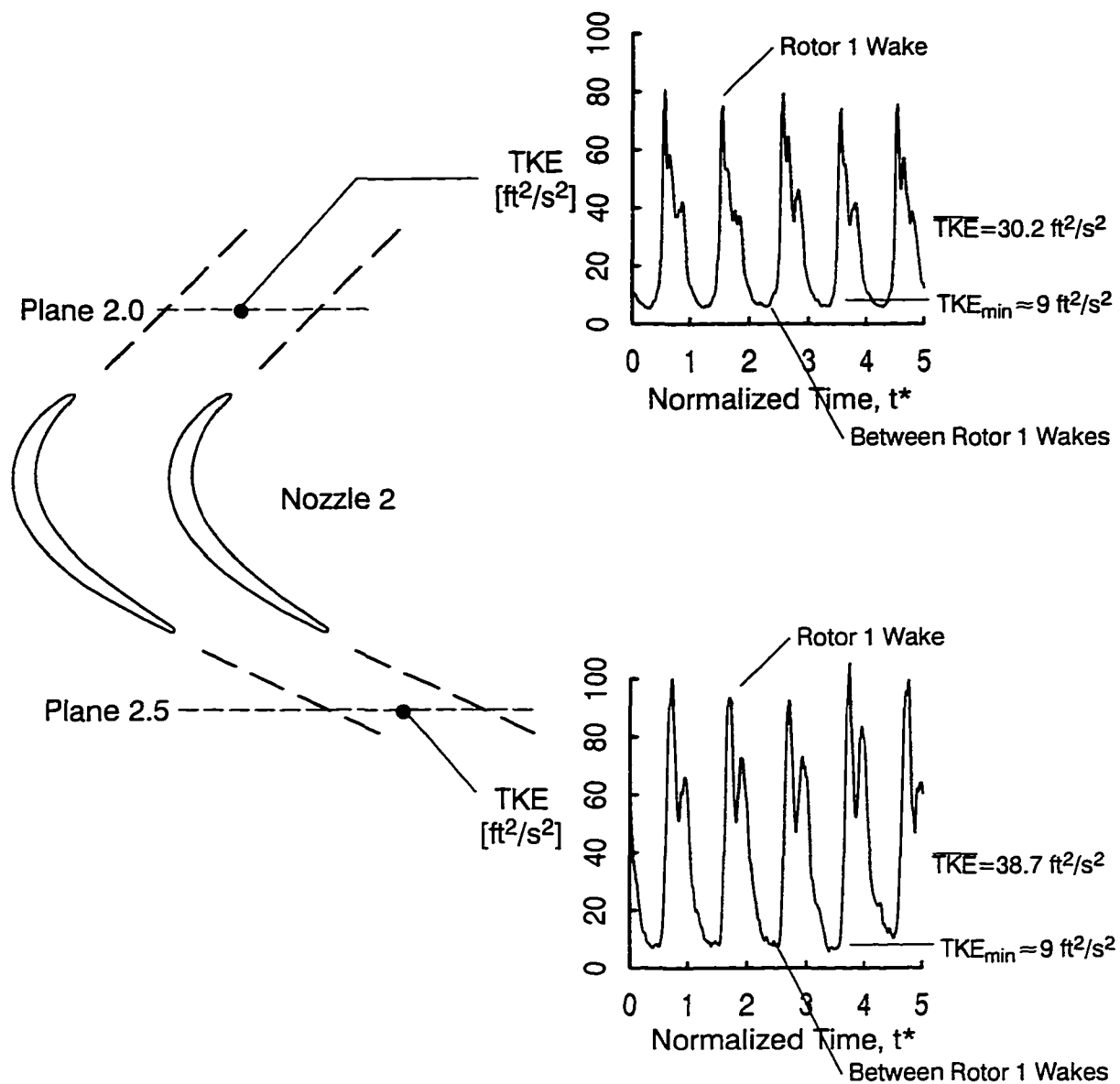


Figure 8.11. Variation in turbulence kinetic energy across Nozzle 2 bladerow

data, Nozzles 1 and 2 were moved in tandem from one location to the next. The measured distributions are given in terms of the absolute frame of reference and hence represent inlet conditions to a downstream nozzle bladerow, if present.

The wake from Rotor 2, labeled R2, is discerned clearly from the periodic variation in velocity and corresponding underturning evident from the flow angle in the lower two rows of

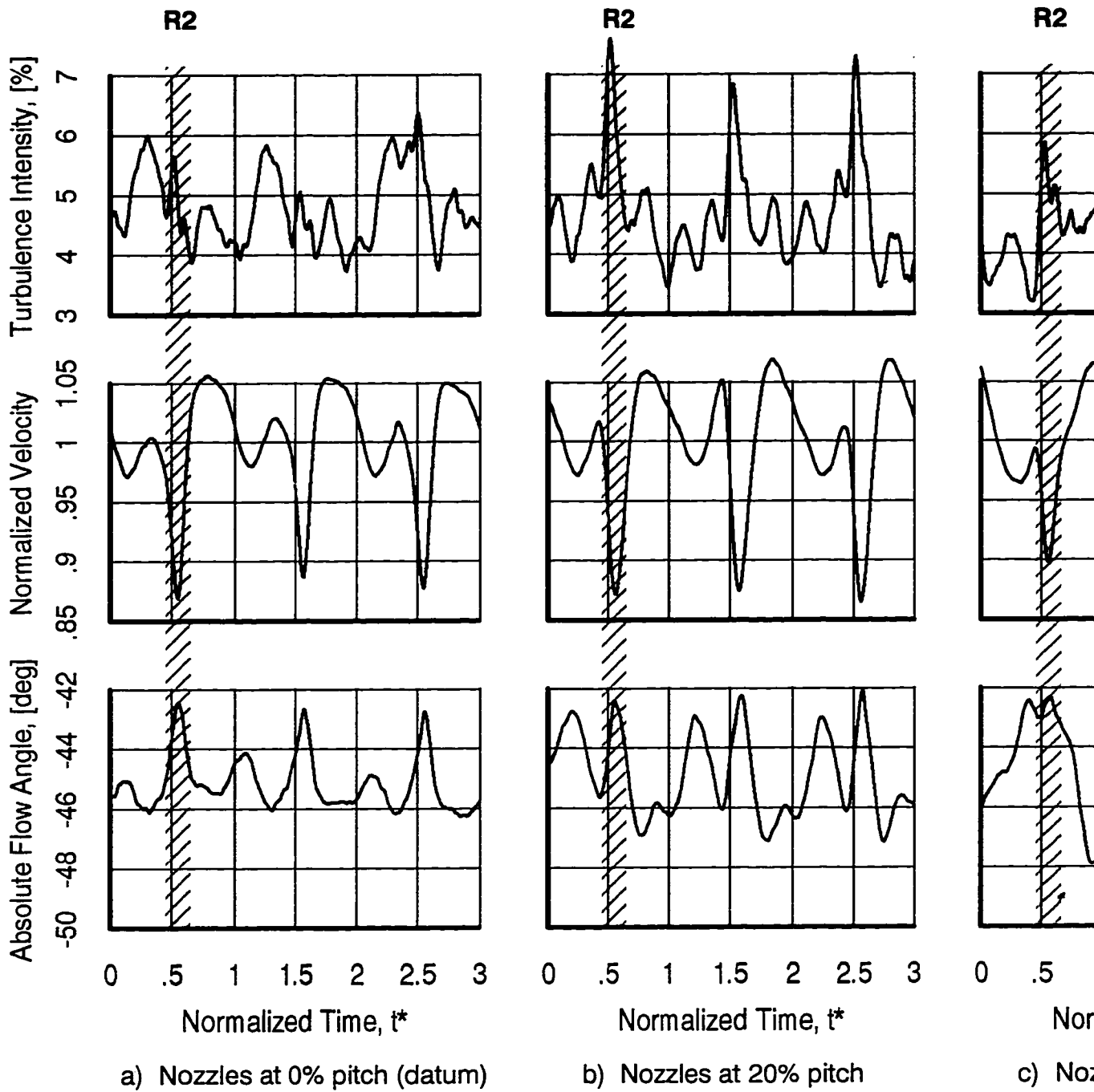
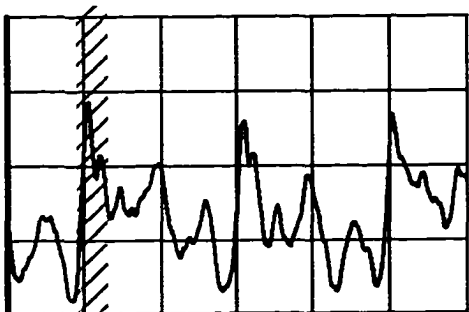


Figure 8.12. Measurements of unsteady flowfield at exit of Rotor 2 (Plane 3.0)



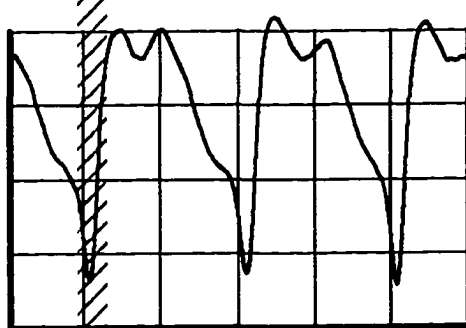
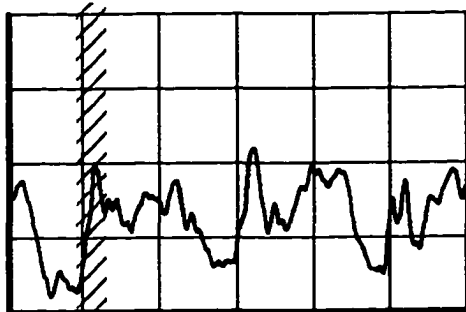
R2



0 .5 1 1.5 2 2.5 3
Normalized Time, t^*

c) Nozzles at 40% pitch

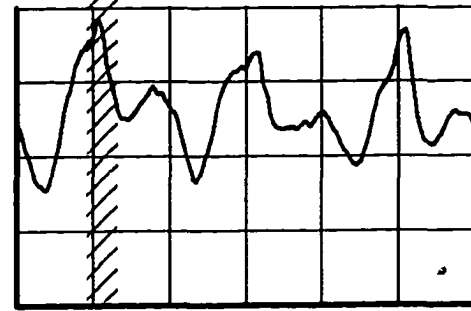
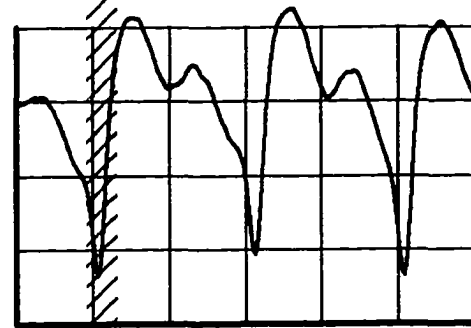
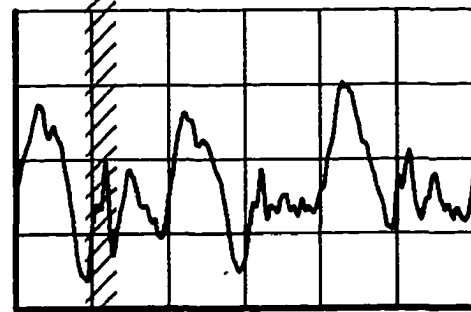
R2



0 .5 1 1.5 2 2.5 3
Normalized Time, t^*

d) Nozzles at 60% pitch

R2



0 .5 1 1.5 2 2.5 3
Normalized Time, t^*

e) Nozzles at 80% pitch



distributions in Figure 8.12. Between Rotor 2 wakes, the amplitude of variation in velocity and flow angle is similar qualitatively to that observed behind Rotor 1 (Figure 8.9).

The variation of turbulence intensity, however, exhibits a much higher degree of complexity and irregularity than found at Plane 2.0. At 20 percent and 40 percent, distinct periodic variation at four times blade-passing is evident. The peak levels of turbulence at 0 percent and 80 percent nozzle pitch amazingly *do not* coincide with the wakes of Rotor 2 but rather are found in the region between wakes. Such behavior is far different from conventional thought whereby the flow is envisioned to consist of a wake portion, exhibiting high relative values of turbulence, and a core flow region between wakes where turbulence intensity is lower and approximately constant. The results from Figure 8.12 suggest it is likely that wakes and wake segments from *all four* upstream bladerows still persist at Plane 3.0, albeit with varying degrees of strength.

CHAPTER 9. ANALYSES AND DISCUSSION

This chapter consists of four sections. In the first, selected computational analyses and experimental measurements are compared to provide additional insight into the observed boundary layer behavior. In the second section, the LSRT measurements are considered in the larger context of general LP turbine performance. Modeling and computational issues that relate to transitional boundary layers are considered in the third section. Lastly, issues important to the simulation of the disturbance environment in multi-stage LP turbines are discussed.

9.1 Comparisons of Computational and Experimental Results

The discussion below is divided into four parts. In the first, a very brief description of the boundary layer codes used for this assessment is provided. Next, consideration is given to the influence of turbulence intensity and pressure gradient on boundary layer development. Third, predictions of the location of transition are compared with measurements for two LSRT test points. Lastly, a comparison is made between predicted and measured values of bladerow loss coefficient.

9.1.1 Description of Boundary Layer Codes

Boundary layer calculations for the analyses described in this section were carried out using two steady flow codes available at GE Aircraft Engines.

STANX. The STANX code is a version of STAN5 originally developed by Crawford and Kays (1976). It solves the steady, two-dimensional, compressible form of the boundary layer equations. Turbulence modeling is accomplished using an algebraic mixing length modified to account for pressure gradients. The code allows the user to specify the location of transition onset (i.e., the location where the turbulence model is turned on). The length of transition is not modeled.

KEP. The KEP code is a modified version of STANX that includes a low Reynolds number, k - ϵ turbulence model (Zerkle and Lounsbury, 1987). Boundary conditions for k (turbulence

kinetic energy) and ϵ (dissipation rate of turbulence kinetic energy) are determined from user–provided values of turbulence intensity and length scale. The code assumes constant k across the bladerow. An inherent feature of k – ϵ models is that transition is simulated implicitly by the diffusion of turbulence kinetic energy from the freestream into the boundary layer. Hence, no information regarding transition onset or length is required from the user. To emphasize, this feature *simulates* transition and *is not* a physically–based model of transition.

9.1.2 Influence of Turbulence Intensity and Pressure Gradient

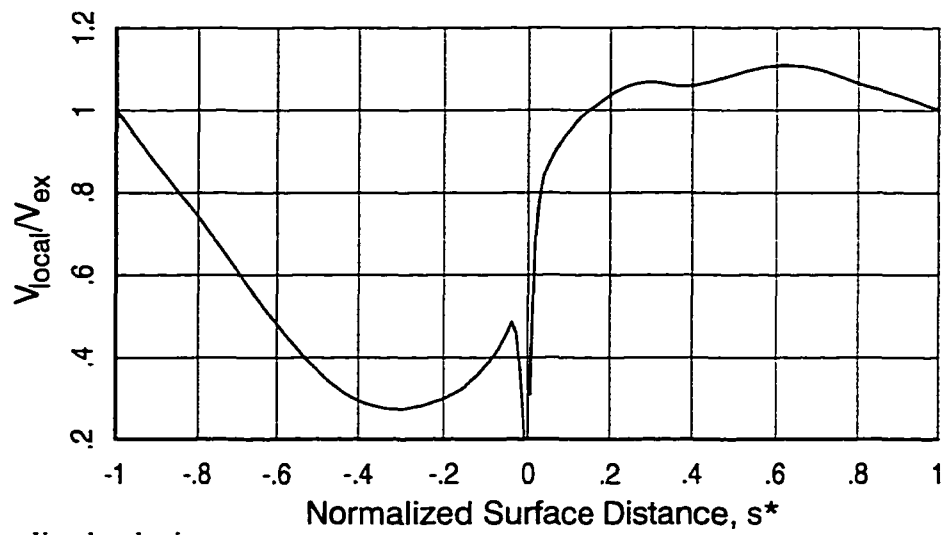
It is well known that boundary layer development and transition are influenced strongly by turbulence intensity and streamwise pressure gradient. Both effects are quantified in Figures 9.1–2 for the takeoff Reynolds number condition, test point 5A, and cruise Reynolds number, test point 5E. Part a of each figure is normalized velocity distribution identical to that reported in Figure 7.2a. They are repeated here for the sake of comparison.

When considering the effect of turbulence intensity on transition along an airfoil, it is the *local* value of intensity, not that at the bladerow inlet, that is of importance. For test points 5A and 5E, the ratio of local–to–inlet turbulence intensity is given as part b of Figures 9.1–2. A simple relationship used to calculate this ratio is derived below and follows from Zerkle and Lounsbury (1987). If we assume negligible turbulence dissipation across Nozzle 2, we can equate the inlet turbulence kinetic energy (TKE) of the bladerow to the local value occurring within the bladerow. This is written as

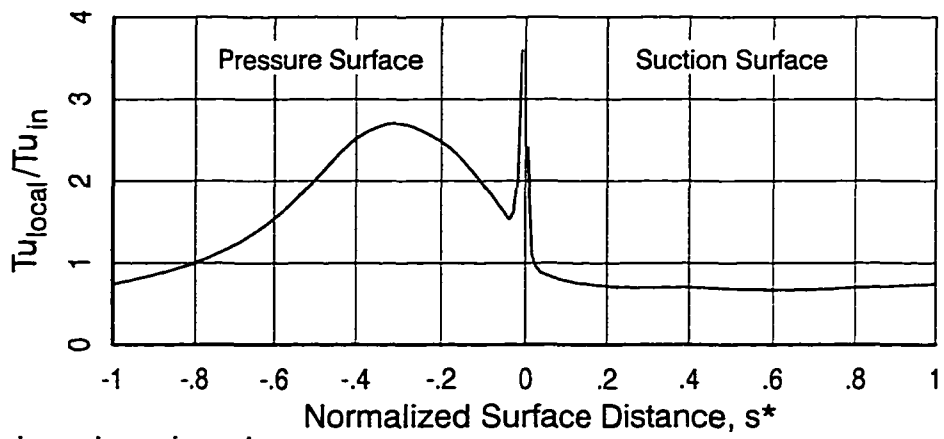
$$k_{\text{local}} = k_{\text{in}} \quad (9.1)$$

Applying the definition of TKE given in Chapter 6, the expression for the ratio of local–to–inlet turbulence intensity is determined as indicated by Equation 9.2.

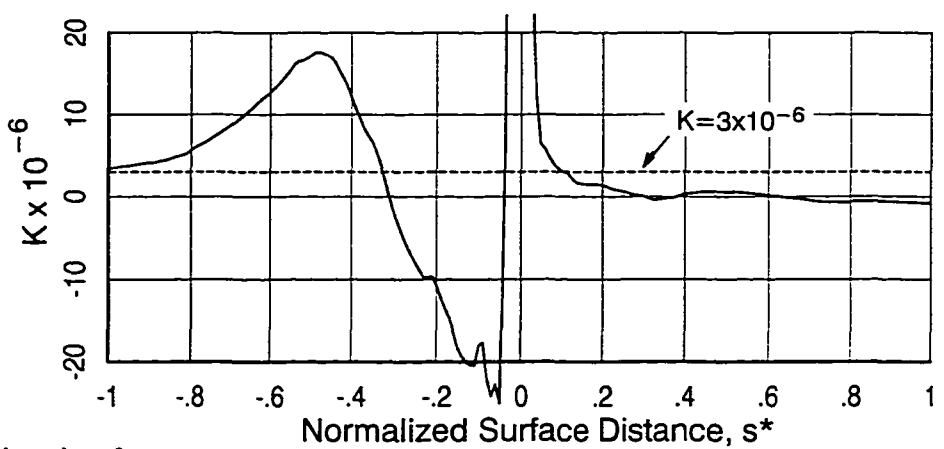
$$\begin{aligned} \frac{3}{2} T u_{\text{local}}^2 V_{\text{local}}^2 &= \frac{3}{2} T u_{\text{in}}^2 V_{\text{in}}^2 \\ \frac{T u_{\text{local}}}{T u_{\text{in}}} &= \frac{V_{\text{in}}}{V_{\text{local}}} \end{aligned} \quad (9.2)$$



a) normalized velocity

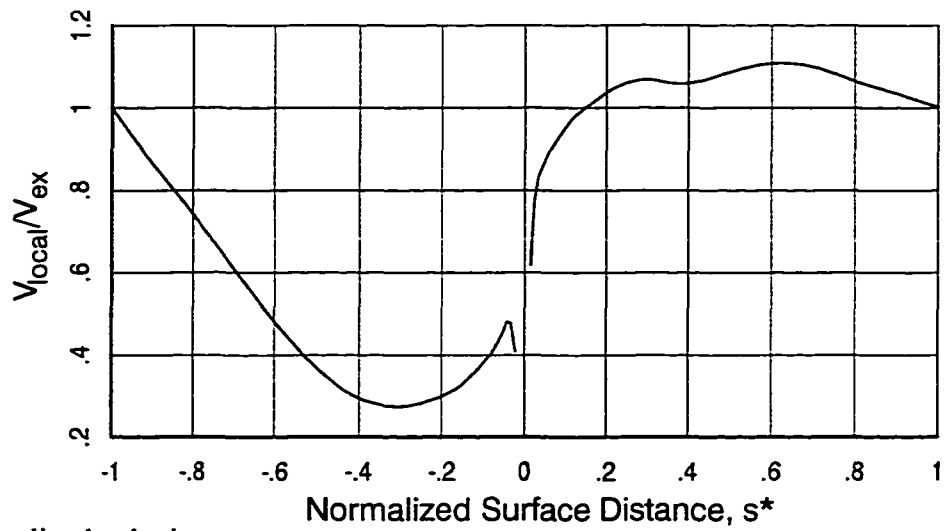


b) turbulence intensity ratio

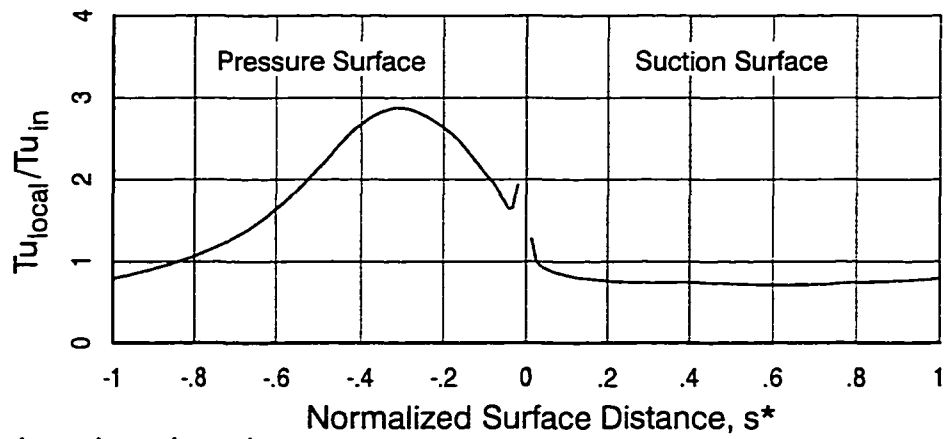


c) acceleration factor

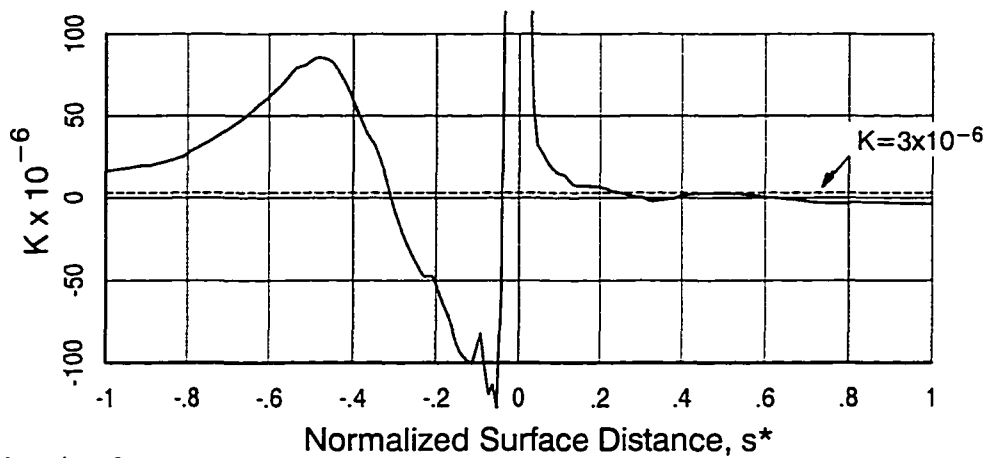
Figure 9.1. Aerodynamic characteristics along Nozzle 2, test point 5A



a) normalized velocity



b) turbulence intensity ratio



c) acceleration factor

Figure 9.2. Aerodynamic characteristics along Nozzle 2, test point 5E

Comparing the distributions of turbulence intensity ratio with those of velocity in part a, we find that flow acceleration attenuates the inlet turbulence intensity while deceleration augments it. Along the suction surface after the initial acceleration, the local-to-inlet turbulence ratio is equal to about 0.7 for both test cases. In contrast, significant augmentation occurs along the pressure surface with local values of turbulence approaching three times that of the inlet. Because the normalized velocity distributions did not vary significantly with Reynolds number, the distributions of turbulence intensity ratio for test points 5A and 5E are nearly identical.

The streamwise pressure gradient for each test condition is quantified in Figures 9.1c and 9.2c in terms of acceleration factor. It is defined as

$$K = \frac{v}{V_{\infty}^2} \frac{dV_{\infty}}{ds} \quad (9.3)$$

As noted in Schlichting (1979), positive values of acceleration factor can suppress transition of laminar boundary layers and, for values of K greater than about 3×10^{-6} , can relaminarize turbulent boundary layers. In each of the above-mentioned figures, the value of $K=3 \times 10^{-6}$ is demarcated by the horizontal dashed line.

For test point 5A in Figure 9.1c, we see that K is greater than the value required for relaminarization along the initial 11 percent of the suction surface. This is consistent with the contour plots of frequency spectra in Chapter 7 which indicated a dissipation of random unsteadiness downstream of the leading edge. The local region of flow diffusion in the velocity distribution manifests itself as negative values of K extending from 0.31 to 0.38s*. Downstream of 0.63s*, negative values of K extend to the trailing edge.

A very different distribution is found along the pressure surface. Immediately downstream of the leading edge, the acceleration factor decreases to large negative values — as low as -20×10^{-6} (extending off the plot). This results from the strong diffusion evident in the velocity distribution. It is apparent that this diffusion coupled with the local turbulence augmentation work together to bring about transition (attached or separated) very near the leading edge as doc-

umented in Chapter 7. Downstream of minimum velocity at $0.31s^*$, the acceleration factor becomes positive and reaches values greater than 17×10^{-6} — well above that at which relaminarization is expected. As we observed from the contour plots of frequency spectra and from the instantaneous time traces, significant dissipation of random unsteadiness did take place along this portion of the pressure surface. However, it did not appear that complete relaminarization occurred. As Zerkle and Lounsbury (1987) suggest, this is likely due to the elevated levels of local turbulence intensity that occur along the pressure surface.

The acceleration factor distribution from the cruise Reynolds number (test point 5E) in Figure 9.2c has the same trends as for 5A but with significantly higher magnitudes. This follows from Equation 9.3 as we see that, for equivalent normalized velocity distributions, the acceleration factor is inversely proportional to Reynolds number. As Reynolds number is decreased then, positive values of K become more positive and negative values more negative. Along the suction surface, K is greater than 3.0×10^{-6} from the leading edge to $0.25s^*$. Along the pressure surface, large negative values occur downstream of the leading edge followed by large positive values as the flow accelerates to the trailing edge.

It is important to note that both Equations 9.2 and 9.3 are determined from aerodynamic data that constitute input conditions for a steady boundary layer code. Consequently, such insight into the characteristics of the bladerow flowfield as just described can be gleaned prior to actually running a boundary layer analysis.

9.1.3 Predictions of Transition Location

Predictions of the transition onset location were obtained using a two-step process. First, the STANX boundary layer code was run in laminar-only mode until program execution was halted by flow separation. Secondly, a boundary layer characteristics diagram was constructed using the laminar solution from step one.

Characteristics diagrams constructed for the suction surface on Nozzle 2 are given in Figure 9.3 for the takeoff and cruise Reynolds numbers, test points 5A and 5E, respectively. The

diagrams themselves represent a visual correlation for the location of transition onset (in terms of momentum Reynolds number, $Re_{\theta, tr}$) as a function of the flowfield parameters of turbulence intensity, Tu , and streamwise pressure gradient, λ_{θ} . The definition of the pressure gradient parameter is given by Equation 9.4.

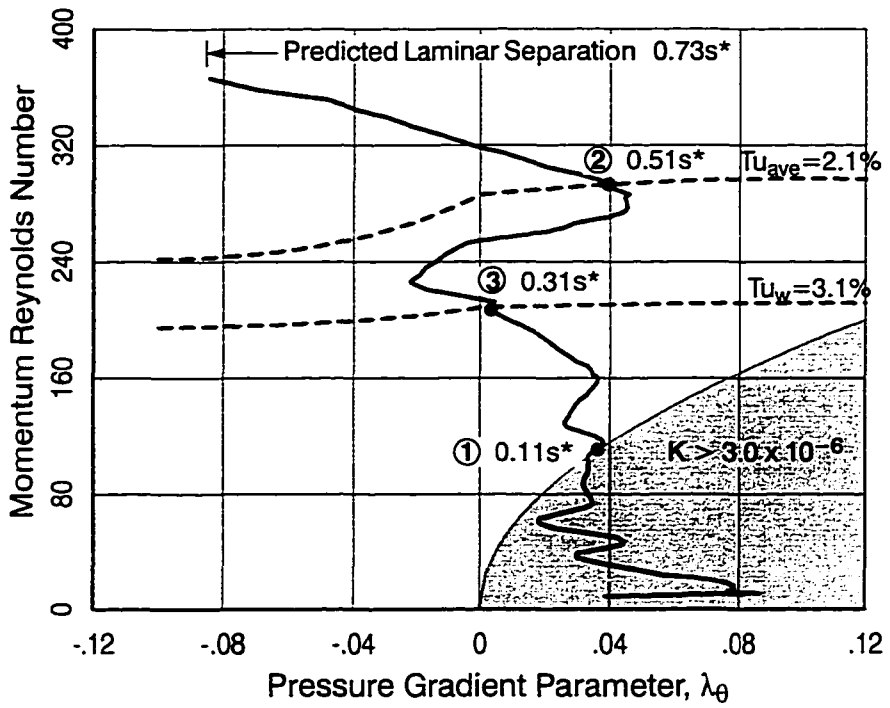
$$\lambda_{\theta} = \frac{\theta^2 dV_{\infty}}{v ds} \quad (9.4)$$

In Figure 9.3, the correlations of Abu-Ghannam and Shaw (1980) for transition onset are plotted as dashed lines for two levels of turbulence intensity.

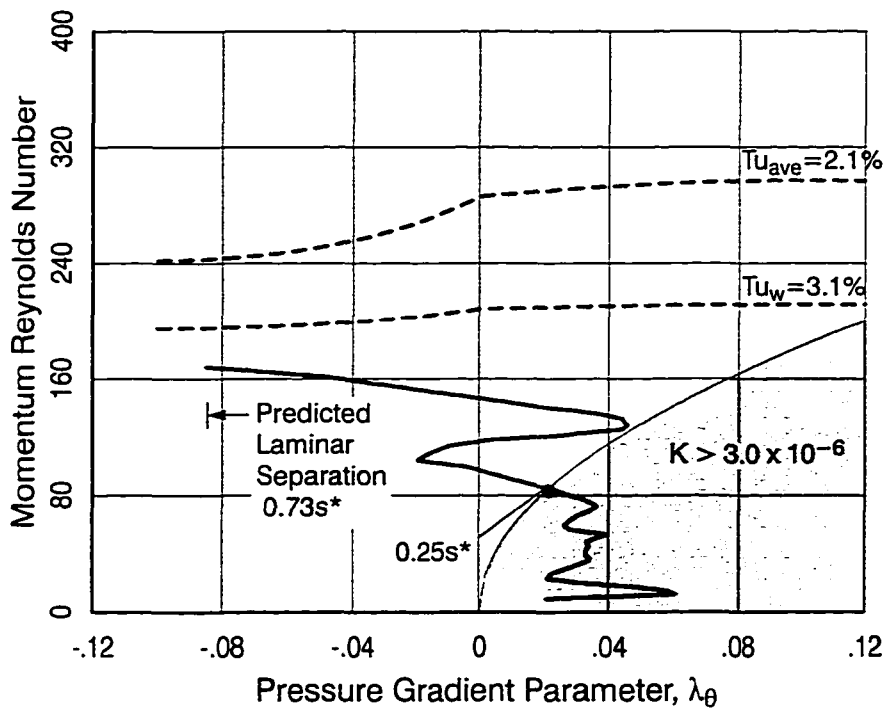
The laminar solutions from STANX, in $\{\lambda_{\theta}, Re_{\theta}\}$ coordinates, are plotted as the heavy solid lines in Figure 9.3. The predicted location of transition onset is determined by where the STANX solution intersects the appropriate correlation line. Also identified in Figure 9.3 are regions where the acceleration factor, K , is greater than 3×10^{-6} . Defined previously by Equation 9.3, acceleration factor can be calculated directly in terms of λ_{θ} and Re_{θ} , as indicated by Equation 9.5.

$$\begin{aligned} K &= \frac{v}{V_{\infty}^2} \frac{dV_{\infty}}{ds} \\ &= \frac{v^2}{V_{\infty}^2 \theta^2} \frac{\theta^2 dV_{\infty}}{v ds} = \frac{\lambda_{\theta}}{Re_{\theta}^2} \end{aligned} \quad (9.5)$$

Results for the takeoff Reynolds number (test point 5A) are given in Figure 9.3a. Correlations of transition onset are plotted for turbulence intensities of 3.1% and 2.1%. They are identified as being associated with the wake (subscript w) and the time average (subscript ave). It is important to remember that these pertain to *local* values of turbulence intensity and not those measured at the inlet to Nozzle 2. Consistent with Figure 9.1, the acceleration factor upstream of 0.11s* (point 1) is greater than 3×10^{-6} . The predicted location of transition for the time-averaged, local turbulence intensity occurs at 0.51s* (point 2). In comparison with measurements from Chapter 7, this coincides with the earliest observed transition occurring along the path between wakes (i.e., point 4 of Figure 7.26a). Along the wake-induced path where the turbulence



a) takeoff Reynolds number, test point 5A



b) cruise Reynolds number, test point 5E

Figure 9.3. Boundary layer characteristics diagrams for suction surface of Nozzle 2

intensity is higher, the predicted onset location is at $0.31s^*$ (point 3), which agrees exactly with the observed location, point 1 of Figure 7.26a. Because the Abu-Ghannam and Shaw (A-S) correlation accounts for turbulent but not periodic unsteadiness, this agreement provides further evidence that jet-wake interaction does not play a significant role in initiating transition. For this takeoff Reynolds number condition then, the A-S correlation does a credible job predicting transition onset. Specifically, it appears that the onset location determined using the time-averaged, local turbulence intensity is appropriate for a steady boundary layer calculation.

For the cruise Reynolds number (test point 5E), we find a significantly different result. From the characteristics diagram in Figure 9.3b, we see that laminar separation is predicted to occur at $0.73s^*$ *prior* to the onset of transition. In contrast, our experimental measurements described in Section 7.4.3 indicated that no separation was present and, rather, that wake-induced transition began at about $0.73s^*$. Also, between wake paths, non-turbulent flow persisted to the trailing edge as a result of calming effects and periodicity of the boundary layer. Clearly, a “conventional” laminar solution like that from STANX coupled with the A-S correlation does not account for these complexities. Consequently, separation is predicted to occur when, in actuality, it does not.

9.1.4 Aerodynamic Loss

A comparison of measured and predicted values of profile loss coefficient for Nozzle 2 at increased loading is shown in Figure 9.4. Measurements are indicated by the open symbols and are identified by test point. Calculated values are given by the closed symbols.

The lowest values of measured profile loss occur at the highest takeoff Reynolds number, test point 5A. As Reynolds number is decreased from takeoff to cruise, loss increases monotonically. At test point 5E, the loss coefficient is 65 percent greater than at test point 5A.

The trend of increasing loss with decreasing Reynolds number may appear paradoxical given that the boundary layer along the suction surface of Nozzle 2 is increasingly laminar as Reynolds number is reduced. This is explained as follows. First, it is well known that boundary

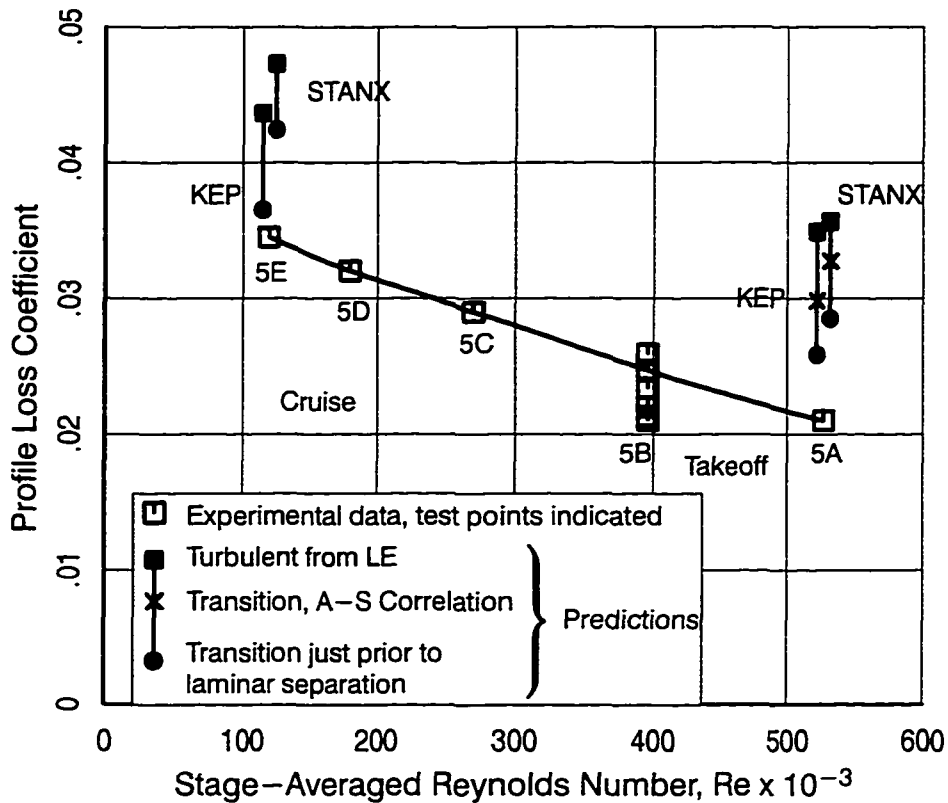


Figure 9.4. Comparison of measured and predicted values of profile loss coefficient for Nozzle 2

layer thickness varies in inverse proportion to Reynolds number. Secondly, as shown by Denton (1993) using a 2-D wake mixing analysis, the loss coefficient of a bladerow increases as the momentum and displacement thicknesses of the boundary layer increase. For transition at a *fixed location* along the airfoil then, we can conclude that loss coefficient will increase as Reynolds number is decreased. In addition, we also know that for a given Reynolds number, the longer transition is postponed, the smaller the boundary layer thickness is at the trailing edge. Taken together then, we see that the variation of loss with Reynolds number in Figure 9.4 simply reflects that the decrease in boundary layer thickness (and profile loss) as transition moves further aft is more than offset by the increase in boundary layer thickness (and profile loss) as Reynolds number is reduced.

At test point 5B, the profile loss coefficient of Nozzle 2 was determined for five relative clocking positions of Nozzle 1. With everything else held constant, the data points in Figure 9.4 indicate a 25 percent variation in the loss coefficient of Nozzle 2 due to Nozzle 1/Nozzle 2 interaction. For this LP turbine then, we conclude that Nozzle 1 clocking markedly influences both the detailed development of the boundary layer (Section 7.6) and the overall aerodynamic performance of the Nozzle 2 bladerow. Similar findings relating to overall aerodynamic performance of a high pressure turbine were documented by Huber et al. (1995).

Given the above findings, it is logical to ask: is there an optimal clocking position that will result in a higher overall efficiency of a multi-stage LP turbine configuration? In reality, the answer is generally “no” since, almost without exception, successive nozzle and rotor bladerows have differing blade counts for aero-mechanical and acoustical reasons. This is not the end of the issue though. As these data and the data of Huber et al. (1995) indicate directly, and those of Arndt (1993) indicate indirectly, the aerodynamic performance (and possibly heat transfer characteristics) vary from one blade passage to the next around the circumference of the turbine. The designer must, at minimum, be concerned with the “worst case.” From an aerodynamics standpoint, the worst case could be a loss-producing laminar separation along some blade passages, whereas along others the boundary layers remain attached. Such was the conclusion drawn by Arndt (*ibid.*) from his measurements obtained in the V2500 LP turbine. From a heat transfer standpoint, the worst case might be a localized hot spot that requires additional cooling relative to the average.

Predicted values of profile loss coefficient also are shown in Figure 9.4 for test points 5A and 5E. As indicated in the legend, a range of loss is obtained by varying the specified location of transition onset along the suction surface. The highest loss is identified by the filled square symbol and pertains to a turbulent boundary layer extending from the leading edge. With transition onset specified just prior to laminar separation, the lowest values of loss are predicted (filled circles). In total, the magnitude of loss coefficient varies by up to 35 percent as a conse-

quence of changing the location of transition onset. For modern LP turbines that already operate at high efficiencies, this level of difference is certainly significant and underscores the need to account accurately for transition.

The “X” symbols for test point 5A denote the predicted loss with transition onset specified using the A–S correlation as described in Section 9.1.3. When running the KEP code using the measured level of turbulence as input, transition onset was predicted too far aft relative to the A–S correlation. In addition, the onset location was found to be very sensitive to the value of input turbulence. Similar findings relating to k – ϵ turbulence models in general and to the KEP code in particular have been documented by Schmidt and Patankar (1991) and Zerkle and Lounsbury (1987), respectively. To obtain the KEP result that is included in Figure 9.4 then, the input turbulence intensity was varied until the predicted location of transition agreed with the A–S correlation.

At the cruise Reynolds number, test point 5E, the loss calculation that most closely simulates the measurements of Chapter 7 pertains to specifying transition onset just prior to predicted separation. However, as noted in the previous section, the laminar solution coupled with the A–S correlation erroneously predicts laminar separation to occur prior to transition onset. This contradicts the measurements of Chapter 7 and clearly identifies a deficiency in the calculation approach. As expected, the highest values of loss are calculated when assuming turbulent flow from the leading edge.

Overall, values of profile loss calculated using STANX and KEP boundary layer solutions consistently are over–predicted relative to the measurements for both test conditions. Not accounting for transition length in the boundary layer calculations and uncertainties in the base pressure coefficient used when calculating loss likely both contribute to this discrepancy. However, the trend of increasing loss with decreasing Reynolds number is predicted reasonably.

Before concluding this discussion on aerodynamic loss, it is instructive to consider the magnitudes of its various components. Such a breakdown is obtained directly from the 2–D

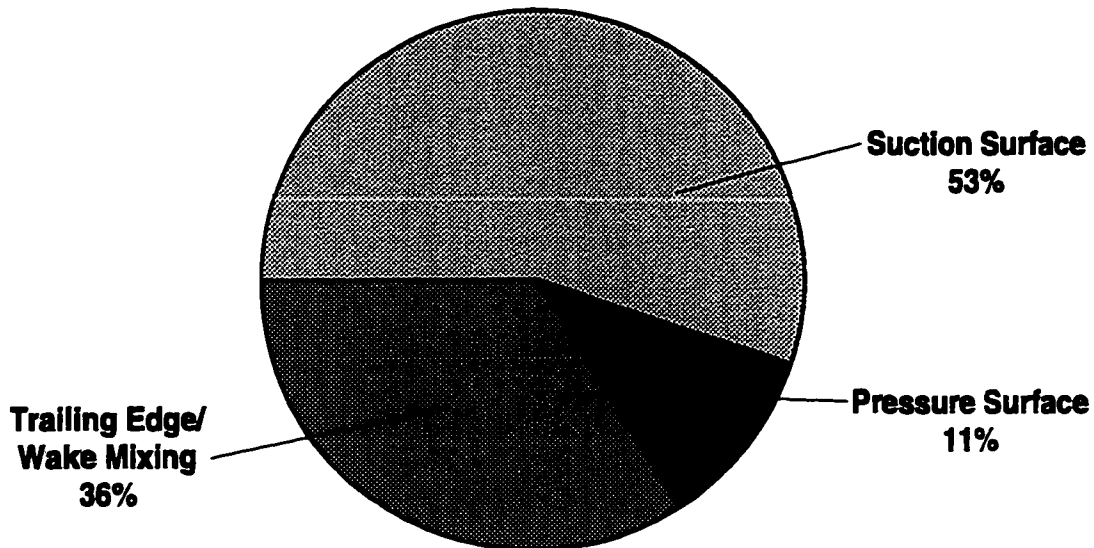


Figure 9.5. Breakdown of predicted loss coefficient for Nozzle 2, test point 5A, boundary layer calculation from KEP

wake mixing analysis used to calculate loss. An example result is contained in Figure 9.5 for the KEP boundary layer solution at test point 5A, symbol “X”. The overall loss is subdivided into three components. By far the largest pertains to the suction surface boundary layer. In contrast, even though the boundary layer along the pressure side transitions to turbulent near the leading edge, its contribution to the total is not large due to the strong flow acceleration along this surface. The trailing edge and wake mixing losses make up about one-third of the total.

From a design perspective then, we can draw the following conclusions from Figure 9.5.

1. Optimization of the suction surface boundary layer affords the largest potential benefit in improving aerodynamic performance. Clearly, postponing attached-flow transition and avoiding loss-increasing separations at a given test condition will yield the lowest loss characteristics.
2. Design changes that impact the pressure-side boundary layer will likely have a minimal impact on overall loss.

- 3 Minimizing trailing edge thickness / blockage has the potential to moderately reduce overall loss. As shown by Denton(1993), trailing edge losses are related directly to trailing edge thickness.

The loss breakdown just considered is applicable along the entire span of an LP turbine bladerow except in the endwall regions. However, because of the high aspect ratio, the profile loss portion of the total loss of the turbine should be appreciable, making it a good candidate for optimization.

9.2 LP Turbine Performance – the Bigger Picture

It is important to remember that the LSRT configuration utilized for this research represents one out of many possible LP turbine designs. We see from the cascade and rotating rig test cited in Chapter 2 that LP designs can differ significantly — especially in terms of airfoil velocity distributions (e.g., location of V_{\max} and magnitude of V_{\max}/V_{exit} along suction surface). As these studies document, the boundary layer development and aerodynamic performance differ as well. In the discussion that follows, the LSRT results are considered in the larger context of these studies.

An excellent review of LP turbine performance as relating to design methodology was provided by Hourmouziadis (1989). In this work, he identified a more broad range of boundary layer flow regimes than observed in the LSRT. Based in part on his Figure 23 and on new findings reported since then, the flow characteristics of an LP turbine are described schematically in Figure 9.6 for a typical range of Reynolds numbers. Profiles of an LP turbine airfoil are shown in black. Laminar and transitional/turbulent boundary layers along the suction surface are indicated by the white and shaded regions, respectively. Additionally, separated-flow regions appear along the suction surface for the three right-most airfoils in the figure.

A number of flow regimes are identified by Roman numeral. Region I is furthest to the right and denotes the highest Reynolds numbers. Here, transition occurs at or near the leading edge. Loss along the suction surface is dominated by turbulent skin friction. As Reynolds num-

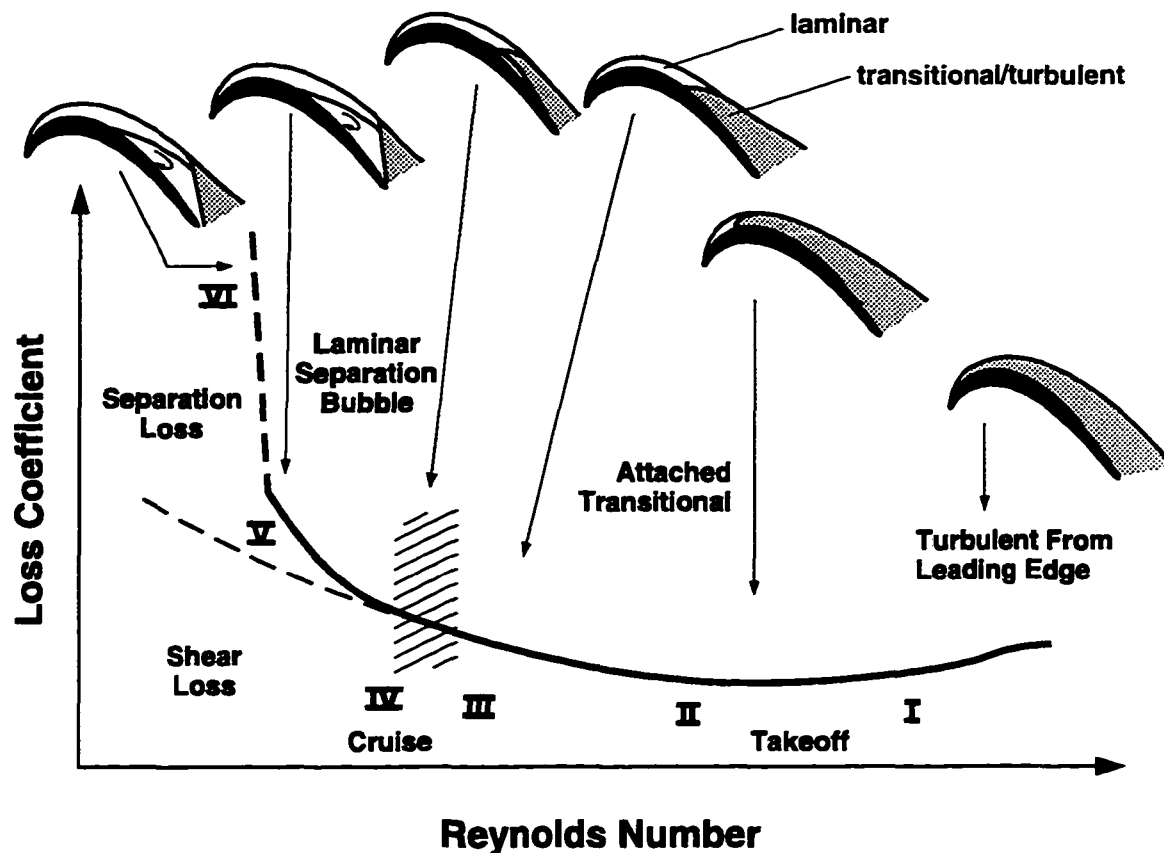


Figure 9.6. Effects of Reynolds number on LP turbine performance (after Hourmouziadis, 1989)

ber is reduced, transition moves downstream of the leading edge. As shown, profile loss at Region II can be less than at I provided the decrease in loss from transition moving aft more than offsets the increase with reducing Reynolds number. Flow regime II is similar to test point 5A of the LSRT.

As Reynolds number is decreased further, transition onset shifts to the aft portion of the airfoil. Loss increases gradually in a manner that reflects the reduction of Reynolds number. Flow regime III represents the limit at which the suction surface boundary layer is at all times attached. It is analogous to test point 5E of this work. In Regime IV, the Reynolds number is sufficiently low that a laminar separation occurs prior to attached-flow transition. The separated shear layer will transition quickly and, provided the separation is far enough from the trailing edge, will reattach forming a bubble. Measurements of Schulte and Hodson (1996) indicate that

laminar separation will occur at first intermittently when wakes are present, hence the hatching in Figure 9.6. Their results also suggest that the rate at which loss increases with Reynolds number does not change greatly when the intermittent separation first appears.

For still lower Reynolds numbers, the reattachment point moves aft and, at regime V, occurs just prior to the trailing edge. Here, laminar separation occurs along both the wake and non-wake paths of the suction surface. Loss increases progressively from IV to V as the more pronounced bubble produces a thicker boundary layer at the trailing edge. The difference in loss between the light dashed line and the solid line is attributed to the presence of the bubble. Various measurements from Hourmouziadis, Buckl, and Bergmann (1987) and Schroder (1991) indicate that the PW2037 and V2500 LP turbines operate at and to the left of regime IV at cruise Reynolds numbers.

Finally, in regime VI, a dramatic increase in loss occurs as the separated shear layer is not able to reattach prior to the trailing edge. With respect to aerodynamic performance, this regime is fittingly termed the “cliff”.

The precise characteristics of the aerodynamic performance curve for a given LP turbine depend largely on the airfoil velocity (loading) distribution (Hourmouziadis, 1989). To illustrate, three possible distributions are drawn schematically in Figure 9.7. Profile A is similar to those of the rotor and nozzle in the LSRT. Maximum velocity is located aft of mid-chord and the diffusion gradient prior to the trailing edge is moderate. A second candidate, profile B exhibits a higher degree of loading which enables one to reduce airfoil count. Maximum velocity for “B” is increased relative to that of “A” producing a stronger diffusion gradient prior to the trailing edge. Values of V_{\max}/V_{exit} as high as 1.40 have been reported (Hourmouziadis, Buckl, and Bergmann, 1987). For profile C, increased loading has been achieved by moving maximum velocity forward of mid-chord. This concept is known as “front-loading.” Performance of front-loaded airfoils is documented in Curtis et al. (1996) and Hoheisel et al. (1987).

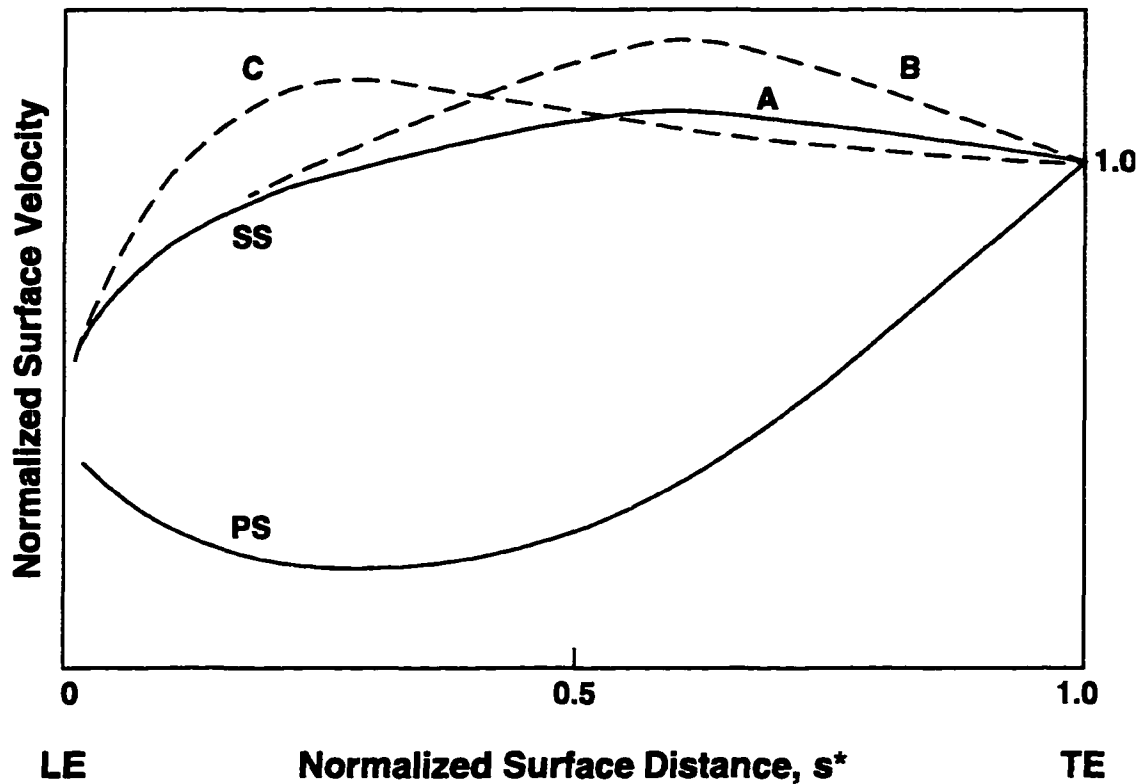


Figure 9.7. Different loading distributions for turbine airfoils (after Halstead et al., 1995)

How do such variations in airfoil loading influence overall turbine performance? For a design that incorporates moderate, aft loading, such as profile A, the suction surface boundary may remain attached over the entire range of Reynolds number, operating in regimes II and III. Profile loss is dominated by wetted surface area. If airfoil loading is too conservative, the result will be an airfoil count per bladerow that is too high, which in turn produces high wetted-area loss (Wilson, 1984). In the context of Figure 9.6, this would produce an upward shift in profile loss relative to that shown for regimes II and III of Figure 9.6.

A design incorporating more aggressive airfoil loading (i.e., higher V_{\max}/V_{exit}) requires fewer airfoils to do the same flow turning. For profile B, the stronger diffusion gradient increases the likelihood of laminar separation compared to profile A — especially at cruise Reynolds numbers. Consequently, the variation of loss with Reynolds number may be similar to

regimes III–V of Figure 9.6. The design objective sought when employing a front-loaded profile like “C” is to achieve increased loading while avoiding non-reattaching separation at cruise Reynolds number by moving transition forward. To date, studies indicate that the increased turbulent skin friction losses which characterize front-loaded profiles make them less attractive compared to aft-loaded.

In summary, the choice of airfoil loading is one in which minimizing airfoil count (which may equate to savings in cost and weight) is balanced with a potential decrease in performance due to flow separation coupled with the risk of operating closer to the cliff (regime VI) at low cruise Reynolds numbers. It is clear from the discussion above that a designer *must* be able to account accurately for the effects of boundary layer development (i.e., laminar, transitional, turbulent, separational) in order to optimize an LP turbine design confidently. The inability to carry this out may lead to overly-conservative designs or expensive redesigns.

9.3 Accounting for Transition

In this section, modeling and computational issues are considered as they relate to the prediction of transitional boundary layers.

9.3.1 Location of Transition Onset

From the discussion in Section 9.1.3, we observed that for high Reynolds numbers, accurate predictions of transition onset can be obtained using conventional correlations. For low Reynolds numbers, this approach was not successful. It is apparent from the measurements that both periodic variations in the laminar boundary layer and calming effects play a role in suppressing separation and postponing transition. A conventional steady boundary layer analysis with a correlation for transition onset does not account for these complexities. As noted in the review article of Sharma, Ni, and Tanrikut (1994), no model exists to date that will predict accurately this periodically unsteady, transitional/separational boundary layer.

9.3.2 Length of Transition

As noted previously, one shortcoming of the STANX and KEP calculations was that transition length was not taken into account. In recent years, a number of promising models have been developed to this end. For codes utilizing k - ϵ models, improved predictions of both onset location and length have been achieved by modifying terms in the equations for k and ϵ (Schmidt and Patankar, 1991). This method is appealing as the capability to simulate transition is enhanced while retaining the attractive features of a k - ϵ turbulence model.

A second modeling approach that is more relevant to turbomachines accounts for the effects of wake-induced transition on the development of airfoil boundary layers. Four such models are referenced in Sharma, Ni, and Tanrikut (1994). The models all have exhibited a degree of success for particular data sets.

It is important to note, however, that these two modeling approaches apply to attached boundary layers only.

9.3.3 Unsteady Boundary Layer Analysis

An unsteady boundary layer code for application to turbomachinery was recently completed by Fan and Lakshminarayana (1996). They first solve the unsteady flowfield using a time-accurate, unsteady Euler solver. This solution provides the input conditions for a two-dimensional, unsteady boundary layer code. Variations of both velocity and turbulence fields from the upstream bladerow are taken into account. The boundary layer code employs a k - ϵ turbulence model developed for unsteady turbulent boundary layers. Comparison of calculations with measurements from test point 5A (Halstead et al. 1995) shows some promise. However, as expected, transition length was greatly under-predicted in a manner consistent with k - ϵ models. More importantly, calming effects are not resolved and laminar separation is not predicted accurately. In its present form then, it is not applicable to low, cruise Reynolds number conditions of an LP turbine.

9.3.4 Advanced Computational Fluid Dynamics (CFD)

In recent years, the use of advanced CFD to optimize the design of turbomachinery components has become more commonplace (AGARD, 1994). A number of Navier–Stokes solvers with various capabilities are now available to designers. To date, most calculations are carried out assuming turbulent flow from the leading edge. As shown herein, this assumption clearly is not valid for LP turbines. One simplified approach that does account for transition employs the algebraic, Baldwin–Lomax turbulence model (e.g., Turner, 1995). The turbulence model is activated at the location of transition onset specified by the user. As noted by Dailey (1993), however, adequate grid resolution in both the streamwise and transverse directions are required to predict correctly the laminar portion of the boundary layer that extends from the leading edge to the location of transition. This is an unattractive proposition for 3–D, multi–stage calculations as increased grid density leads to excessive run times. Further, it must again be pointed out that the above approach applies to attached boundary layers only. As noted previously, no model is available to predict the laminar separation problem in LP turbines at low Reynolds numbers.

9.4 Simulating the LP Turbine Disturbance Environment

The measurements obtained in this two–stage LP turbine show that the disturbance environment plays a key role in the subsequent boundary layer development. This point is emphasized repeatedly from the comparisons made in Chapter 7 of inlet turbulence intensity to the corresponding contour plots of surface hot–film quantities. Further, the influence of turbulence intensity on transitional boundary layers in general is well documented. From correlations (e.g., Mayle, 1991, and Abu–Ghannam and Shaw, 1980), we see that for turbulence levels below about 5%, the location of transition onset varies significantly with intensity. For turbulence intensities much above 5%, this functional dependence is much weaker. When carrying out investigations using facilities that simulate LP turbines, it is self–evident then that the disturbance environment must be properly developed.

What are the characteristics of the disturbance environment in an actual LP turbine? To the knowledge of this author, no quantitative measurements from real engine hardware have been published to date. (As noted previously, turbulence measurements from the five-stage LP turbine of the V2500 (Arndt, 1993) were not accurate in an absolute sense.) However, some important conclusions can be drawn from the work reported herein.

From the time-averaged measurements reported in Chapter 8, we observed that turbulence kinetic energy and intensity continued to increase from the inlet to exit of the two-stage LSRT. This certainly implies that the minimum turbulence intensity that we would expect in an engine LP turbine would be equal to that at the exit of the LSRT Rotor 2 — that is, about 4.5%. Actually, it may be even higher. Given what is known about turbulence levels in high pressure turbines (e.g., Zerkle and Lounsbury, 1987), we conclude that the 2.5% intensity measured at the inlet to the LSRT blading is too low relative to the engine environment. Based on these findings, future tests in the LSRT are planned in which the inlet turbulence will be increased using a turbulence-generating grid.

The unsteady X probe measurements suggest that the turbulence variation at the exit of a bladerow can be considered in terms of wake and between-wake components. In the LSRT, the highest levels of wake turbulence were measured at the exits of the rotors and ranged from about 4–6% intensity. Values for Rotor 2 were nominally about 1% higher than for Rotor 1 and likely result from the difference in stage loading noted in Chapter 8. In comparison to these LSRT data, wake turbulence levels achieved by a number of researchers using rods are higher by a factor of two or more. For example, the rod-generated wakes for the flat plate tests of Funazaki (1996) had turbulence levels ranging from 12 to 18%. The rods employed by Schulte and Hodson (1996) produced wakes with intensities of 10–14%. Clearly, such differences in comparison to the LSRT wakes will influence the extent to which the wake influences boundary layer development. In fact, Funazaki's measurements indicated that the wake-influenced boundary

layer was turbulent from the leading edge of his plate. This is far different from the LSRT observations reported herein.

An additional note of caution is in order concerning the use of rods to generate wakes. Our LSRT measurements suggested that both the wake turbulence intensity and wake deficit play a role in boundary layer development. The latter (wake deficit) influences the strength of the jet–wake effect. At the low cruise Reynolds number (test point 5E), we observed that the periodicity from the jet–wake effect, as well as calming, appeared to suppress separation. However, measurements reported in Halstead et al. (1995) indicated that wakes from a rod could not be generated that satisfactorily matched a turbine airfoil wake. When velocity deficit was matched, the turbulence level of the rod wake was too high. If turbulence intensity was matched, the velocity deficit was too low.

In light of the issues, appropriate caution should be taken when extrapolating results from cascade/rod experiments to actual LP turbines.

We now turn our attention to the magnitude of turbulence intensity between wakes. For the LSRT, values ranged from about 1.5–3.5% at the exit of Stage 1 (i.e., inlet to Nozzle 2) and from about 3.5–6.0% at the exit of Stage 2. As noted previously, the latter is probably more representative of an engine LP turbine. In retrospect then, the relevance of boundary layer studies from a number of the rotating turbine and cascade/rod tests cited in Chapter 2 is somewhat compromised due to low between–wake turbulence intensity. For example, the freestream turbulence between rod–generated wakes reported in Schulte and Hodson (1996) was just 0.5%.

Before leaving this issue, it is equally important to recall the periodic complexity of the between–wake turbulence reported in Chapter 8. This variation appeared to be related directly to the presence of wake segments from upstream bladerows that had not yet mixed out. In fact, at the exit of Rotor 2, between–wake levels of turbulence were higher than from the Rotor 2 wake for some clocking positions of Nozzles 1 and 2. Simply put, the “conventional” model of high turbulence intensity in the wakes and lower, almost constant levels between wakes is not valid

in multi-stage LP turbines. Simulation of this complex interaction requires at least three blade-rows in a rotating turbine and hence is missed entirely in single-stage and cascade/rod tests.

It is generally believed that turbulence length scale as well as intensity influences boundary layer transition (Mayle, 1991). In addition, for CFD codes that employ k - ϵ turbulence models, it is an important input parameter (e.g., Dailey, 1993). In spite of this, length scale is rarely reported in the literature. It is hoped that the measurements obtained as part of this work provide at least a basis for those researchers seeking to simulate both turbulence intensity and scale. At minimum, values of length scale, whatever they may be, should be reported in the future to facilitate code validation and the comparison of data sets.

CHAPTER 10. CONCLUSIONS

Comprehensive experiments were conducted to document the development of boundary layers along airfoil surfaces in a multi-stage LP turbine. At all test conditions, the suction surface boundary layers were predominantly laminar and transitional. Generally, the periodically unsteady boundary layers developed along two distinct paths coupled by calmed regions. A wake-induced path occurred approximately beneath the wakes that convect through the bladerows. The second path developed between the passing wakes. Along both paths, regions of laminar, transitional, and turbulent flow were identified. Regions of calmed flow developed behind turbulent spots of both paths. The elevated shear stress in the calmed regions effectively suppressed separation of non-turbulent flow in regions of adverse pressure gradients.

At high takeoff Reynolds numbers, the suction surface boundary layers were found to be laminar and transitional for as much as 70 to 80 percent of the airfoil surface. Isolated regions of non-turbulent, calmed flow persisted to the trailing edge. Flow along the wake path was initially laminar downstream of the leading edge in spite of the higher levels of wake turbulence. For low cruise Reynolds numbers, the boundary layers were strictly laminar for more than seventy percent of the suction surface after which wake-induced transitional strips were formed. Between strips, calming effects and the periodic variation of the laminar boundary layer suppressed separation back to the trailing edge.

As airfoil loading was varied, it was observed that even a slight region of local diffusion was sufficient to initiate transition. Transition was postponed longest when continuous acceleration was maintained from the leading edge to maximum velocity.

The relative clocking of bladerows in the same reference frame had a substantial impact on boundary layer development and aerodynamic loss. Flowfield measurements showed that the most important aspect of this interaction was the variation to the turbulence environment entering the downstream bladerow.

Along the pressure surface for all test conditions, laminar–turbulent transition occurred in the region of adverse pressure gradient downstream of the leading edge. At decreased loading (increased negative incidence), transition took place via a laminar separation bubble. At increased loading (decreased negative incidence), attached–flow transition was observed. Downstream of transition, little periodicity in boundary layer development was observed. Aft of minimum velocity, the strong flow acceleration extending to the trailing edge produced a partial relaminarization of the turbulent boundary layer.

Measurements of the unsteady velocity and turbulence fields were made at all measurement planes from the inlet to exit of the turbine. The flowfield was increasing complex behind each successive bladerow. The conventional model of the flow behind bladerows (i.e., a wake component and “freestream” component) was found to not apply in multi–stage LP turbines. At the exit of Stage 2 for this turbine, turbulence intensities in the core flow region were higher than of the wakes for certain nozzle clocking positions. Turbulence length scales, reported for the first time from an LP turbine, measured nominally 30 percent of the throat width of the upstream bladerow.

Significant differences in levels of wake turbulence and core flow turbulence were found when comparing measurements from this multi–stage turbine with those from test facilities that simulate the turbine environment. In particular, turbulence intensities of rod–generated wakes were sometimes two or three times larger than those measured here. Core flow turbulence intensities were often lower than one percent. Consequently, appropriate care must be exercised when extrapolating results from these facilities to multi–stage LP turbines. When simulating the turbulence environment, both intensity and length scale should be considered and reported.

The boundary layer measurements reported here indicate clearly that engineers must have the means to account for laminar–turbulent transition to optimize LP turbine designs confidently. At high Reynolds numbers for this work where the boundary layers were unquestionably attached, predictions of transition onset using a conventional correlation agreed well with the

measurements. At low Reynolds numbers, transition onset could not be predicted accurately using the conventional, steady boundary layer approach. Instead, the measurements suggest that both periodic unsteadiness and calming effects must be taken into account. Even for attached boundary layers, the existing models for wake-induced transition need to account for the effect of calming on boundary layer development.

CHAPTER 11. RECOMMENDATIONS FOR FUTURE RESEARCH

The need clearly exists for further study of boundary layer development in LP turbines. The LP blading utilized in this study had a moderate level of airfoil loading. No boundary layer separation along the suction surfaces was observed over the operating range of Reynolds number. Studies using turbines with higher airfoil loadings will provide much-needed insight into the interaction of wakes with separated laminar boundary layers. Specifically, additional understanding is required of the process by which attached-flow transition gives way to reattaching and non-reattaching separated-flow transition. Such a test program would be best carried out in a multi-stage facility such as the LSRT. This would enable detailed measurements in a flow environment that most closely simulates an actual LP turbine.

Additional experiments also should be directed to the endwall regions of the LP turbine. Here, uncertainty as to the state of the boundary layer remains owing to the more three-dimensional and unsteady nature of the flow.

Clearly, one of the surprises from the present study was the role of calming on boundary layer development. The suppression of separation at low Reynolds numbers had not been documented previously. Additional investigations are required to better understand this aspect of calming. Its importance is underscored in that it makes very uncertain the a priori prediction of separation in wake-disturbed boundary layers. At high Reynolds numbers, calmed regions that formed behind wake-induced strips significantly extended the length of transition. There is a need to account for this effect as well in models of wake-induced transition.

Lastly, the need for additional measurements in turbulence intensity and length scales in multi-stage LP turbines especially is apparent. Also, future investigations carried out using facilities that simulate this environment should employ adequate flow conditioning in order to broaden the relevance of the resulting measurements.

APPENDIX A. GENERAL DISCUSSION OF TRANSITION

Contained in this appendix is a general discussion of boundary layer transition that provides a background to results reported in this dissertation. The material included below was taken directly from the ASME paper by Halstead et al. (1995) where it makes up their Section 4.0. Descriptions of the following are provided: 1) the processes associated with transition from laminar to turbulent flow, 2) the characteristics of individual turbulent spots and their calmed regions, and 3) terminology associated with transition.

4.0 GENERAL DISCUSSION OF TRANSITION

The development of unsteady boundary layers on turbomachinery blading is influenced significantly by laminar to turbulent transition. Therefore to facilitate the reading of this paper, we describe the transition processes and associated terminology used throughout this work.

4.1. Transition Processes.

The three fundamental processes by which transition occurs in steady flow are also relevant for the unsteady flow in turbomachinery. These are:

Tollmien-Schlichting (TS) Transition. The process of Tollmien-Schlichting, or "natural" attached-flow transition, is shown schematically in Fig. 8a (White, 1974). For very low freestream disturbance where TI is less than 1.0 percent, the laminar boundary layer develops linear oscillations of well-defined frequency when the Reynolds number exceeds a critical value. This is shown as region 1 in the figure. These oscillations, called Tollmien-Schlichting (TS) waves, are two-dimensional and convect at a typical speed of $0.30\text{--}0.35 V_\infty$. As the amplitude of the TS waves increases, spanwise distortions of the vortical structure develop (region 2) and grow in an increasingly three-dimensional and non-linear manner (region 3). They eventually burst into turbulent spots (region 4). Within this region, the boundary layer alternates between laminar and turbulent states. Eventually the turbulent spots originating from different locations merge and form a fully developed, continuously turbulent boundary layer as transition is completed (region 5).

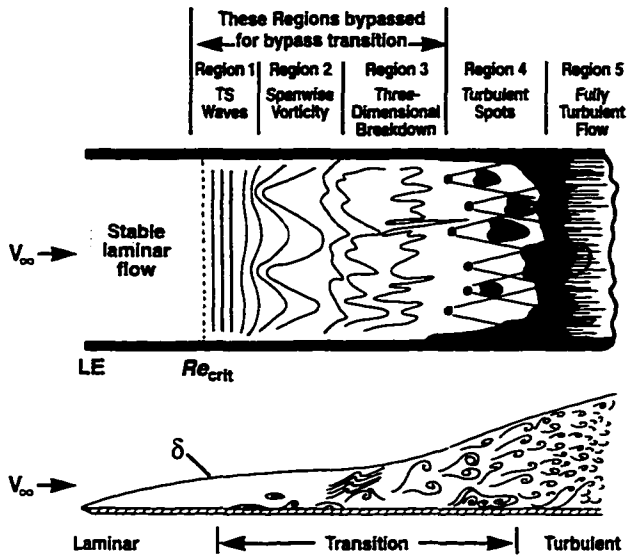
Bypass Transition occurs when the formation and amplification process of two-dimensional TS waves in natural transition is "bypassed" due to the presence of forced disturbances

of sufficient amplitude. Sources of such disturbances include higher freestream turbulence and surface roughness. In this mode of transition, TS waves are less evident, if present at all. Rather, the first indication of transition may be the direct formation of turbulent spots thus "bypassing" regions 1–3 of Fig. 8a. This process significantly reduces the length of unstable laminar flow and will promote earlier transition.

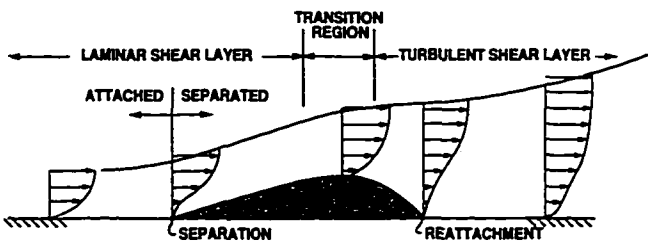
Separated-Flow Transition. Under certain instances, e.g., at high positive or negative incidence, rapid diffusion or low Reynolds number, the laminar boundary layer may separate from the airfoil surface. Rapid transition then occurs within the separated shear layer. Provided the Reynolds number is not too low or the local pressure gradient too large, the resulting turbulent-like layer will reattach to form a closed region of separated flow called a separation bubble (Roberts, 1980). The region beneath the separated laminar shear layer within the bubble is quiescent, with very low wall shear stress and nearly constant static pressure. This process is shown schematically in Fig. 8b.

4.2. Turbulent Spots, Intermittency, and the Calmed Region

Turbulent Spots. Bypass transition and the latter stages of T-S transition are characterized by the production and propagation of turbulent spots in the laminar boundary layer. As shown in Fig 9a, turbulent spots are approximately triangular in shape and spread laterally at an angle of about 22° as they move downstream of their origin. The region swept out by the spot is its zone of influence. The convection velocities of the leading and trailing boundaries of the spot are $0.88 V_\infty$ and $0.50 V_\infty$, respectively, as measured in zero pressure gradient by Schubauer and Klebanoff (1956). Their values do not vary



a) Tollmien-Schlichting transition (after White, 1974) and bypass transition



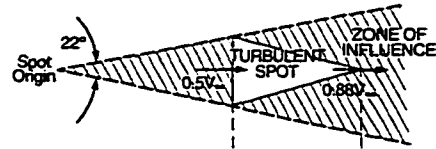
b) Separated flow transition with separation bubble shaded (after Walker, 1975 and Roberts, 1980)

Fig. 8 Schematics of transition process.

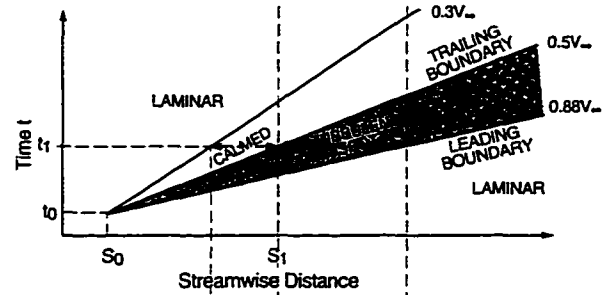
with streamwise direction. Consequently, the spot maintains a self-similar shape as it moves downstream.

Various characteristics of a turbulent spot are conveniently described using a space-time (s - t) diagram as shown in Fig. 9b. Lines of constant time drawn parallel to the “ s ” axis provide the instantaneous state of the flow along the surface. Likewise, vertical lines parallel to the “ t ” axis provide the unsteady behavior of the flow at a given location along the surface. Trajectories, drawn in Fig. 9b at $0.88 V_\infty$ and $0.50 V_\infty$, define the leading and trailing boundaries of the turbulent spot in the s - t diagram. For a constant streamwise velocity, the boundaries are straight lines in s - t space, otherwise they are curved. The convective velocity of each boundary is the inverse slope of its trajectory. The shaded region in the figure describes the streamwise and temporal growth of the spot as it convects along the surface.

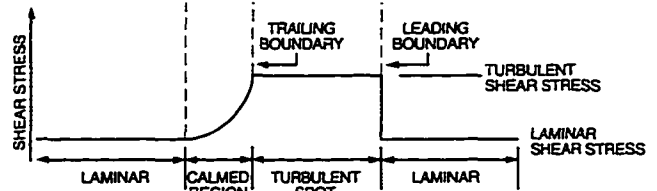
The streamwise distribution of wall shear stress at the spanwise position of the spot center line is shown for $t = t_1$ in Fig. 9c. At the leading boundary of the spot, shear stress increases



a) Plan view of turbulent spot at time t_1 in part b below (after Schubauer and Klebanoff, 1956, and as idealized by McCormick, 1968)



b) S- t diagram of turbulent spot



c) Variation in wall shear stress along spot centerline at $t=t_1$

Fig. 9 Characteristics of turbulent spots.

abruptly from a laminar to turbulent level. Behind the trailing boundary, shear stress gradually decreases to a laminar level in the calmed region.

Intermittency. Transition from a laminar to turbulent flow takes place as individual spots merge together. The fraction of time the flow is turbulent is known as intermittency. Its value is equal to zero for laminar flow, varies from zero to unity from the beginning to the end of the transition region, and is unity for turbulent flow.

Calmed Region. A “calmed” (becalmed) region of laminar-like flow occurs immediately behind a turbulent spot (Schubauer and Klebanoff, 1956) or turbulent strip (Schubauer and Klebanoff, 1956, Orth, 1993). Its existence is endemic to turbulent spots or strips regardless of the transition process which brought about the turbulent event. The calmed region is identified as the region of decreasing, but still elevated, wall shear stress behind the spot or strip. An example is sketched in Fig. 9c. The calmed region, whose trailing boundary convects at $0.3 V_\infty$, appears on an s - t diagram as shown in Fig. 9b.

The calmed region is not accessible to TS waves originating upstream of the spot inception point because the veloc-

ity of the trailing boundary of the spot exceeds the propagation velocity of the TS wave ($\approx 0.3 V_\infty$). In addition, the formation of new instabilities, whether by T-S or bypass transition processes, is suppressed within the calmed region. This occurs because the boundary layer profile, which is relaxing from a turbulent to laminar level of shear stress, is more stable than the surrounding undisturbed laminar boundary layer. The calmed region can therefore be terminated only by the merging of neighboring turbulent spots or by strong bypass transition events. In the case of pure turbulent strips, merging occurs only in the streamwise direction. This has the effect of extending significantly the streamwise length of the transition zone (Schubauer and Klebanoff, 1956, and Orth, 1993).

Calmed regions are more resistant to flow separation in adverse pressure gradients due to their elevated levels of shear stress and low shape factor.

4.3. Transition in Turbomachines

Wake-Induced Transition is used in this paper to describe boundary layer transition brought about directly by disturbances in a convecting wake. It can occur by any of the three processes described in Sect. 4.1. In actuality, transition induced by wakes is brought about primarily by the process of bypass transition given the level of wake turbulence intensity (typically about 5 percent or greater).

Non Wake-Induced Transition is used to categorize all boundary layer transition occurring between passing wakes. Because of the lower associated levels of turbulence, transition between wakes can occur via either of the three processes described above although we observed only bypass and separated-flow transition in our work. In some cases, as will be reported herein, more than one process can work in concert to bring about transition along a non-wake induced path.

APPENDIX B. FREQUENCY RESPONSE OF HOT-FILM ANEMOMETRY SYSTEM

B.1 Electronic Frequency Response

The electronic frequency response of the hot-film anemometry system was determined using the square-wave test procedure as outlined by Freymuth and Fingerson (1977) and Borgos (1980). They showed conclusively that optimal frequency response of the anemometer system is determined accurately using this straightforward technique. The test involves introducing a square wave input to the bridge circuit with the sensor exposed to the maximum expected flow velocity. Various anemometer controls are then adjusted to achieve the desired response (i.e., bridge output waveform) from the system. For the IFA-100 system, these adjustments include bridge and cable compensation which control capacitance and inductance, respectively, of the bridge circuit. The optimal shape of the response waveform for hot-films is shown in Figure B.1. The primary pulse is followed by a single undershoot and overshoot. Borgos (1980) documented that the amplitudes of the undershoot and overshoot should be about 25 percent and 28 percent, respectively, of the pulse amplitude. The cutoff frequency of the hot-film anemometer system is then determined by

$$f_{\text{cutoff}} = \frac{1}{\tau} \quad (\text{B.1})$$

and is the frequency at which the input is attenuated 3 decibels. The time constant associated with the cutoff frequency, τ , is determined as shown in Figure B.1.

The result from a typical square-wave test applied to the surface hot-film anemometry employed in this investigation is shown in Figure B.2. The time constant of the response waveform is 19 μsec resulting in a cutoff frequency of about 53 khz. Amplitudes of the undershoot and overshoot agree well with suggested values. Tests conducted under zero and maximum-flow conditions yielded nominally identical system frequency response unlike the results of Freymuth and Fingerson (1977). They showed for hot-wire and hot-film probes that the increased heat transfer from the sensor at maximum flow conditions due to convective cooling re-

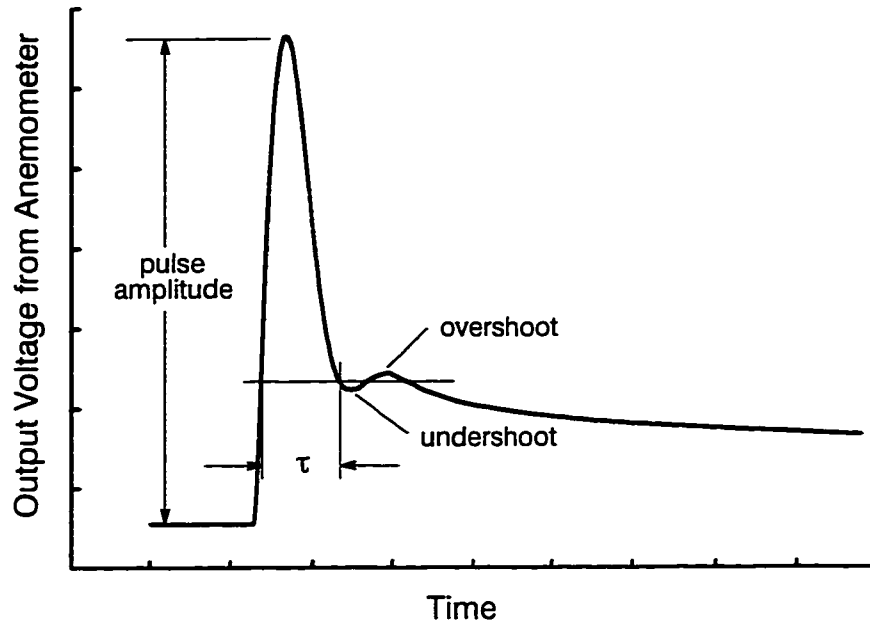


Figure B.1. Optimal response waveform for hot-films using the square-wave test

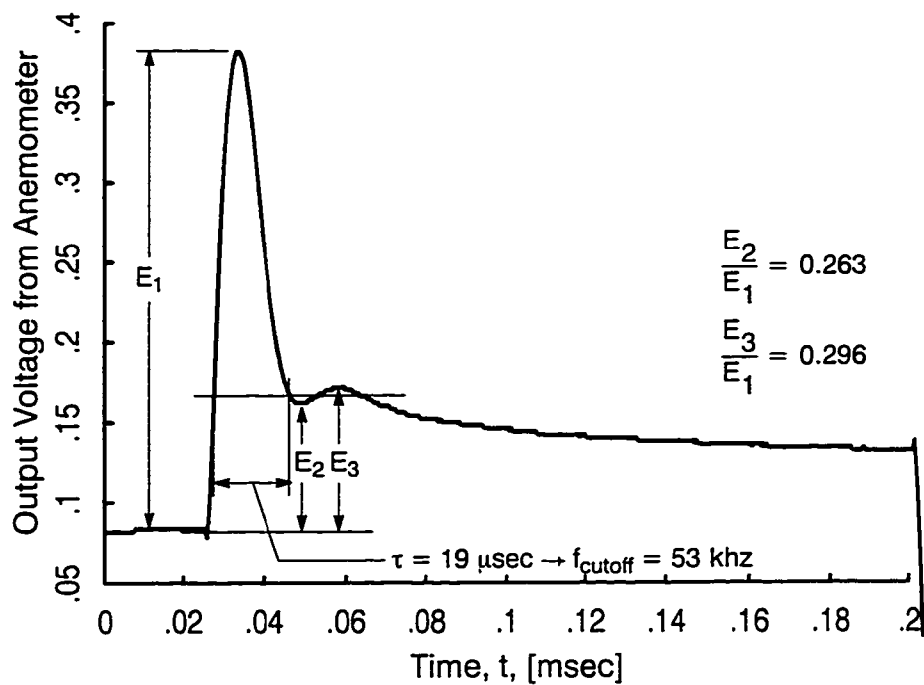


Figure B.2. Typical response waveform for surface hot-film anemometry system

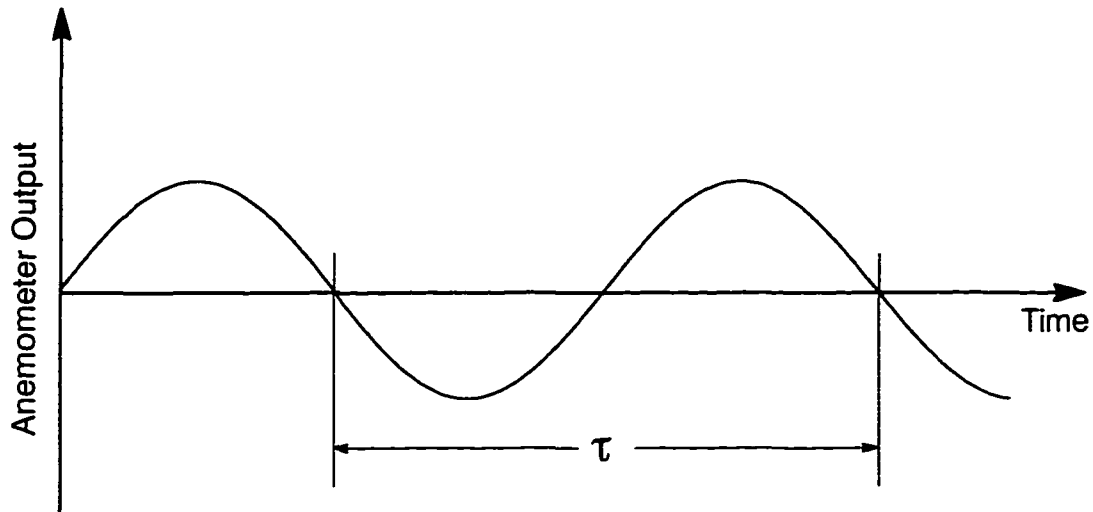


Figure B.3. Temporal response from an idealized disturbance convecting past a sensor fixed in space

sults in an increased cutoff frequency. For surface hot-film sensors, however, the heat loss is dominated by substrate conduction both with and without flow (Hanratty and Campbell, 1983). This may account for the invariance of frequency response to flow conditions found using these sensors. Incidentally, the step-wise variations visible in the waveform of Figure B.2 are due to the resolution of the digital oscilloscope and do not affect this analysis.

B.2 Influence of Sensor Spatial Resolution on Frequency Response

The maximum resolvable frequency in a given flowfield is related directly to the spatial resolution (or size) of the sensor used to acquire the measurement. Certainly, if the largest dimension of the sensor exceeds that of given eddies in a fluctuating flow, these effects of the eddies will be averaged along its length. The effect of an idealized eddy (or disturbance) convecting past a sensor fixed in space can be characterized as shown in Figure B.3. The time period and convection velocity of the disturbance are used to determine its wavelength and frequency as follows

$$\lambda = V\tau \quad \text{and} \quad f = \frac{V}{\lambda} \quad (\text{B.2})$$

Equation B.2 can be rewritten in terms of the largest sensor dimension, L_{\max} , and a constant, ϵ , as

$$f = \frac{V}{\epsilon L_{\max}} \quad (\text{B.3})$$

where $\lambda = \epsilon L_{\max}$. Fingerson and Freymuth (1983) noted that for one-dimensional turbulence measurements, investigators report attenuation errors in energy spectra of as much as 20 percent for disturbance wavelengths as small as two times the sensor length ($\epsilon=2$) and smaller errors of about 5 percent for larger disturbance wavelengths of 10 times sensor length. Hence for disturbances with length scales of order L_{\max} and smaller (i.e., ϵ of order 1 or less), significant attenuation of the turbulence energy spectra would occur. This corresponds to disturbance frequencies of order V/L_{\max} and higher. Fingerson and Freymuth (1983) further point out that this is commonly the most restrictive condition concerning the frequency response of anemometry systems. It must be emphasized that this limitation of frequency response is attributed to sensor size and flowfield kinematics. It is *entirely unrelated* to the electronic frequency response of the anemometry system discussed in Section B.1. For this investigation, the order of magnitude of the maximum resolvable frequencies, given by V/L_{\max} , varied from about 12 khz at low Reynolds numbers to about 53 khz at high Reynolds numbers.

APPENDIX C. GENERAL ANALYSIS OF TIME UNSTEADY MEASUREMENTS

Flowfield unsteadiness in turbomachines consists of deterministic and random components. Deterministic(or periodic) unsteadiness is classified as that which correlates with shaft rotational frequency and harmonics of blade-passing frequency. In turbomachines, such unsteadiness results from relative motion between rotating and stationary components. Random unsteadiness is that unsteadiness which does not correlate with shaft or blade-passing frequency and is associated primarily with the turbulent character of the flow.

C.1 Ensemble Averaging

The technique of ensemble averaging is suited ideally for analysis of time unsteady measurements obtained from turbomachinery flowfields (Gostelow, 1977). It provides a convenient means for separating the periodic and random components of the measurement. This is accomplished by acquiring a number of individual time records from which averaging is carried out. Such a set of time records, an example of which is shown in Figure C.1a, is referred to as an “ensemble.” Acquisition of each time record is carried out *in phase* with the periodic unsteadiness of the flowfield. This synchronization is referred to as “phase locking.” In turbomachines, phase locking typically is accomplished using once-per-revolution triggering from the rotor.

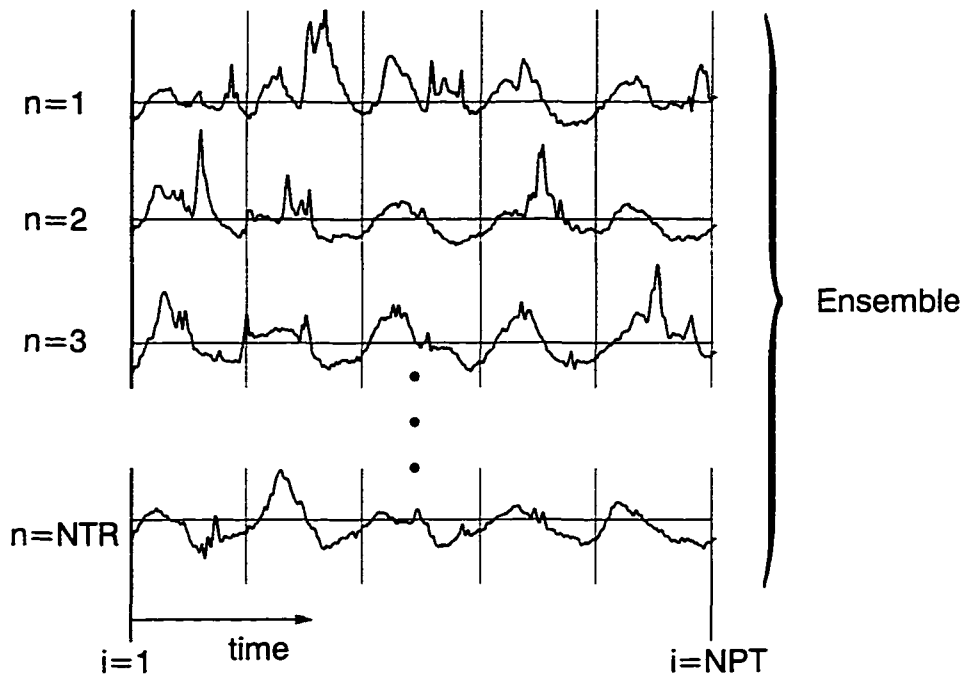
The ensemble of time unsteady measurements from Figure C.1a is represented symbolically as

$$f_{ni} \quad i = 1, NPT \quad n = 1, NTR$$

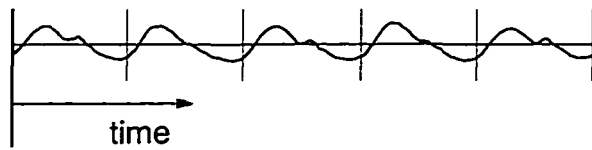
where f_{ni} denotes the i^{th} data sample of the n^{th} time record of the ensemble. The total number of data samples per time record is equal to NPT while the total number of time records per ensemble is NTR. The ensemble-averaged mean value of f_{ni} is then computed as

$$\tilde{f}_i(t_i) = \frac{1}{NTR} \sum_{n=1}^{NTR} f_{ni} \quad i = 1, NPT \quad (\text{C.1})$$

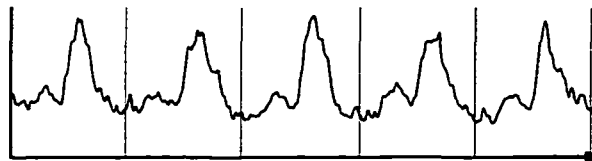
For the example set of time records, its ensemble-averaged mean is given in Figure C.1b.



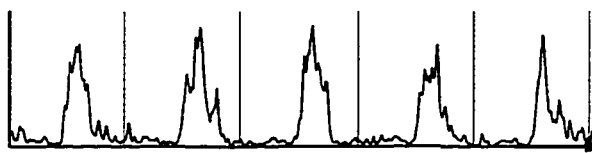
a) ensemble of individual time records



b) ensemble-averaged mean



c) ensemble-averaged random unsteadiness



d) ensemble-averaged skew

Figure C.1. Example of time unsteady measurements obtained from a surface hot-film sensor

The nature of the random unsteadiness is determined using higher-order statistical moments which are written generally as (Bendat and Piersol, 1971)

$$\tilde{f}_{i,R}^k(t_i) = \frac{1}{NTR} \sum_{n=1}^{NTR} (f_{ni} - \tilde{f}_i(t_i))^k \quad i = 1, NPT \quad (C.2)$$

Note that these moments are centered not about the time mean but instead the ensemble-averaged mean. In this manner, the periodic unsteadiness is removed from the analysis.

For the index $k=2$, Equation C.2 provides the mean square value of f_{ni} which is a measure of the amplitude of random unsteadiness. This quantity routinely is normalized into an intensity of root-mean-square (RMS) random unsteadiness utilizing the ensemble-averaged mean as shown by Equation C.3

$$\tilde{F}_{i,R}(t_i) = \frac{\sqrt{\tilde{f}_{i,R}^2(t_i)}}{\tilde{f}_i(t_i)} \quad i = 1, NPT \quad (C.3)$$

For illustration, the distribution of ensemble-averaged, random unsteadiness for the example time records is given in Figure C.1c.

The third-order central moment is determined by evaluating Equation C.2 with $k=3$. It provides a measurement of the asymmetry of the fluctuations about the mean. This quantity typically is normalized using either the ensemble-averaged mean or mean square. The former will be employed in this work with the resulting quantity being referred to as skew, shown here as Equation C.4. The distribution of skew for the example data set is given in Figure C.1d.

$$\tilde{F}_{i,R}^3(t_i) = \frac{\tilde{f}_{i,R}^3(t_i)}{\tilde{f}_i^3(t_i)} \quad i = 1, NPT \quad (C.4)$$

C.2 Time Averaging

Time averages are obtained by numerical integration of the ensemble-averaged quantities. For the mean value, the mean-square random unsteadiness, and random skew, these relationships are written, respectively, as

$$\bar{f} = \frac{1}{\text{NPTS}} \sum_{i=1}^{\text{NPTS}} \tilde{f}_i(t_i) \quad (\text{C.5})$$

$$\overline{f_R^2} = \frac{1}{\text{NPTS}} \sum_{i=1}^{\text{NPTS}} \tilde{f}_{i,R}^2(t_i) \quad (\text{C.6})$$

$$\overline{f_R^3} = \frac{1}{\text{NPTS}} \sum_{i=1}^{\text{NPTS}} \tilde{f}_{i,R}^3(t_i) \quad (\text{C.7})$$

To determine time-averaged, periodic unsteadiness, we employ the equality

$$\overline{f_T^2} = \overline{f_R^2} + \overline{f_P^2} \quad (\text{C.8})$$

where $\overline{f_T^2}$ and $\overline{f_P^2}$ are the total and periodic components of unsteadiness, respectively. Rewriting Equation C.8 in terms of ensemble-averaged quantities, we find

$$\overline{f_P^2} = \overline{f_T^2} - \overline{f_R^2} = \frac{1}{\text{NPTS}} \sum_{i=1}^{\text{NPTS}} (\tilde{f}_i^2 - \tilde{f}_R^2)^2 \quad (\text{C.9})$$

Further simplification is achieved by substituting Equation C.2 (with $k=2$) and the analogous relation for total unsteadiness into Equation C.9. The resulting expression is

$$\overline{f_P^2} = \frac{1}{\text{NPTS}} \sum_{i=1}^{\text{NPTS}} (\tilde{f}_i - \bar{f})^2 \quad (\text{C.10})$$

Intensities of time-averaged random and periodic unsteadiness are found by normalization of their root-mean-squares with the time mean value as indicated by Equation C.11.

$$\overline{F_R} = \frac{\sqrt{\overline{f_R^2}}}{\bar{f}} \quad (\text{C.11a})$$

$$\overline{F_P} = \frac{\sqrt{\overline{f_P^2}}}{\bar{f}} \quad (\text{C.11b})$$

Time-averaged skew is normalized in a fashion analogous to Equation C.4 as shown below.

$$\overline{F_R^3} = \frac{\overline{f_R^3}}{\overline{f^3}} \quad (\text{C.12})$$

When computing the time average of any ensemble-averaged quantity, the summation (i.e., integration in time) is carried out *strictly* over an integer number of periodic events of a given time record to prevent bias errors.

APPENDIX D. FOURIER TRANSFORM METHODS

Time-resolved measurements of a flowfield contain fluctuations characterized by widely varying spatial and temporal scales. Fourier transform methods provide a useful means in which to analyze such phenomena associated with fluid dynamics. A number of these methods were used for the analysis of data reported in this dissertation. Hence, a detailed summary of Fourier transform methods and their applications is provided in this appendix. In the first two sections, the definition of the continuous Fourier transform is given and its properties described. This is followed in the third and fourth sections by the development of the Fourier transform as applied to discrete time records. Lastly, the application of computer routines for computation of the Fourier transform is discussed in the fifth section.

D.1 The Fourier Transform

A physical process can be described in either the *time domain*, as some quantity “x” varying with time “t” (i.e., $x(t)$), or in the *frequency domain* where the process is specified as an amplitude X (generally a complex quantity) varying with frequency “f” (i.e., $X(f)$). The functions $X(f)$ and $x(t)$ can be considered as two different representations of the same process. The functions are related through the *Fourier transform* equations.

The Fourier transform (FT) of $x(t)$ is given as

$$X(f) = \int_{-\infty}^{\infty} x(t)e^{-2\pi ift} dt \quad (D.1)$$

using complex notation and is defined for $-\infty < f < \infty$. Equation D.1 simply resolves the function $x(t)$ into its harmonic components. The Fourier integral (or inverse Fourier transform) of $X(f)$ is written as

$$x(t) = \int_{-\infty}^{\infty} X(f)e^{2\pi ift} df \quad (D.2)$$

This relation is defined for $-\infty < t < \infty$ and synthesizes the harmonic components, $X(f)$, into

the original time function, $x(t)$. Taken together, Equations D.1 and D.2 are referred to as a *Fourier transform pair*. Conditions for the existence of these relations are given rigorously by Brigham (1974) and will not be repeated here except as needed.

The engineering units associated with Equations D.1 and D.2 as applied to the measurements acquired in this work are as follows. Time is measured in seconds, thus frequency is in units of [1/s], or hertz. The quantity $x(t)$ is given in the desired units of measure, [units] (e.g., volts, velocity, pressure, etc.). From Equation D.1, this implies that the units of $X(f)$ are [units/hz]. Obviously, the assignment of units are problem-dependent with the only requirement that they be consistent.

Before proceeding, it is useful to consider a few basic characteristics of this Fourier transform pair that will be employed in later analysis. First, Equations D.1 and D.2 represent a linear transformation (Press et al., 1992) which is to say

$$\begin{aligned} \int_{-\infty}^{\infty} [x(t) + y(t)]e^{-2\pi ift} dt &= \int_{-\infty}^{\infty} x(t)e^{-2\pi ift} dt + \int_{-\infty}^{\infty} y(t)e^{-2\pi ift} dt \\ &= X(f) + Y(f) \end{aligned}$$

Secondly, if $x(t)$ is a real-valued function, the Fourier coefficients of the negative frequencies are complex conjugates of those corresponding to the positive frequencies (ibid.). That is to say, $X(-f) = X^*(f)$. All unsteady measurements acquired in this work are real-valued functions in time.

Lastly, a note is in order concerning the concept of “negative” frequency which appears in Equation D.1. Negative frequency has been introduced as a purely mathematical artifice resulting from formulating the FT using complex variables. While negative frequency is not physically real, and may be confusing, its incorporation is mathematically justified and, as will be seen, is very convenient from an analytical point of view.

D.2 Properties of the Fourier Transform

Described below are a number of useful properties of the Fourier transfer.

D.2.1 Parseval's Theorem

Parseval's theorem provides a useful means of converting time integration into frequency integration (Thomson, 1981). Given two real-valued functions, $x_1(t)$ and $x_2(t)$, we can write the following using Equation D.1.

$$x_1(t) x_2(t) = x_2(t) \int_{-\infty}^{\infty} X_1(f) e^{2\pi i f t} df$$

Integrating both sides with respect to time and changing the order of integration on the right-hand side gives

$$\begin{aligned} \int_{-\infty}^{\infty} x_1(t) x_2(t) dt &= \int_{-\infty}^{\infty} x_2(t) \left[\int_{-\infty}^{\infty} X_1(f) e^{2\pi i f t} df \right] dt \\ &= \int_{-\infty}^{\infty} X_1(f) \underbrace{\left[\int_{-\infty}^{\infty} x_2(t) e^{2\pi i f t} dt \right]}_{= X_2^*(f)} df \\ \int_{-\infty}^{\infty} x_1(t) x_2(t) dt &= \int_{-\infty}^{\infty} X_1(f) X_2^*(f) df \end{aligned} \quad (D.3)$$

Equation D.3 is known as Parseval's theorem. A second form of this theorem results from considering $x_1(t) = x_2(t) = x(t)$. In this case, Equation D.3 is rewritten as

$$\begin{aligned} \int_{-\infty}^{\infty} x^2(t) dt &= \int_{-\infty}^{\infty} \underbrace{X(f) X^*(f)}_{= |X(f)|^2} df \\ \int_{-\infty}^{\infty} x^2(t) dt &= \int_{-\infty}^{\infty} |X(f)|^2 df \end{aligned} \quad (D.4)$$

Here, the term $X(f)$ multiplied by its complex conjugate $X^*(f)$ has been replaced with its modu-

lus. Equation D.4 simply reflects the fact that the “total power” associated with the signal is identical whether determined in the time or frequency domains (Press et al., 1992).

D.2.2 Mean Square (Power) Spectral Density

The frequency composition of a fluctuating quantity can be described in terms of the spectral density of its mean square value. Traditionally, this is referred to as the power spectral density. In retrospect however, a more accurate designation is that of mean square spectral density (MSSD) (McConnell, 1980). This latter designation will be used herein. The mean square spectral density is defined over the frequency spectrum as the contribution of the Fourier transform to the mean square at a given frequency, per unit hertz. As indicated below, the MSSD can be defined both in terms of positive and negative frequencies (two-sided) or in terms of positive (physical) frequencies only (one-sided). We will have need to consider both. Two-sided spectral density functions are highly desirable for analytical purposes. One-sided functions are obviously more suited to actual applications requiring information about the mean square density over physical (positive-valued) frequencies (Bendat and Piersol, 1980). The mean square spectral densities, in terms of two-sided and one-sided functions, are defined below as Equations D.5 and D.6, respectively [ibid., Thomson, 1981)

$$\text{two-sided: } S(f) = \lim_{T \rightarrow \infty} \frac{1}{T} X(f)X^*(f) = \lim_{T \rightarrow \infty} \frac{1}{T} |X(f)|^2 \quad -\infty < f < \infty \quad (\text{D.5})$$

$$\text{one-sided: } G(f) = 2 S(f) \quad 0 < f < \infty \quad (\text{D.6})$$

Their graphical relationship is illustrated in Figure D.1. The engineering units associated with each are [units²/hz].

D.2.3 Mean Square Value

The mean square value of a continuous time record, $x(t)$, is determined by (Thomson, 1981)

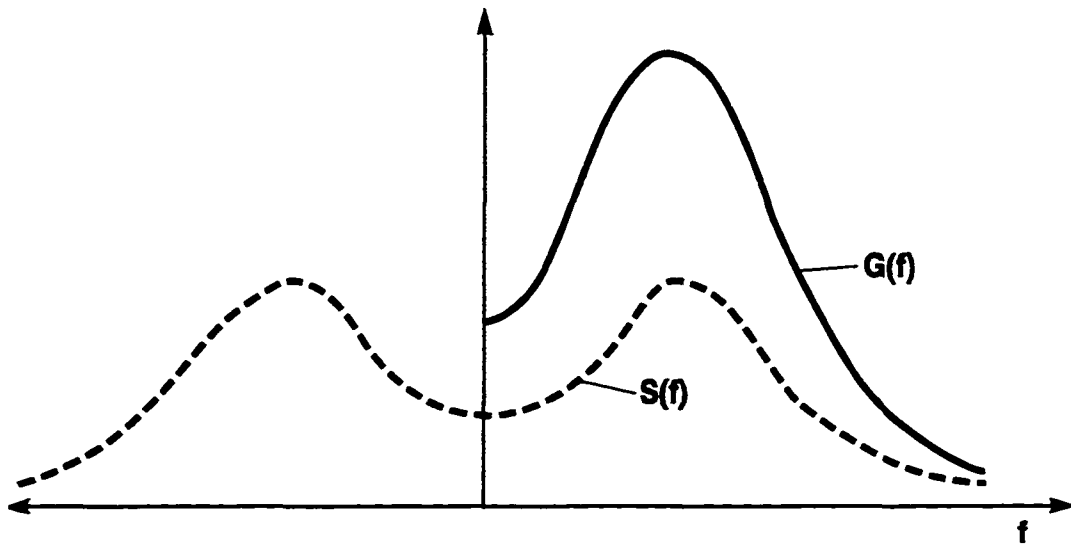


Figure D.1. Graphical representation of the mean square spectral density of $X(f)$ (one-sided: $G(f)$, two-sided: $S(f)$)

$$\overline{x^2} = \lim_{T \rightarrow \infty} \frac{1}{T} \int_{-\frac{T}{2}}^{\frac{T}{2}} x^2(t) dt \quad (\text{D.7})$$

This integration with respect to time also can be evaluated in the frequency domain as follows

$$\begin{aligned} \overline{x^2} &= \lim_{T \rightarrow \infty} \frac{1}{T} \int_{-\frac{T}{2}}^{\frac{T}{2}} x^2(t) dt = \int_{-\infty}^{\infty} \lim_{T \rightarrow \infty} \frac{1}{T} x(t) \left[\int_{-\infty}^{\infty} X(f) e^{2\pi i f t} df \right] dt \\ &= \int_{-\infty}^{\infty} \lim_{T \rightarrow \infty} \frac{1}{T} X(f) \underbrace{\left[\int_{-\infty}^{\infty} x(t) e^{2\pi i f t} dt \right]}_{= X^*(f)} df \\ &= \int_{-\infty}^{\infty} \underbrace{\lim_{T \rightarrow \infty} \frac{1}{T} X(f) X^*(f)}_{= S(f)} df \\ \overline{x^2} &= \int_{-\infty}^{\infty} S(f) df \quad (\text{D.8}) \end{aligned}$$

Comparing Equations D.5 and D.8 indicates that the mean square value of $x(t)$ is in terms of the two-sided MSSD. It follows that, for the one-sided MSSD, the mean square can be determined from

$$\overline{x^2} = \int_0^{\infty} G(f) df \quad (\text{D.9})$$

Thus the mean square value of the function, $x(t)$, is equal to the integral of the MSSD over its frequency range.

D.2.4 Correlation Functions

The autocorrelation of a continuous time function, $x(t)$, is defined as (Thomson, 1981)

$$R(\tau) = \lim_{T \rightarrow \infty} \frac{1}{T} \int_{-\infty}^{\infty} x(t)x(t + \tau) dt \quad (\text{D.10})$$

Applying Equation D.1, the Fourier transform of the function $x(t + \tau)$ is given as

$$x(t + \tau) = \int_{-\infty}^{\infty} X(f)e^{2\pi if(t+\tau)}df = \int_{-\infty}^{\infty} X(f) e^{2\pi ift} e^{2\pi if\tau} df \quad (\text{D.11})$$

Using this relation along with Equation D.10, the autocorrelation function can be expressed in terms of the Fourier transform as follows

$$\begin{aligned} R(\tau) &= \lim_{T \rightarrow \infty} \frac{1}{T} \int_{-\infty}^{\infty} x(t)x(t + \tau) dt \\ &= \lim_{T \rightarrow \infty} \frac{1}{T} \int_{-\infty}^{\infty} x(t) \left[\int_{-\infty}^{\infty} X(f)e^{2\pi ift}e^{2\pi if\tau}df \right] dt \end{aligned}$$

as

$$\lim_{T \rightarrow \infty} \frac{1}{T} \int_{-\frac{T}{2}}^{\frac{T}{2}} x(t)y(t + \tau) dt \neq \lim_{T \rightarrow \infty} \frac{1}{T} \int_{-\frac{T}{2}}^{\frac{T}{2}} x(t + \tau)y(t) dt$$

D.3 Fourier Transform of Discretely Sampled Data

For the Fourier transform defined by Equations D.1 and D.2 to exist, the integral

$$\int_{-\infty}^{\infty} |x(t)| dt$$

must be bounded (Brigham, 1974). However, for a continuous time record of a random process, which theoretically exists for all time, the integral is in fact unbounded. However, in the laboratory, we do not measure $x(t)$ for all time but instead measure a representative portion of it for a finite time interval, T . The Fourier transform, $X(f)$, can now be estimated by computing the *finite Fourier transform* given by

$$X(f, T) = \int_0^T x(t)e^{-2\pi i f t} dt \quad (D.16)$$

This transform will always exist for finite time records of random processes encountered in typical engineering applications (Bendat and Piersol, 1971).

Before expounding on the details required to compute the finite Fourier transform, we must first consider characteristics of the measured data which represent the random process. For many data acquisition and processing techniques, including those utilized in this work, the continuous time record itself, $x(t)$, is not analyzed. Instead, a set of discrete data samples are used to represent it.

D.3.1 Discretization of a Continuous Time Record

Experimental measurements of random processes often are carried out “digitally.” That is, the continuous time record, $x(t)$, is converted to a discrete time record, x_n , using analog-to-

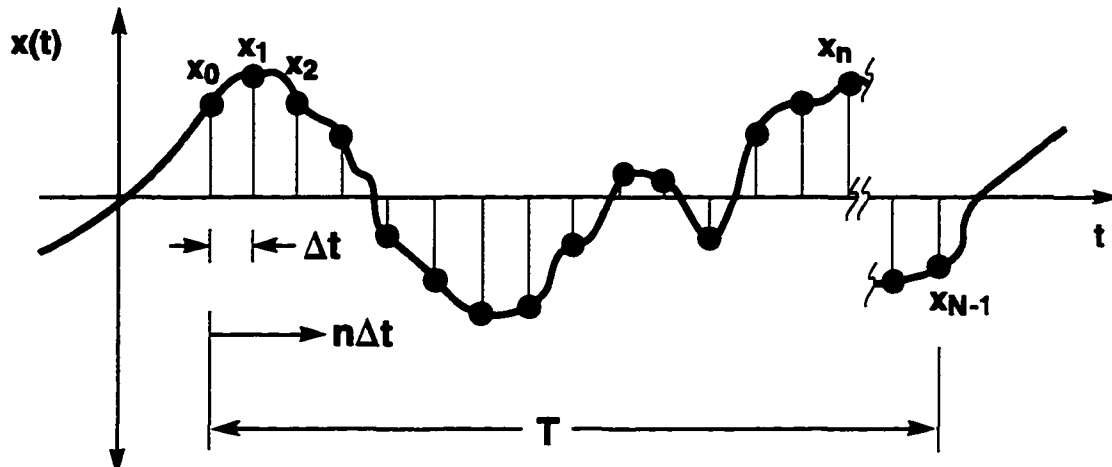


Figure D.2. Discretization of a continuous waveform

digital conversion. An example of such a discretization is shown in Figure D.2 and described symbolically below. Here, N consecutively sampled values are used to represent the continuous time record, $x(t)$.

$$x_n = x(t_n) \quad t_n = n\Delta t \quad n = 0, 1, 2, \dots, N - 1$$

The samples are acquired at equally-spaced time increments of Δt . The reciprocal of the sample period, Δt , is called the sampling rate

$$f_s = \frac{1}{\Delta t}$$

For this work, the sampling rate is simply the number of data samples acquired per second. The total time interval for the data set is $T = N\Delta t$ and the fundamental frequency is given as

$$f_o = \frac{1}{T}$$

This is the lowest frequency that can be resolved for a given discretization and, as will be shown later, is also equal to the frequency interval, Δf , of the discrete Fourier transform.

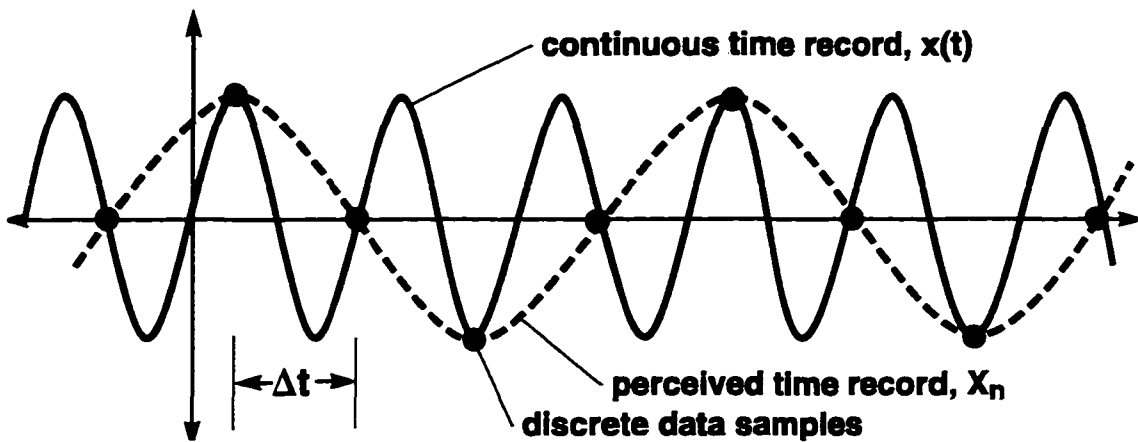


Figure D.3. Graphical illustration of aliasing

When digitizing a continuous time record, an appropriate sample interval, Δt , must be selected. Sampling with too small a value of Δt will result in redundant information in the data set and will unnecessarily increase cost and time required for analysis. On the contrary, sampling with too large a value of Δt has very profound consequences which will lead to confusion between high and low frequency components in the original continuous record. This latter problem is termed “aliasing” and is an inherent feature related to the very act of discrete sampling (Bendat and Piersol, 1980).

A graphical illustration of aliasing is shown in Figure D.3. The continuous time record $x(t)$ varies sinusoidally in time (for simplicity). Samples are acquired at intervals of Δt as denoted. It can be shown that a minimum of two samples are required to resolve a given frequency component in the continuous time record. As a result, the maximum frequency that can be accurately resolved corresponds to a time period, $2\Delta t$, in other words, to one half the value of the sample frequency, f_s . This frequency is commonly called the *Nyquist* or *folding* frequency and is given as

$$f_c = \frac{f_s}{2} = \frac{1}{2\Delta t} \quad (\text{D.17})$$

As shown in Figure D.3, however, the continuous time record $x(t)$ consists of a sinusoid at a frequency greater than f_c . The samples occurring at increments of Δt are those used to represent, in a discrete fashion, the continuous function $x(t)$. The dashed line connecting the samples reveals that the frequency component actually resolved by the discrete data set is lower than that of the continuous function. A simple analysis explains this anomaly (*ibid.*). Denote the frequency component of the continuous function as f_1 where $f_1 > f_c$. The frequency f_1 can be represented in form $f_1 = 2nf_c \pm f$. We can then write

$$\cos 2\pi f_1 t = \cos 2\pi(2nf_c \pm f)t \quad (\text{D.18})$$

Evaluating the left and right hand sides of Equation D.18 at Δt and simplifying using Equation D.17 gives the following

$$\begin{array}{l|l} \text{LHS} = \cos 2\pi f_1 \Delta t & \text{RHS} = \cos(2\pi(2nf_c \pm f)\Delta t) \\ = \cos\left(\frac{2\pi f_1}{2f_c}\right) & = \cos\left(\frac{2\pi(2nf_c \pm f)}{2f_c}\right) \\ \text{LHS} = \cos\left(\frac{\pi f_1}{f_c}\right) & = \cos\left(2\pi n \pm \frac{\pi f}{f_c}\right) \\ & \text{RHS} = \cos\left(\frac{\pi f}{f_c}\right) \quad \text{for any } n \end{array} \quad (\text{D.19}) \quad (\text{D.20})$$

From Equations D.19 and D.20 it is evident that any frequency component f_1 occurring in the continuous time record, such that $f_1 > f_c$, will “fold back” to the frequency, f , in the discretized data set, where $f < f_c$. This is equivalent to saying that data at frequencies of $2nf_c \pm f$ all have the same cosine function as data at f_1 when sampled $1/2f_c$ apart, as shown graphically in Figure D.3. For example then, if $f_c = 1000$ hz, frequency components at $f=650$ hz will be aliased with those occurring at 1350, 2650, 3350, 4650, ... (i.e., $2nf_c \pm f$). Just as aliasing of frequencies

greater than f_c will contaminate the discrete time record, so too the resulting frequency spectra will be erroneous.

The serious nature of aliasing errors can be avoided entirely by incorporating simple procedures during the digitization process. If the origin of the continuous function, $x(t)$, is an analog voltage, which is often the case for laboratory measurements, its frequency spectra can be examined prior to digitization using a spectrum analyzer. The maximum significant frequency occurring in the measured waveform can be determined. With this information known, procedures can be applied during digitization to ensure aliasing does not occur.

Two such procedures commonly used to protect against aliasing errors are as follows. The first involves selecting the time period between samples such that the Nyquist frequency f_c is greater than any frequency occurring in the measured waveform. This procedure is not suited for measurements containing high-frequency noise or for situations where the selection of sampling frequency is limited. In such cases, a second technique commonly used incorporates an analog low-pass filter to remove all frequency content in a waveform above a selected filter cutoff frequency, f_{lp} . After filtering, the upper frequency occurring in the waveform to be digitized is now known and directly controllable. Theoretically, the sampling frequency can then be set to two times the low-pass filter cutoff (i.e., a user-imposed value of f_c) in order to resolve all frequencies in the filtered waveform. However, since analog low-pass filters used for this purpose are not "perfect," frequency components greater than f_{lp} may be attenuated only partially and hence can still fold back, contaminating the discrete time record. This problem is addressed by selecting a sample frequency of greater than $2f_{lp}$. The exact setting f_s obviously depends on the quality of the filter (i.e., steepness of its roll-off) and can be determined by examining its frequency response function. For this work, the filters provided in the TSI signal conditioners exhibited an amplitude rolloff of -59 dB/decade. Consequently, sampling was carried out at frequencies of up to five times the cutoff in order to prevent aliasing.

D.3.2 The Discrete Fourier Transform

As given in Section D.3, the finite Fourier transform of the continuous function $x(t)$ for the interval $0 \leq t \leq T$ is given as

$$X(f, T) = \int_0^T x(t) e^{-2\pi i f t} dt \quad (\text{D.16})$$

Assume that the function $x(t)$ has been discretized in the manner as discussed in Section D.3.1 where

$$x_n = x(n\Delta t) \quad n = 0, 1, 2, \dots, N - 1$$

Then, for arbitrary frequency, f , the finite Fourier transform can be discretized as follows

$$X(f, T) \approx \Delta t \sum_{n=0}^{N-1} x_n e^{-2\pi i f n \Delta t}$$

The discrete frequency values for the computation of $X(f, T)$ are given as

$$f_k = \frac{k}{N\Delta t} \quad k = 0, 1, 2, \dots, N - 1 \quad (\text{D.21})$$

Consequently, the frequency increment is simply $\Delta f = 1/N\Delta t$. At the discrete frequencies, the Fourier coefficients are defined by (Press et al., 1992)

$$X_k = \frac{X(f, T)}{\Delta t} = \sum_{n=0}^{N-1} x_n e^{-2\pi i k n \Delta t / (N\Delta t)}$$

$$X_k = \sum_{n=0}^{N-1} x_n e^{-2\pi i k n / N} \quad k = 0, 1, 2, \dots, N - 1 \quad (\text{D.22})$$

Equation D.22 is known as the *discrete Fourier transform* (DFT) of the set $\{x_n\}$. The inverse DFT is determined as follows

$$X_k = \sum_{n=0}^{N-1} x_n e^{-2\pi i k n / N}$$

$$\sum_{k=0}^{N-1} X_k e^{2\pi i k n / N} = \sum_{k=0}^{N-1} \sum_{n=0}^{N-1} x_n e^{-2\pi i k n / N} e^{2\pi i k n / N}$$

$$= \sum_{n=0}^{N-1} x_n \underbrace{\sum_{k=0}^{N-1} 1}_{= N}$$

Hence

$$x_n = \frac{1}{N} \sum_{k=0}^{N-1} X_k e^{2\pi i k n / N} \quad n = 0, 1, 2, \dots, N - 1 \quad (\text{D.23})$$

Taken together, Equations D.22 and D.23 are referred to as a discrete Fourier transform pair. As implied by these relationships, there is a one-to-one correspondence between the sets $\{x_n\}$ and $\{X_k\}$. That is, for N discrete samples of the set $\{x_n\}$, there are N discrete frequency components $\{X_k\}$. The engineering units associated with $\{x_n\}$ and $\{X_k\}$ from Equations D.22 and D.23 are in units of measure, [units].

There are several important characteristics of the DFT pair derived above. First, consider the index k which varies from 0 to $N-1$ and corresponds to the discrete frequency components as given by Equations D.21 and D.22. Using the definition for X_k , we can write for the $N+k$ component

$$X_{N+k} = \sum_{n=0}^{N-1} x_n e^{-2\pi i (N+k)n / N} = \sum_{n=0}^{N-1} x_n e^{-2\pi i k n / N} e^{-2\pi i n}$$

From Euler's formula ($e^{i\theta} = \cos \theta + i \sin \theta$) and trigonometric relations, we find that $e^{-2\pi i n} = 1$ for all "n" hence $X_{N+k} = X_k$. This implies that the set $\{X_k\}$ is periodic in k with period N . Also, for the negative k^{th} frequency component

$$X_{-k} = \sum_{n=0}^{N-1} x_n e^{2\pi i k n / N} = X_k^*$$

Hence X_{-k} is the complex conjugate of X_k . The significance of these properties is shown graphically in Figure D.4.

Based on the discussion above, the following indexing conventions apply to the frequency components X_k defined for $k = 0, 1, 2, \dots, N-1$ (Press et al., 1992):

1. the zero frequency value corresponds to $k = 0$
2. the positive frequencies $0 < f < f_c$ correspond to $1 \leq k \leq \frac{N}{2} - 1$
3. the negative frequencies $-f_c < f < 0$ correspond to $\frac{N}{2} + 1 \leq k \leq N - 1$
4. the frequencies f_c and $-f_c$ both correspond to $k = N/2$.

Repeating for emphasis, the frequency components of the DFT as defined by Equation D.22 are determined for the frequency interval, $-f_c < f < f_c$, with the negative frequencies represented by the values of $k \geq N/2$. This is consistent with the restrictions found in Section D.3.1 which indicate the maximum resolvable frequency for a given discrete time record is the Nyquist frequency.

An additional characteristic of this DFT pair is found by evaluating Equation D.23 at $N+n$. This gives the result $x_n = x_{N+n}$ which reveals that the discrete time record is also periodic in N with respect to this discrete transform pair.

To conclude then, the continuous time record, $x(t)$, originally defined for $-\infty < t < \infty$ has been replaced by the discrete time record $x_n, n = 0, 1, 2, \dots, N-1$ which, with respect to the discrete transform, is periodic with period $T(=N\Delta t)$. The frequency spectrum, continuous over the range $-\infty < f < \infty$, is replaced by the discrete transform sequence, $X_k, k = 0, 1, 2, \dots, N-1$ with the discrete frequency components varying from $-f_c < f < f_c$ in increments of Δf . Last-

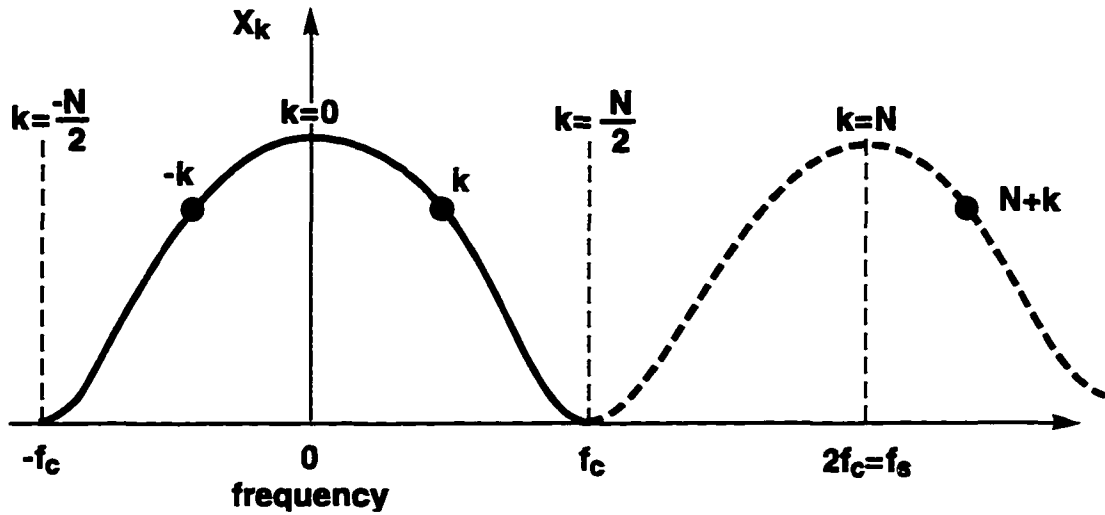


Figure D.4. Schematic of discretized Fourier transform

ly, the transform from the x_n 's to X_k 's and vice versa using Equations D.22 and D.23 are exact. That is to say, the inverse transform of the X_k 's will produce the original x_n 's values exactly.

D.4 Properties of the Discrete Fourier Transform

Just as several important properties were identified for the continuous Fourier transform pair, similar relations exist for the DFT pair.

D.4.1 Parseval's Theorem

Analogous to its continuous counterpart, the discrete form of Parseval's theorem provides a useful means of converting temporal domain summation to frequency domain summation. Given two real-valued discrete time records, $x_{1,n}$ and $x_{2,n}$ for $n = 0, 1, 2, \dots, N-1$, we can use Equation D.23 to write

$$x_{1,n}x_{2,n} = x_{2,n} \frac{1}{N} \sum_{k=0}^{N-1} X_{1,k} e^{2\pi i k n / N}$$

Summation with respect to "n" gives

$$\sum_{n=0}^{N-1} x_{1,n} x_{2,n} = \sum_{n=0}^{N-1} x_{2,n} \frac{1}{N} \sum_{k=0}^{N-1} X_{1,k} e^{2\pi i k n / N}$$

Reversing the order of summation on the right-hand side and simplifying yields

$$\sum_{n=0}^{N-1} x_{1,n} x_{2,n} = \frac{1}{N} \sum_{k=0}^{N-1} X_{1,k} \underbrace{\sum_{n=0}^{N-1} x_{2,n} e^{2\pi i k n / N}}_{= X_{2,k}^*}$$

$$\sum_{n=0}^{N-1} x_{1,n} x_{2,n} = \frac{1}{N} \sum_{k=0}^{N-1} X_{1,k} X_{2,k}^* \quad (\text{D.24})$$

If $x_{1,n} = x_{2,n} = x_n$, Equation D.24 can be rewritten as

$$\sum_{n=0}^{N-1} x_n^2 = \frac{1}{N} \sum_{k=0}^{N-1} X_k X_k^* = \frac{1}{N} \sum_{k=0}^{N-1} |X_k|^2 \quad (\text{D.25})$$

Equations D.24 and D.25 are then the discrete forms of Parseval's theorem (Press et al., 1992).

D.4.2 Mean Square (Power) Spectral Density

The mean square spectral density can be defined in terms of either the one-sided or two-sided spectra, analogous to the continuous forms developed in Section D.2.2. By combining Equation D.5 with the relationship for the finite Fourier transform given in Section D.3.2, the discrete form of the two-sided MSSD becomes

$$S_k \approx \frac{1}{T} |X(f, T)|^2 = \frac{\Delta t^2}{T} |X_k|^2$$

This expression can be simplified further using the relations

$$T = N\Delta t \quad \text{and} \quad \Delta f = 1/N\Delta t$$

such that

$$S_k = \frac{\Delta t^2}{T} |X_k|^2 = \frac{\Delta t}{N} |X_k|^2 = \frac{1}{\Delta f} \left| \frac{X_k}{N} \right|^2 \quad k = 0, 1, 2, \dots, N-1 \quad (\text{D.26})$$

Likewise, the discrete form of the one-sided MSSD becomes

$$G_k = 2S_k = \frac{2}{\Delta f} \left| \frac{X_k}{N} \right|^2 \quad k = 0, 1, 2, \dots, N/2 \quad (\text{D.27})$$

The units of the discrete mean square spectral density are [units²/hz]. As with their continuous counterparts, the one-sided function is utilized for applications requiring information of the actual MSSD over physical (positive) frequencies while the two-sided function is used for analytical procedures relating to the entire frequency domain.

D.4.3 Mean Square Value

The mean square value of the discrete time record is computed as follows

$$\begin{aligned} \overline{x^2} &= \lim_{T \rightarrow \infty} \frac{1}{T} \int_{-\frac{T}{2}}^{\frac{T}{2}} x^2(t) dt \approx \frac{1}{T} \sum_{n=0}^{N-1} x_n^2 \Delta t \\ \overline{x^2} &= \frac{1}{N} \sum_{n=0}^{N-1} x_n^2 \end{aligned} \quad (\text{D.28})$$

Using the discrete form of Parseval's theorem, the summation over time can be replaced with summation over frequency to yield

$$\begin{aligned} \overline{x^2} &= \frac{1}{N} \sum_{n=0}^{N-1} x_n^2 = \frac{1}{N^2} \sum_{k=0}^{N-1} |X_k|^2 \\ \overline{x^2} &= \sum_{k=0}^{N-1} \left| \frac{X_k}{N} \right|^2 \end{aligned} \quad (\text{D.29})$$

The mean square value also can be expressed in terms of the discrete MSSD expressions given by Equations D.26 and D.27 resulting in the following relationships:

$$\overline{x^2} = \Delta f \sum_{k=0}^{N-1} S_k \quad (\text{D.30})$$

and

$$\overline{x^2} = \Delta f \sum_{k=0}^{N/2} G_k \quad (\text{D.31})$$

D.4.4 Correlation Functions

The autocorrelation was defined previously as

$$R(\tau) = \lim_{T \rightarrow \infty} \frac{1}{T} \int_{-\infty}^{\infty} x(t)x(t + \tau) dt \quad (\text{D.10})$$

It can be approximated by the following discretized formulation

$$R_j = \frac{1}{T} \sum_{n=0}^{N-1} x_n x_{n+j} \Delta t = \frac{1}{N} \sum_{n=0}^{N-1} x_n x_{n+j} \quad (\text{D.32})$$

Using the discrete Fourier transform of x_{n+j} , the terms within the summation of Equation D.32 can be rewritten as

$$x_n x_{n+j} = x_n \frac{1}{N} \sum_{k=0}^{N-1} X_k e^{2\pi i k(n+j)/N} = x_n \frac{1}{N} \sum_{k=0}^{N-1} X_k e^{2\pi i k n/N} e^{2\pi i k j/N}$$

Summing both sides with respect to n and reversing order of summation on the right hand side gives

$$\begin{aligned} \sum_{n=0}^{N-1} x_n x_{n+j} &= \sum_{n=0}^{N-1} x_n \frac{1}{N} \sum_{k=0}^{N-1} X_k e^{2\pi i k n/N} e^{2\pi i k j/N} \\ &= \frac{1}{N} \sum_{k=0}^{N-1} X_k \underbrace{\sum_{n=0}^{N-1} x_n e^{2\pi i k n/N}}_{= X_k^*} e^{2\pi i k j/N} \\ \sum_{n=0}^{N-1} x_n x_{n+j} &= \frac{1}{N} \sum_{k=0}^{N-1} X_k X_k^* e^{2\pi i k j/N} = \frac{1}{N} \sum_{k=0}^{N-1} |X_k|^2 e^{2\pi i k j/N} \end{aligned} \quad (\text{D.33})$$

The autocorrelation function can now be determined by combining Equations D.32 and D.33 into

$$R_j = \frac{1}{N^2} \sum_{k=0}^{N-1} |X_k|^2 e^{2\pi i k j / N} = \sum_{k=0}^{N-1} \left| \frac{X_k}{N} \right|^2 e^{2\pi i k j / N}$$

This can be written conveniently in terms of the two-sided spectral density (Equation D.26) as

$$R_j = \Delta f \sum_{k=0}^{N-1} S_k e^{2\pi i k j / N} \quad j = 0, 1, 2, \dots, N-1 \quad (D.34)$$

The inverse of Equation D.34 is simply

$$S_k = \Delta t \sum_{j=0}^{N-1} R_j e^{-2\pi i k j / N} \quad k = 0, 1, 2, \dots, N-1 \quad (D.35)$$

Equations D.34 and D.35 form the discrete Fourier transform pair relating mean square spectral density, S_k , and the autocorrelation function, R_j . These equations represent the discrete form of the Wiener–Khinchine equations.

In analogous fashion, a DFT pair relating the cross correlation, $R_{xy,j}$ to the cross-spectral density, $S_{xy,k}$, are written as

$$R_{xy,j} = \Delta f \sum_{k=0}^{N-1} S_{xy,k} e^{2\pi i k j / N} \quad j = 0, 1, 2, \dots, N-1 \quad (D.36)$$

and

$$S_{xy,k} = \Delta t \sum_{j=0}^{N-1} R_{xy,j} e^{-2\pi i k j / N} \quad k = 0, 1, 2, \dots, N-1 \quad (D.37)$$

The symmetry relations for R_j and $R_{xy,j}$ are identical to those of their continuous counterparts discussed in Section 2.4.

D.5 Calculation of the Discrete Fourier Transform

For the present investigation, the discrete Fourier transform is calculated using computer subroutines from the IMSL Math Library (IMSL Inc., 1989). These routines utilize a Fast Fourier Transform (FFT) computational procedure modeled on the Cooley–Tukey algorithm.

The formulation of the discrete Fourier transform solved by these FFT routines is defined by

$$Z_m = \sum_{n=0}^{N-1} z_n \omega_{nm} \quad m = 0, 1, 2, \dots, N - 1 \quad (\text{D.38})$$

where, for the forward transform,

$$\omega_{nm} = e^{-2\pi i n m / N} \quad (\text{D.39a})$$

and, for the inverse transform,

$$\omega_{nm} = e^{2\pi i n m / N} \quad (\text{D.39b})$$

The routine operates on an input data set, z_n , of length N and returns its transform, Z_m , also of length N . This definition is identical in form to the discrete transform pairs derived above (Equations D.22 and D.23, Equations D.34 and D.35, and Equations D.36 and D.37). Direct comparison reveals that the user must scale the computed transform values as needed based on the particular DFT to be calculated.

A few additional comments are in order concerning implementation of the FFT routines described above. The input data set can contain an arbitrary number of samples N . However, significant computational savings result if N is a product of small primes. Optimal performance is realized if N is an integer power of 2 (i.e., $N = 2^n$).

The storage arrangement of the input and output arrays associated with the calculation of a forward transform is shown in Figure D.5. The input array is taken to be a discrete time record while the output array is its discrete transform. In general, both arrays are complex-valued and of length N . For real-valued, discrete time records, the imaginary portion of the input array is equal to zero. This array contains N discrete elements with the first corresponding to time $t = 0$ and the last to $t = T$. The output array contains the complex-valued Fourier transform. The first component corresponds to zero frequency. Subsequent array elements from 2 to $\frac{N}{2} - 1$ correspond to the positive frequency components, $0 < f < f_c$, in increments of Δf . The $\frac{N}{2}$

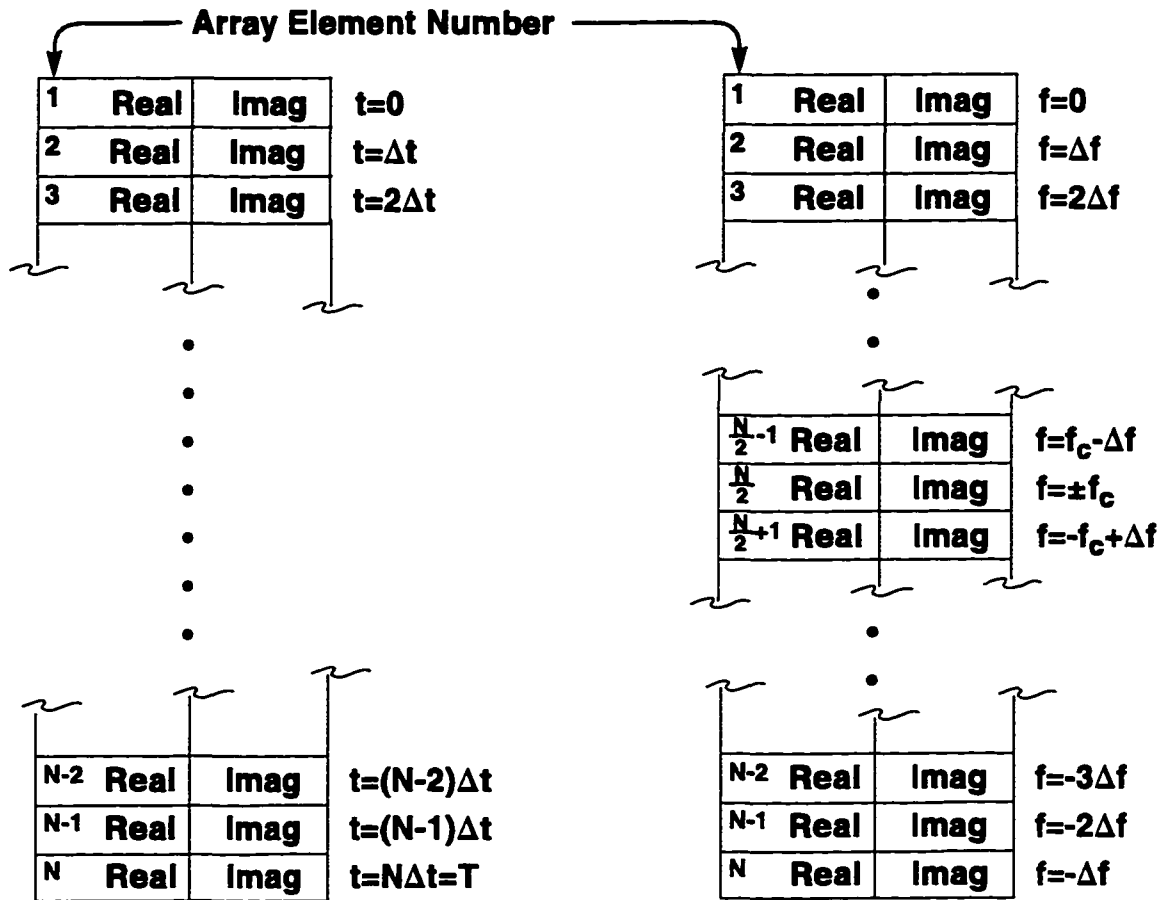


Figure D.5. General storage arrangement of arrays associated with FFT computer routine (after Press et al., 1992)

array element contains the Fourier component of the Nyquist frequencies, $\pm f_c$. Lastly, the array elements numbering from $\frac{N}{2} + 1$ to N correspond to the negative frequencies $0 > f > -f_c$ in increasing order as shown. This indexing scheme for the frequency components is analogous to that discussed in Section D.3.2.

APPENDIX E. A PROCEDURE TO CALCULATE TURBULENCE LENGTH SCALE FOR PERIODICALLY UNSTEADY FLOWFIELDS

Described in this appendix are the procedures used to compute integral length scales and turbulence energy spectra of the measured flowfields. Because turbomachinery flowfields consist of both periodic and random unsteadiness, conventional methods applied to steady flows (e.g., Suder, O'Brien, and Reshotko, 1988) can not be used directly. Instead, a modified approach is required. The method described herein is based in part on that of Camp and Shin (1995) which they developed and applied to multi-stage compressors. To the knowledge of this author, their work represents the first documented procedure for the determination of turbulence length scale in turbomachine flowfields.

A flow diagram describing the calculation procedure applied herein is provided in Figure E.1. Intermediate and final results associated with this approach are denoted by the boxes. Mathematical operations employed to proceed from one step to the next are encircled. A description of each step is provided in the sections below. Special emphasis is placed on procedures differentiating these analyses for a periodically unsteady mean flow from those pertaining to steady flow. Examples from X probe measurements will be provided throughout to illustrate key results. Some noteworthy differences of the method described herein to that of Camp and Shin (*ibid.*) are discussed in the last section.

E.1 Fluctuation Velocities

The first step of the analysis consists of determining the random (i.e., turbulent) fluctuation velocities, $u'(t)$ and $v'(t)$, from the measured velocity ensemble. The mathematics of this decomposition involve a straightforward transformation from the measured $\{V, \alpha\}_{ni}$ ensemble to $\{u', v'\}_{ni}$. The details were presented in Section 6.2.2 and thus will not be repeated here. It is instructive, however, to consider the transformation by way of an example set of time traces as shown in Figure E.2. Part a of this figure contains raw time traces of velocity magnitude, V_{ni} , for $n = 1, 2$, and 3 out of the 300 phase-locked traces acquired per ensemble. As before, subscript

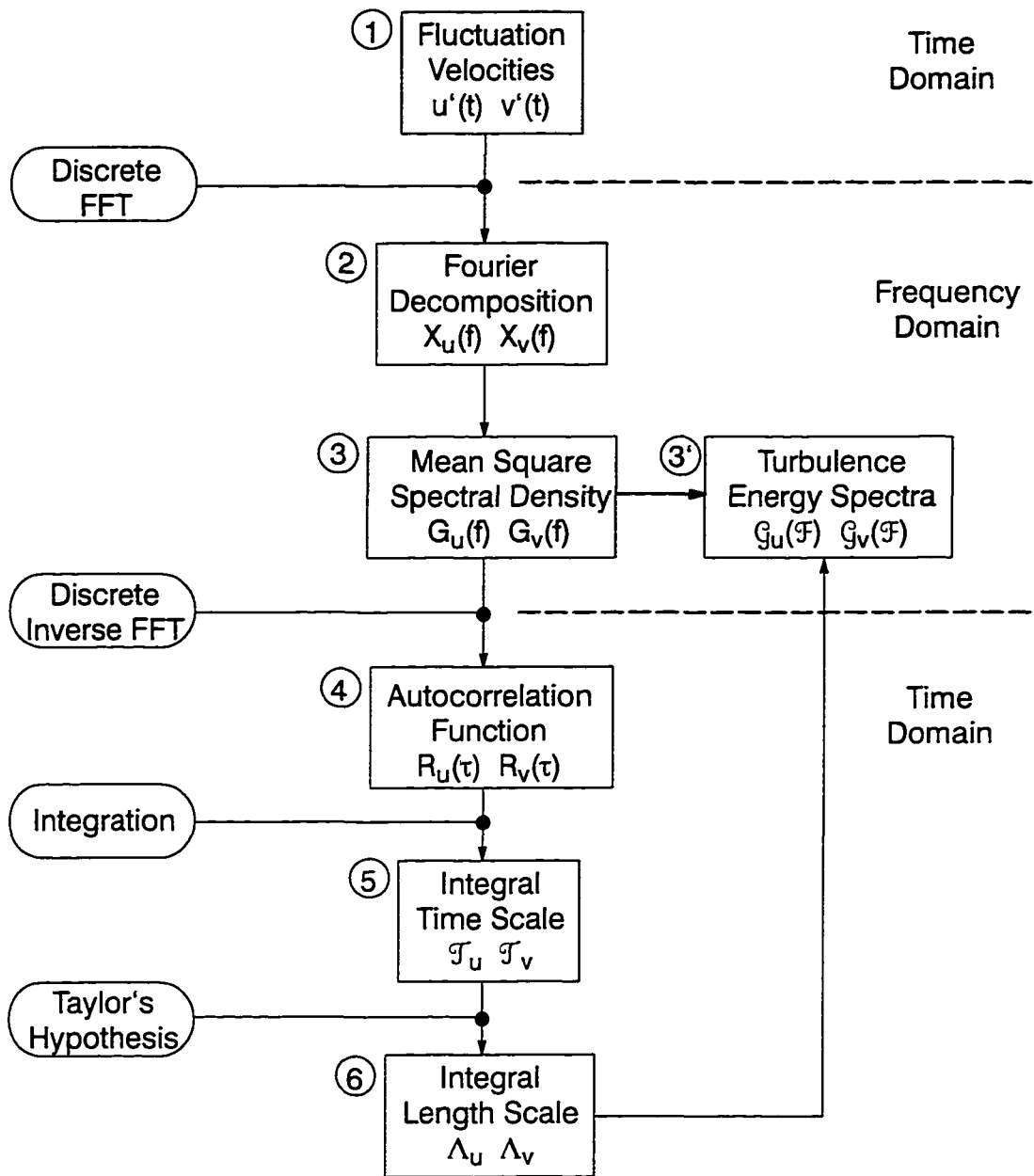
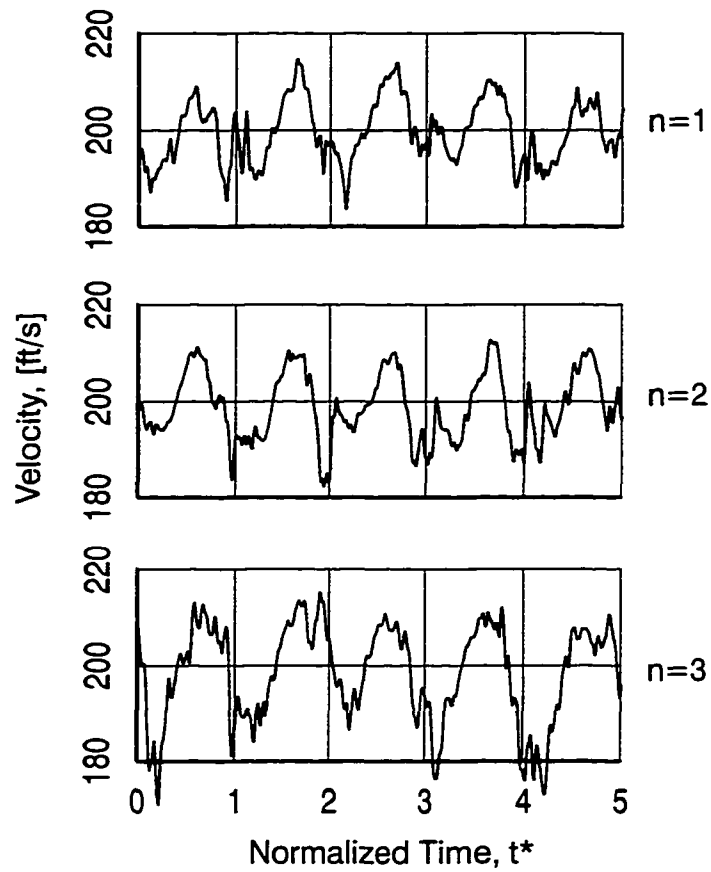
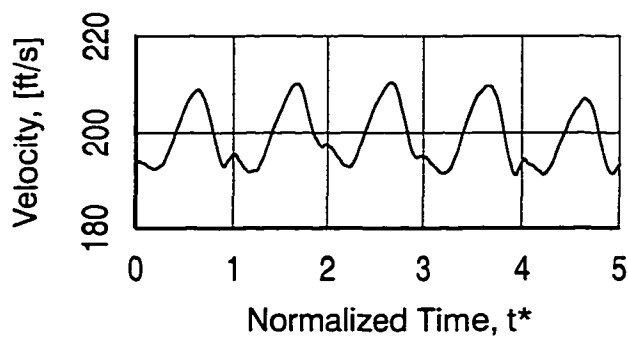


Figure E.1. Calculation procedure to determine integral length scale and turbulence energy spectra

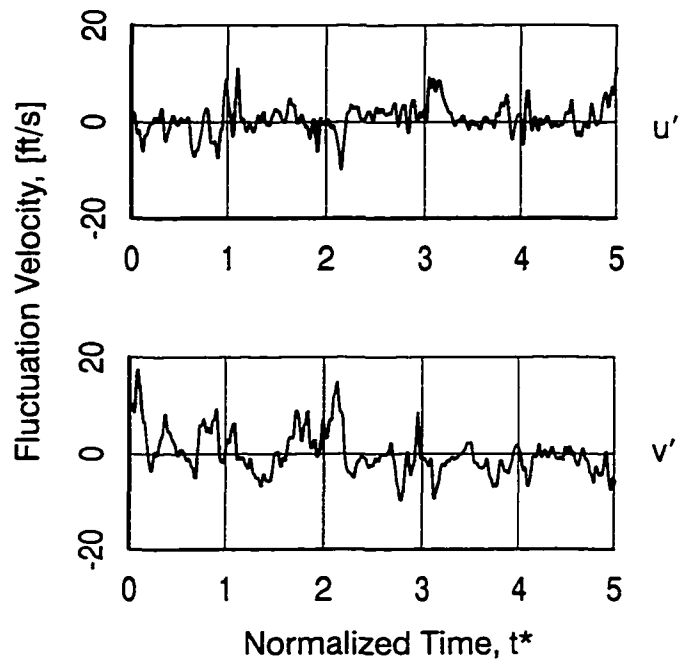


a) instantaneous time traces of velocity magnitude

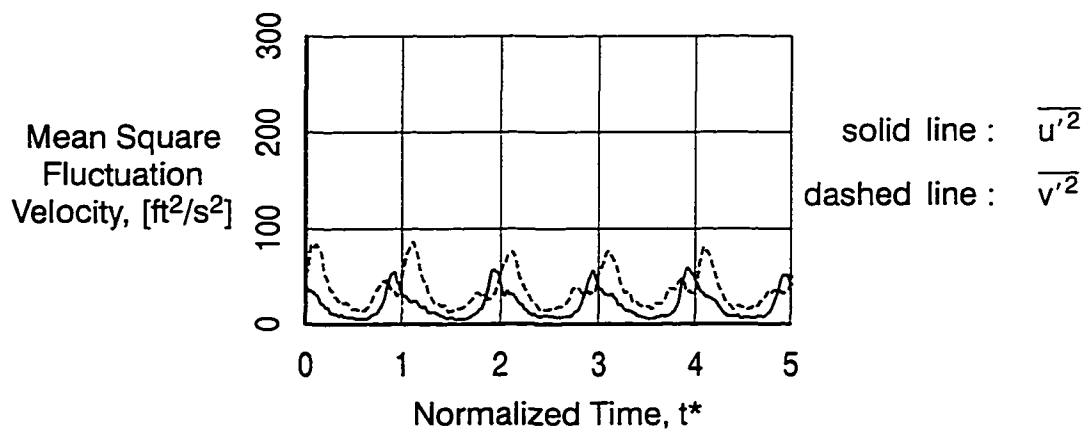


b) ensemble-averaged distribution of velocity magnitude

Figure E.2. Example set of velocity time traces measured using an X hot-film probe, data acquired at exit to Nozzle 2 (Plane 2.5)

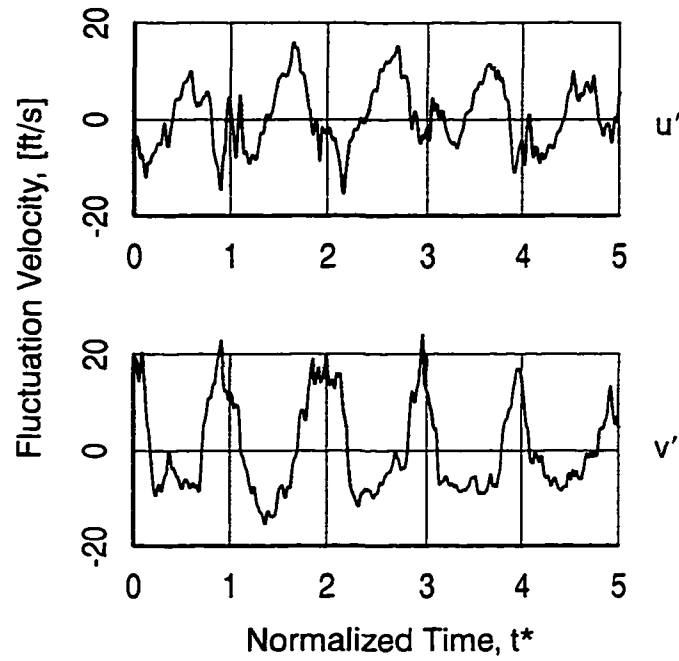


c) instantaneous time traces of random fluctuation velocity for $n=1$

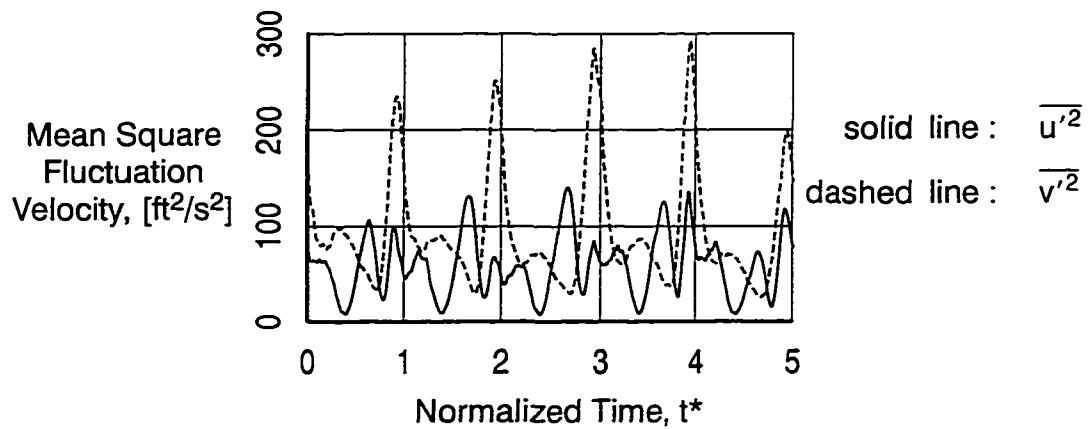


d) ensemble-averaged, mean square fluctuation velocity, random unsteadiness

Figure E.2. continued



e) instantaneous time traces of total fluctuation velocity for $n=1$



f) ensemble-averaged, mean square fluctuation velocity, total unsteadiness

Figure E.2. continued

“i” pertains to time. Each trace is shown for a time duration of 5 blade-passing periods. The ensemble used for this example was obtained at the exit to the second stage nozzle. Consequently, both periodic and random unsteadiness are evident in the instantaneous traces. For brevity, companion traces of flow angle are not shown.

The ensemble-averaged distribution of velocity magnitude, computed from the entire set of time traces, is provided in part b of Figure E.2. The fluctuation velocities then are calculated from the difference of the instantaneous and ensemble-averaged vectors by way of Equation 6.31. Example distributions of fluctuation velocity obtained in this manner are given in part c for the streamwise and transverse components. These correspond to the $n=1$ time trace. The ensemble-averaged distributions of the mean square fluctuation velocities, computed using Equation 6.32, appear in Figure E.2d.

For comparison, instantaneous time traces and ensemble mean square distributions associated with *total* unsteadiness are given in parts e and f of Figure E.2, respectively. They were determined from the difference between the instantaneous and *time-averaged* velocities. It is apparent visually that the fluctuations in the time traces of part e are composed of both random and periodic unsteadiness. Also, as expected, levels of the ensemble-averaged mean squares are significantly greater than those pertaining to the random component of unsteadiness only.

E.2 Mean Square Spectral Density

The next step of the calculation procedure is to determine the mean square spectral density of the random unsteadiness. This is denoted by the second and third boxes in Figure E.1. Raw time traces of the fluctuation velocities for each coordinate direction (e.g., $\{u', v'\}_{ni}$ from Figure E.2b) are first transformed from the temporal to the frequency domain by way of the discrete Fourier transform. Details of this transform are given in Appendix D. For the streamwise direction, the relationship is written as

$${}_uX_{nk} = \sum_{i=0}^{NPT} u'_{ni} e^{-2\pi i k i / NPT} \quad k = 1, NPT \quad (E.1)$$

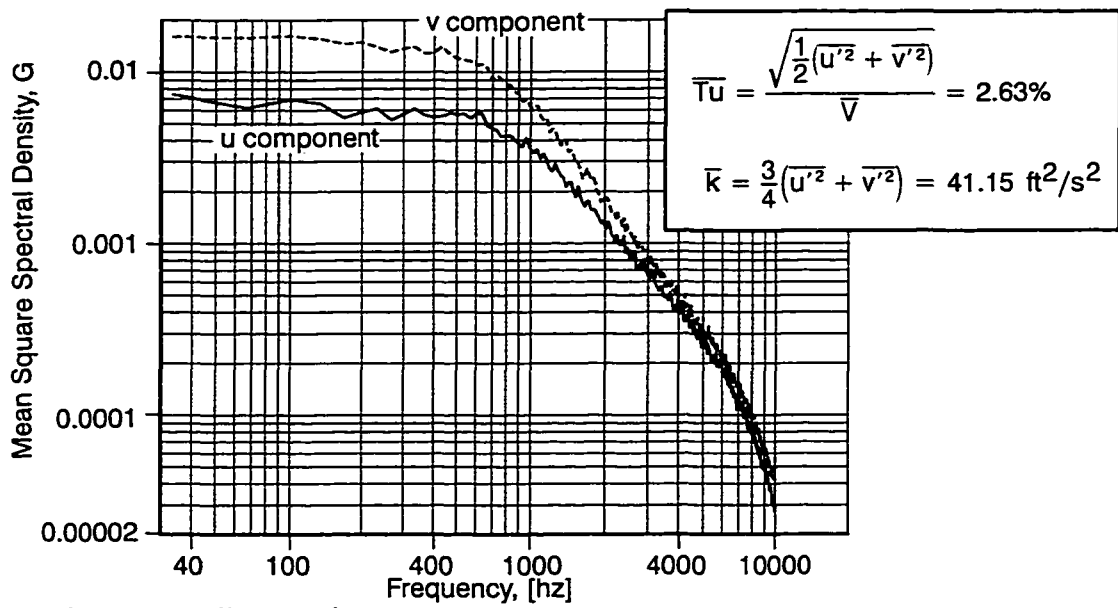
The Fourier transform, ${}_uX_{nk}$, has units of [ft/s] and represents the magnitude in fluctuation velocity for the k^{th} frequency bandwidth. Individual transforms are computed for each of the “n” time traces of fluctuation velocity. Hence for the example set of time traces from Figure E.2, 300 separate Fourier transforms are computed per coordinate direction. For this calculation, care was taken that an exact, integer number of blade-passing periods were processed when carrying out the Fourier analysis. This minimizes “filter leakage” associated with the periodic frequency components (McConnell, 1980).

Next, the frequency-averaged, mean square spectral density (MSSD) is computed from “n” Fourier transforms by way of Equation E.2. As described in the fourth section of Appendix D, the corresponding one-sided spectral density is determined using Equation E.3 and pertains to the positive (physical) frequencies only. The units of mean square spectral density are $\frac{\text{ft}^2/\text{s}^2}{\text{hz}}$ (i.e., energy per unit hertz). Relationships analogous to Equations E.1–E.3 can be written directly for the transverse coordinate direction.

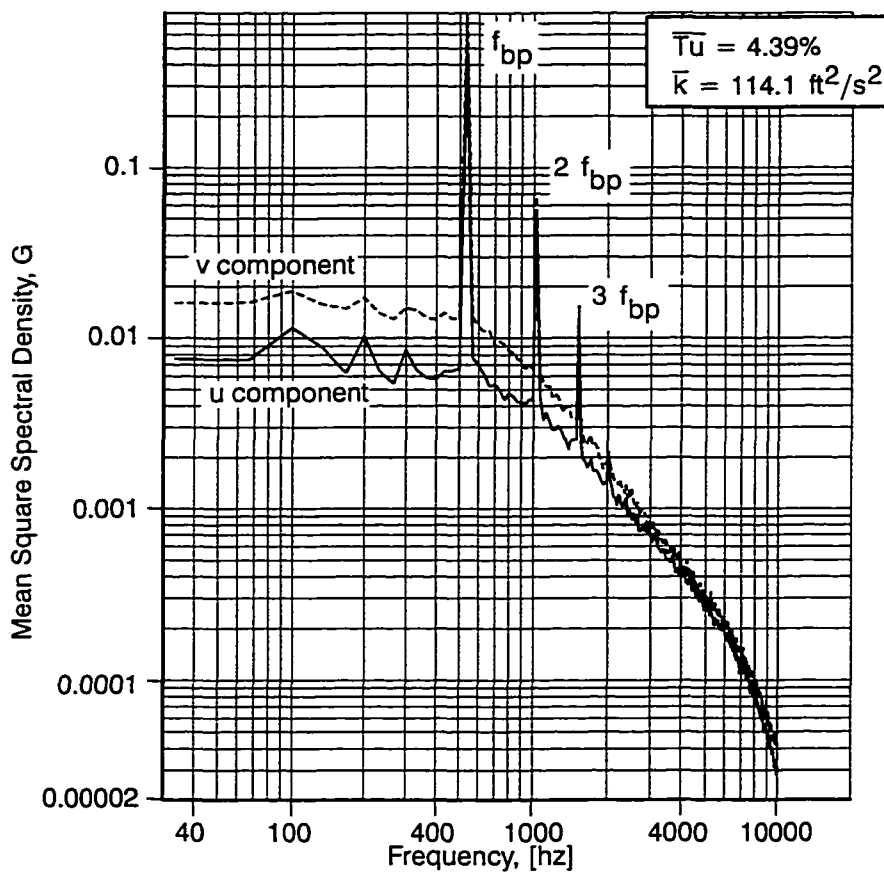
$${}_uS_k = \frac{1}{NTR} \sum_{n=1}^{NTR} \frac{1}{\Delta f} \left[\frac{{}_uX_{nk}}{NPT} \right]^2 \quad k = 1, NPT \quad (E.2)$$

$${}_uG_k = 2 {}_uS_k \quad k = 1, NPT/2 \quad (E.3)$$

Examples of the frequency-averaged MSSD for both components of fluctuation velocity are shown in Figure E.3a. Here, the abscissa is frequency which extends from 0 to 10 khz, the latter corresponding to the cutoff of the low-pass filter. The ordinate is mean square spectral density. Because of frequency averaging, the spectra are relatively smooth and continuous. For comparison, the energy spectra of the *total* fluctuation velocity (i.e., those obtained by Fourier decomposition of the time traces from Figure E.2e) are shown in Figure E.3b. Here, very distinct spikes in energy occur at blade-passing and multiples of blade-passing frequency. The spectral



a) random unsteadiness only



b) total unsteadiness

Figure E.3. Mean square spectral density for streamwise and transverse coordinate directions, data acquired at exit to Nozzle 2 (Plane 2.5)

components of random (turbulent) unsteadiness, however, remain essentially unchanged from those observed in part a of the figure, as expected.

As noted in Appendix D, integration of the MSSD over the entire frequency domain is equal to the total mean square of the unsteadiness. The discrete form of this relationship is given by Equation E.4 for the streamwise component.

$$\overline{u'^2} = \Delta f \sum_{k=1}^{NPT/2} u G_k \quad (\text{E.4})$$

Here, the summation is carried out over the positive frequencies using the one-sided MSSD.

For the sake of comparison, values of time-averaged turbulence intensity and kinetic energy are provided along with the spectra in Figure E.3. All required components of mean-square fluctuation velocity were determined in a manner analogous to Equation E.4. As expected, the energy level of the total unsteadiness is significantly greater than that for the random unsteadiness only. Their difference is that attributed to periodic unsteadiness.

E.3 Autocorrelation Coefficient

The next step of the calculation procedure, denoted by the fourth box in Figure E.1, is to determine the autocorrelation coefficient. This is accomplished by way of the inverse Fourier transform of the mean square spectral density. Prior to this calculation however, the MSSDs were modified systematically in the following manner. First, it was observed on occasion that small spikes in energy occurring at blade-passing frequency and higher harmonics persisted in the frequency-averaged spectra. This was in spite of computing the fluctuation velocities with respect to the ensemble-averaged vector. However, from Equation 6.42 (repeated below), it is evident that the definition of integral length scale is valid for random unsteadiness only. This follows from the fact that if a time trace possesses periodic unsteadiness, the autocorrelation itself will be periodic and hence the integral on the right-hand side of the equation will not con-

verge to a constant value with increasing time shift, τ .

$$\Lambda = \bar{V} \int_0^{\infty} \mathcal{P}_b(\tau) d\tau = \bar{V} \mathcal{T} \quad (6.42)$$

In order to obtain well-behaved autocorrelations then, it was necessary to remove all remaining period components. To this end, any spikes in energy occurring at blade-passing frequency or higher harmonics were set equal to the average of their neighboring mean square components prior to calculation of the autocorrelation. Comparison of before and after values of mean square unsteadiness verified that this modification had a negligible effect on the overall energy content of the spectra. Incidentally, for the particular example MSSD shown in Figure E.3a, no such spikes were present.

A second modification of the MSSDs involved the DC (zeroeth) frequency component. Even though the fluctuation velocities are determined with respect to the ensemble mean, the value of the DC component was sometimes large enough to produce a slight offset in the computed autocorrelation. This was perceptible by observing that the “tail” of the correlation function sometimes tended to a small but constant, non-zero value for large time shifts. Hence, prior to computing the inverse transform, the DC component of the MSSD was set equal to the average value of the first 4 non-zero frequency components. This modification successfully alleviated the offset problem and, as before, had a negligible effect on spectral energy content.

The autocorrelation coefficient is now computed from the inverse Fourier transform of the modified MSSD. The discretized form of this relationship, derived in Appendix D, is given by Equation E.5 for the streamwise component. The transform is calculated in terms of both positive and negative frequencies. It is normalized by the mean square, $\overline{u'^2}$, which is equal to the autocorrelation function evaluated at time shift equal zero.

$${}_u\mathcal{R}_i = \frac{\Delta f}{\overline{u'^2}} {}_u S_k^{-1} \quad i = 1, \text{NPT} \quad (E.5)$$

Correlation coefficients determined from the example spectra in Figure E.3a are shown in Figure E.4a for both the u' and v' components. The abscissa for this figure is time shift, τ , while the ordinate is correlation coefficient, \mathcal{R}_i . The temporal domain of the discrete autocorrelation extends from $-t_{\text{tot}}/2 < \tau < +t_{\text{tot}}/2$ where t_{tot} is the duration of the time trace. Because \mathcal{R}_i is an even function about $\tau=0$, it is shown for positive time only. After the initial zero crossing, the coefficients vary little from zero correlation (i.e., the tail tends to zero). For comparison, the autocorrelation computed from the frequency spectra of the total unsteadiness, part b of Figure E.3, is shown in Figure E.4b. As expected, significant periodic variation in the correlation persists after the initial zero crossing. Such a result is unsuitable for the calculation of turbulence length scales.

Before moving on, it is worth noting that the autocorrelation function varies sharply with respect to time near $\tau=0$. Consequently, it is imperative that the time period between samples (i.e., reciprocal of sampling frequency) be small enough to resolve the variation. For this work, the sample period was on the order of 15–20 times less than τ at the initial zero crossing which proved adequate.

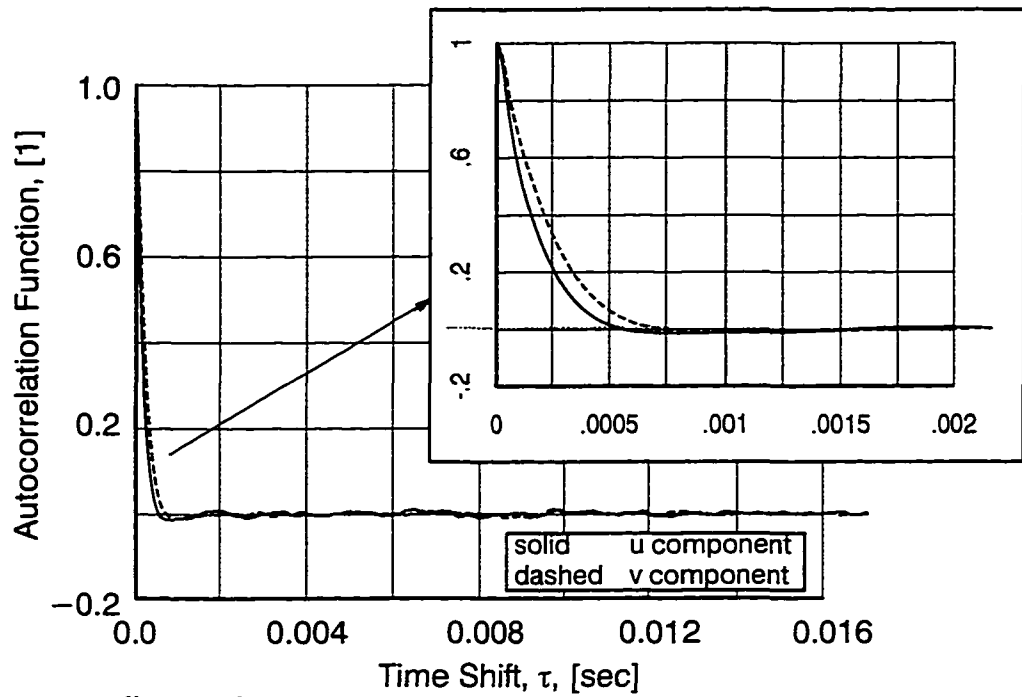
E.4 Integral Scales

Determination of the integral time and length scales are denoted by steps 5 and 6 in Figure E.1.

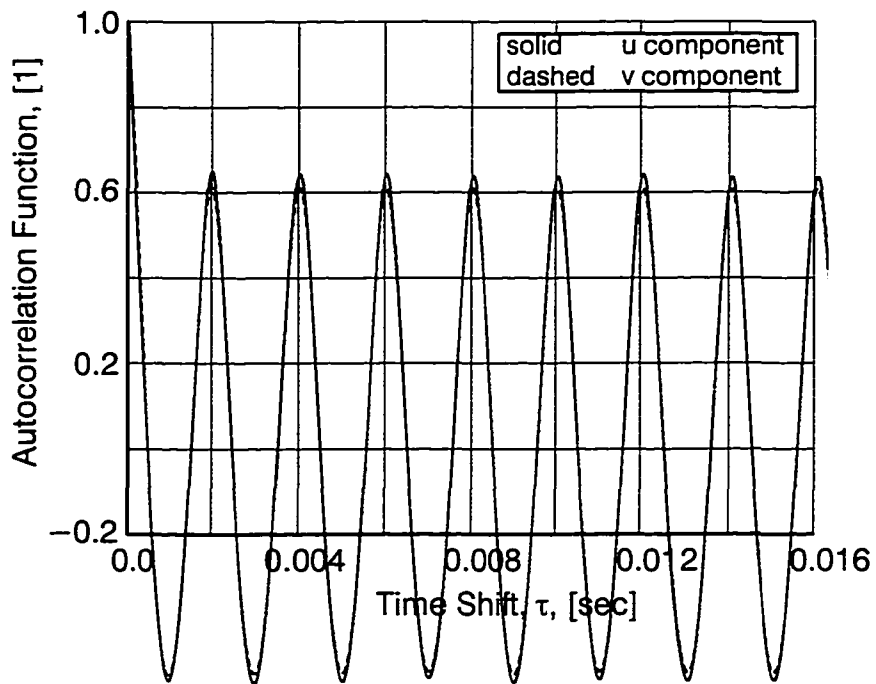
The integral time scale of the random unsteadiness is calculated by integrating the autocorrelation coefficient with respect to time shift, τ , as indicated by Equation E.6.

$$\mathcal{T} = \int_0^{\infty} \mathcal{R}_i(\tau) d\tau \quad (\text{E.6})$$

The discrete integration of \mathcal{R}_i was carried out using a least-squares technique. Results computed from the autocorrelations of Figure E.4a are presented in Figure E.5. They are in the form of a cumulative summation of each integral as a function of time shift, τ . As denoted, the right-most values of the distributions correspond to the final value of the integration and hence are



a) random unsteadiness only



b) total unsteadiness

Figure E.4. Autocorrelation functions for streamwise and transverse coordinate directions. data acquired at exit to Nozzle 2 (Plane 2.5)

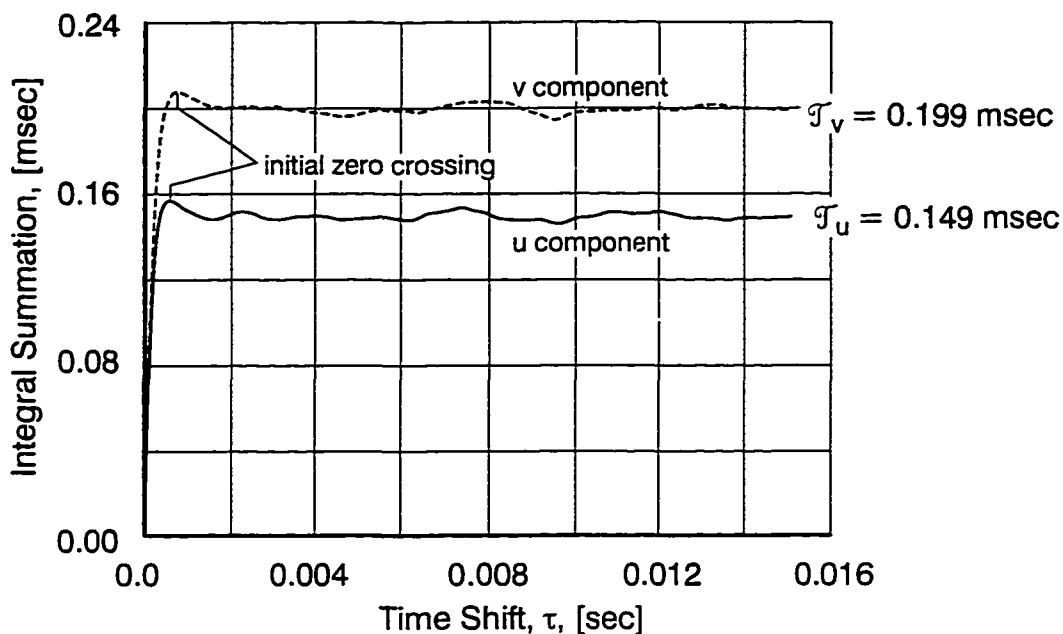


Figure E.5. Cumulative summations of correlation integrals to determine integral time scales, data acquired at exit to Nozzle 2 (Plane 2.5)

equal to the integral time scales. For both coordinate directions, the time scales converge to constant values as τ approaches τ_{\max} , indicating well-behaved integrations.

With the integral time scales determined, Taylor's hypothesis is employed as indicated below to compute the longitudinal length scales.

$$\Lambda_u = \bar{V} \mathcal{T}_u \quad \text{and} \quad \Lambda_v = \bar{V} \mathcal{T}_v \quad (\text{E.7})$$

E.5 Turbulence Energy Spectrum

From the turbulence quantities determined in the previous sections of this appendix, the mean square spectral density is normalized into what commonly is referred to as the turbulence energy spectrum. This is denoted by box 3' in Figure E.1. As an example, the MSSD associated with the streamwise coordinate direction (i.e., uG_k of Figure E.3a) is shown normalized in Figure E.6. The ordinate is the dimensionless spectral density

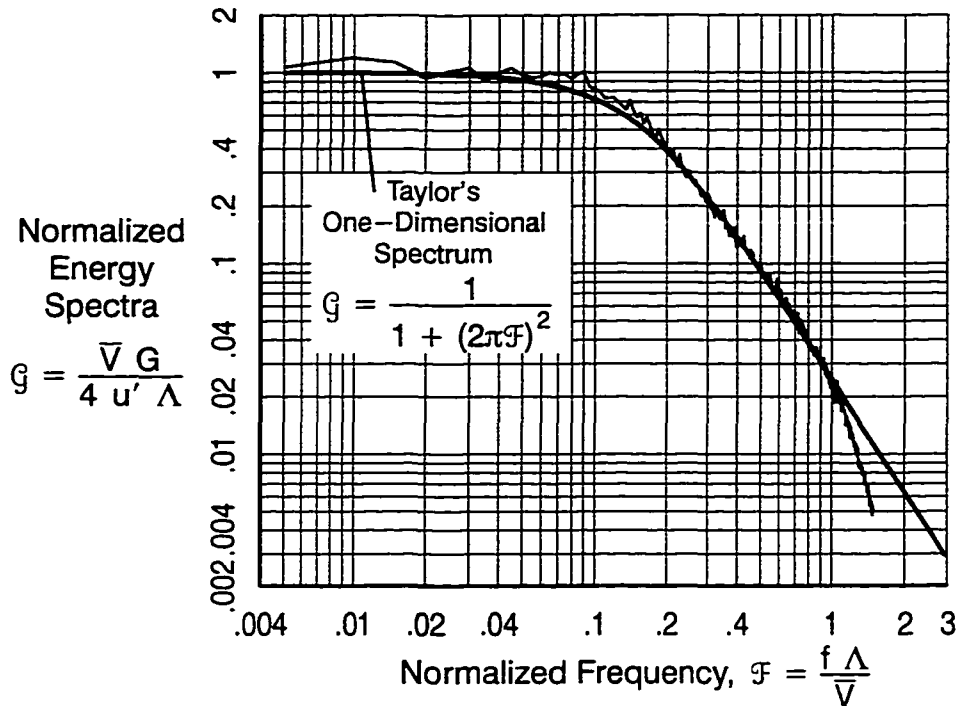


Figure E.6. Turbulence energy spectra for streamwise coordinate direction, data acquired at exit to Nozzle 2 (Plane 2.5)

$${}_u\mathcal{G}_k = \frac{{}_uG_k \bar{V}}{4 u'^2 \Lambda_u} \quad (\text{E.8})$$

while the abscissa is that of dimensionless wave number

$$\mathcal{F}_k = \frac{\Lambda_u f_k}{V} \quad (\text{E.9})$$

Also shown in Figure E.6 for comparison is Taylor's theoretical spectrum for one-dimensional isotropic turbulence (Hinze, 1975).

It is noteworthy that close agreement between the theoretical and measured spectra is found for much of the distribution. For wave numbers greater than about 1.0, however, the energy content of the measured flow increasingly deviates from the theoretical spectrum. Much of this difference is attributed to the low-pass filter employed for anti-aliasing during data acquisition. The response function for this filter is such that an amplitude attenuation of -3 dB occurs at the cutoff frequency. This results in a reduction in spectral energy of nearly 50 percent. That

is,

$$\frac{\text{energy}_{\text{meas}}}{\text{energy}_{\text{actual}}} = 10^{-3\text{dB}/10} = 0.501$$

This situation could be alleviated in the future by using a stiffer probe that would then allow a higher cutoff setting of the low pass filter (see discussion of prong vibration in Section 5.3.2). It should be pointed out, though, that the effect of this attenuation on the total mean square unsteadiness was not significant for these measurements.

E.6 Departures from the Method of Camp and Shin

As mentioned previously, the methodology employed herein to determine turbulence length scale was based in part on that of Camp and Shin (1995) (hereafter denoted C–S). There are, however, a number of noteworthy differences between the C–S method and the present implementation. These are described below.

The first involves the determination of the MSSD which is subsequently used to calculate the autocorrelation function. In contrast to the approach described above in Section E.2, C–S recommend calculating the MSSD by way of a single, “long–duration” time trace. In their context, “long duration” is taken to be at minimum about 50 times the blade–passing period. The MSSD is then calculated from the FFT of this single trace. The rationale put forth for this approach is that 1) the longer the time trace, the higher the resolution of the frequency spectra, and 2) data acquisition, storage and analysis of a single trace can be accomplished much more efficiently than for an ensemble of traces.

Experience from this work, however, indicates that significant variations in the MSSD from one time trace to the next can be present even for such long–duration traces. Such variations in turn can bias the calculation of the autocorrelation depending on which trace was used to determine it. This is evident from Figure E.7 where two individual–trace MSSDs (lighter weight lines) are compared with the corresponding frequency–averaged MSSD (heavier weight line, from Figure E.3a). As one would expect, the former are much more “noisy” than the latter as a consequence of being computed from less information. In contrast, it was found that no

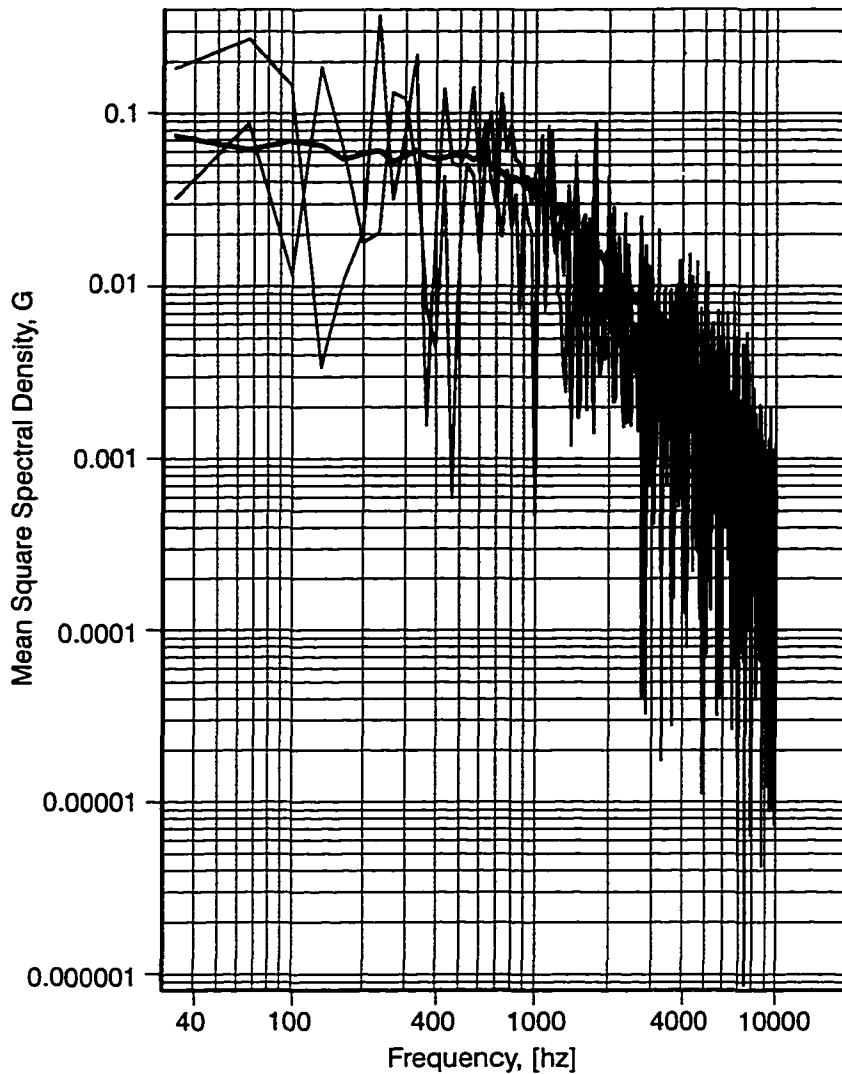


Figure E.7. Individual trace MSSDs for streamwise coordinate direction, data acquired at exit to Nozzle 2 (Plane 2.5)

significant variation was observed when comparing two *frequency-averaged* MSSDs obtained back-to-back at the same measurement conditions. In a statistical sense then, these findings indicate that frequency averaging produces a more accurate MSSD than when a single (albeit long) trace is used.

A second significant difference between the present method and that of C-S involves the decomposition of periodic and random unsteadiness. Because only a single time trace is acquired when applying the C-S approach, ensemble averaging can not be employed in the time

domain to remove periodic unsteadiness prior to computing the Fourier transform. Instead, components of periodic unsteadiness are removed directly from the MSSD itself. To this end, C–S recommend that spikes in energy occurring at blade–passing frequency and higher harmonics be set equal to zero amplitude. Inspection of spectra obtained from this work, an example being those of Figure E.3a, indicates that, in reality, this procedure removes too much energy. Instead, it seems more appropriate to remove only that portion of the spectral component that is above the “background” random spectra rather than zeroing it out altogether. Such a modification is easily accomplished with respect to the frequency–averaged spectra, again evident from Figure E.3a and E.3b. In contrast, it is exceedingly more difficult to discern the random level using an individual–trace spectrum such as in Figure E.7.

Concerning the time duration of the traces required for an accurate frequency domain analysis, 15 blade–passing periods was found to be adequate for this work. The subsequent data ensembles, consisting of 300 phase–locked traces, could be acquired, stored, and analyzed conveniently using the available instrumentation and computer systems. Hence, unlike for the C–S approach, the *identical* times traces could be used to determine turbulence intensity and integral length scale.

A final difference in methodology involves the integration of the autocorrelation to determine integral time scale. C–S recommend halting the integration at the initial zero crossing of the autocorrelation function. For the example correlations presented in Figure E.4a, the time scales corresponding to these initial zero crossings are noted in Figure E.5. That this criterion does not provide for negative correlation is readily apparent from these results. Negative values of $\Re(\tau)$, such as those exhibited in Figure E.4, are, however, entirely plausible (Cebeci and Smith, 1974). Consequently, it seems more appropriate to continue the integration for all positive time as the definition of integral time scale suggests (i.e., Equation E.6). This is especially apparent in Figure E.5 for the transverse component. Here, the integral peaks initially at the first zero crossing but then decreases and becomes nearly constant with increasing τ . In fact, the be-

havior of the integral (whether for the streamwise or transverse direction) *after* the zero crossing provides a strong indication as to whether the autocorrelation function has been determined adequately. A problem clearly exists if \mathcal{I} does not converge to a constant value.

APPENDIX F. TEMPERATURE ADJUSTMENT OF ZERO-FLOW VOLTAGES

During acquisition of zero-flow voltages from the surface hot-film sensors, the ambient temperature is generally different from that of the air flow during operation of the LSRT during which the actual hot-film measurements are obtained. This difference results from changes in test floor temperature and from changes in local total temperature within the turbine due to work extraction across rotor blade rows. Hence prior to application of the data analysis procedures described in Section 6.1, values of the zero-flow voltages, E_0 , acquired at temperature, T_0 , were adjusted to reflect the local total temperature, T_t , associated with the hot-film measurements obtained during turbine operation.

The output voltage from a hot-film sensor operated at constant temperature is related to the temperature difference between the sensor and air flow as described by Equation F.1 (Fingerson and Freymuth, 1983).

$$E \propto \sqrt{\Delta T} \quad (\text{F.1})$$

where $\Delta T = T_{\text{op}} - T_{\text{air}}$
 T_{op} = sensor operating temperature
 T_{air} = local air operating temperature

In terms of the nomenclature in the previous paragraph, the zero-flow voltage from a given sensor can be related to temperature as shown below.

$$\frac{E_{0,\text{adj}}}{E_0} = \frac{\sqrt{T_{\text{op}} - T_t}}{\sqrt{T_{\text{op}} - T_0}} \quad (\text{F.2})$$

It is evident from this relationship that as temperature, T_t , increases above or decreases below T_0 , the corresponding value of $E_{0,\text{adj}}$ will decrease and increase in the manner indicated. For reasons that will be evident shortly, Equation F.2 is rewritten into the following form

$$E_{0,\text{adj}} = \sqrt{1 + \frac{T_0 - T_t}{T_{\text{op}} - T_0}} E_0 \quad (\text{F.3})$$

The relationship between temperature and resistance of a hot–film sensor is given by Equation F.4 (TSI, 1983).

$$R_{\text{sen,hot}} + R_{\text{lead}} = R_{\text{sen,cold}} + R_{\text{lead}} + \alpha R_{\text{sen,cold}}(T_{\text{op}} - T_0) \quad (\text{F.4})$$

Here, α is the temperature coefficient of resistance of the sensor and the variable “R” represents various sensor and lead resistances. Incorporating the definition of overheat ratio(OHR), the above relationship can be rewritten as

$$\text{OHR} = \frac{R_{\text{sen,hot}}}{R_{\text{sen,cold}}} = 1 + \alpha (T_{\text{op}} - T_0)$$

and, hence

$$(T_{\text{op}} - T_0) = \frac{\text{OHR} - 1}{\alpha} \quad (\text{F.5})$$

Equations F.3 and F.5 are then combined as indicated below to give the temperature adjustment in its final form.

$$E_{0,\text{adj}} = \sqrt{1 + \frac{\alpha (T_0 - T_1)}{\text{OHR} - 1}} E_0 \quad (\text{F.6})$$

As evident from Equation F.6, this correction is a function of the overheat ratio at which a sensor is operated, the temperature coefficient of resistance of the sensor, and the difference in local total temperature between that at which E_0 was acquired and that at which the surface hot–film measurements were obtained during turbine operation.

APPENDIX G. TRAJECTORY OF FLUID ELEMENTS/EVENTS IN s^*-t^* SPACE

The trajectory or pathline of a unique fluid element (also referred to herein as a measurable “event” as associated with the Eulerian or “field” point of view) is determined by computing the position of the element as a function of time (Karamcheti, 1966). At an arbitrary location along an airfoil surface, the steady-state, freestream velocity field can be written as

$$V_{\infty}(s) = \frac{ds}{dt} \quad (\text{G.1})$$

where $V_{\infty}(s)$ = local freestream velocity at s

Separating variables, Equation G.1 can be rewritten in its differential form

$$dt = \frac{ds}{V_{\infty}(s)} \quad (\text{G.2})$$

The above result can be integrated directly from a given location along the airfoil surface, s_0 , and starting at arbitrary time $t_0=t(s_0)$ as shown by Equation G.3. This relationship is a mathematical representation of the trajectory of a fluid element (or event) convecting at freestream velocity along the airfoil.

$$\int_{t_0}^t dt' = \int_{s_0}^s \frac{ds'}{V_{\infty}(s')}$$

$$t - t_0 = \int_{s_0}^s \frac{ds'}{V_{\infty}(s')} \quad (\text{G.3})$$

In general, the velocity distribution of an airfoil is not available in the form of an analytical function but is known instead at discrete locations along its surface from leading to trailing edge. In such cases, integration described by Equation G.3 is accomplished in discretized fashion as shown below.

$$t_N - t_0 = \sum_{n=1}^N \frac{\Delta s_n}{V_{\infty,n}} \quad (\text{G.4})$$

Here, $t_N - t_0$ is the time required for a fluid element, moving at local freestream velocity, to con-

vect a distance $s_N - s_0$ where

$$s_N - s_0 = \sum_{n=1}^N \Delta s_n \quad \text{and} \quad \Delta s_n = s_n - s_{n-1}$$

Equation G.4 is generalized further by normalizing of each of its terms. This normalization is accomplished as follows:

$$1. \quad \text{time:} \quad t_N^* = \frac{t_N}{\tau_{bp}} = t_N f_{bp} \quad (\text{G.5a})$$

where τ_{bp} = blade-passing period
 f_{bp} = blade-passing frequency

$$2. \quad \text{surface distance:} \quad \Delta s_n^* = \frac{\Delta s_n}{s_{tot}} \quad (\text{G.5b})$$

where s_{tot} = surface distance from leading to trailing edge

$$3. \quad \text{velocity:} \quad V_{\infty, n}^* = \frac{V_{\infty, n}}{V_{ex}} \quad (\text{G.5c})$$

where V_{ex} = bladerow exit velocity

Thus, the normalized formulation of Equation G.4 follows as

$$\begin{aligned} t_N^* - t_0^* &= \frac{f_{bp} s_{tot}}{V_{ex}} \sum_{n=1}^N \frac{\Delta s_n^*}{V_{\infty, n}^*} \\ &= k \sum_{n=1}^N \frac{\Delta s_n^*}{V_{\infty, n}^*} \end{aligned} \quad (\text{G.6})$$

Here, the multiplier on the summation is a reduced frequency, k . It is simply a ratio of convective and periodic time scales. For a given test condition then, the locus of (s_n^*, t_n^*) computed using Equation G.6 represents, in s^*-t^* space, the trajectory of a fluid element/event convecting along the airfoil surface at the local freestream velocity.

Further generalization of Equation G.6 can be realized by allowing for events that convect at fractions of the freestream velocity (an example being the leading and trailing boundaries of turbulent spots). This is accomplished by substituting the quantity " $cV_{\infty, n}^*$ " for " $V_{\infty, n}^*$ " in Equation G.6. For events moving at velocities of less than freestream, the coefficient " c " will

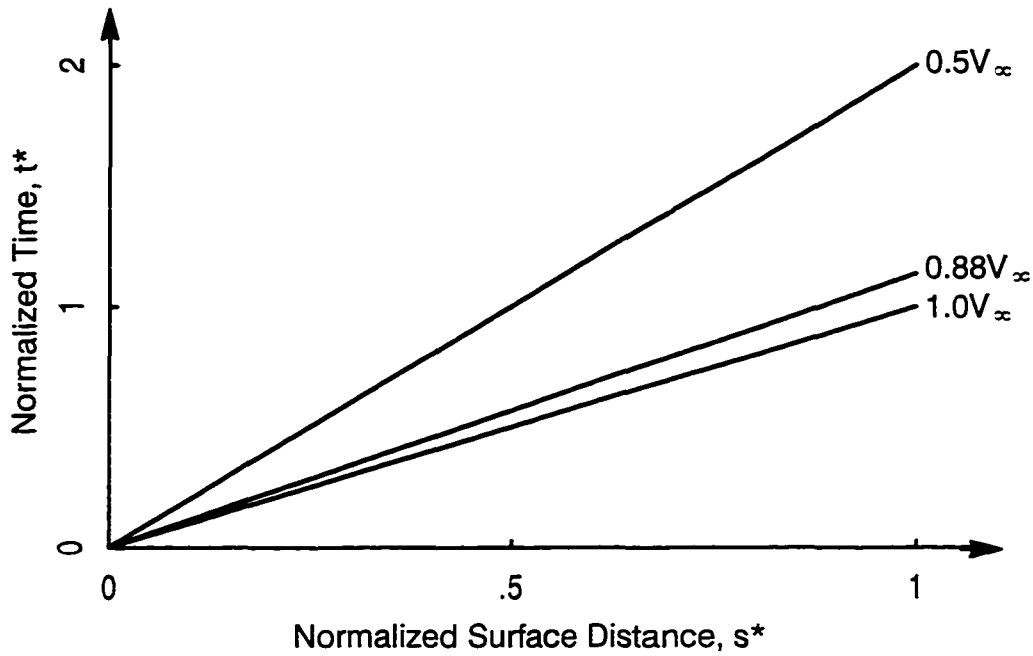


Figure G.1. Illustration of event trajectories in s^*-t^* space ($k=1.0, V_{\infty,n}^*=1.0$)

be less than one. In its most general form then, Equation G.6 is written as

$$t_N^* - t_0^* = k \sum_{n=1}^N \frac{\Delta s_n^*}{c V_{\infty,n}^*} \quad (G.7)$$

For illustration, trajectories calculated by way of Equation G.7 appear in Figure G.1. Trajectories for values of “c” equal to 1.0, 0.88, and 0.5 are given as examples. The latter two correspond to the leading and trailing boundaries of an individual turbulent spot (Schubauer and Klebanoff, 1956).

BIBLIOGRAPHY

- AGARD Lecture Series 195, "Turbomachinery Design using CFD," Neuilly Sur Seine, France.
- Abu-Ghannam, B. J., and R. Shaw, 1980, "Natural Transition of Boundary Layers – The Effects of Turbulence, Pressure Gradient, and Flow History," Journal of Mechanical Engineering Sciences, Vol. 22, pp. 213–228.
- Arndt, N., 1993, "Blade Row Interaction in a Multistage Low-Pressure Turbine," ASME Journal of Turbomachinery, Vol. 115, pp. 137–146.
- Ashworth, D. A., J. E. LaGraff, and D. L. Schultz, 1989, "Unsteady Interaction Effects on a Transitional Turbine Blade Boundary Layer," ASME Journal of Turbomachinery, Vol. 111, pp. 162–168.
- Ashworth, D. A., and J. E. LaGraff, 1989, "Measurement and Modeling of Turbulent Spot Growth on a Gas Turbine Blade," AIAA Paper 89–0328.
- Baines, W. D., and E. G. Peterson, 1951, "An Investigation of Flow Through Screens," Transactions of the ASME, Vol. 73, pp. 467–480.
- Blair, M. F., 1992, "Influence of Free-Stream Turbulence on Boundary Layer Transition in Favorable Pressure Gradients," ASME Journal of Engineering for Power, Vol. 104, pp. 743–750.
- Bellhouse, B. J. and D. L. Schultz, 1966, "Determination of Mean and Dynamic Skin Friction, Separation and Transition in Low-Speed Flow with a Thin-Film Heated Element," Journal of Fluid Mechanics, Vol. 24, pp. 379–400.
- Bendat, J. S., and A. G. Piersol, 1971, Random Data: Analysis and Measurement Procedures, John Wiley & Sons, Inc., New York, NY.
- Bendat, J. S., and A. G. Piersol, 1980, Engineering Applications of Correlation and Spectral Analysis, John Wiley & Sons, Inc., New York, NY.
- Blackwelder, R. F. and H. Eckelmann, 1977, "Influence of the Convection Velocity on the Calibration of Heated Surface Elements," Euromech. 90 Proc., Session I.a.1, pp. 1–10.
- Borgos, J. A., 1980, "A Review of Electrical Testing of Hot-Wire and Hot-Film Anemometers," TSI Quarterly, Vol. 6, Is. 3, pp. 3–9.
- Bradshaw, P., 1971, An Introduction to Turbulence and its Measurement, Pergamon Press, Oxford, England.
- Brideman, M. J., D. G. Cherry, and J. Pedersen, 1983, "Low Pressure Turbine Scaled Test Vehicle Performance," NASA CR–168290.

- Brigham, E. O., 1974, The Fast Fourier Transform, Prentice-Hall, Inc., Englewood Cliffs, NJ.
- Camp, T. R., and H.-W. Shin, 1995, "Turbulence Intensity and Length Scale Measurements in Multistage Compressors", ASME Journal of Turbomachinery, Vol. 117, pp. 38-46.
- Cebeci, T., and A. M. O. Smith, 1974, Analysis of Turbulent Boundary Layers, Academic Press, Inc., Orlando, FL.
- Crawford, M. E., and W. M. Kays, 1976, "STAN5 – A Program for Numerical Computation of Two-Dimensional Internal and External Boundary Layer Flows," NASA CR-2742.
- Curtis, E. M., H. P. Hodson, M. R. Baniaghbal, J. D. Denton, R. J. Howell, and N. W. Harvey, 1996, "Development of Blade Profiles for Low Pressure Turbine Applications," ASME Paper 96-GT-358.
- Dailey, L. D., 1993, "Simulating Laminar-Turbulent Transition with a Low Reynolds Number $k-\epsilon$ Turbulence Model in a Navier-Stokes Flow Solver," MS Thesis, University of Cincinnati.
- Denton, J. D., 1993, "Loss Mechanisms in Turbomachines," ASME Journal of Turbomachinery, Vol. 115, pp. 621-656.
- Dring, R. P., H. D. Joslyn, L. W. Hardin, and J. H. Wagner, 1982, "Turbine Rotor-Stator Interaction," ASME Journal of Engineering for Power, Vol. 104, pp. 729-742.
- Dubiel, D. J., and D. E. Gray, and D. C. Howe, 1989, "Energy Efficient Engine – Final Report," NASA CR-182300.
- Emmons, H. W., 1951, "The Laminar-Turbulent Transition in a Boundary Layer – Part 1," Journal of Aeronautical Sciences, Vol. 18, pp. 490-498.
- Fan, S., and B. Lakshminarayana, 1996, "Computation and Simulation of Wake-Generated Unsteady Pressure and Boundary Layers in Cascades: Parts 1 and 2," ASME Journal of Turbomachinery, Vol. 118, pp. 96-122.
- Fingerson, L. M., and P. Freymuth, 1983, "Thermal Anemometers," in Fluid Mechanics Measurements, pp. 99-154, edited by R. J. Goldstein, Hemisphere, New York, NY.
- Freymuth, P., and L. M. Fingerson, 1977, "Electronic Testing of Frequency Response for Thermal Anemometers," TSI Quarterly, Vol. 3, pp. 5-12.
- Funazaki, K., 1996, "Unsteady Boundary Layers on a Flat Plate Disturbed by Periodic Wakes: Parts 1-2," ASME Journal of Turbomachinery, Vol. 118, pp. 327-346.
- Glassman, A. J., 1972, "Basic Turbine Concepts," in NASA SP-290, edited by A. J. Glassman, NASA, Washington, D. C.

- Gostelow, J. P., G. J. Walker, W. J. Solomon, G. Hong, and N. Melwani, 1996, "Investigation of the Calmed Region Behind a Turbulent Spot," ASME Paper 96-GT-489.
- Gostelow, J. P., N. Melwani, and G. J. Walker, 1995, "Effects of Streamwise Pressure Gradient on Turbulent Spot Development," ASME Paper 95-GT-303.
- Gostelow, J. P., A. R. Blunden, and G. J. Walker, 1994, "Effects of Free-Stream Turbulence and Adverse Pressure Gradients on Boundary Layer Transition," ASME Journal of Turbomachinery, Vol. 116, pp. 392-404.
- Gostelow, J. P., 1977, "A New Approach to the Experimental Study of Turbomachinery Flow Phenomena," ASME Journal of Engineering for Power, Vol. 99, pp. 97-105.
- Gresko, L. S., 1988, "Characteristics of Wall Pressure and Near-Wall Velocity in a Flat Plate Turbulent Boundary Layer," Massachusetts Institute of Technology, Fluid Dynamics Research Laboratory Report FDRLR #88-2.
- Halstead, D. E., D. C. Wisler, T. H. Okiishi, G. J. Walker, H. P. Hodson, H.-W. Shin, 1995, "Boundary Layer Transition in Axial Compressors and Turbines - Parts 1-4," ASME Papers 95-GT-461 to 95-GT-464.
- Halstead, D. E., T. H. Okiishi, and D. C. Wisler, 1990, "Boundary-Layer Transition and Separation on a Turbine Blade in Plane Cascade," AIAA Paper 90-2263.
- Halstead, D. E., 1989, "The Use of Surface-Mounted Hot-Film Sensors to Detect Turbine-Blade Boundary-Layer Transition and Separation," MS Thesis, Iowa State University.
- Hanratty, T. J., and J. A. Campbell, 1983, "Measurement of Wall Shear Stress," in Fluid Mechanics Measurements, pp. 559-615, edited by R. J. Goldstein, Hemisphere, New York, NY.
- Hinze, J. O., 1975, Turbulence, McGraw-Hill, Inc., New York, NY.
- Hodson, H. P., I. Huntsman, and A. B. Steele, 1994, "An Investigation of Boundary Layer Development in a Multistage LP Turbine," ASME Journal of Turbomachinery, Vol. 116, pp. 375-383.
- Hodson, H. P. and J. S. Addison, 1989, "Wake-Boundary Layer Interaction in an Axial Flow Turbine Rotor at Off-Design Conditions," ASME Journal of Turbomachinery, Vol. 111, pp. 181-192.
- Hodson, H. P., 1985a, "Measurements of Wake-Generated Unsteadiness in the Rotor Passages of Axial-Flow Turbines," ASME Journal of Engineering for Gas Turbines and Power, Vol. 107, pp. 467-476.
- Hodson, H. P., 1985b, "An Inviscid Blade-to-Blade Prediction of a Wake-Generated Unsteady Flow," ASME Journal of Engineering for Gas Turbines and Power, Vol. 107, pp.337-343.

- Hodson, H. P., 1985c, "Boundary-Layer Transition and Separation near the Leading Edge of a High-Speed Turbine Blade," ASME Journal of Engineering for Gas Turbines and Power, Vol. 107, pp. 127–134.
- Hodson, H. P., 1984, "Boundary Layer and Loss Measurements on the Rotor of an Axial-Flow Turbine," ASME Journal of Engineering for Gas Turbines and Power, Vol. 106, pp. 391–399.
- Hoheisel, H., R. Kiock, H. J. Lichtfuss, and L. Fottner, 1987, "Influence of Free-Stream Turbulence and Blade Pressure Gradient on Boundary Layer and Loss Behavior on Turbine Cascades," ASME Journal of Turbomachinery, Vol. 109, pp. 210–219.
- Hourmouziadis, J., 1989, "Aerodynamic Design of Low Pressure Turbines," AGARD Lecture Series 167.
- Hourmouziadis, J., F. Buckl, and P. Bergmann, 1987, "The Development of the Profile Boundary Layer in a Turbine Environment," ASME Journal of Turbomachinery, Vol. 109, pp. 286–295.
- Huber, F. W., P. D. Johnson, O. P. Sharma, J. B. Staubach, and S. W. Gaddis, 1995, "Performance Improvement Through Indexing of Turbine Airfoils, Part 1 – Experimental Investigation," ASME Paper 95–GT–27.
- IMSL Incorporated, 1989, "Users Manual – FORTRAN Subroutines for Mathematical Applications," Houston, Texas.
- Karamcheti, K., 1966, Principles of Ideal-Fluid Aerodynamics, Robert E. Krieger Publishing Co., Malabar, FL.
- Kline, S. J., and F. A. McClintock, 1953, "Describing Uncertainties in Single Sample Experiments," Mechanical Engineering, Vol. 75, pp. 3–8.
- Ladwig, M., and L. Fottner, 1993, "Experimental Investigations of the Influence of Incoming Wakes on the Losses of a Linear Turbine Cascade," ASME Paper 93–GT–394.
- Loehrke, R. I., M. V. Morkovin, and F. A. Fejer, 1975, "REVIEW – Transition in Nonreversing Oscillating Boundary Layers," ASME Journal of Fluids Engineering, Vol. 109, pp. 534–549.
- Lueptow, R. M., Breuer, K. S., and J. H. Haritonidis, 1988, "Computer-Aided Calibration of X-Probes using a Lookup Table," Experiments in Fluids, Vol. 6, pp. 115–118.
- Mayle, R. E., 1991, "The Role of Laminar-Turbulent Transition in Gas Turbine Engines," ASME Journal of Turbomachinery, Vol. 113, pp. 509–537.
- Mangalam, S. M., M. S. Wusk, and S. Kuppa, 1991, "In-Flight Detection of Stagnation Transition and Separation using Micro-Thin Surface Hot-Films," Society of Flight Test Engineers 22nd Annual Symposium, St. Louis, Mo.

- McConnell, K. G., ca. 1980, "Notes on Vibration Frequency Analysis," prepared for Spring Annual Meeting of The SESA.
- McCormick, M. E., 1968, "An Analysis of the Formation Turbulent Patches in the Transition Boundary Layer," ASME Journal of Applied Mechanics, Vol. 35, pp. 216–219.
- Meyer, R. X., 1958, "The Effect of Wakes on the Transient Pressure and Velocity Distributions in Turbomachines," Transactions of the ASME, Vol. 80, pp. 1544–1552.
- Narasimha, R., 1985, "The Laminar–Turbulent Transition Zone in the Boundary Layer," Prog. Aerospace Sci., Vol. 22, pp. 29–80.
- Obremski, H. J., and A. A. Fejer, 1967, "Transition in Oscillating Boundary Layer Flows," Journal of Fluid Mechanics, Vol. 29, pp. 93–111.
- Orth, U., 1993, "Unsteady Boundary Layer Transition in Flow Periodically Disturbed by Wakes," ASME Journal of Turbomachinery, Vol. 15, pp. 707–713.
- Pfeil, H., R. Herbst, and T. Schroder, 1983, "Investigation of the Laminar–Turbulent Transition of Boundary Layers Disturbed by Wakes," ASME Journal of Engineering for Power, Vol. 105, pp. 130–137.
- Pfeil, H., and R. Herbst, 1979, "Transition Procedure on Instationary Boundary Layers," ASME Paper 79–GT–128.
- Press, W. H., S. A. Teukolsky, W. T. Vetterling, and B. P. Flannery, 1992, Numerical Recipes in FORTRAN, Cambridge University Press, Cambridge, MA.
- Pucher, P., and R. Gohl, 1987, "Experimental Investigation of Boundary Layer Separation with Heated Thin–Film Sensors," ASME Journal of Turbomachinery, Vol. 109, pp. 303–309.
- Roberts, W. B., 1980, "Calculation of Laminar Separation Bubbles and their Effect on Airfoil Performance," AIAA Journal, Vol. 18, pp. 25–31.
- Schlichting, H., 1979, Boundary–Layer Theory, McGraw–Hill, New York, NY.
- Schmidt, R. C., and S. V. Patankar, 1991, "Simulating Boundary Layer Transition with Low–Reynolds Number k – ϵ Turbulence Models: Parts I and II," ASME Journal of Turbomachinery, Vol. 113, pp. 10–26.
- Schroder, T., 1991, "Investigations of Blade Row Interaction and Boundary Layer Transition Phenomena in a Multistage Aero Engine Low Pressure Turbine by Measurements with Hot–Film Probes and Surface Mounted Hot–Film Gauges," in Boundary Layers in Turbomachines, von Karman Institute for Fluid Dynamics, Lecture Series 1991–06.
- Schubauer, G. B., and P. S. Klebanoff, 1956, "Contributions on the Mechanics of Boundary–Layer Transition," NACA Report No. 1289.

- Schubauer, G. B., and H. K. Skramstad, 1948, "Laminar Boundary-Layer Oscillations and Transition on a Flat Plate," NACA Report No. 909.
- Schulte, V. and H. P. Hodson, 1996, "Unsteady Wake-Induced Boundary Layer Transition in High Lift LP Turbines," ASME Paper 96-GT-486.
- Schulte, V. and H. P. Hodson, 1994, "Wake-Separation Bubble Interaction in Low Pressure Turbines," AIAA Paper 94-2931.
- Seifert, A., 1995, "The Turbulent Spot as a Stabilizing Agent of a Transitional Boundary Layer," personal communication.
- Sharma, O. P., R. H. Ni, and S. Tanrikut, 1994, "Unsteady Flows in Turbines – Impact on Design Procedure," AGARD Lecture Series 195, Neuilly Sur Seine, France.
- Shin, H., 1993, private communication.
- Smith, L. H., 1966, "Wake Dispersion in Turbomachines," Transactions of the ASME, Series D, Vol. 88, pp. 688-690.
- Smith, S. F., 1965, "A Simple Correlation of Turbine Efficiency," Journal of The Royal Aeronautical Society, Vol. 69, pp. 467-470.
- Solomon, W. J. and G. J. Walker, 1995, "Observations of Wake-Induced Transition on an Axial Compressor Blade," ASME Paper 95-GT-381.
- Stack, J. P., S. M. Mangalam, and S. A. Berry, 1987, "A Unique Measurement Technique to Study Laminar-Separation Bubble Characteristics on an Airfoil," AIAA Paper 87-1271.
- Suder, K. L., J. E. O'Brien, and E. Reshotko, 1988, "Experimental Study of Bypass Transition in a Boundary Layer," NASA TM-100913.
- Thomsom, W. T., 1981, Theory of Vibrations with Applications, Prentice-Hall, Inc., Englewood Cliffs, New Jersey.
- TSI Incorporated, 1983, "IFA 100 Intelligent Flow Analyzer Instruction Manual," St. Paul, MN.
- TSI Incorporated, 1970, "Hot Film and Hot Wire Anemometry Theory and Application," Technical Bulletin 5, St. Paul, MN.
- Turner, M. G., 1995, "Multistage Turbine Simulations with Vortex-Blade Interaction," ASME Paper 95-GT-288.
- Vijayaraghavan, S. B. and P. Kavanagh, 1987, "Flow Experimentation in a Large-Scale Cascade Facility," Iowa State University, ERI Report TCRL-35.

- Walker, G. J., 1993, "The Role of Laminar-Turbulent Transition in Gas Turbine Engines: A Discussion," ASME Journal of Turbomachinery, Vol. 117, pp. 207-217.
- Walker, G. J., 1989, "Modeling of Transitional Flow in Laminar separation Bubbles," 9th ISABE, Athens, Greece.
- Walker, G. J., 1975, "Observations of Separated Laminar Flow on Axial Compressor Blading," ASME Paper 75-GT-63.
- White, F. M., 1974, Viscous Fluid Flow, McGraw-Hill, New York, NY.
- Wilson, D. G., 1984, The Design of High-Efficiency Turbomachinery and Gas Turbines, MIT Press, Cambridge, MA.
- Wisler, D. C., 1985, "Loss Reduction in Axial-Flow Compressors Through Low-Speed Model Testing," ASME Journal of Engineering for Gas Turbines and Power, Vol. 107, pp. 354-363.
- Zerkle, R. D., and R. J. Lounsbury, 1987, "The Influence of Freestream Turbulence and Pressure Gradient on Heat Transfer to Gas Turbine Airfoils," AIAA Paper 87-1917.